DEPARTMENT OF PHYSICS
UNIVERSITY OF JYVÄSKYLÄ
RESEARCH REPORT No. 10/2009

TOOLS FOR PHYSICS WITH LHC AND RIB

BY
TOMASZ MALKIEWICZ

Academic Dissertation
for the Degree of
Doctor of Philosophy

To be presented, by permission of the
Faculty of Mathematics and Science
of the University of Jyväskylä,
for public examination in Auditorium FYS-1 of the
University of Jyväskylä on August 31, 2009
at 12 o'clock noon

Jyväskylä, Finland
August 2009

PREFACE

The progress in almost all domains of science over the last century does not have its equivalent in history. The Greeks and Romans believed in the Goddess of the Moon, Artemis and Luna, respectively. Looking from their perspective, we are approaching the divine, with commercial trips to the moon soon to become a reality. But what we know about the Universe actually shows how much we still do not understand. We are not sure how the Universe originated in the so–called Big Bang some 14 billion years ago, why we exist, i.e. why there is more baryonic matter in which the Earth is formed than anti–matter and why we can account only for about 4.5% of the matter in the Universe. We do not know what was before the Big Bang. In order to find out answers for these questions, there is a need for more research and experimental efforts.

In many fields of science it may seem that all interesting things have already been discovered. One such domain is accelerator–based nuclear physics. Stable beams were used for the first time in 1932, when Cockroft and Walton developed a 400 keV proton accelerator, to probe and learn about the properties of atomic nuclei. Although almost 8 decades have passed, the most promising areas of study in nuclear and particle physics are still based on the accelerator. The available energy has increased significantly since the 1930s. The proton beam energy in the case of the Large Hadron Collider (LHC) at CERN is 5 orders of magnitude higher than in 1932, while Radioactive Ion Beam facilities (RIBs, e.g. SPES or SPIRAL 2) will use 2 orders of magnitude higher energies and much more intense beams. Modern accelerators can deliver stable beams of charged particles of almost any desired type and with a wide range of possible energies and intensities. For the ALICE experiment, the LHC will collide protons, lead and other ions to recreate, under laboratory conditions, the circumstances just after the Big Bang. The obtained data will allow the study of a state of matter known as quark–gluon plasma, which is believed to have existed about hundred microseconds after the Big Bang. The next generation of RIBs shall give to physicists intense beams of exotic nuclei, i.e. far from the valley of beta stability. To understand better the nature of nuclear forces, the internal structure of the nucleus and the way nuclei have been formed in the early universe and are still being formed during the evolution of stars, one needs to explore the outer regions of the chart of nuclei.

In some natural sciences, such as biology or chemistry, experiments and significant discoveries performed by a single person or a small group are still possi-

ble. In particle and nuclear physics, experiments are nowadays large scale, long–lasting projects. The preparations for the ALICE experiment at CERN started in 1989, whereas for SPES and SPIRAL 2 in 1999. In the ALICE Collaboration there are more than 1000 people, a few hundred are involved in SPES and SPIRAL 2. A single person contribution is usually limited to some part of the project. Nevertheless, the small developments that the individual does bring us closer and closer to the goal, which is understanding better the world around us. It often happens that one does not even see the final result of her/his work. I was taught at the Computer–Aided Analysis of Experimental Data course in 2002 at Warsaw University of Technology, that ALICE will take the first data in April 2005. When completing the MSc degree and starting the PhD studies in Finland in 2004, it became clear that this timeline would not be fulfilled. Therefore, to be able to analyse real experimental data, in addition to work on the ALICE T0 detector I agreed to dedicate some of my time to the experimental efforts for RIBs. Indeed, the first physics data shall be recorded by ALICE only by the end of 2009. The neutron flux measurements for SPES and SPIRAL 2 have been basically performed by a small number of people, typically 3–4, including myself. The impact of our results on the design of RIBs has been evaluated as significant, yet the goals of SPES and SPIRAL 2, the highly intense radioactive ion beams, are expected to be produced in years 2013–2014.

ABSTRACT

My thesis consists of two parts. T0, the fast timing and trigger detector for the ALICE experiment at CERN LHC, is the subject of the first part. My contribution included simulations, design, construction, tests, installation and commissioning of the detector. We hope that the T0 will play a noticeable role in extracting the first physics results and providing the beam diagnostics during the restart of LHC in autumn 2009. This part of my thesis concludes with how T0 can be used for ALICE luminosity and multiplicity measurements as well as for a verification of the position of the interaction along the longitudinal and transverse axis already during the runs in the LHC commissioning period. The outcome of the first LHC injection and extraction tests performed in August 2008 and July 2009 is presented. The results indicate that T0 is functioning well and is ready for the first collisions at the LHC. The development and construction of the T0 detector as a part of the ALICE experiment is discussed. In essence all hardware and software parts of the T0 system, including all the electronics, Offline, Detector Control System, Databases, and so on are described. The consequences of the T0 detector tests including that with a mixted beam of 6 GeV/c negative pions and kaons at CERN PS when the time resolution of 28 ps r.m.s., a world record at that time, was reached, are discussed. The results of simulations of the T0 detector performance for $p + p$ collisions at $\sqrt{s}$ = 900 GeV – 14 TeV using Pythia and Phojet event generators, and for $\sqrt{s_{NN}}$ = 5.5 TeV $Pb + Pb$ collisions using Hijing prove that, despite the small acceptance (the T0 efficiency for $p + p$ minimum bias events is about 40%), the shape of the charged particle density can be estimated based on T0 data alone. The physics framework is outlined in the introductory part, introducing the heavy ion physics concept and formalism with special emphasis on luminosity, particle production in the ultra-relativistic heavy ion collision and QGP signatures. The introductory part is concluded with the role of the ALICE experiment in the LHC scientific program and the description of the ALICE detector.

The second part of my thesis focuses on the measurements of neutron yields by the activation and TOF method performed for SPES and SPIRAL 2 radioactive beam facilities. The work involved several experiments carried out during the years 2004–2008 at JYFL. The results are compared with Monte–Carlo calculations and are discussed in the framework of a converter method for the SPES and SPIRAL 2. Our results have indicated that at 20 MeV the p+^{13}C reaction proposed for SPES is

not competitive. Consequently the converter method has been abandoned in favour of the direct method. Measurements for SPIRAL 2 show that the neutron yield has been overestimated during the modelling of the converter–fission target ensemble, so that the expected number of fissions with a carbon converter is of order 2 – 2.5 $\cdot 10^{13}$ and not 5 $\cdot 10^{13}$ fissions/s, as was initially expected. Measurements also show that the number of fissions achievable with a heavy–water converter is only about 1.4 – 1.5 $\times$ higher than with a carbon converter. It was hoped that a gain close to 2 could be achieved. Following the outcome of the measurements, a re–evaluation of the converter + fission target module has been recommended by the SPIRAL 2 Technical Advisory Committee.

ACKNOWLEDGEMENTS

The work presented in this thesis has been carried out at the JYFL Accelerator Laboratory at the University of Jyväskylä and at CERN during the years 2004–2008.

I'm most grateful to my supervisors, W.H. Trzaska and G. Lhersonneau for their guidance, support, encouragement and patience during all these years. I have been privileged to share their profound ideas and knowledge of particle and nuclear physics.

I'm indebted to W.H. Trzaska for giving me an opportunity to work on the ALICE experiment at CERN. His help at all stages of my work has been essential and invaluable. I'm very grateful to R. Julin who has supported my work since the beginning. I wish to thank J. Rak for interesting discussions, providing the means to work at CERN and to attend conferences. Many thanks are also due to T. Karavicheva, V. Kaplin, D. Kim, L. Betev, P. Hristov, R. Grosso, A. Colla, A. Maevskaya, M. van Leeuwen, J.-Y. Grossiord, B. Cheynis, T. Renk, M. Oledzki, V. Grigoriev, A. Kurepin, and T. Nayak who invited me to participate in the QM2008 conference in Jaipur, India. I thank my Russian and Polish ALICE T0 collaborators for fruitful work.

Neutron yield measurements in the framework of SPES and SPIRAL 2 were proposed by G. Lhersonneau who introduced methods of precise measurements in gamma spectroscopy to me. I express my gratitude to W.H. Trzaska for creating an opportunity to work on the neutron yields measurement. I was in charge of preparing and maintaining almost all parts of the experimental setup and participated in the analysis phase during the years 2004–2008. This would not have worked out so well without the concept of measurement designed by G. Lhersonneau and W.H. Trzaska, and the substantial help at various stages of the measurements from V. Lyapin, K. Ranttila, V. Hänninen, J. Kumpulainen, D. Vakhtin, S. Khlebnikov, G. Tyurin, K. Kolos, Gamma (P. Jones, S. Ketelhut, M. Nyman), RADEF (A. Javanainen, H. Kettunen, A. Virtanen) and IGISOL (I. Moore, H. Penttilä, V. Rubchenya, T. Eronen) groups, and the JYFL workshop which fulfilled our multiple urgent requests, e.g. compressing ^{13}C powder into a pellet and rebuilding the target chamber built at JYFL that was moved to Catania without giving us notice. I wish to thank G. Prete, J. Kurpeta, M.-G. Saint-Laurent, M. Fadil, A. Pichard and L. Cousin for help during experiments and fruitful discussions. I also want to express my gratitude to

P. Heikkinen and J. Hyvönen who changed the beam from d^- to d^+ just before the start of one of the experiments, as well as to S. Valtonen, T. Ropponen and M. Savonen for agreeing to work as operators for us and their involvement in providing us with stable beam. I'm indebted to L. Tecchio and F. Gramegna who supported the SPES measurements at JYFL and invited me for a seminar at LNL. Support allowing the participants from GANIL to come for an unforeseen but highly needed last experiment in September 2008 was granted in emergency by M.H. Moscatello and the SPIRAL 2 project manager M. Jacquemet.

I extend my thanks to J. Pluta and N. Alahari who reviewed the original manuscript of this thesis. The financial support from the University of Jyväskylä and Graduate School in Particle and Nuclear Physics are gratefully acknowledged.
This work is a part of Finnish Centre of Excellence (CoE) in Nuclear and Accelerator Based Physics at the University of Jyväskylä.
The work has been supported by the EU within the 6th framework programme "Integrating Infrastructure Initiative - Transnational Access", Contract Number: 506065 (EURONS).
Part of the simulations for this thesis were performed using the supercomputing resources of the CSC – IT Center for Science Ltd.

I would like to thank the whole staff of JYFL for an inspiring and friendly working atmosphere. Special thanks are due to I. Moore for proofreading and to T. Vesalainen, P. Heinonen, M. Palomäki, S. Päiviö, P. Rahkila, J. Hakala, A. Pekkanen, M. Zgirski, V. Apaja, P. Prus and J. Toppari.

Last but not least I wish to thank my wife Dominika for infinite patience in allowing me to spend so much time at the University, my daughter Zuzanna, my parents, relatives and friends for their support.

Jyväskylä, August 2009
Tomasz Malkiewicz

Contents

List of Figures

List of Tables

XVIII

List of Abbreviations

A

ACORDE	ALICE Cosmic Ray Detector
AOD	Analysis-Object Data
API	Application Programming Interface
ALICE	A Large Ion Collider Experiment
ATLAS	A Toroidal LHC Apparatus

B

BBC	Beam Beam Counter
BNCT	Boron Neutron Capture Therapy

C

CAF	CERN Analysis Facility
CERN	Conseil Europeen de la Recherche Nucleaire (European Organization for Nuclear Research)
CERN PS	CERN Proton Synchrotron accelerator
CFD	Constant Fraction Discriminator
CMS	Compact Muon Solenoid
CPDM	Clock and Pulse Distribution Module
CPU	Central Processing Unit
CTP	Central Trigger Processor

D

DA	Detector Algorithm
DAQ	Data Acquisition System
DCS	Detector Control System
DD	Double-Diffractive
DDL	Detector Data Link
DP	Data Point
DRM	Data Readout Module

E

EMCal	Electromagnetic Calorimeter
ESD	Event-Summary Data

F

FMD	Forward Multiplicity Detector

G

GANIL	Grand Accelerateur National d'Ions Lourds (National Large Heavy Ion Accelerator)
GDC	Global Data Collector
GRPG	Gate and Reference Point Generator
GRS	Global Reference System

H

HIJING	Heavy-Ion Jet Interaction Generator
HLT	High-Level Trigger
HMPID	High-Momentum Particle Identification Detector
HPTDC	High Performance TDC

I

IFMIF	International Fusion Material Irradiation Facility
ISOL	Isotope Separator On Line
ITEP	Institute of Theoretical and Experimental Physics
ITER	International Thermonuclear Experimental Reactor
ITS	Inner Tracking System

L

LCS	Laser Calibration System
LDC	Local Data Concentrator
LED	Leading Edge Discriminator
LHC	Large Hadron Collider
LNL	Laboratori Nazionali di Legnaro (Legnaro National Laboratories)

M

MB	Minimum Bias
MIP	Minimum Ionising Particle
MPD	Multiplicity Discriminator

N

ND	Non-Diffractive
NSD	Non Single-Diffractive

0

OCDB	Offline Condition Database

P

PDC	Physics Data Challenge
PHENIX	Pioneering High Energy Nuclear Interaction eXperiment
PHOS	Photon Spectrometer
PID	Particle Identification
PMD	Photon Multiplicity Detector
PMT	Photomultiplier Tube
PMTs	Photomultiplier Tubes

Q

QCD	Quantum ChromoDynamics
QDC	Charge to Digital Converter
QED	Quantum ElectroDynamics
QGP	Quark-Gluon Plasma
QTC	Charge to Time Converter

R

RHIC	Relativistic Heavy Ion Collider
RIB	Radioactive Ion Beam

S

SM	Standard Model
SPES	Study and Production of Exotic Species
SPIRAL	Production System of Radioactive Ion and Acceleration On–Line
SPS	Super Proton Synchrotron

T

T0TU	T0 Trigger Unit
TDC	Time-to-Digital Converter
TOF	Time Of Flight
TOTEM	Total Elastic and Diffractive Cross-section Measurement
TRD	Transition-Radiation Detector
TRM	TDC Readout Module
TTCrx	Timing, Trigger and Control Receiver ASIC
TVDC	T0 Vertex Unit

V

VDU	Variable Delay Unit

Z

ZDC	Zero-Degree Calorimeter

Part I

ALICE T0 detector

1 Introduction

According to our present knowledge, there are no free quarks in nature. However, with rising temperature hadrons melt into their constituents, quarks and gluons, which can move freely within a new state of matter called the quark–gluon plasma (QGP). Following the current theoretical knowledge, the QGP should be formed in the process of collisions of opposing beams of ultra–highly energetic heavy nuclei. The phase transition leading to the creation of the QGP is the only one of those predicted by the Standard Model (SM), that can be reached within laboratory experiments. Ultra–relativistc heavy–ion collisions are thus expected to be a milestone in verifying the SM predictions. The experimental observables achieved so far are not a definite proof of the existence of QGP.

An objective of the ultrarelativistic collision experiment is to create in a laboratory environment a tiny amount of matter at extremely high temperatures. The present centres of experimental activities are the Relativistic Heavy Ion Collider (RHIC) at Brookhaven National Laboratory [1] and the Large Hadron Collider (LHC) at CERN [2]. The latter provides a qualitative improvement with respect to previous programmes, with collisions at a centre of mass energy per nucleon almost 30 times larger than at RHIC. The four major LHC experiments are ALICE, ATLAS, CMS and LHCb. The ALICE experiment [4], depicted in Fig. 1.1, is a general–purpose heavy–ion experiment. It is devoted to the study of the strong force binding the quarks in nucleons by examining the QGP signatures. Further evidence for the existence of QGP is expected to be found and the properties of this new state of matter systematically studied by ALICE.

The T0 [5, 6, 7], which is the subject of the first part of this thesis, is one of the ALICE forward detectors. It consists of two arrays of Cherenkov counters, placed on opposite sides of the Interaction Point (IP), as shown in Fig. 1.2. The T0 detector is significant for the operation of ALICE. It fixes the time when opposing accelerated particles collide with better than 50 ps resolution. The Time-Of-Flight detector, the only detector in need of such precise timing information, will hence be able to measure the time it takes a particle to travel from the IP to the outer rim with better than 100 ps accuracy. In addition, the T0 determines on–line the point of collision with an accuracy of 1.5 cm. After full track reconstruction the location of the IP will be known with a precision of microns but rough on–line vertex determination is crucial for choosing the events suitable for ALICE. T0 is also capable of measuring the multiplicity of particles emerging from the collision, thereby generating signals

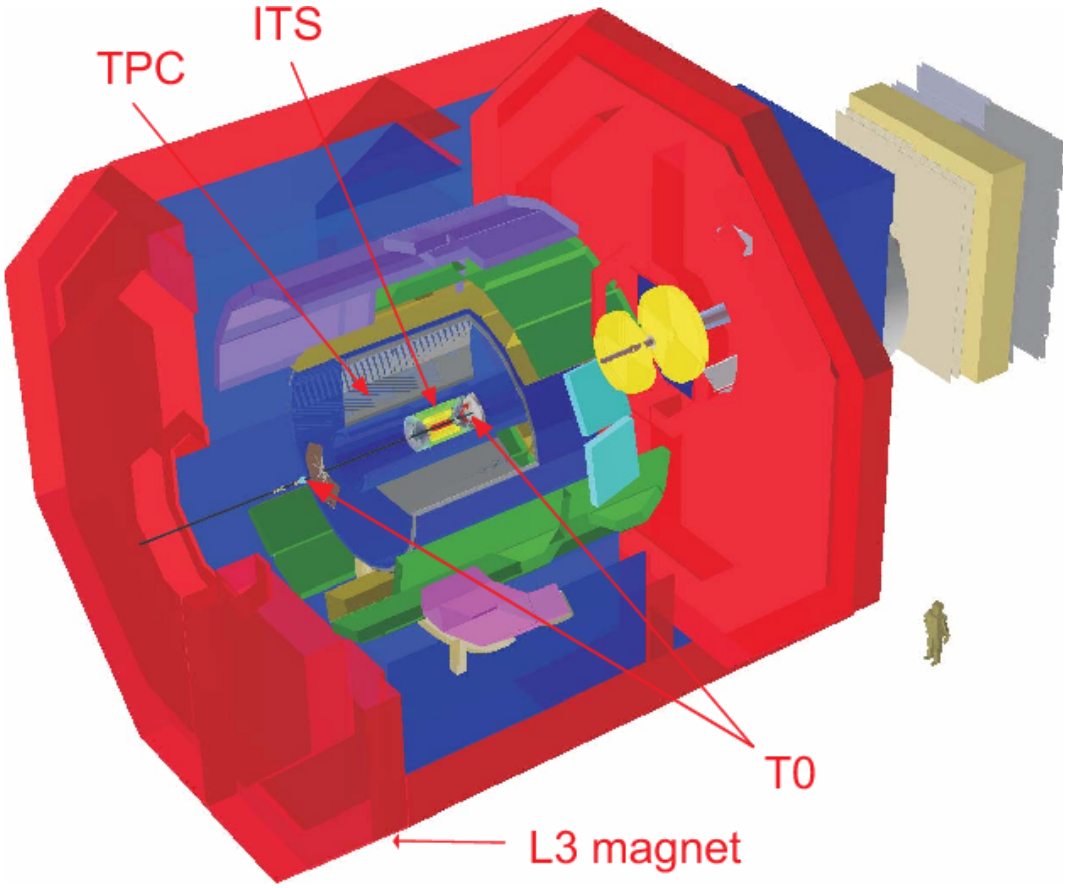

FIGURE 1.1 The ALICE detector [3].

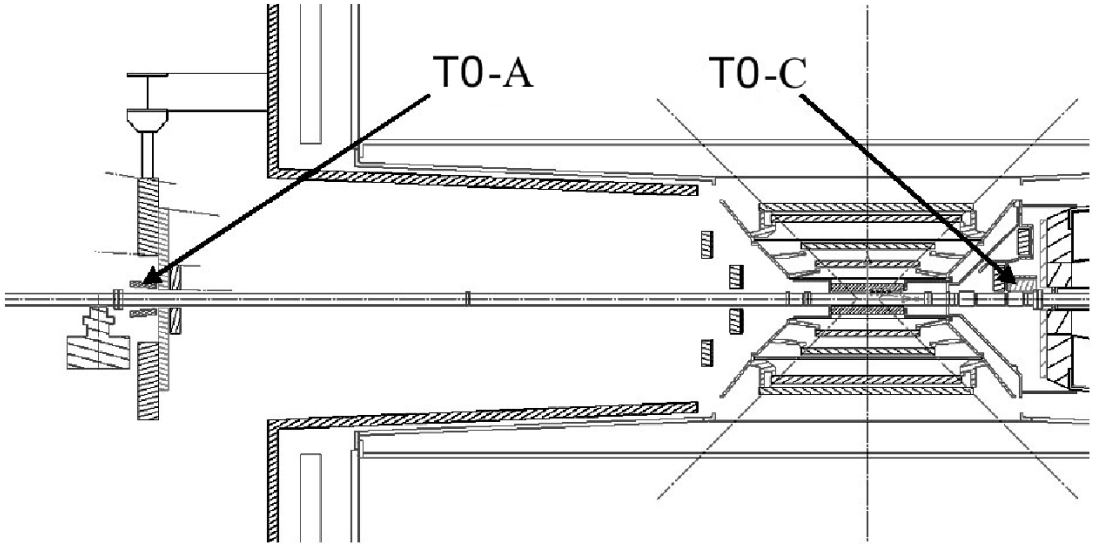

FIGURE 1.2 Location of T0 detector arrays in ALICE.

allowing event registration by the other detector. Last but not least, T0 will be one of the first detectors to be switched on during the restart of the LHC later this year

(2009). T0 will provide rudimentary beam diagnostics, measure the luminosity and the charged particle density of the first collision events registered in ALICE.

A short introduction to heavy ion physics and ultra–relativistic heavy ion collisions with the particular emphasis on the observables relevant to the ALICE T0 is given in the following chapter. An overview of the LHC and the ALICE experiment is then presented. The remaining chapters of the first part of the thesis are dedicated to the T0, describing the hardware and the software in detail as well as its use in ALICE, with emphasis on the first physics.

2 Relativistic hadron collisions

The Standard Model (SM) is the most successful theory of elementary particles and their fundamental interactions developed so far. The theory includes three fundamental interactions[1] and the 12 elementary particles plus their corresponding antiparticles (see Table. 2.1). They make up all the visible matter in the Universe[2]. In

TABLE 2.1 Three generations of elementary particles with gauge bosons (rightmost column) in Standard Model. Matter, constituted out of point-like particles, is grouped into three families. Each family consists of two quarks and two leptons. All leptons are affected by weak force mediated by $W^{\pm}$ and Z^0 bosons, charged ones in addition by the electromagnetic force mediated by photons. Quarks are affected by strong (mediated by gluons), weak and electromagnetic force. It is worth noting that in this theory both matter and interactions are described as particles.

Family	I		II		III		Gauge bosons	
		[MeV/c^2]		[MeV/c^2]		[MeV/c^2]		Force
Quarks	u	1.5 – 3.3	c	$1.27(0.11)\cdot 10^3$	t	$171.2(2.1)\cdot 10^3$	g(8)	1
	d	3.5 – 6.0	s	104(34)	b	$4.2(0.2)\cdot 10^3$	γ	$\sim 10^{-2}$
Leptons	e^-	0.511	μ^-	106	τ^-	$1.78 \cdot 10^3$	$W^{\pm}$	$\sim 10^{-7}$
	ν_e	$< 2\cdot 10^{-6}$	ν_μ	< 0.19	ν_τ	< 18.2	Z^0	

[1]The three fundamental interactions included in the SM are: strong, weak and electromagnetic. Gravity is not included. Weak and electromagnetic interactions are sometimes grouped together in the Electroweak theory. The gravitons, the postulated gauge bosons of the gravitation which are not included in the SM, have not been found yet. The strength of gravitational force with respect to strong force is $\sim 10^{-39}$ (see also Table. 2.1).

[2]Standard Model is however still incomplete, it does not explain:

- The relationship between different interactions (strong, electroweak and gravity);
- The nature of dark matter and dark energy;
- The matter–antimatter asymmetry of the universe;
- The existence of three generations of quarks and leptons;

analogy to the electric charge, a property called $color$ is assigned to each quark included in the SM. The color, which can take one of the three possible values: red, $blue$ and $green$, determines how particles interact with each other. The quarks carry color charge and hence interact via the strong force. The confining behaviour of the strong force results in quarks being perpetually bound to one another, forming color–neutral hadrons[3] containing either a quark and an antiquark (mesons) or three quarks (baryons[4]). Quarks also carry electric charge and weak isospin. They thus interact with other fermions both electromagnetically and weakly. Up, $charm$ and top quarks posses an electric charge of 2/3 e; $down$, $strange$ and $bottom$ of –1/3 e. The remaining six fermions included in the SM do not carry color charge. The electron, the muon and the tauon carry an electric charge of $-e$ thus interact electromagnetically and weakly. The three neutrinos in turn do not carry electric charge with their motion being directly influenced only by the weak nuclear force.

Our current understanding of the evolution of the early Universe is such that prior to one hundredth of a second after the Big Bang, the Universe had become hotter and denser until matter actually changed its phase. The Universe evolved from an initial state of extreme energy density to its present state through rapid expansion and cooling, traversing the series of phase transitions. The SM predicts the occurrence of phase transitions in quantum fields at characteristic energy densities. Phase transitions involving elementary quantum fields are intrinsically connected to the breaking of fundamental symmetries of nature and thus to the origin of mass. Global features of our Universe, like baryon asymmetry or the large scale structure, i.e. galaxy distribution, are believed to be linked to characteristic properties of these phase transitions. The intrinsic symmetries predicted by theory, valid at high energy densities, are broken below certain critical energy densities. Particle content and particle masses originate as a direct consequence of the symmetry–breaking mechanism.

One of the aims of ultra–relativistic heavy–ion physics is to apply and extend the SM to complex, dynamically evolving systems of finite size. Collisions of heavy–ions at the velocities close to the velocity of light allows the study of nuclear matter under conditions of extreme density and temperature. The theory of strong interactions, Quantum ChromoDynamics (QCD), predicts that at a critical temperature, $T_c \simeq 170$ MeV, corresponding to an energy density of $\varepsilon_c \simeq 1$ GeV/fm^{-3}, nuclear matter undergoes a phase transition to a deconfined state of quarks and gluons

- Conservation of lepton and baryon number;
- Neutrino masses and mixing;
- The pattern of weak quark couplings (CKM matrix).

Even if it would have been complete, it would describe a mere five percent of the Universe. What comprises the remaining 95% is not certain.

[3]Hadrons are colorless (also called white) which is the consequence of the fact that in the corresponding SU(3)-algebra the constituent quarks sum up to 0 (i.e. red + $blue$ + $green$ = $white$).

[4]The proton(uud) and the neutron(udd) are the two baryons having the smallest mass.

called QGP. Moreover, chiral symmetry restoration leads to quark masses being reduced from their large effective values in hadronic matter to the small bare ones. In ultra–relativistic heavy–ion collisions (URHIC), one expects to attain energy densities which reach and exceed ε_c. This makes the QCD phase transition the only one predicted by the Standard Model that is reachable in laboratory conditions.

In order to look closer into the topics described above, I introduce now the formalism used in URHIC.

2.1 Notations and conventions

Natural units with $c = \hbar = 1$, and a notation of Bjorken and Drell [8] are widely used in URHIC and in this work. The space–time coordinates of a point x are represented by a contravariant vector:

$$x^\mu \;=\; (x^0, x^1, x^2, x^3) \;=\; (t, x, y, z) \;=\; (t, \mathbf{x}). \tag{2.1}$$

Similarly, the momentum vector p is defined by a contravariant vector:

$$p^\mu \;=\; (p^0, p^1, p^2, p^3) \;=\; (E, p_x, p_y, p_z) \;=\; (E, \mathbf{p}_T, p_z) \;=\; (E, \mathbf{p}). \tag{2.2}$$

The space–time metric tensor in Minkowski space, given in Eq. 2.3, is used to relate the covariant vector x_μ to x^μ: $x_\mu \equiv (x_0, x_1, x_2, x_3) \equiv g_{\mu\nu}\, x^\nu$ = (t, –x, –y, –z).

$$g_{\mu\nu} \;=\; \begin{pmatrix} 1 & 0 & 0 & 0 \\ 0 & -1 & 0 & 0 \\ 0 & 0 & -1 & 0 \\ 0 & 0 & 0 & 1 \end{pmatrix} \tag{2.3}$$

2.2 Kinematic variables

It is common in URHIC to use kinematic variables which have simple properties under a change of the frame of reference.

2.2.1 Light–cone variables

Considering a high–energy reaction: a + b $\rightarrow$ c + X , a detected particle c can be identified as originating from one of the colliding particles a or b. The longitudinal axis, designated as the z–axis, is along the direction of the incident beams. For convenience, the same symbol is used to represent a particle and its four–momentum, e.g. c = (c_0, $\mathbf{c}_T$, c_z), where c_0 is the energy of the particle, $\mathbf{c}_T$ is its two–dimensional transverse momentum in the plane perpendicular to z–axis and c_z is its longitudinal momentum.

Linear combinations of c_0 and c_z have special properties under a Lorentz transformation in the z–direction. $c_+ = c_0 + c_z$ is called the forward light–cone momentum, while $c_- = c_0 - c_z$ – the backward light–cone momentum of c. c_+ of any particle in one frame is related to c_+ of the same particle in another boosted Lorentz frame by a constant factor[5]. If one considers a particle c as fragmenting from particle b, then the ratio of their forward light–cone momenta is independent of the Lorentz frame. This ratio defined as:

$$x_+ = \frac{c_0 + c_z}{b_0 + b_z} \tag{2.4}$$

is called the forward light–cone variable, while:

$$x_- = \frac{c_0 - c_z}{b_0 - b_z} \tag{2.5}$$

is called a backward light–cone variable. x_+ and x_- are always positive, e.g. x_+ is positive because a daughter particle can not possess higher forward light–cone momentum than its parent particle. Due to its Lorentz invariant property, x_+ is used not only to specify the ratio between daughter and parent particle. It may also specify the relationship between the momentum of particle c relative to another reference particle.

The particle c may be detected as a free particle as well. As it is not subject to any interaction, its four–momentum obeys the relation appropriate for a free particle:

$$c^2 = c_0^2 - \mathbf{c}^2 = m_c^2. \tag{2.6}$$

where m_c^2 represents the rest mass of c. Eq. 2.6 is called the mass–shell condition. If in turn particle c is not considered a free particle and it is subject to interactions with other products of the reaction, X, it is convenient to separate the transverse degree of freedom from the longitudinal one, and write Eq. 2.6 as:

$$c_0^2 - c_z^2 = m_c^2 - \mathbf{c}_T^2 = m_{c_T}^2, \tag{2.7}$$

where $m_{c_T}^2$ is the transverse mass of particle c.

2.2.2 Collision energy

Let's consider that the undetected collection of particles X in the reaction a + b $\rightarrow$ c + X consists of a single particle with a rest mass m_X corresponding to the minimum value the rest mass of X allowed by conservation laws of baryon number, charge,

[5]That factor for forward light–cone momentum is: $\gamma(1+\beta)$ and for backward light–cone momentum: $\gamma(1-\beta)$, where $\beta = \frac{v}{c}$. Here, v is a velocity of a particle and c is the speed of light.

etc. The three–momentum of c is then equal to the three momentum of X. From the energy conservation law, the center–of–mass (CM) energy of the collision, denoted $\sqrt{s}$ [6], can be written as:

$$\sqrt{s} = \sqrt{(c_z^*(max))^2 + m_c^2} + \sqrt{(c_z^*(max))^2 + m_X^2}, \quad (2.8)$$

where * marks the quantities in the center–of–mass system (CMS).

It is worth comparing the amount of energy available in the CMS in a collider and in a fixed target experiment. Assuming that the colliding beams have the same energy, i.e. E_{beam}, we can write:

$$\sqrt{s} = 2 \cdot E_{beam}. \quad (2.9)$$

In a fixed target experiment, with a beam of energy E_{beam} impinged on the target at rest with rest mass m_0, we get:

$$\sqrt{s} = \sqrt{2 \cdot m_0 \cdot E_{beam}}. \quad (2.10)$$

In the latter, much of the energy goes toward moving the particles forward which results from the impact with the target. In a collider experiment the total energy is available for producing new particles. When the colliding beams consist of nucleons or antinucleons, i.e. p, $\bar{p}$, n or $\bar{n}$, the collisions are named N + N. A + A collisions mean that the beams consist of nuclei, e.g. Pb, Au, Ar or U. In A + A collisions, the CM energy per nucleon, $\sqrt{s_{NN}}$, is used:

$$\sqrt{s_{NN}} = \frac{\sqrt{s}}{2N}, \quad (2.11)$$

where N is the number of nucleons in each of the colliding ions. Collision energies envisaged for the LHC are discussed in detail in Chapter 3.1.

2.2.3 Rapidity

The rapidity variable y, defined in Eq. 2.12, is commonly used to describe a particle in terms of its energy p_0, and transverse momentum p_z.

$$y = \frac{1}{2} \cdot ln\left(\frac{p_0 + p_z}{p_0 - p_z}\right). \quad (2.12)$$

Rapidity is a dimensionsless quantity which relates the forward and the backward light–cone momenta of a particle. It is worth noting that in a nonrelativistic limit,

[6] See Appendix A.1 for the definition of the Mandelstam variable s.

the rapidity of a particle travelling in a longitudinal direction is equal to the velocity of the particle in the units of speed of light. The rapidity y of the particle in the laboratory frame F is related to the rapidity y' in a boosted Lorentz frame F', which moves with a velocity β in the z direction, by:

$$y' = y + \frac{1}{2} \cdot ln\left(\frac{1-\beta}{1+\beta}\right) = y - \frac{1}{2} \cdot ln\left(\frac{1+\beta}{1-\beta}\right). \quad (2.13)$$

This property of y variable under the Lorentz transformation makes it suitable for describing the dynamics of relativistic particles.

2.2.4 Pseudorapidity

In order to obtain the rapidity of the particle, one needs to measure its energy and longitudinal momentum. In most of the experiments it is only possible to measure the angle of a detected particle with respect to the beam axis. The pseudorapidity variable η is in that case a convenient quantity to characterise the particle:

$$\eta = -ln\left(tan\frac{\theta}{2}\right), \quad (2.14)$$

where θ is the angle between the particle's momentum $\mathbf{p}$ and the beam axis.

In terms of momentum, the pseudorapidity can be written as:

$$\eta = \frac{1}{2} \cdot ln\left(\frac{|\mathbf{p}| + p_z}{|\mathbf{p}| - p_z}\right). \quad (2.15)$$

As can be seen from the comparison of Eq. 2.12 and Eq. 2.14, η coincides with rapidity when the momentum is large, i.e. $|\,\mathbf{p}\,| \approx \mathrm{p_0}$.

In some experiments, only pseudorapidity is measured to obtain a particle distribution $\mathrm{dN/d}\eta$. $\mathrm{dN/d}\eta$ is the integral of $\mathrm{dN/d}\eta\mathrm{d}\mathbf{p}_T$ with respect to transverse momentum. Similarly for rapidity, dN/dy is the integral of $\mathrm{dN/dyd}\mathbf{p}_T$. The dependence between the two integrals is:

$$dN/d\eta d\mathbf{p}_T = \sqrt{1 - \frac{m^2}{m_T^2 cosh^2 y}} \cdot dN/dy d\mathbf{p}_T. \quad (2.16)$$

Eq. 2.16 infers that in the region of rapidities much greater than 0, $\mathrm{dN/d}\eta$ and dN/dy are approximately the same, while in the region close to zero η has a depression with respect to the y distribution.

2.3 Particle production in nucleon–nucleon collisions

Nuclei are composed of many nucleons thus their collisions involve the dynamics of their colliding constituents. Nucleon–nucleon data give insight and provide valuable information on nucleus–nucleus collisions. The important question for ultra–relativistic nucleus–nucleus collisions is to which extent the longitudinal kinetic energies carried initially by colliding nuclei are dissipated in the collision with the release of energy into other degrees of freedom.

The total nucleon–nucleon cross–section, σ_{NN}, for 3 GeV < $\sqrt{s}$ < 100 GeV is relatively constant and equal to approximately 40 mb [10]. The inelastic cross–section is much larger than the elastic one, e.g. for the energy range mentioned above the former is about 30 mb, hence the latter is $\sim$ 10 mb. The inelastic processes can be divided into diffractive and non–diffractive dissociation processes. After the diffractive process, one or both of the colliding nuclei may become slightly excited and lose a relatively small amount of energy. After the non–diffractive dissociation, the colliding nucleons lose a substantial fraction of kinetic energy. An important property of URHIC is that the probability for the colliding nucleons to lose a substantial fraction of energy is large. Only some 10% of the inelastic cross–section is attributed to diffractive events. The lost energy is taken up in producing particles.

2.3.1 Charged particle density

Most particles produced in URHIC, $\sim$ 80–90%, are pions. The rest consist of kaons, baryons, anti–baryons and other particles. The total number of particles produced is called the multiplicity of the collision and marked with N. Ionising particles are easier to detect and the majority of the detection methods are only sensitive to them. There is withal a good estimate for the number of neutral particles produced: based on experimental data, roughly equal numbers of π^+, π^- and π^0 are produced [15]. It is thus sometimes useful to use charged–particle multiplicity N_{ch}, since the total multiplicity can be well assessed from N_{ch}.

Fig. 2.1 presents a simulated charged particle density $dN_{ch}/d\eta$ for $p+p$ collisions at $\sqrt{s}$ = 14 TeV. For comparison: at the incident beam momentum of 100 GeV/c a nucleon–nucleon collision produces on average 6 charged particles. The concept of measuring $dN_{ch}/d\eta$ in ALICE is discussed in detail in Chapter 6.2. The simulated charged particle yield in $p+p$ collisions at $\sqrt{s}$ = 14 TeV is shown in Fig. 2.2.

Charged particle density in $\sqrt{s_{NN}}$ = 200 GeV $Au+Au$ collisions measured at RHIC is presented in Fig. 2.3. In A + A collisions there is a high probability of finding leading particles, i.e. the ones resembling the incident particles in the respective fragmentation regions[7]. It is worth noting that the leading particle effect, a

[7]Fragmentation region is the small–angle (centre–of–mass) region of an interaction. Particles in the fragmentation region have momenta similar to the incident particles and are among the fastest registered in the forward or the backward direction.

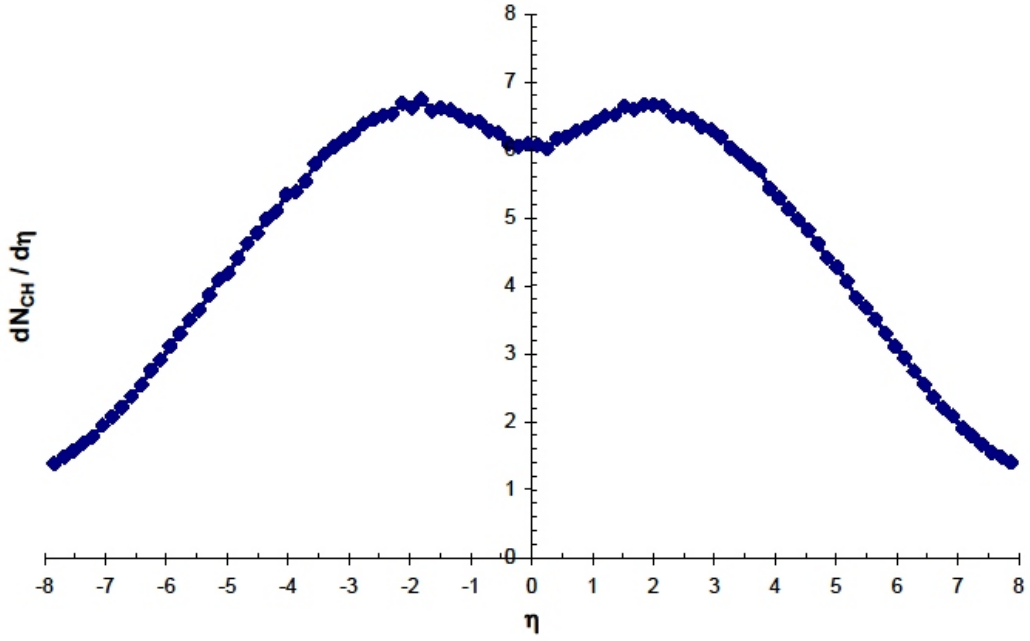

FIGURE 2.1 Charged–particle multiplicity distribution for a $p+p$ collision at $\sqrt{s}$ = 14 TeV.

phenomenon of leading particles appearing in the fragmentation region, appears in $p+p$ collisions but not in e^+e^- annihilation. In $p+p$ collisions, the colliding baryons retain about half of their momentum after the collision thus only about half of their CM energy is used to produce particles. Therefore the multiplicity of particles produced in a $p+p$ collision is smaller than in e^+e^- collision with the same CM energy.

Various phenomenological models have been proposed to describe the multiparticle production at high energies. The Pomeron exchange, which dominates at asymptotic energies, is one of them [12]. The model relates the energy dependence of the total cross–section to the multiplicity production using a small number of parameters. It is the basis for many Monte Carlo event generators describing soft hadron collisions [29, 30, 31]. The energy dependence of charged–particle density in the central rapidity region is described in this model as:

$$\frac{dN}{d\eta_{ch}}|\eta \approx 0 \quad \sim \quad \left(\frac{s}{s_0}\right)^{\alpha_p - 1} . \tag{2.17}$$

Here, α_p = 1.12±0.02 is the intercept of the pomeron trajectory, and $s_0 \approx 1$ GeV^2 is a model parameter which defines the energy–mass scale [12].

As far as charged–particle densities in $p+\overline{p}$ collisions are concerned, the difference in densities between $p+p$ and $p+\overline{p}$ interactions is predicted to decrease as $1/\sqrt{s}$ at high energies [55]. This difference was last measured at the CERN ISR to be

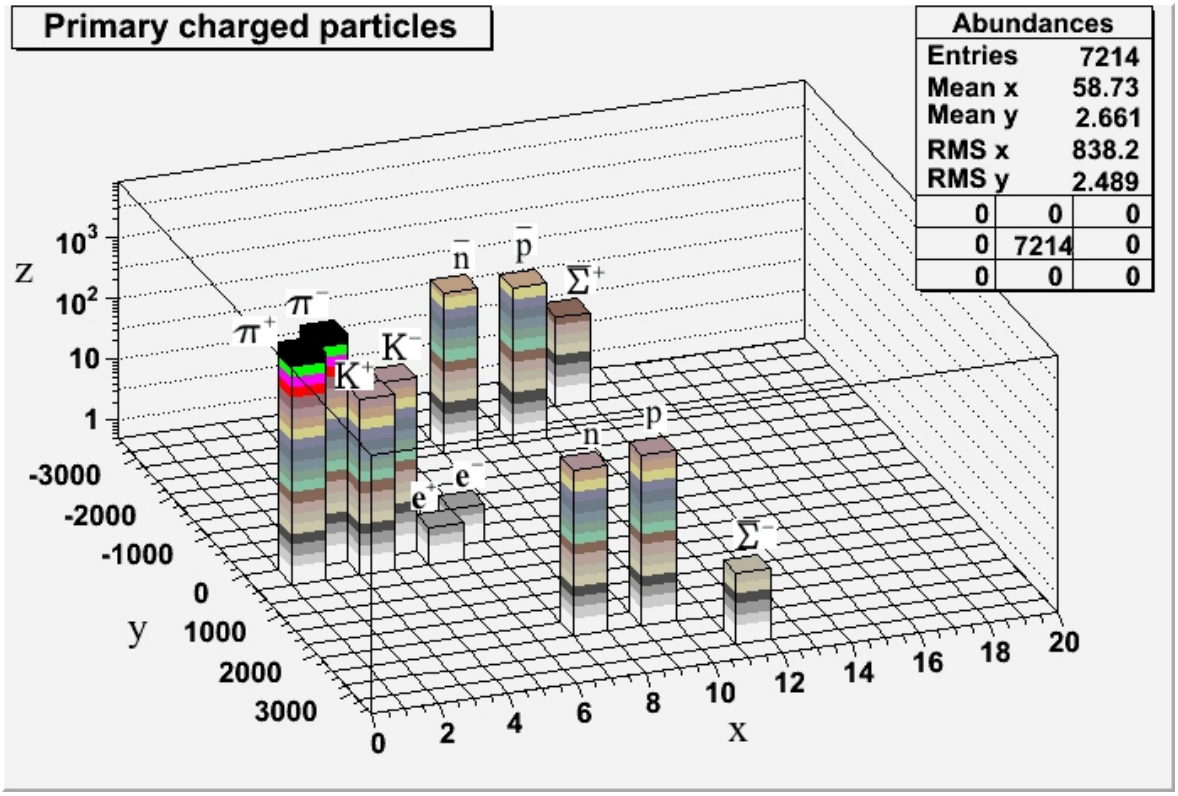

FIGURE 2.2 Abundances of the charged particles produced in $p+p$ collisions at $\sqrt{s}$ = 14 TeV. PDG codes [11] of the particles are marked on y axis.

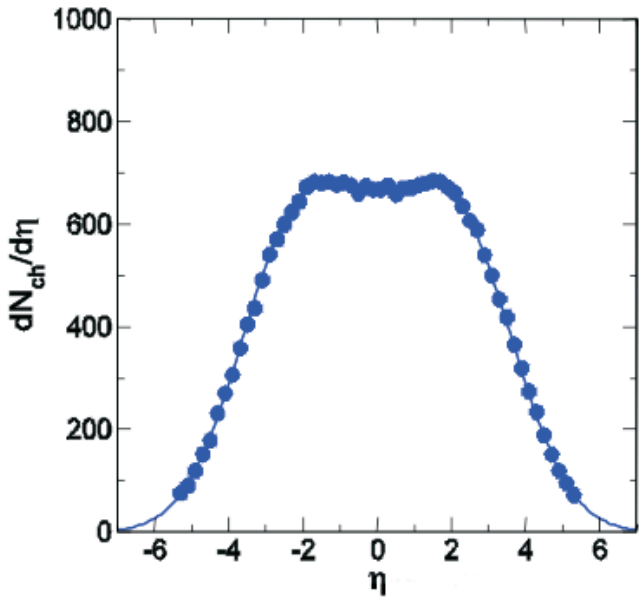

FIGURE 2.3 Charged particle density at $\sqrt{s_{NN}}$ = 200 GeV $Au+Au$ collisions measured by PHOBOS experiment at RHIC [23].

1.5–3% at $\sqrt{s}$ = 53 GeV. Extrapolating to $\sqrt{s}$ = 900 GeV one obtains a hardly measurable difference of about 0.1–0.2%. All the same, Pythia [29] and Phojet [30] predict a difference of about 2–3%, practically independently of the energy. There are also models involving odderon[8] exchange, which predict a non–vanishing difference between $p + p$ and $p + \overline{p}$ interactions even at asymptotic energies, depending on the intercept of the odderon trajectory. Some controversy remains however about such a possibility, both in experimental results and in theoretical investigations.

2.3.2 Impact parameter and Centrality

The impact parameter b represents the transverse distance that the two particles would fly by in a collision if there was no interaction. The presence of particles with properties typical for a fragmentation process among products of nuclear interaction led to the formulation of the participant–spectator model [13]. The participants are the nucleons that interact in the collision, while the spectators essentially are unaffected by the collision and do not contribute to the particle production. The collision geometry (i.e. the impact parameter) determines the number of nucleons that participate in the collision, as shown in Fig. 2.4. The impact parameter is not directly measurable in experiments. Instead, a measure called centrality is often used. The exact definition of centrality varies from experiment to experiment, usually involving a cut in the total observed charged particle multiplicity. The cuts, e.g. 0-5%, 5-10%, 10-20%, define the centrality of the collision. Fig. 2.5 presents charged particle densities for various cuts measured at three different CM energies in $Au + Au$ collisions at RHIC. Further discussion on centrality classes relevant for ALICE and the T0 detector can be found in Chapter 6.2.

2.4 Luminosity

Luminosity is the factor connecting the event rate and the interaction cross–section: R = L $\cdot \sigma$. Assuming symmetry in the transverse plane, it can also be expressed as:

$$L = f \cdot N_b \frac{N^2}{2\pi\left(\sigma_1^2 + \sigma_2^2\right)} \cdot F. \tag{2.18}$$

Here, f, N_b, N, and $\sigma_{1,2}$ are, respectively, the revolution frequency, the number of bunches, the number of particles per bunch and the transverse beam sizes of the

[8] Odderon is considered to be the C-parity – 1 partner of the pomeron.

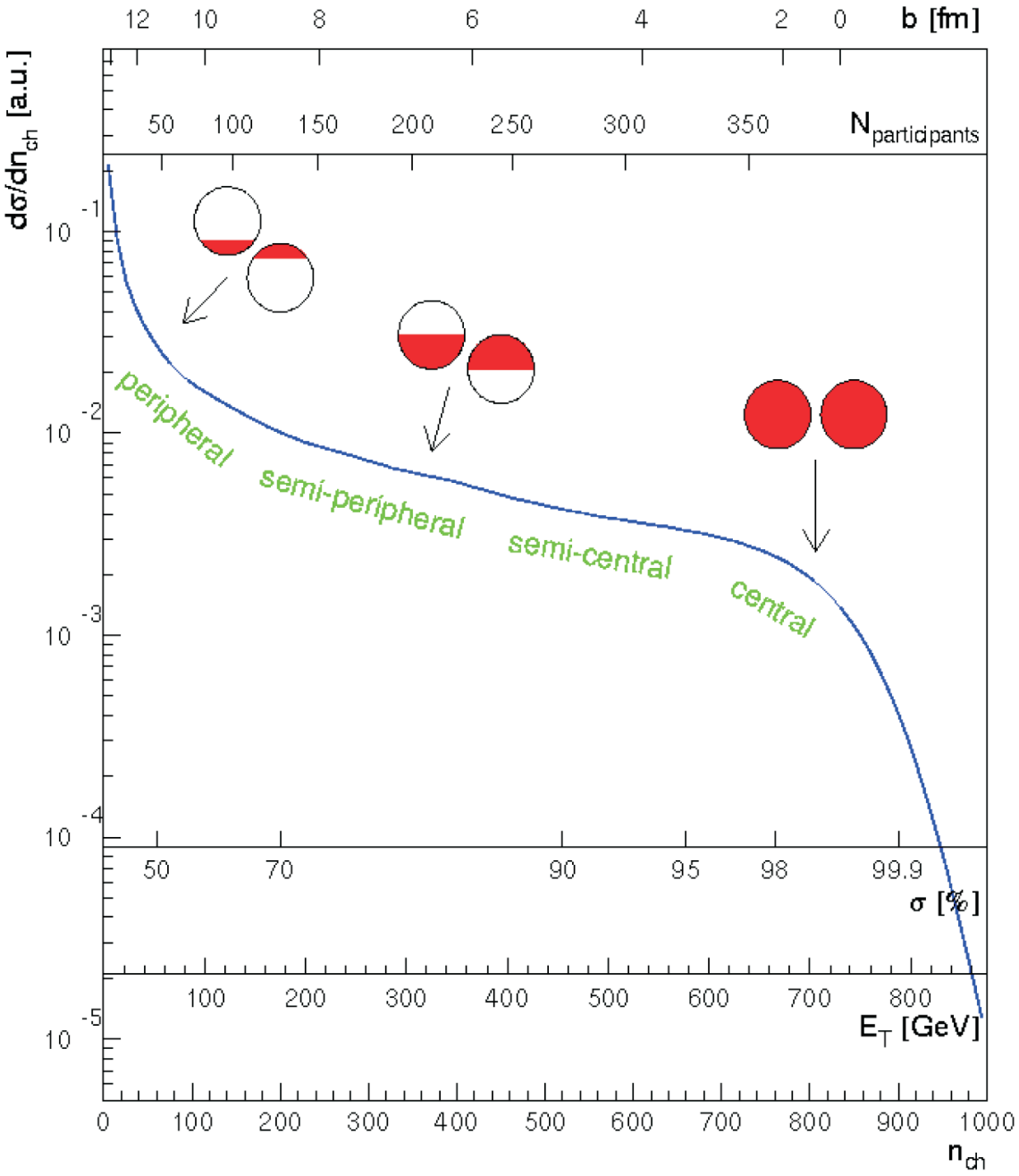

FIGURE 2.4 Simulated cross–section for emitting charged particles in $\sqrt{s_{NN}}$=200 GeV $Au + Au$ collision [14]. The impact parameter and number of nucleons participating in the collision are presented on top axes. The transverse energy and percent of the total cross–section are shown at the bottom. The simulation has been done with Hijing version 1.36 in the pseudorapidity range of $|\eta| < \pm 0.5$.

two beams[9]. F is the reduction factor due to the finite crossing angle ϕ:

$$F = \frac{1}{\sqrt{1 + \left(\frac{tan(\phi/2) \cdot \sigma_{long}}{\sigma_{trans}}\right)^2}}, \tag{2.19}$$

[9]If the colliding beams have opposite charge, e.g. e^+e^-, which is not the case in LHC, the luminosity calculated with Eq. 2.18 would be underpredicted by a factor of two. In case of opposite charges,

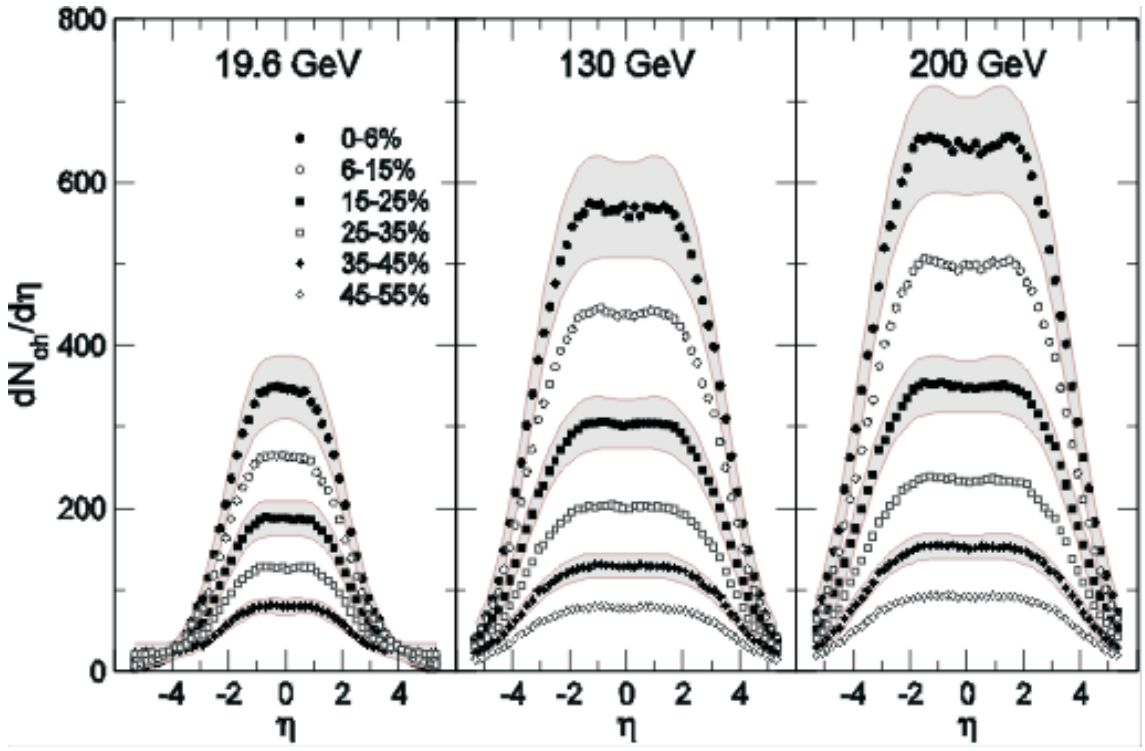

FIGURE 2.5 Charged particle density obtained for various centrality classes (0-6% represents most central collisions). Measurements were performed by PHOBOS experiment at RHIC for $Au + Au$ collisions at three different center–of–mass energies [23].

where σ_{long} is the longitudinal and σ_{trans} the transverse beam size [4].

Eq. 2.18 is one way to determine the luminosity – by measuring the beam parameters. The accuracy is limited to about 10% due to the extrapolation of σ_{trans} from beam profile measurements outside the Interaction Point (IP). Another way is via the rate of some well–known process. E.g. a dependence between the total rate of $p + p$ interactions R_{tot} and the rate of elastic events R_{el} in the forward direction with the momentum transfer $\sqrt{t}$ = 0 can be written as:

$$L = \frac{(1+\rho^2)}{16\pi} \frac{R_{tot}^2}{(dR_{el}/dt)_{t=0}}, \tag{2.20}$$

with ρ being the ratio of the real to imaginary parts of the elastic–scattering forward amplitude. A specialised forward experiment with dedicated beam optics is needed for the measurement of the elastic rate at zero momentum transfer. The key feature is a low beam divergence in the IP. The TOTEM experiment [20] will perform such a measurement at the LHC.

the EM field would 'attract' one beam to another, which would yield an increase in the effective luminosity L^{eff}. This increase can be expressed by the pinch enhancement factor, H_D, as: $L^{eff} = H_D \cdot L$. H_D is of the order of 1.5 – 2.

Finally, knowing the event rate in the detector and the cross–section, the luminosity can also be calculated as:

$$L = \frac{dN/dt}{\sigma \cdot \epsilon \cdot A}. \tag{2.21}$$

Here, dN/dt is the event rate, σ is the cross–section, ϵ is the efficiency of the physics process for a given acceptance A of the detector.

For heavy–ion collisions, there are two cross–sections that can be calculated with sufficient precision: the total hadronic cross–section σ_{tot}, and the cross–section of mutual electromagnetic dissociation. Luminosity calculation in ALICE is discussed in detail in Chapter 6.3 for $p + p$ and A + A collisions separately.

Cross–section and detector simulations are the main source of uncertainty in luminosity determination in ALICE. The uncertainty is initially expected to be $\sim 10\%$. Later it is expected to go down to 5 % with known cross–sections and improved knowledge about the detector parameters.

2.5 Strong and electroweak interactions

2.5.1 Strong interaction

Quantum ChromoDynamics (QCD) explains how quarks couple together in the nucleus. According to this theory, gluons are mediating the interactions between the colored objects such as quarks[10]. Gluons themselves are also colored hence they can interact or couple to one another. The interaction of gluons gives rise to so–called confinement. In the low momentum transfer regime, the quarks in a baryon or meson can not decouple from the other quarks. Therefore we can not study the properties of a free i.e., noninteracting, isolated quark[11]. On the other hand, if two quarks are very close to each other, their coupling is small or may become free (asymptotic freedom).

2.5.2 Electroweak interaction

Quantum ElectroDynamics (QED) describes the interaction of electrically charged particles. The interactions between the particles are mediated by photons (γ), which, unlike in QCD, are not electrically charged and can not couple to each other. The forces of QED, analogous to gravity, get smaller with increasing distance between the interacting particles.

[10] Color charge is a property of quarks and gluons that is related to the particles' strong interactions in QCD.

[11] Up to now no colored particles have been observed in nature.

The Higgs boson is the only Standard Model particle that has not yet been observed[12]. Experimental detection of the Higgs boson would explain the origin of mass in the Universe. More specifically, the Higgs boson would explain the difference between the massless photon and the massive W and Z bosons, which mediate the weak force. If the Higgs boson exists, it is an integral and pervasive component of the material world. The experimental efforts in quest of the Higgs are discussed in Chapter 3.1.

2.6 QGP

2.6.1 Phase transition

When hadronic matter is compressed and heated, the quarks' interactions become stronger. Also the momentum transfers become very large at very short distances. As a critical temperature T_c is reached, the quarks are expected to become deconfined, as shown in Fig. 2.6. The quarks and gluons are basically expected not to in-

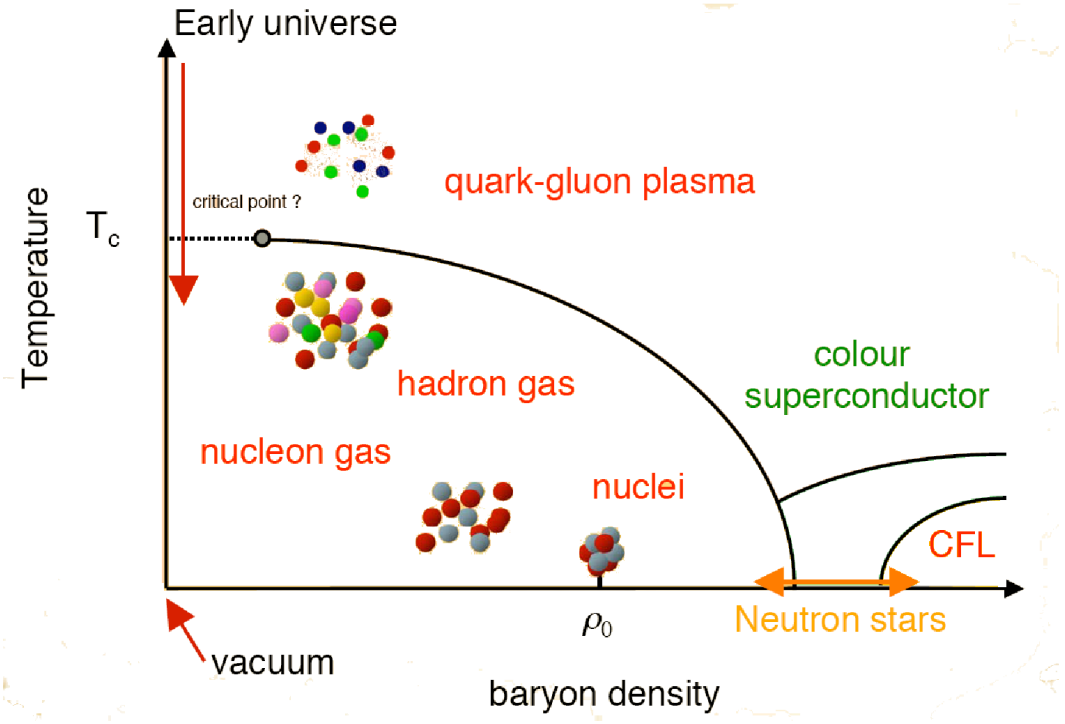

FIGURE 2.6 Phase diagram of QCD showing a critical temperature, T_c, at which the quarks are expected to become deconfined [9].

teract strongly in a deconfined state. A sharp increase in the energy density ε as well

[12]In the LHC, ATLAS and CMS experiments are expected to provide experimental evidence confirming or refuting the Higgs boson's existence. Due to the LHC accident in September 2008, the recently upgraded RHIC may be first to detect the Higgs boson.

as a more humble growth in pressure P are predicted by the Lattice QCD (LQCD) calculations, what motivates the idea of a phase transition from confined, hadronic matter to a deconfined state[13].

The symmetry of chirality[14] is broken both explicitly and spontaneously in the QCD. The symmetry is explicitly broken in QCD because the quark masses are not exactly zero. Spontaneous breaking occurs when the quarks interact and become confined to the nucleon or meson. The chiral symmetry breaking implies the distinct masses of the π^0 and π^+. If nevertheless the nuclear matter is heated above T_c and/or compressed above a certain density ρ_c, chiral symmetry is expected to be restored. A degenerate mass of π mesons is the effect of chiral symmetry restoration.

The expectation value of the quark–condensate $\langle\overline{\psi}\psi\rangle$, or the content of quarks and antiquarks in the vacuum of the nucleon, is the measure of chirality [16]. At low temperatures and low densities $\langle\overline{\psi}\psi\rangle$ is high, meaning that the nucleon vacuum is filled with virtual quarks that interact with the regular (or valence) quarks of the nucleon, but it is expected to drop above T_c. The onset of deconfinement and chiral symmetry restoration is anticipated at roughly same temperature.

If a phase transition from chiral asymmetric and confined matter does exist, measuring it could give us insight into QCD which is much less known than QED. That is why hadron colliders have generated excitement in the search for a quark–gluon plasma.

2.6.2 Signatures of QGP

The detection of QGP is not easy. The charge particle multiplicity in $\sqrt{s_{NN}}$ = 200 GeV $Au + Au$ collisions is about 5 000, around 40 000 charged particles are expected in a central $Pb+Pb$ collision at $\sqrt{s_{NN}}$ = 5.5 TeV. The majority of the detected particles have interacted after the initial production which makes understanding their origin more difficult. I'll describe now a number of proposed signatures for the detection of QGP.

The study of the temperature T of the collision allows one to gain insight into the QCD phase diagram, i.e. to analyse the phase transition and the mechanisms leading to hadronization. The extraction of T and its interpretation is however based on the assumption, that the hot state of matter generated in the collision is in thermal and chemical equilibrium. Such assumption is questionable because it is not certain whether the system has time to become equilibrated. Despite this, if the critical temperature is high enough, the thermalisation time maybe as short as 0.4 fm. The ALICE will measure the yields of various particles near mid–rapidity with a

[13]It is worth noting that LQCD calculations have until recently only been possible at zero baryon chemical potential μ_b = 0 i.e., which means that an equal amount of baryonic and anti–baryonic matter would be present. Only recently LQCD calculations have been extended to $\mu_b \neq 0$.

[14]Chirality is the sign of the projection of the spin vector onto the momentum vector of the particle.

very high precision using ITS, TPC, TRD, TOF, HMPID and PHOS detectors, and hence obtain the information of the collision's temperature.

The ratio of anti–particles to particles provides information about the kinematics of the collision. A different ratio of anti–particle to particle number than that predicted by conservation laws, e.g. $\overline{p}$ to p, π^+ to π^- or K^+ to K^- as a function of rapidity, indicates that something other than pure kinematics, such as pair production, takes place in the collision. According to baryon, isospin and strangeness conservation, particles are assumed to be produced in particle anti–particle pairs. The $\overline{p}$ to p ratio near y = 0 provides information on how much of the colliding nuclei is left over in the other rapidity regions [16].

The measurement of the elliptic flow has recently received a lot of attention. Azimuthal anisotropy (v_2) of the particles emitted from the A + A collision is one the most often raised arguments in favour of creation of QGP. The relatively large v_2 has been observed in non–central collisions at RHIC [23]. Fig. 2.7 shows an artistic view of this phenomenon. The elliptic flow is defined by the second coefficient of

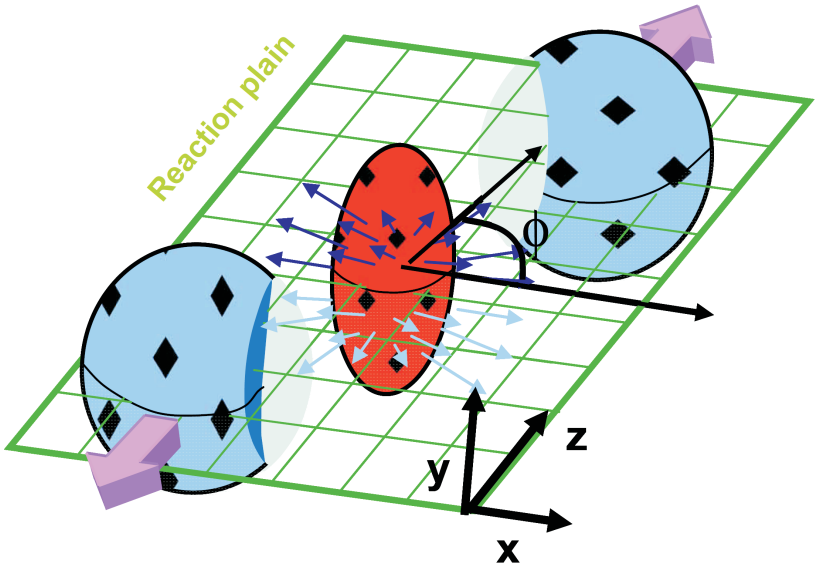

FIGURE 2.7 Artistic view of elliptic flow as a result of In non–central $Au+Au$ collision at RHIC. The reaction plane is determined by the impact parameter and the beam direction [23].

the Fourier expansion:

$$\frac{dN}{d\eta dp_T d\varphi} \simeq 1 + 2v_1 cos\varphi + 2v_2 cos2\varphi + ..., \tag{2.22}$$

where φ is an azimuthal angle (see Fig. 2.8) and v_1 is a parameter describing the radial flow. The azimuthal anisotropy of the flow is associated in the some models with a rather quick thermalisation of quarks and gluons, e.g. within 0.6 fm, which

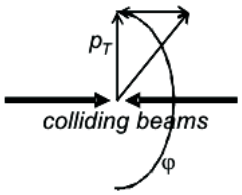

FIGURE 2.8 Azimuthal angle in the collision.

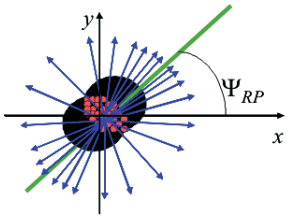

FIGURE 2.9 Angle defining the reaction plane.

results in preservation of the initial anisotropy of the collision. On the other hand, it points to Hydro model as a suitable description of the hot medium created in the collision [18]. The medium can be recognised as a perfect liquid consisting of quarks and gluons moving around freely. Experimentally v_2 can be accessed via:

$$E\frac{d^3N}{d^3p} = \frac{1}{\pi}\frac{d^2N}{dp_T dy}\left[1 + 2v_1 cos\left(\varphi - \Psi_{RP}\right) + 2v_2 cos2\left(\varphi - \Psi_{RP}\right) + ...\right], \quad (2.23)$$

where Ψ_{RP} is the angle defining the reaction plane, as sketched in Fig. 2.9. The v_2 and v_4 (hexadecupole anisotropy) for various collision centralities measured at RHIC are shown in Fig. 2.10. Elliptic flow will be measured by in ALICE by several detectors

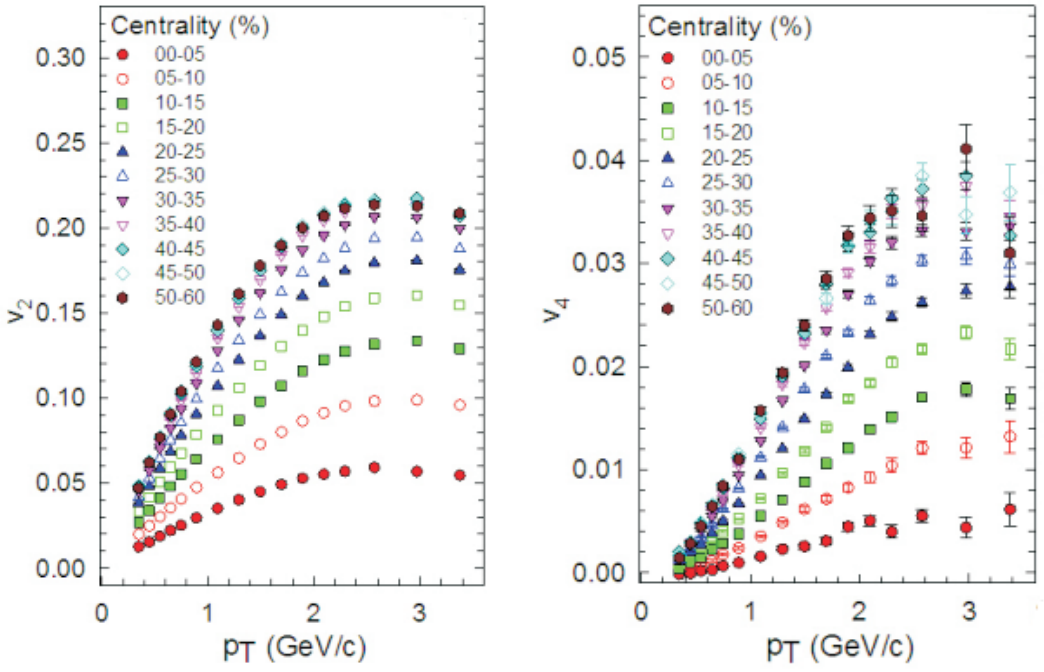

FIGURE 2.10 Azimuthal (v_2) and hexadecupole (v_4) anisotropies measured at RHIC (PHOENIX preliminary [23]).

including ITS, TPC and FMD. The first two will measure the transverse momentum

and azimuthal distribution of charged particles hence can determine the anisotropy around mid–rapidity. FMD can perform the same measurements and determine the anisotropy in the forward regions. The determination of the reaction plane, which is crucial for measuring v_2, can be performed also by the T0 – there is an ongoing study of this topic.

Chiral symmetry restoration or partial chiral symmetry restoration is expected to take place in extremely hot and dense nuclear matter, such as in QGP. Initially, according to the model [17], the quark matter is in the asymmetric state of spontaneous and explicitly broken symmetry. Once the quarks become deconfined, the spontaneously broken symmetry is restored. When the system cools down and becomes less dense, the symmetry is spontaneously broken again. The interesting experimental consequences is that when the symmetry is partially restored, π and ρ meson masses will change. The ρ meson decays into dileptons, which do not interact strongly with the surrounding nuclear matter [16]. Hence one can expect to measure the change in the ρ mass by measuring the invariant mass spectrum of the dileptons.

Another signature of QGP is jet quenching. It is well known that jets can be produced by gluon radiation. Back in the 1980s jets were not expected to be seen in any significant amount in the hot and dense medium formed in heavy–ion collisions. However, not only are jets observed, but an interesting phenomenon occurs in jet production. Namely when a jet is formed, due to momentum conservation, one expects to see a corresponding jet in the opposite direction, the so-called away–side jet, as shown in Fig. 2.11. However, at RHIC, the away–side jet almost disappears in

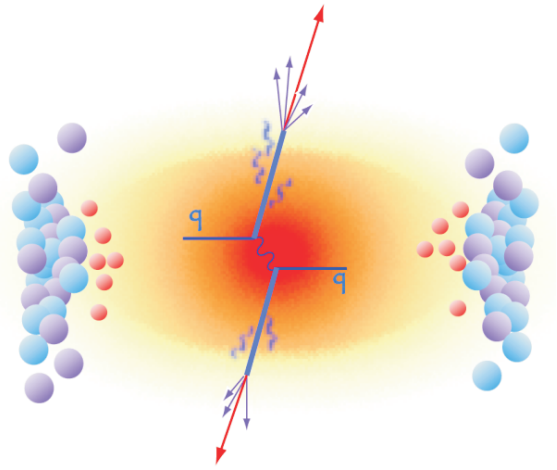

FIGURE 2.11 Artistic view of jet emission as a result of A + A collision [23].

central $Au + Au$ collisions. The suitable parameter for studying that phenomenon is

a nuclear modification factor, R_{AA}, defined as:

$$R_{AA}(p_T) = \frac{d^2N^{AA}/dp_T d\eta}{T_{AA} d^2\sigma^{NN}/dp_T d\eta}, \tag{2.24}$$

where T_{AA} is a ratio of the number of binary collisions to the total inelastic cross–section for $p+p$ collisions. Jet quenching shows up as a suppression of high p_T particles, as depicted in Fig. 2.12. Moreover, broadening of the away–side jet has

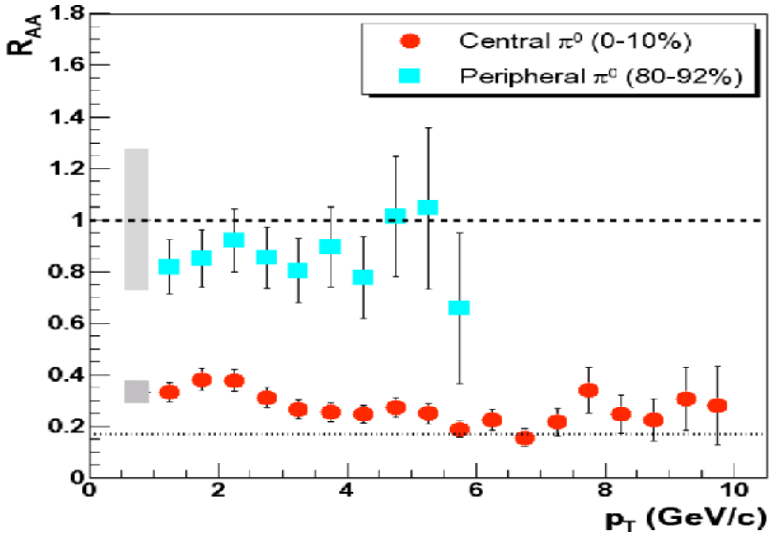

FIGURE 2.12 Nuclear modification function, R_{AA}, calculated from central and peripheral π^0 data from Au–Au collisions in Run 2001/2002 at RHIC [9].

been observed at RHIC. It is seen as an indication of the quarks and gluons interacting strongly with the hot and dense medium. ALICE has a dedicated program to study the high–p_T physics.

The enhanced production of s quarks might be a QGP signature as well. Due to the abundance of $q\bar{q}$ pairs produced in URHIC close in phase space, the Fermi sea for u and d quarks is expected to be quickly filled. Then the $s\bar{s}$ pairs are energetically favourable to be produced. Therefore strangeness enhancement is a good probe for the formation of a hot and dense phase of nuclear matter, in particular the ratios N_{K^-} to N_{π^-} and N_{K^+} to N_{π^+} [16]. On the contrary, the production of $c\bar{c}$ is expected to be strongly suppressed in the deconfined phase. This shows up in the suppression of the formation of J/ψ particles. ALICE Muon spectrometer measures dileptons and will study this phenomenon in $\sqrt{s_{NN}}$ = 5.5 TeV $Pb+Pb$ collisions.

2.7 Outlook

The system created in heavy–ion collisions undergoes a fast dynamical evolution from the extreme initial conditions to the dilute final hadronic state. The under-

standing of this fast evolving system is a theoretical challenge which goes far beyond the exploration of equilibrium QCD. It provides the opportunity to further develop and test a combination of concepts from elementary–particle physics, nuclear physics, equilibrium and non–equilibrium thermodynamics, and hydrodynamics in an interdisciplinary approach.

There is no well–established prediction for what will be observed at the LHC[15]. It is expected that we will be able to verify some theoretical approaches currently being pursued, e.g. lattice QCD and classical QCD, which are directly related to the fundamental QCD Lagrangian. Their range of applicability remains to be determined in an interplay of experiment and theory. Other theories involve model parameters that are not solely determined by the Standard Model Lagrangian but provide powerful tools to study the origin of collective phenomena. The predictions of these approaches and their uncertainties can to some extent be verified by comparison to experimental data and determine the underlying physics of various collision scenarios. In heavy–ion collisions at the LHC we hope to obtain a definitive proof of the existence of the QGP, where the most elementary known particles, quarks, become free. One of the open questions is could we observe a QGP already in $p+p$ collisions at $\sqrt{s_{NN}}$ = 14 TeV, i.e. is there an experimental data signature that could prove its existence.

[15]It may seem that the theory has been outpacing the experimental efforts practically since the beginning of accelerator physics. The result of Cockroft and Walton's 400 keV p on Li reaction had been predicted 4 years before, in 1928, by Gamow, and, independently, by Gurney and Condon. Likewise, findings of ν_μ at BNL in 1962 and the c quark at SLAC in 1974 had been predicted much earlier by the theory. It seems that until now the role of accelerators in particle physics was rather to prove the existence of particles.

3 Role of ALICE at LHC

3.1 From SPS to LHC

The quest for the quark–gluon plasma has been carried out by NA35, NA44, NA45 (CERES), NA49, NA50, NA57 and NA60 experiments at the SPS at CERN. Since the year 2000, the experimental data in the quest of the QGP has been collected at the RHIC accelerator at Brookhaven National Laboratory. The RHIC's four experiments: STAR, BRAHMS, PHENIX and PHOBOS provided a number of interesting experimental results. The basic conclusions, which may be drawn, are as follows:

- the nuclear matter, emerging in central $Au + Au$ collisions at RHIC, appeared to be an almost perfect quark–gluon liquid (instead of a gas of free quarks and gluons);
- the matter consists of very high densities of energy and unscreened color charges, an order of magnitude higher than in a nucleon. It has features of large capture cross–sections between highly interacting particles and intensive collective movement;
- the matter can not be described within the theory of ordinary color–neutral hadrons, since there does not exist a self–consistent theory of matter composed of ordinary hadrons at high densities;
- the definite proof of the existence of QGP has not been obtained so far [19].

Later this year a new era of high energy physics begins with the first collisions in the LHC. The LHC is now the most powerful particle collider in the world, already capable of producing beams seven times more energetic than any previous machine. Table 3.1 presents the experimental infrastructure and Fig. 3.1 the luminosity evolution in hadron colliders in the last half a century. When the LHC reaches its design performance, heavy ion collisions will be carried out at energies $\sqrt{s_{NN}}$ = 5.5 TeV, exceeding that of RHIC by almost 30 times[1]. It leads to:

[1]RHIC was designed to accelerate nuclei to an energy of $\sim$ 100 GeV per nucleon, which gives for $Au + Au$ collisions the energy carried by each nucleus: $197 \cdot 100$ GeV, and the center–of–mass energy of $2 \cdot 19.7$ TeV, or 39.4 TeV. At the LHC, the energy carried by each Pb nucleus is: $208 \cdot 2.75$ TeV, which leads to a centre-of-mass energy of 1144.0 TeV, or 1.14 PeV, that is 29 times more than at Brookhaven.

TABLE 3.1 Heavy ion accelerators.

Accelerator	Type	Location	Length [km]	$\sigma_{INELASTIC}$ [mb]	$\sqrt{s_{NN}}$ [GeV]
AGS	fixed–target	BNL	0.8	21	5.2
SPS	fixed–target	CERN	7	33	17
RHIC	collider	BNL	4.6	42	200
LHC	collider	CERN	27	60	5 500

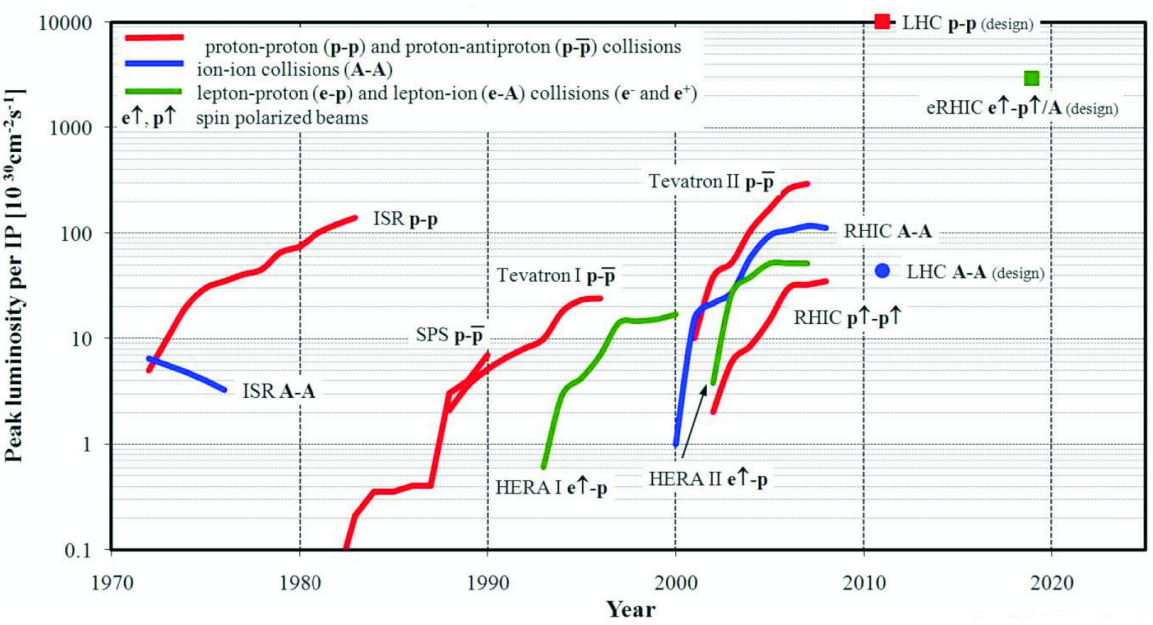

FIGURE 3.1 Luminosity evolution in hadron colliders [57].

- high energy density and temperature of the created nuclear medium, see Fig. 3.2;
- shorter thermalization time of the system
  - longer lifetime in the QGP phase
  - larger background contribution has a consequence of hadron interaction in the final state;
- high yields of hadrons with transverse momenta up to $p_T \sim 100$ GeV/s as well as of particles containing c, b quarks;
- possibility to study the $\gamma(1S)$ state melting.

One of the questions to be addressed at the LHC is the connection between phase transitions involving elementary quantum fields, fundamental symmetries of nature and the origin of mass. Theory distinguishes symmetries of the dynamical

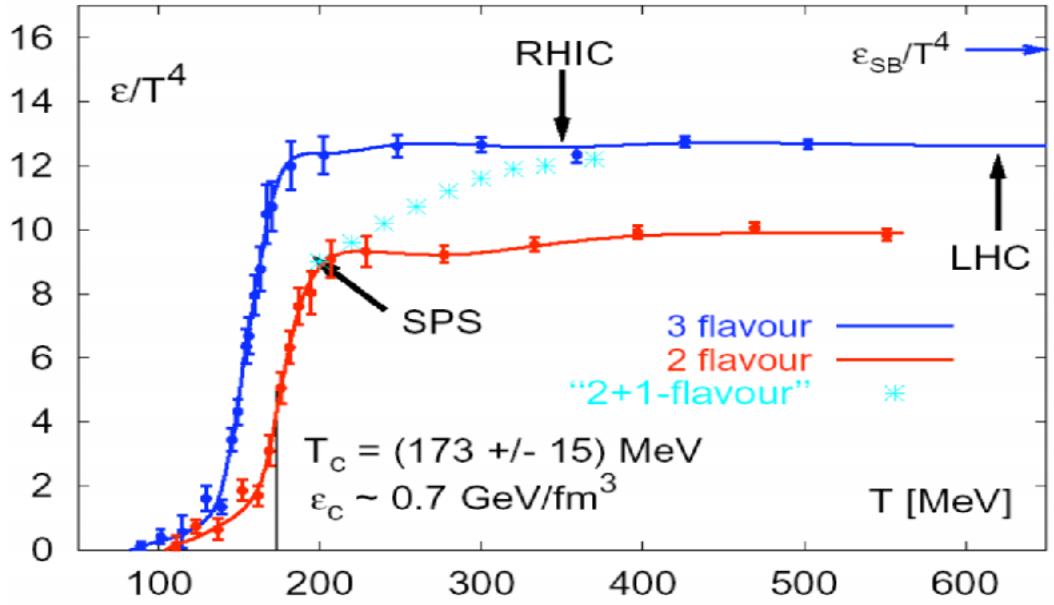

FIGURE 3.2 Phase diagram showing the temperatures available with SPS, RHIC and LHC according to our present understanding of QCD [9].

laws of nature (i.e. symmetries and particle content of the Lagrangian) and symmetries of the physical state with respect to which these dynamical laws are evaluated (i.e. symmetries of the vacuum or of an excited thermal state). The experimental programme at the LHC will evaluate both aspects of the symmetry–breaking mechanism through complementary experimental approaches. ATLAS and CMS will search for the Higgs particle, which generates the mass of the electroweak gauge bosons and the bare mass of elementary fermions through spontaneous breaking of the electroweak gauge symmetry. They will also search for supersymmetric particles which are manifestations of a broken intrinsic symmetry between fermions and bosons in extensions of the SM. LHCb, focusing on precision measurements with heavy b quarks, will study CP–symmetry–violating processes. These measure the misalignment between gauge and mass eigenstates which is a natural consequence of electroweak symmetry breaking via the Higgs mechanism. The role of ALICE in the LHC experimental programme is described in Chapter 3.2.

All LHC experiments are expected to have an impact on various astrophysical fields. The top LHC energy $\sqrt{s}$ = 14 TeV corresponds to 10^{17} eV in the laboratory reference frame. Hence, LHC may contribute to the understanding of cosmic–ray interactions at the highest energies, especially to the open question of the composition of primaries in the region around the 'knee' at 10^{15}–10^{16} eV.

3.1.1 LHC startup

The first beam was officially circulated in the LHC's 27–kilometre long tunnel in September 2008. The preparations for the LHC startup began with the cooling down

of each of the machine's eight sectors. This was followed by the electrical testing of the 1600 superconducting magnets and their individual powering to nominal operating current. These steps were followed by the powering of all of the circuits of each sector, and then of the eight independent sectors simultaneously in order to operate as a single machine. All eight sectors reached their operating temperature of 1.9 K (-271 °C) in July 2008. The next phase was synchronisation of the LHC with the Super Proton Synchrotron (SPS) accelerator, which forms the last link in the LHC's injector chain, as depicted in Fig. 3.3. Timing between the two machines has been adjusted

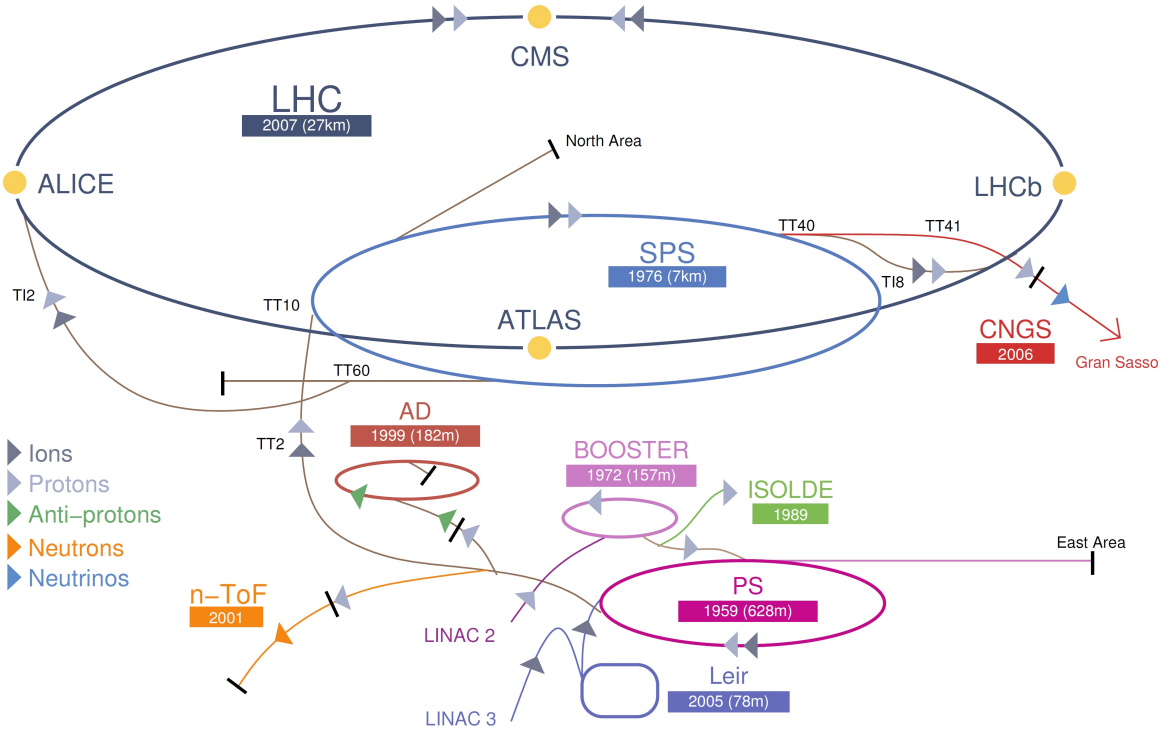

FIGURE 3.3 The CERN accelerator complex. The radius of the LHC is $\sim$ 4.3 km.

with an accuracy within a fraction of a nanosecond in August 2008. In September 2008 the entire machine was ready to accelerate and collide beams and saw its first circulating beam at the injection energy of 0.45 TeV on September 10th.

An incident occurred on 19 September 2008 during commissioning of the LHC sector 34 at high current for operation at 5 TeV. The problem was a faulty electrical connection between two magnets which melted at high current leading to mechanical failure. Sector 34 had to be warmed up for repairs to take place, which implied a long down time. Hence, the LHC will resume in the autumn 2009. Presently (status from 20/07/2009) there is a period of cosmic runs, calibration and off–line measurements for the LHC's four major experiments (ATLAS, CMS, LHCb and ALICE).

3.1.2 Plans for LHC (status from 20/07/2009)

LHC is designed to collide two counter-rotating beams of protons or heavy ions, in two separate vacuum chambers. The nominal centre-of-mass energy for $p + p$ collisions is 14 TeV, however, collisions can be obtained down to the injection energy of 900 GeV. The current plans for the LHC are as follows:

- October - December 2009: 0.9 and 10 TeV $p + p$
- January - September 2010: 10 TeV $p + p$
- October 2010 – 2011: 5.5 TeV $Pb + Pb$
- 2011: 14 TeV $p + p$

It is beneficial to start with $p + p$ collisions. The obtained data can be validated by comparison with the same energy $p + p$ runs at SPS and RHIC as well as provide the reference for the results obtained in $Pb + Pb$ collisions. Lead has been chosen as a heavy element to be accelerated at the LHC. It is easy to handle, carrying at the same time 208 protons and neutrons, which yields 1.14 PeV centre-of-mass energy, assuming LHC's nominal energy of 2.75 TeV/nucleon for $Pb + Pb$ collisions. Moreover, at CERN there is a know–how in accelerating Pb. Already in 1993-94 CERN has put into operation its second heavy–ion source capable of extracting lead ions and used it in a very successful heavy–ion programme at SPS [22]. Even heavier ions, especially uranium, are not used because they are far from being spherical, which has many consequences in defining the centrality etc. and are more difficult to handle[2]. Runs with lighter ions, such as argon or gold, are envisaged for the LHC in the future. It would allow variations in the energy density and the volume of the produced system.

3.2 ALICE

ALICE is designed to address the physics of strongly interacting matter and the quark–gluon plasma in nucleus–nucleus collisions at the LHC. The experimental programme of ALICE is very broad and includes for instance:

- the role of chiral symmetry in the generation of mass in composite particles (hadrons) using heavy–ion collisions to attain high–energy densities over large volumes and long timescales;
- equilibrium as well as non–equilibrium physics of strongly interacting matter in the energy density regime $\varepsilon \simeq$ 1–1000 GeV/fm^{-3};

[2]There are some discussions to use uranium, however, it goes with the development of a system to keep the orientation of the nuclei during the acceleration under control.

- physics of parton densities close to phase–space saturation and their collective dynamical evolution towards hadronization (confinement) in a dense nuclear environment;
- the structure of the QCD phase diagram and the properties of the QGP phase.

The ALICE detector is capable of simultaneously studying the properties of the bulk soft probes (large cross–sections) as well as the rare hard ones (small cross–sections). ALICE consists of subdetectors, which can be divided into three sections: the central system[3], the forward detectors[4], and the Muon spectrometer. These detectors will measure and identify hadrons, electrons, photons and muons, allowing:

- study of global processes (multiplicity, fluctuations of multiplicity, angular distributions, etc.)
- detailed event–by–event analysis, including identification of the secondary particles formed as result of the collision of relativistic heavy ions, performed with an inner tracker based on pixel, strip and drift silicon detectors, the Time Projection Chamber, the detector of transition radiation, a Photon spectrometer, Time Of Flight detector and others.

The best coverage is provided for the mid–rapidity region, as depicted in Fig. 3.4. ALICE is able to fully track and identify particles from very low up to high transverse momenta, i.e. from some 100 MeV/c up to 100 GeV/c, and to reconstruct the decays of hyperons and D and B mesons in an environment with multiplicity densities up to $dN/d\eta \sim 8000$.

3.2.1 Central detectors

The central detectors will measure the momentum and identify particles produced in the region $|\eta| < 0.9$. They use diverse technologies to measure hadrons, electrons and photons. Fig. 3.5 shows a section through the L3 magnet and the central detectors.

The region in the proximity of the IP, i.e. $\pm 1\sigma \approx 10.6$ cm along the longitudinal direction, is characterised by extreme particle density. According to the theoretical predictions, several thousands particles will be emitted in the central η region. In order to measure these, the ALICE central detectors are placed as close as possible to the IP allowing a coverage of $|\eta| < 0.9$ for all vertices located within the length of the interaction diamond (ID). Such η window is also necessary to detect with a good efficiency the decay of large mass, low p_T particles. The charged particle tracking is provided by the three detectors: ITS, TPC and TRD.

[3]Central system includes the ITS, TPC, TRD, TOF, HMPID, EMCal, PHOS and ACORDE detectors.

[4]The forward detectors are FMD, T0, V0, PMD and ZDC.

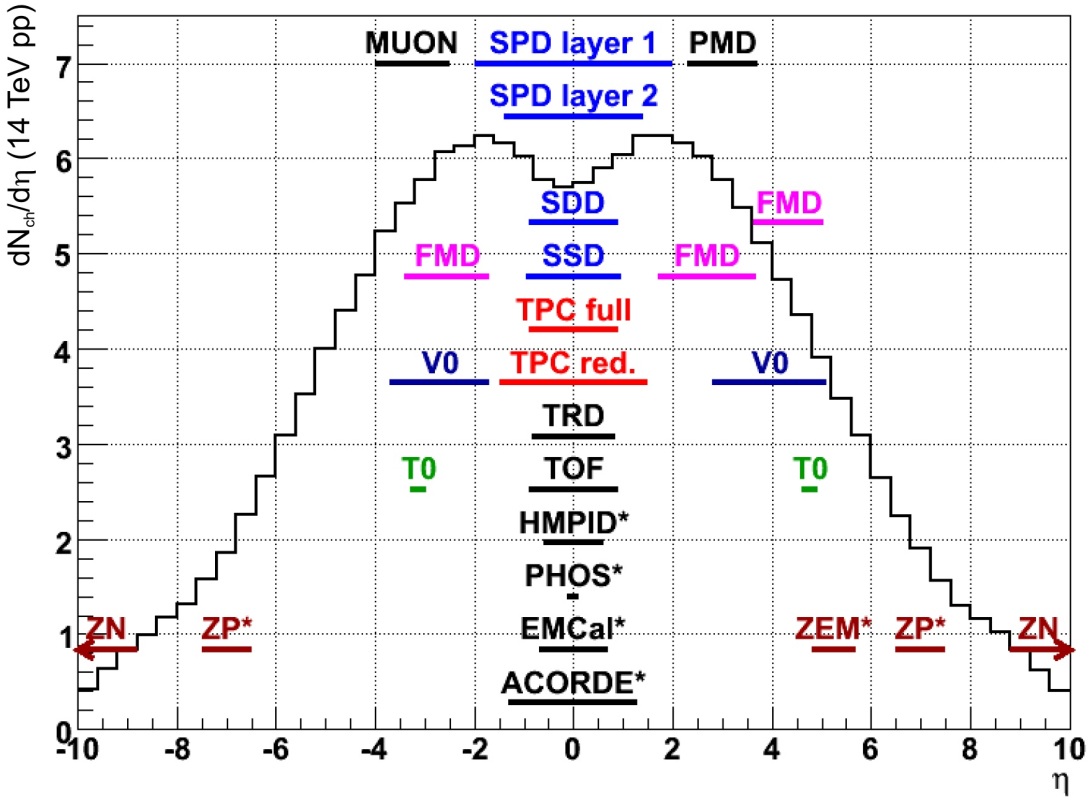

FIGURE 3.4 Acceptance of ALICE detectors on top of charged–particle multiplicity for $p+p$ collisions at $\sqrt{s}$ = 14 TeV. Detectors marked with stars are capable of registering not only charged particles [37].

The Inner Tracking System (ITS) is a high–resolution silicon detector. With its inner radius of 4 cm, it is the closest detector to the IP. The ITS consists of 3 subdetectors, starting from the center and going outwards: The Silicon Pixel Detectors (SPD), the Silicon Drift Detectors (SDD), and the Silicon Strip Detectors (SSD). Each of them has 2 layers. The active elements of the SPD are small pixels on the face of a silicon sensor. The first layer of the SPD has a more extended pseudorapidity coverage, up to $|\eta| < 1.98$, to provide, together with the FMD, a continuous coverage in rapidity for a measurement of charged–particle multiplicity. Fig. 3.4 illustrates the η coverage of separate ITS layers. The other two subdetectors in the ITS, the SDD and SSD, have less granularity than the SPD. They provide further tracking points and charged–particle multiplicity measurements in $|\eta| < 0.9$ for all vertices located within the ID. The ITS as a whole provides tracking of charged particles near the IP. Due to its fine granularity, the ITS can resolve decays of short–lived particles (such as Λ, and Ξ) and determine the point of decay. One can further improve the determination of the position of the primary interaction by forming tracklets in all 6 layers of the three subdetectors. This information is used to restrict the global tracking of particles in the barrel detectors: tracks that do not seem to originate relatively

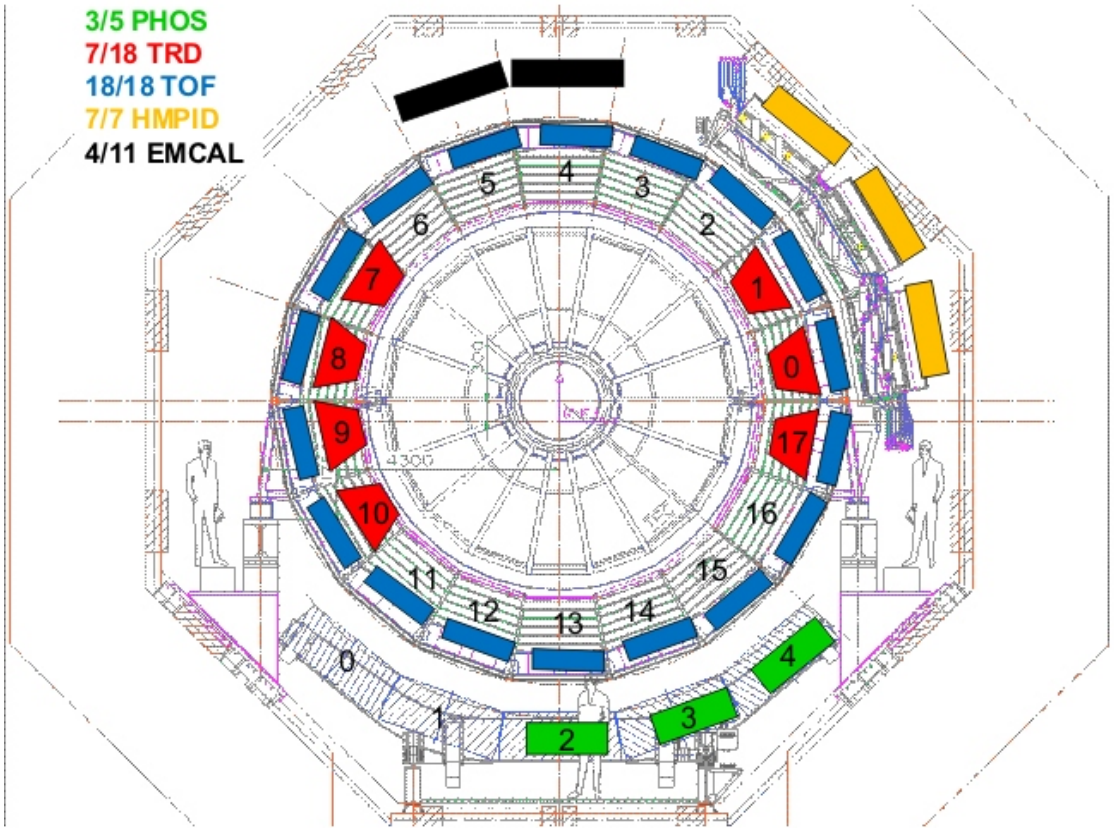

FIGURE 3.5 ALICE central detectors. They are embedded in the large L3 solenoidal magnet providing a weak field of $\leq$ 0.5 T and cover the polar angles from 45°to 135°over the full azimuth. Readiness of selected ALICE central detectors: EMCal, HMPID, PHOS, TOF and TRD by the end of LHC shutdown period 2008/2009 is marked in the top left corner.

close to the IP can be discarded as background tracks from cosmic–rays, scattering in material, or other such sources. The important constraint for the ITS has been the material budget: the material in the active volumes of the system had to be reduced to the minimum. This is due to the fact that the values of momentum and impact parameter resolution for particles with small p_T are dominated by multiple scattering effects in the material of the detector.

The Time Projection Chamber (TPC) is the largest TPC ever built. It is an 80 m^3 gaseous detector providing tracking and particle identification in the region $|\eta| < 0.9$. When charged particles traverse the gas volume, they ionise the gas and electrons drift toward the read–out planes on either end–cap. The end–caps are instrumented with several thousand front–end cards with the custom built ALTRO Analog–to–Digital–Converter (ADC) chip. This highly advanced chip has been reused by several ALICE subdetectors, including the FMD, PHOS, and EMCal. The front–end cards are grouped together in partitions and each partition is controlled by a Read–out Controller Unit (RCU) mother card. Data is transfered from the RCU

directly to the data acquisition system via optical fibres – there are 280 of these in total. The full drift–time of the TPC is roughly 88 μs which sets the trigger scale. Within a window of 88 μs starting from a collision, there should be no other collisions. If there were collisions within the drift time, it would pollute the event being read–out. Unlike ATLAS and CMS, where each read–out can be tagged with a time–stamp, the ALICE TPC can not resolve particles from multiple interactions. The maximum trigger rate of ALICE will therefore be around 10 kHz. Particle identification in the TPC is done by using the energy loss of particles in the gas. The information on the energy loss is picked up during the tracking and can be used to adjust the assumptions of the Kalman filter used for tracking [16].

The Transition Radiation Detector (TRD) is located just outside the main TPC barrel. The working principle is based on detecting the radiation emitted during transition between two media. For example when a charged particle crosses over the boundary between two materials with different dielectric constants, it radiates light. The amount of radiation emitted depends on the particle's γ factor in the rest frame of the materials, and the TRD can therefore be used for particle identification. Practically, the TRD consists of layers of plastic, inter–spaced with wire chamber layers. The wire chamber layers detect the radiation emitted in the transition with a resolution of 400 μm in the rφ plane, and 2.3 cm in the z direction [16]. The holes in the φ coverage are there to provide open windows with little material for the PHOS and HMPID detectors.

The Time Of Flight (TOF) detector, placed outside of TRD, has a cylindrical shape, covering polar angles between 45 degrees and 135 degrees over the full azimuth. It has a modular structure with 18 sectors in ϕ, each divided into 5 modules[5] along the beam direction. TOF measures the time it takes a particle to travel from the IP to the detector itself. The time measurement with the TOF, in conjunction with the momentum and track length measured by the tracking detectors is used to calculate the particle mass. The particle momentum p can be expressed as:

$$p = m_0 \cdot v \cdot \gamma = \frac{m_0}{\sqrt{\frac{1}{v^2} - 1}}. \tag{3.1}$$

Here m_0 is particle's rest mass, v=$\frac{l}{t}$, where l is the TOF trajectory length and t is the time of flight, and $\gamma = (1 - \beta^2)^{-1}$. The momentum and trajectory of particle are known from tracking in the ITS, TPC, and TRD. Hence, knowing the time of flight, the particle mass can be calculated as:

$$m_0 = p \cdot \sqrt{\frac{t^2}{l^2} - 1}. \tag{3.2}$$

[5]The modules contain a total of 1638 detector elements (MRPC strips), covering an area of 160 m^2 with 157248 readout channels (pads).

The TOF detector is built of Multigap Resistive Plate Chambers. The resistive plates are put perpendicular to the particle trajectories, and spaced with gas volumes. A HV is applied over the full chamber so when a charged particle traverses the gas volume, it loses energy through ionisation and creates an avalanche. The signal from the avalanche is detected at the anode of the detector. The T0 detector provides a start signal for TOF. The time of flight t is calculated as: $t_{TOF} - t_{T0}$ with $t_{TOF} = t_{stop} + const_{TOF}$ and $t_{T0} = t_0 + const_{T0}$, where t_{stop} is the time when particle hits the TOF detector, t_0 is the collision time and $const_{TOF/T0}$ are the constants coming from signal processing in the two detectors[6]. Fig. 3.6 presents an a TOF spectra obtained at RHIC: The design of the TOF detector in ALICE provides an overall timing resolu-

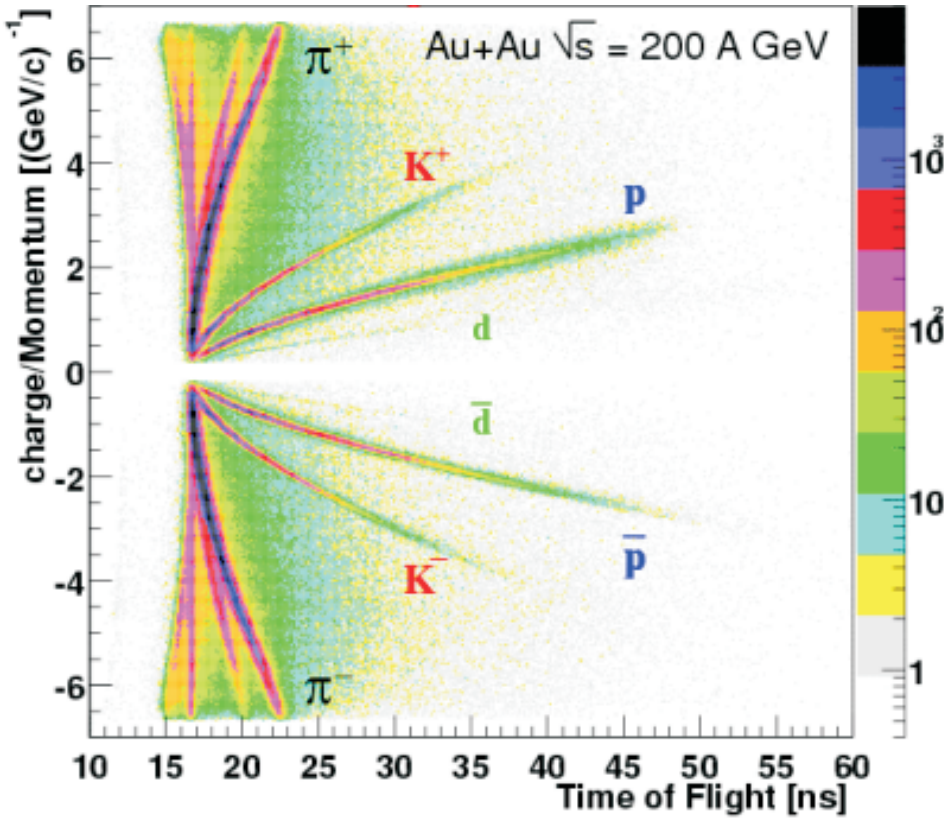

FIGURE 3.6 TOF spectra obtained at RHIC with PHENIX high resolution TOF [23]. Pions, kaons, protons and deuterons are clearly identified. Particles with time of flight shorter than pions are muons (T0F between 17 and 20 ns) and electrons (between 16 and 17 ns). The overall time resolution is $\sim$ 120 ps.

tion of about 100 ps which will provide 3σ π/K separation up to 2.2 GeV/c and K/p separation up to 4 GeV/c.

[6]It is apparent that it is impossible to do the calibration and perform particle identification (PID) based on a single particle registered in the T0 and TOF. The amount of particles emitted in the collision is much larger, hence $const_{TOF/T0}$ are precisely known, making PID possible.

The PHOton Spectrometer (PHOS) is an electromagnetic calorimeter made of lead–tungsten crystals, which measures photons, π_0, and η mesons up to a p_T of 10 GeV. These measurements can be used for jet physics, direct photons measurements as well as for searching for signatures of chiral symmetry restoration.

The ElectroMagnetic Calorimeter (EMCal) covers a large φ segment, and the η range is roughly the same as for the TPC. It measures the transverse energy E_T of particles that hit the detector. Hence, it provides p_T measurements in the region from 100 MeV to 100 GeV. The read–out of the EMCal is fast enough to participate in the L1 trigger decision, allowing for jet triggering. Each individual EMCal detector module, the smallest building block of the calorimeter, is made of 2 $\times$ 2 = 4 towers build up from 76 alternating layers of 1.44 mm Pb and 77 layers of 1.76 mm polystyrene base, injection moulded scintillator (BASF143E + 1.5% pTP + 0.04% POPOP) with an intrinsic light output of 50% Anthracene [25]. Light created by traversing charged particles is collected in fibres and sent to a photo–chip for collection.

The High Momentum Particle Identification Detector (HMPID) identifies the particles of very high momentum. The limit for π/K separation is 3 GeV, and for K/p – 5 GeV. The working principle of HMPID is very similar to the one of the T0 detector: charged particles emit Cherenkov radiation when the velocity of the particle is larger than the speed of light in the medium traversed v > c/n (n is the refractive index of the medium). The Cherenkov light is emitted as a shock wave at an angle to the particle track that depends on the speed of the particle. Thus, if one measures opening angle (or equivalent, the radius) of the shock wave, one can determine the velocity of the particle, which is relative to the velocity of the light in the medium: cos ϑ_c = 1/βn. The HMPID uses C6F14 as a radiator and a Multi–Wire Proportionality Chamber (MWPC) to collect the radiated Cherenkov light. The light emitted hits the MWPC forming a ring on the read–out plane. This ring is then identified and associated to a known track via algorithms, which determine the type of particle [16].

ALICE COsmic Ray DEtector (ACORDE) is an array of plastic scintillator counters. It is placed outside of the L3 magnet. It's main function is to provide a fast trigger signal for calibration of tracking detectors. It also allows the study of high–energy cosmic–rays in the energy region of the knee of the cosmic–ray spectrum.

The construction and installation of some of the ALICE central detectors has not yet been completed as shown in Fig. 3.5, which presents the foreseen readiness of EMCal, HMPID, PHOS, TOF and TRD before the restart of the LHC, i.e. at the end of September 2009. The assembly of the remaining parts of incomplete detectors is scheduled for the future breaks in the LHC operation.

3.2.2 Forward detectors

The detectors capable of tracking particles with an accuracy of μm are located in the central region of ALICE (see Fig. 3.4). The forward rapidity regions in ALICE are covered by detectors using less expensive technologies than the central detectors, however able to supply the needed information on the collisions in the forward/backward regions of $|\eta| > 1.5$. They provide the event characteristics in the forward regions, i.e. multiplicity of charged particles and photons, the vertex of the collision, and are used as a fast trigger distinguishing the centrality of the collision. The positioning of the three forward detectors, V0, FMD and T0 is shown in Fig. 3.7.

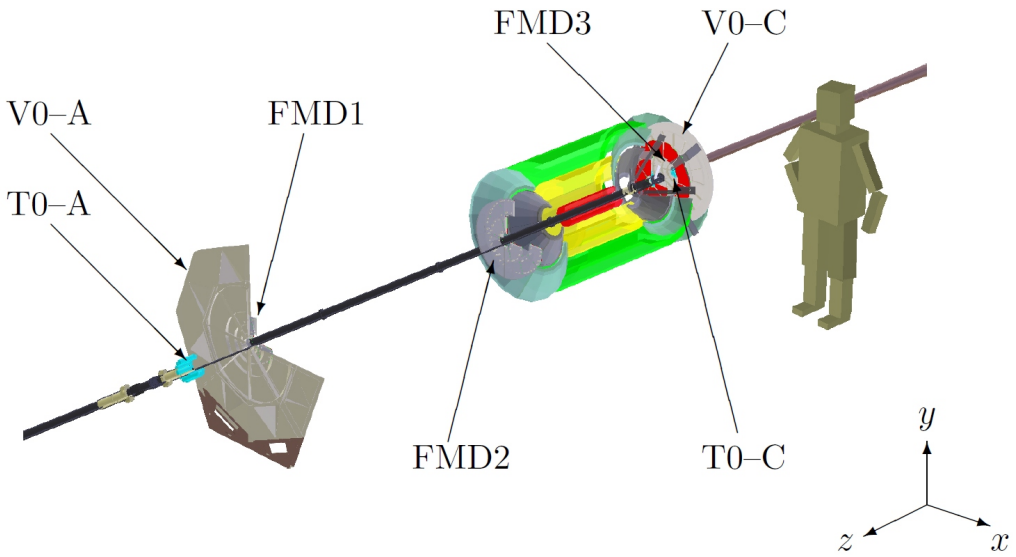

FIGURE 3.7 The three forward detectors in ALICE: T0, V0 and FMD [16].

The primary role of the Forward Multiplicity Detector (FMD) is to measure the number of charged particles outside the main acceptance range, i.e. in the η range of $-3.4 < |\eta| < -1.7$ and $1.7 < |\eta| < 5.0$. It is the main forward multiplicity detector in ALICE. The FMD is made of silicon strip detectors arranged in rings around the beam pipe. It has a high efficiency and high signal–to–noise ratio.

The dominant role in the fast ALICE trigger will be played by the two small forward detectors: T0 and V0. Since they are essential to the operation of ALICE, they are designed with partial overlap in functionality, i.e., both distinguish between central, semi–central, and minimum bias collisions and determine the vertex position. The V0 detector has a large acceptance, which provides a reliable L0 trigger for ALICE. The V0 is made of two arrays of plastic scintillators, V0A and V0C, placed on the opposite sides of the IP and covering the η range of $-3.7 < \eta < -1.7$ and $2.8 < \eta < 5.1$. Each array is made of 4 concentric rings, as depicted in Fig. 3.8. Each ring is subdivided into 8 sectors making 32 cells. The pseudorapidity coverage of each

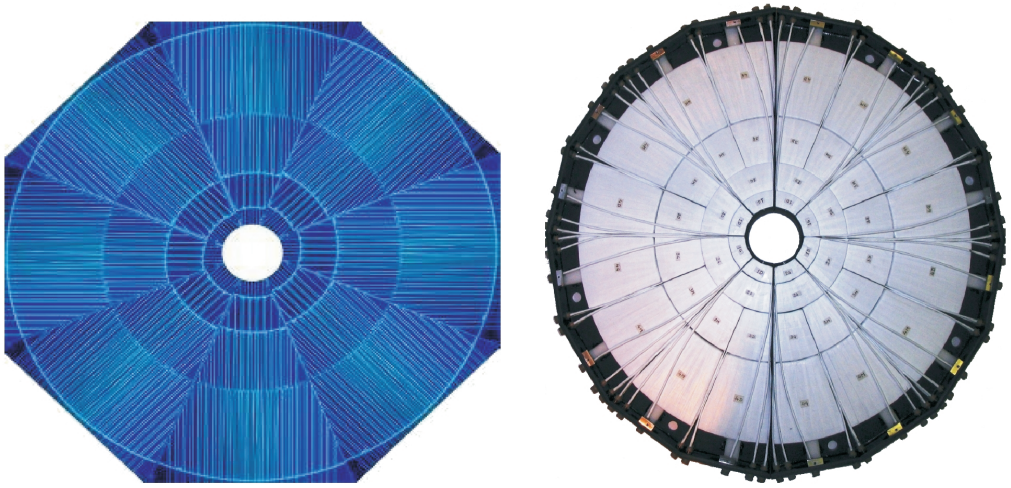

FIGURE 3.8 Illustration of V0A (left) and photo of V0C ring [26].

ring is given in Tab. 3.2. The light from each cell is collected by a grid of wavelength shifting fibers and directed to a photomultiplier tube (one tube per cell). The overall time resolution is below 1 ns and the acceptance assures a trigger efficiency up to 98% for $p+p$ collisions[7]. Last, but not least, the V0C array can be used for validation of the Muon spectrometer's separate trigger chambers.

TABLE 3.2 V0 pseudorapidity coverage.

$\triangle\eta$	V0A	V0C
Ring 1	5.1 / 4.5	–3.7 / –3.2
Ring 2	4.5 / 3.9	–3.2 / –2.7
Ring 3	3.9 / 3.4	–2.7 / –2.2
Ring 4	3.4 / 2.8	–2.2 / –1.7

The T0 detector is a high–resolution timing detector. It consists of Cherenkov radiators glued on photomultiplier tubes. A coincidence between the two T0 arrays (T0–A & T0–C) placed on the opposite sides of the IP serves as a L0 trigger and an early wake–up signal to the TRD. T0 determines the vertex position with an accuracy of a few centimetres and gives the interaction time with the precision needed by the Time Of Flight system. The η coverage of T0 is considerably smaller than V0, but the former has substantially better time resolution (40 ps vs. 1000 ps) and much better amplitude resolution. Chapter 4 is dedicated to the T0 detector.

The Zero Degree Calorimeter (ZDC) measures the energy carried by non–interacting particles, which allows the determination of the centrality of the collision

[7] 98% trigger efficiency is for non–diffractive processes at 14 TeV. The total V0 efficiency (including all processes) for 14 TeV is 82%. The efficiencies are given for coincidence mode, i.e. V0A & V0C.

(impact parameter). It consists of four calorimeters, two to detect protons and two to detect neutrons. It is placed symmetrically on both sides of IP, about 90 m away, along the beam line. The ZDC provides a relatively simple and convenient way to gain insight into the collision event, e.g. is it a central or peripheral event, or just a beam–gas interaction to be discarded.

The Photon Multiplicity Detector (PMD) measures multiplicity and spatial distribution of photons on an event–by–event (E-by-E) basis. This allows the estimation of the reaction plane. The PMD complements the study of photons in the forward region where calorimeters cannot be used due to high particle density. The detector is placed on A–side, approximately 3.6 m from the IP.

3.2.3 Muon spectrometer

An essential tool for probing the early, hot stage of heavy–ion collisions are hard penetrating probes, such as heavy–quarkonia. The ALICE forward Muon spectrometer detects and identifies muons or muon pairs from the decay of quarkonia. Simultaneously it provides a complete spectrum of heavy quark vector mesons, i.e. J/Ψ, Ψ', Υ, Υ' and Υ''; as well as the ϕ meson by measuring the μ^+ μ^- decay channel. By measuring dileptons it is possible to study such physics phenomena as J/Ψ suppression, ρ mass broadening, etc.

The design of the Muon spectrometer on only one side of the IP is a compromise between the acceptance, accessibility and the detector costs. Fig. 3.9 presents the Muon spectrometer. The front absorber is placed $\sim$0.9 m from the IP, covering the –4.0 $\leq \eta \leq$ –2.4 region. It is made of concrete, lead, and other metals which absorbs all particles except energetic muons. All the 5 tracking stations in the Muon spectrometer are cathode plane detectors. The integral part of the spectrometer is the dipole magnet, which bends the trajectory of charged particles in the yz plane. Tracking stations 1 and 2 are positioned just behind the absorber nose. The first one is placed within the L3 volume, tracking station 2 is at the edge of the L3. This allows the Muon spectrometer to precisely determine where the particles left the solenoidal field. Tracking station 3 is in the middle of the dipole magnet to precisely measure the deflection angle. Tracking stations 4 and 5 are further back, on both sides of another muon filter. Finally, behind tracking station 5 are the trigger chambers made of resistive plate chambers, which complete the system of identification of the $\mu^{\pm}$ particles using tracking. The Muon spectrometer will participate in the general ALICE data taking for $Pb+Pb$ collisions at the limited luminosity (up to L = 10^{27} cm^{-2}s^{-1}). For intermediate–mass ion collisions (e.g. $Ar+Ar$), where the luminosity limitations from the machine are less severe, a high luminosity run, with L $\simeq$ 10^{29} cm^{-2}s^{-1}, is also foreseen to improve the statistics. The Muon spectrometer will participate in this run, taking data together with a limited number of ALICE detectors able to sustain such event rates and determine the collision centrality (ZDC, ITS Pixel, PMD, T0, V0 and FMD) [4].

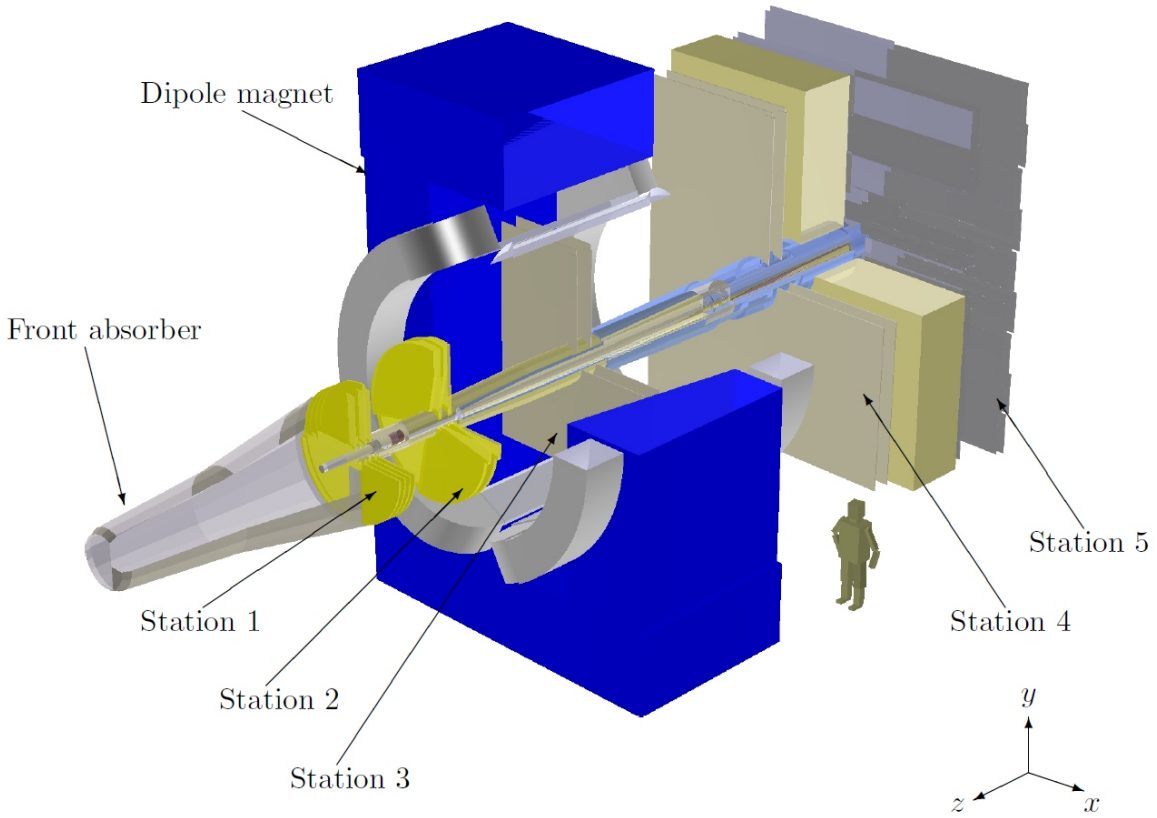

FIGURE 3.9 The Muon spectrometer in ALICE [16].

3.2.4 L3 magnet

The L3 magnet, operated by the L3 experiment during the LEP [24] collider era, is used in ALICE. Its inner radius and length are 5.6 m and 12 m, respectively. L3 provides a uniform magnetic field up to 0.5 T which allows the tracking of p_T down to 250 MeV/c. Particles with smaller transverse momenta will be reconstructed within the ALICE Inner Tracking System. The runs without magnetic field and with 5 kGauss settings (both polarities) are scheduled for ALICE (status from 20/07/2009). The decision to perform runs with 2 kGauss can be made upon a strong motivation from the TPC[8].

[8]Decision about 2 kGauss runs will be probably not physics driven but due to the need for calibration [22].

4 T0 detector overview

4.1 Design Considerations

The final shape of the forward detectors has crystallised late. A forward detector based on Micro–Channel Plates (MCP) has been proposed in the ALICE Technical Proposal [27] to provide the Level 0 (L0) trigger and multiplicity information in the forward/backward regions ($|\eta| > 1.5$). MCP would have been a suitable solution for a forward detector system but would have required substantial funds and a major R&D effort that were impossible within the time scale and budget allocated for the ALICE project. Consequently, the idea of a single detector was abandoned. Instead, a system using proven technologies, based on Cherenkov counters with magnetic field–resistant PMTs, scintillators and Si–strip detectors, has been proposed. Finally, a construction of three independent detectors: T0, V0 and FMD, named Forward Detectors, was decided as a solution for ALICE [5]. The final placement of those detectors in ALICE is sketched in Fig. 4.1.

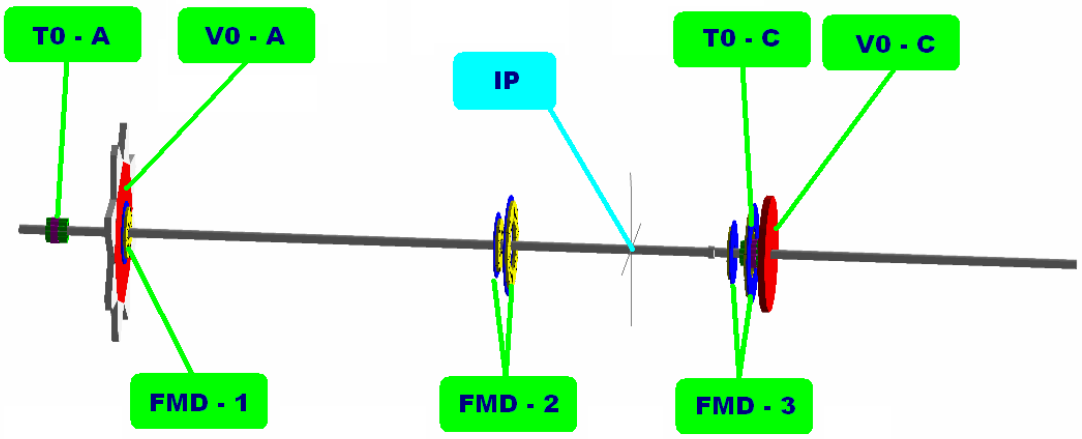

FIGURE 4.1 Placement of the Forward Detectors in ALICE.

The presence of the front absorber on the C–side of ALICE reduced the available space in that area to a small volume around the beam pipe, to be shared by T0,

V0 and FMD. Furthermore, there is no access to that area unless the entire central part of ALICE is disassembled. Hence, for T0 only a small detector system could be considered. It has to been based on well–tested and reliable technology, capable of maintenance–free operation for at least 10 years. The requirement for T0 detector to generate the vertex pulse for the ALICE trigger and to give an on–line, position–independent start signal implied a two–arm design with detectors on each side of the IP [28]. The total dead time of the detector, including pulse generation and processing, should be less than the bunch–crossing period in $p+p$ collisions, that is, less than 25 ns. The detector must tolerate operation inside the L3 magnet in a magnetic field of strength up to 0.5 T. The list of design considerations can be summarised as follows:

- detectors on both sides of the IP;
- compact design;
- time resolution of about 50 ps;
- high efficiency;
- total dead time of less than 25 ns;
- operation in a magnetic field of up to 0.5 T;
- radiation tolerance up to 500 krad;
- reasonable multiplicity resolution for charged particles;
- high reliability;
- maintenance–free operation.

ALICE will study various physics topics using different beam conditions which imply changes in the counting rate by nearly two orders of magnitude. The trigger and DAQ systems in ALICE have been designed to balance the capacity to record central collisions which generate large events with the ability to acquire the largest possible fraction of rare events. Dedicated trigger systems will select rare candidate events in the Muon spectrometer, the EMCal and the TRD, while a minimum bias trigger will provide a fast signal to the slower detectors with good efficiency at all multiplicities and will reject beam–gas interactions. The first response from the trigger has to be fast, i.e. ~ 1.2 μs, to cope with large multiplicities in $Pb+Pb$ collisions at an interaction rate of 8 kHz. The ALICE trigger includes a pretrigger, three hardware trigger levels (L0 at 1.2 μs, L1 at 6.5 μs and L2 at 88 μs) and a processor–based high level trigger. The T0 will play the dominant role in providing ALICE with the fast trigger signals. T0 trigger functions include the measurement of approximate

vertex position, a rough estimate of event multiplicity and informing that at least one of the arms of the T0 detector has registered a valid pulse. The first of the above mentioned trigger functions, determination of the vertex position, is crucial for discriminating against beam–gas interactions. With 50 ps time resolution one obtains $\pm$ 1.5 cm accuracy in vertex determination[1]. If the vertex position falls within the pre–defined values, an L0 trigger signal called T0–vertex is produced. The second function, multiplicity determination, is an important back–up option for the V0 detector, which covers a considerably larger pseudorapidity range. The multiplicity measured by T0 is compared to 2 pre–set values to generate one of the three possible trigger signals: T0 minimum bias, T0 semi–central, or T0 central, corresponding to low, intermediate, and high multiplicities[2]. There are only two threshold values because the minimum bias signal is identical to the T0–vertex, which corresponds to a multiplicity sufficient to have triggered both halves of the T0 detector. The T0 detector is required to generate the earliest (L0) trigger signals, hence they are strictly generated on–line without the possibility of any off–line corrections. The off–line corrections are applied for non–trigger signals, such as the time reference for the TOF detector.

Prior to the L0 trigger signal, T0 supplies the early wake–up signal to the Transition Radiation Detector. Otherwise TRD's front–end electronics is in a standby mode[3].

The T0 is the only subdetector in ALICE capable of delivering a high–precision start signal for the TOF detector. The T0 start signal for TOF must correspond to the real time of the collision (plus a fixed time delay) and be independent of the position of the vertex. The required precision of the T0 signal must be better or at least equal to that of the TOF detector (σ = 50 ps). Generating the TOF start is not done by any other detector in ALICE so the quality of the T0 time resolution directly influences the quality of TOF identification. In favourable cases, mostly for heavy ion collisions, one may expect some further improvement of T0 time resolution in off–line analysis. For that purpose it is important to read out and store the time and amplitude of each PMT of the T0 array.

The T0 detector physics objectives can be summarised as follows:

- to generate a start time (T0) for the TOF detector. This timing signal corresponds to the real time of the collision (plus a fixed time delay) and is independent of the position of the vertex. The required precision of this signal is about 50 ps (r.m.s.);

[1]The time taken for light to travel 1 m is approximately 2.99 ns. 50 ps corresponds thus to $\sim$1.67 cm. Since there are two T0 arrays on opposite sides of IP, the combined result of both is slightly more accurate.

[2]T0 minimum bias signal is generated whenever semi–central and central trigger signals are issued. On the same footing the semi–central signal include the central trigger.

[3]This pretrigger signal must be generated strictly on–line and delivered within 200 ns of the actual collision, which is well ahead of the L0 trigger.

- to measure the vertex position (with a precision $\pm$ 1.5 cm) for each interaction;
- to provide a L0 trigger when the vertex position is within the preset values. This will discriminate against beam–gas interactions;
- to generate an early 'wake–up' signal to the TRD, prior to L0;
- to provide redundancy to the V0 counters;
- to generate minimum bias (one or both arrays hit) and multiplicity triggers (semi–central and central).

4.2 Simulations

4.2.1 Motivation

A special software framework called AliRoot has been created and is continuously developed for the ALICE experiment. One of its applications are simulations. Monte-Carlo simulation of both protons and nuclei interactions in the ALICE experiment are implemented within the framework, with a subsequent tracing of the particles generated in the collisions through the detectors of the ALICE are done within the framework. More information about the AliRoot framework itself, which includes a dedicated T0 detector package consisting of 33 classes and 22 macros (status from 20/07/2009) facilitating simulation, data processing, reconstruction, alignment, etc. of the T0 detector can be found in Chapter 4.6. The detector performance has been simulated using the ALICE simulation framework and verified in several test experiments using the CERN PS, cosmic rays and laser pulses. The detector efficiency for $p + p$ collisions has been calculated. Simulations also included the resolution of the detector in $Pb + Pb$ collisions as well as the detector efficiency in abnormal situations: at the failure of one or several PMTs. Finally, it has been shown by calculations that the definition of the precise instant of collision can be achieved by the use of the time interval averaging technique.

4.2.2 Event generators

The aim of the event generator[4] is that the simulated events are as close as possible to real interactions. The results of event generators together with further simulation software are used to plan and optimise the detector design. The present understanding of the underlying physics limits the predictive power of the generator.

The key issue for an event generator in order to provide a correct description of the pseudorapidity and multiplicity distributions is to correctly estimate the

[4]Event generators make extensive use of random number generators, hence there are also called Monte Carlo (MC) event generators.

amount and strength of partonic interactions. A combined approach can be to describe the interactions in high–energy proton collisions: perturbative QCD is very successful in describing parton interactions with large momentum transfer called hard interactions. In the region of soft interactions the coupling constant α_s of the strong force approaches unity, thus the perturbative approach is not valid [37]. In contrast, many of the particles produced in LHC collisions, especially in events triggered by minimum–bias triggers originate from soft interactions. Soft interactions are also present in an event that initially had a hard interaction. Perturbative QCD is combined with a phenomenological approach that describes soft processes in the region where perturbation theory is not applicable in a combined approach used in event generators.

The three event generators: Pythia, Phojet and Hijing have been used for T0 simulations described in this thesis.

Pythia

Pythia [29] is an event generator that combines perturbative QCD and sophisticated, mostly phenomenologically motivated models. These are connected by a tunable cut–off parameter $p_{T,min}$, where p_T is the momentum transfer in the hard interaction. In general, Pythia's approach results in many tunable parameters especially from phenomenological models. These have a significant influence on the generated distributions.

Phojet

The event generator Phojet [30] is based on a two–component approach that describes high–energy collisions with a soft and a hard component. These are split in the calculation at a p_T cut-off parameter and their results are combined by a unitarization procedure. The ideas of the Dual Parton Model are employed for the soft component. The hard component is calculated by perturbative QCD as in Pythia. Phojet calculates the total cross–section as well as the cross–sections for different processes using unitarized scattering amplitudes. These are derived using Regge arguments in the soft region and perturbative QCD in the hard regime.

Hijing

The Heavy–Ion Jet Interaction Generator (Hijing) [31] is designed to simulate multiple jets and particle production in $p + p$, p + A or A + A collisions. It uses PYTHIA sub–routines and a Lund jet fragmentation scheme. Fig. 4.2 presents a distribution obtained with Hijing for 5.5 TeV $Pb+Pb$ collisions with an impact parameter varying from 0 to 14 fm.

In the following the results of the simulations of T0 detector using Pythia, Phojet and Hijing are discussed.

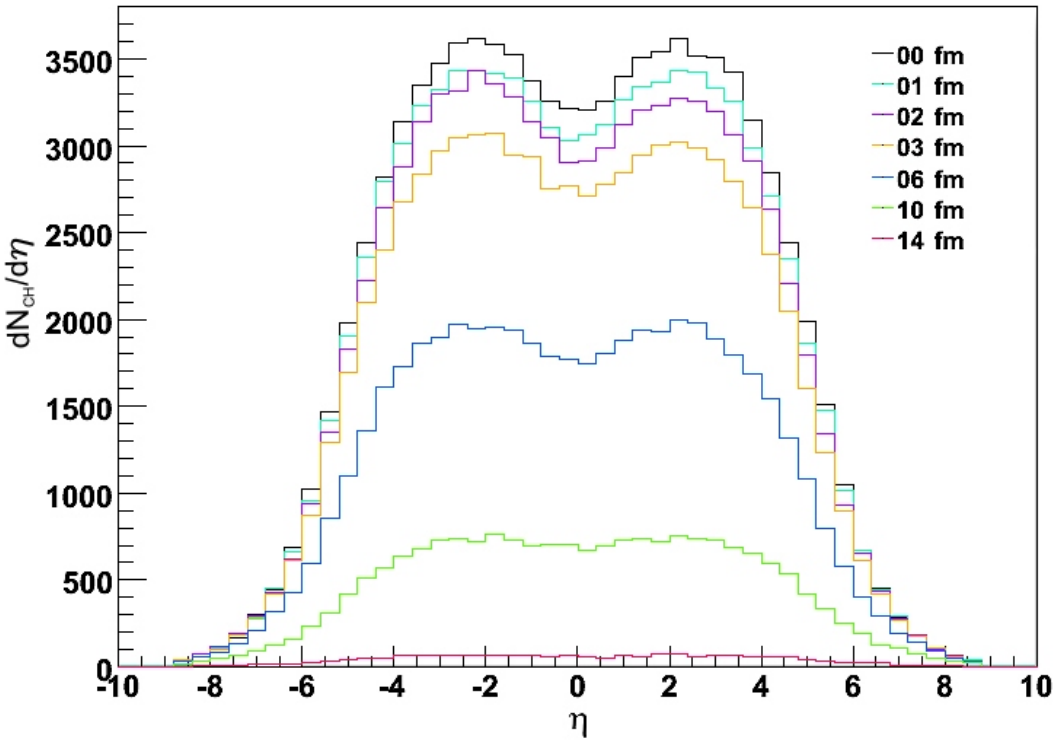

FIGURE 4.2 Charged–particle density for $Pb+Pb$ collisions at $\sqrt{s}$ = 5.5 TeV at various impact parameters.

4.2.3 T0 response function

The T0 detector's response simulations were made with Pythia, assuming the diameter of the T0 sensitive volume (quartz radiator) to be 2 cm (more information about sensitive volumes is given in Chapter 4.6). γ–rays originating from the IP and subsequently converting into electron–positron pairs as well as the Cherenkov light emission and light collection processes [32] have been included in the simulation.

PMT amplitude distribution

In ALICE beam conditions, the amplitude distribution of the PMTs resembles the changing position of the IP. We have studied that by implementing into AliRoot sub–routines, the response function of the Cherenkov counters and generating events with Pythia. During typical 10 or 14 TeV $p+p$ collision only few minimum ionising particles (MIPs)[5], most likely one or two, would reach one of the PMTs on each side of IP. Fig. 4.3 presents number of MIPs registered by 24 T0 PMTs in 20 000 $\sqrt{s}$ = 10 TeV $p+p$ minimum bias (MB) collisions[6]. The amplitude was obtained from QTC in

[5]The particle whose mean energy loss rate through matter is close to the minimum is called a minimum ionising particle (MIP).

[6]Pythia $p+p$ events are minimum bias, unless otherwise stated.

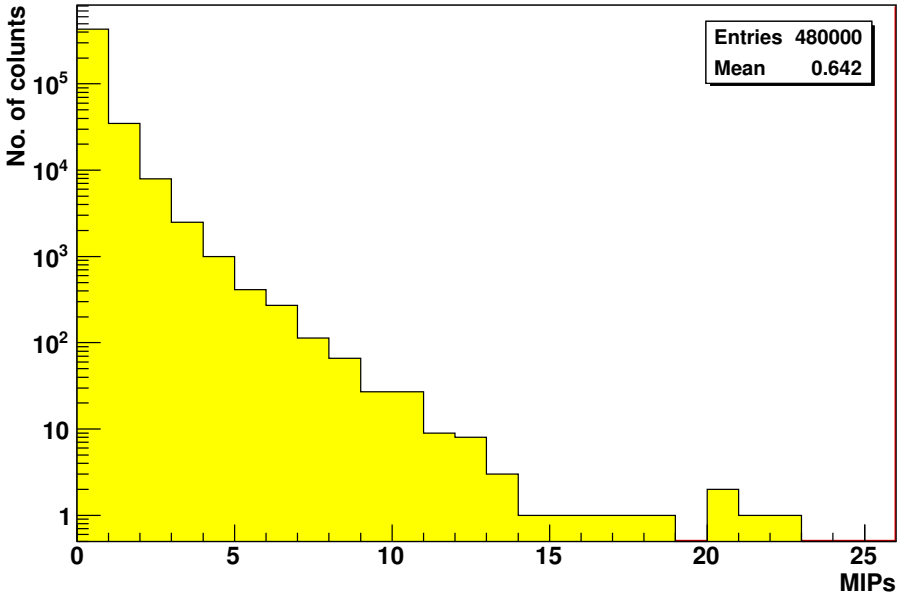

FIGURE 4.3 Total number of MIPs registered by 24 T0 PMTs in 10 TeV $p + p$ MB collisions. Number of events is 20 000, data comes from the Physics Data Challenge 2009 production (PDC09a4).

the manner described later in Chapters 4.5.1 and 4.6.

The amplitude distributions of a single T0 PMT on A– and C–side, obtained from a time difference between LED and CFD, for 10 000 $\sqrt{s}$ = 14 TeV $p + p$ collisions are presented in Fig. 4.4. The angular distribution of particles, γ–ray conver-

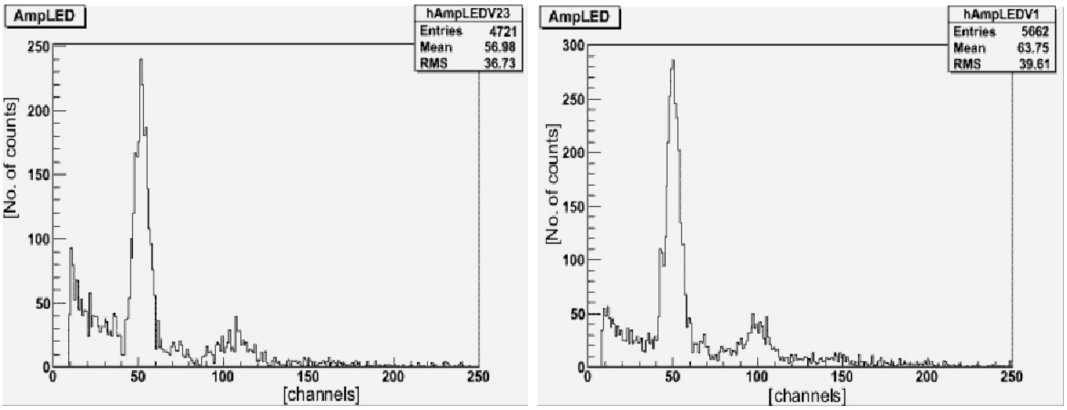

FIGURE 4.4 Amplitude distributions for the T0–C (left), and the T0–A (right) given by Pythia. 50 channels correspond to 1 MIP. It characterises the PMT's response to the flux of relativistic particles emerging from the $\sqrt{s}$ = 14 TeV $p + p$ collisions.

sion in the radiator, the secondary particles (electron–positron pairs and δ-electrons), and the background induced by the beam pipe and surrounding detectors were included in the simulation. As a next step, in order to increase statistics, the amplitude distributions from all 12 PMTs on each side have been summed up, the resulting am-

plitude distributions for T0–C (0.727 m from the IP, on the Muon spectrometer side) and for T0–A (3.75 m from the vertex on the RB24 side [45]) are given in Fig. 4.5. T0's single MIP amplitude resolution is clearly visible in the simulations. Fig. 4.6

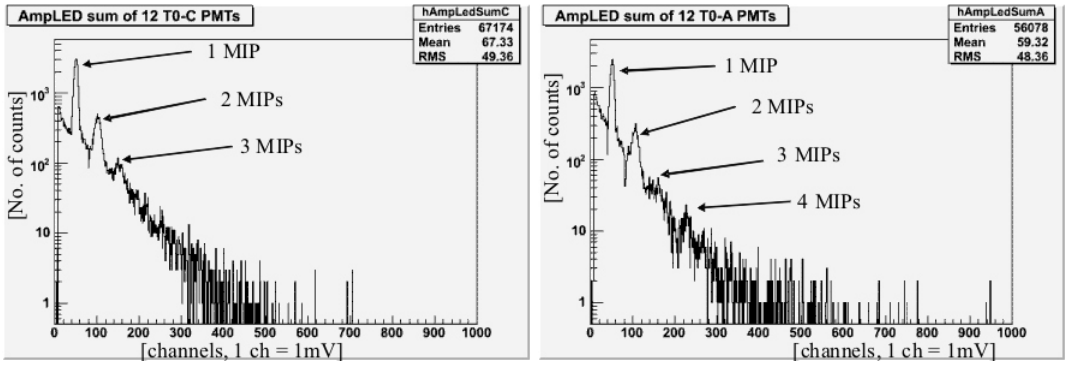

FIGURE 4.5 Summed amplitude distributions for the T0–C (left), and the T0–A (right) given by Pythia for $\sqrt{s}$ = 14 TeV $p + p$ collisions.

presents the acceptance of the T0 detector, which refers to acceptance means here the ratio of the number of particles flying into the sensitive volumes of 24 T0 PMTs to the total number of particles generated in the collision.

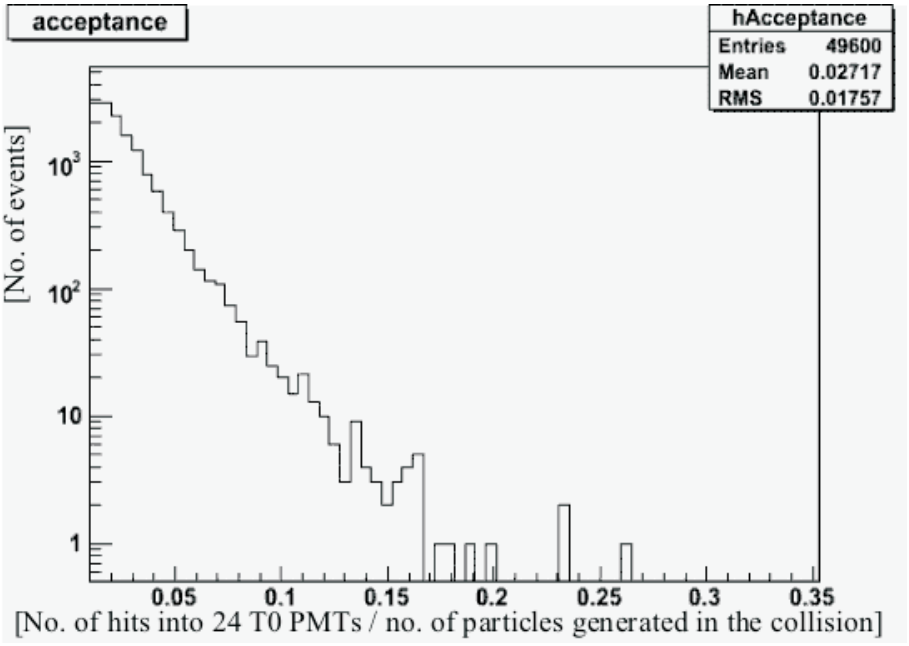

FIGURE 4.6 T0 acceptance in $\sqrt{s}$ = 14 TeV $p + p$.

Response to primary and secondary particles

The T0 response to primary and secondary particles has been studied with Pythia at $p + p$ collision energies of 900 GeV and 14 TeV. Primary particles are all parti-

cles produced in the collision: products of strong and electromagnetic decays as well as weak decays of charmed and beauty particles, but excluding feed–down products from strange weak decays and other secondary particles. These are, for example, γ–conversions and products from secondary hadronic interactions with the detector material. In the simulation these are the final–state particles created by the event generator, which are then propagated (and decayed) in the subsequent detector simulation [37]. Secondary particles are non–primary particles, including decay products. The simulated multiplicity of primary and secondary charged particles emerging from $p + p$ collisions at $\sqrt{s}$ = 14 TeV obtained with Pythia hitting each of the T0 arrays is shown in Fig. 4.7.

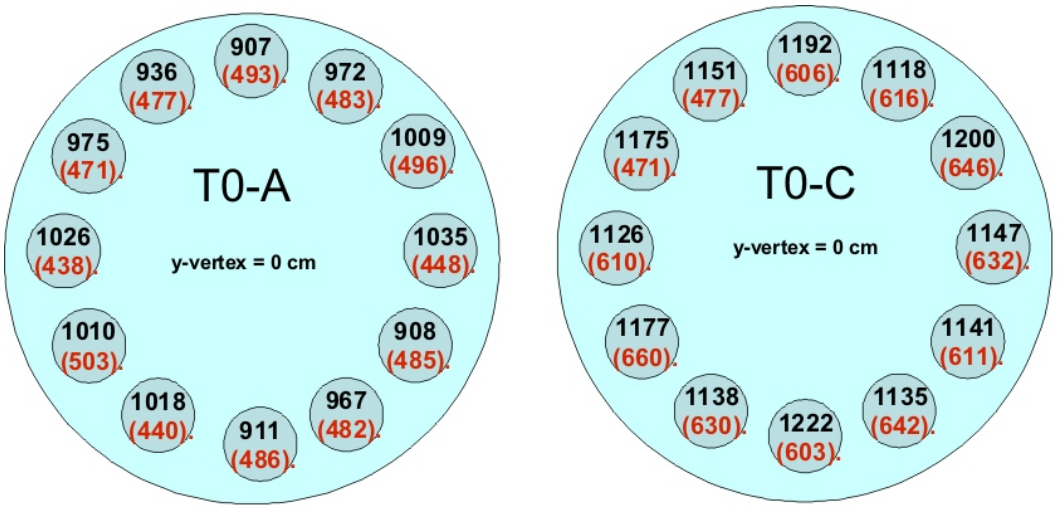

FIGURE 4.7 Total multiplicity (black font) of primary (red font, in brackets) and secondary charged particles registered by the T0–A (left) and by T0–C (right) simulated with Pythia for $\sqrt{s}$ = 14 TeV $p + p$ collisions.

The total multiplicity in both arrays is shown in Fig. 4.8. The secondary particles combine for slightly less than 50% of events registered by T0. The secondaries emerge mostly from the interaction with the beam pipe. The other source of secondary particles is from the detector material between the IP and the T0.

Fig. 4.9 presents a simulated vertex distribution for primary and secondary particles in 900 GeV $p + p$ collisions.

4.2.4 Multiplicity resolution

The T0 detector should generate 3 trigger signals corresponding to the 3 multiplicity levels: minimum–bias, semi–central, and central ion–ion collisions, as discussed in Chapter 4.1. Such signals are produced, for instance, by analysing the sum of all PMT pulses with discriminators. This procedure works best in the case of high multiplicities (i.e. for A + A collisions). In $p + p$ collisions the average occupancy per

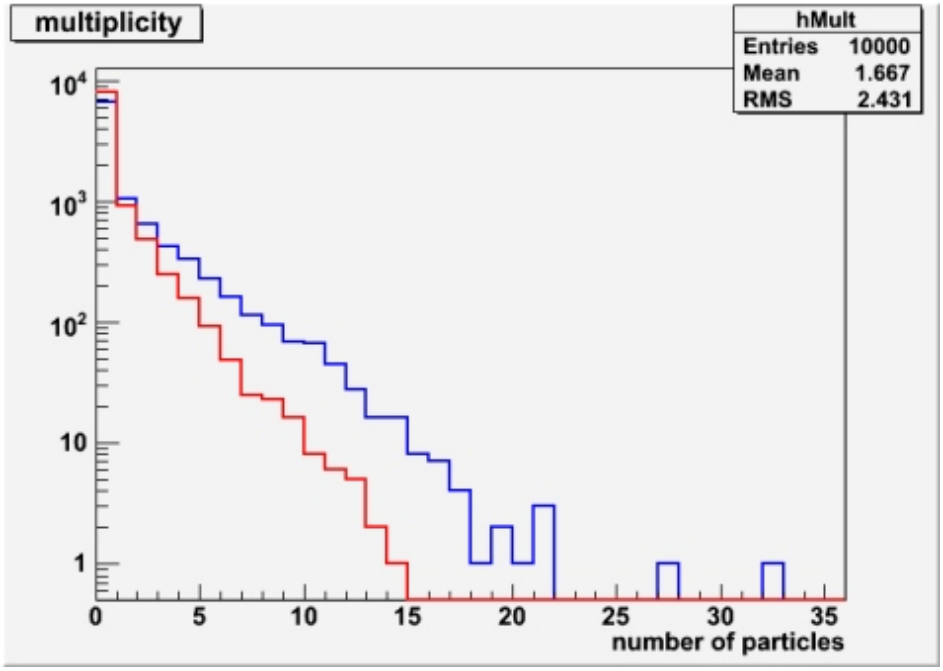

FIGURE 4.8 Total multiplicity distribution of charged primary (blue) and secondary (red) particles for $\sqrt{s}$ = 14 TeV $p + p$ collisions simulated with Pythia.

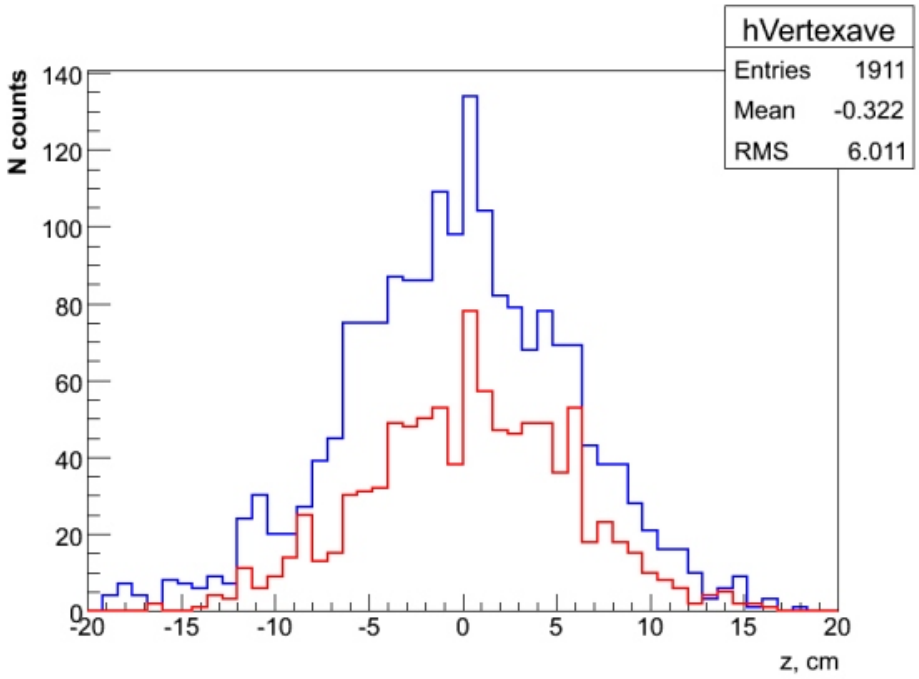

FIGURE 4.9 Simulated longitudinal vertex distributions in the T0 detector for $\sqrt{s}$ = 900 GeV $p + p$ collisions. The red line represents the simulation done with T0, beam pipe and forward detectors included in the geometry, whereas the blue line represents the situation where all ALICE detectors were present in the simulation.

PMT is only about 0.3, but the multiplicity determination is still possible due to the single MIP amplitude resolution of T0.

To estimate the T0 multiplicity resolution from the sum of PMT signals we have first estimated the multi–particle resolution of a single Cherenkov counter in broad–beam geometry. As the distribution of the particles is random and uniform across the surface of the radiator, one can simply sum the number of photoelectrons for 2 particles, 3 particles, etc. When the number of particles exceeds 3 the photo-electron distribution becomes Gaussian. The resolution of a Cherenkov counter for multi–particle events is approximately two times better than the statistical error.

The amplitude distribution for $Pb + Pb$ collisions at $\sqrt{s_{NN}}$ = 5.5 TeV, averaged over all counters and events, in both T0 arrays is shown in Fig. 4.10. Fig. 4.11

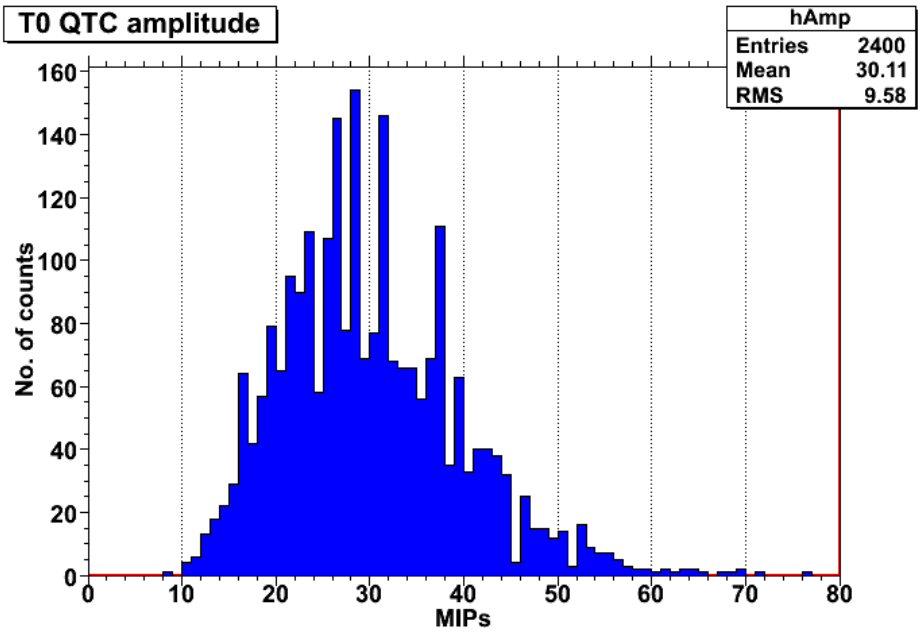

FIGURE 4.10 Amplitudes from 24 T0 PMTs averaged over 100 $\sqrt{s_{NN}}$ = 5.5 TeV Pb+Pb Hijing events from PDC07e production. Data from PDC08d6 production indicates that the T0 amplitudes for central $Pb + Pb$ collisions are higher (see Fig. 4.14). The η cut in the acceptance [-4.2 < η < 4.2] and a different geometry used in the PDC07e production accounts for the difference.

presents the distributions obtained separately for T0–A and T0–C. It is important to note that the average number of MIPs hitting the T0 is 86 for 5.5 TeV $Pb + Pb$ collisions based on more recent simulations (PDC08d6, see Fig. 4.14) – further details are presented in the next chapter. In order to increase the dynamic range to account for the amplitudes above 100 MIP in $Pb + Pb$ collisions the HV on the PMTs will be lowered. This will cause slight worsening of the amplitude resolution for lower multiplicities, however this not a problem for heavy–ion events.

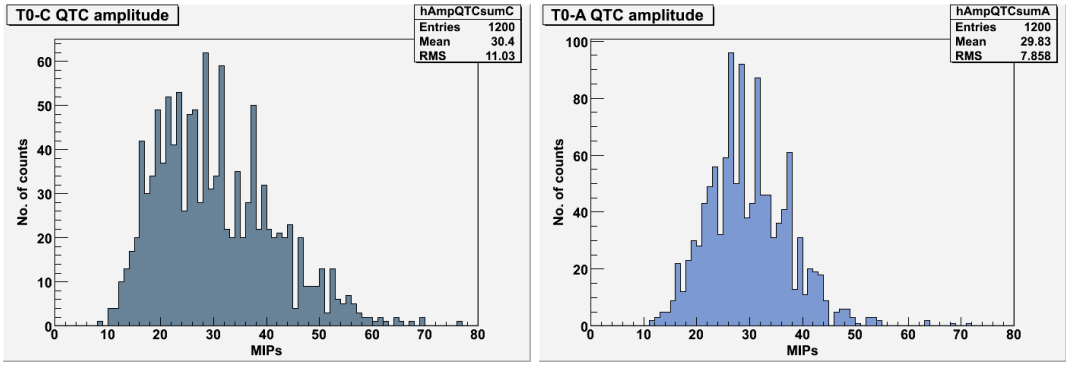

FIGURE 4.11 Amplitude distributions for the T0–C (left), and T0–A (right) obtained with Hijing for 5.5 TeV $Pb + Pb$ collisions based on PDC07e production. Data from PDC08d6 production indicates that the T0 amplitudes for central $Pb + Pb$ collisions are higher – see Fig. 4.14.

4.2.5 T0 efficiency in $p + p$ and $Pb + Pb$ collisions

Due to high multiplicities of produced particles, the triggering efficiency of the T0 detector in $Pb + Pb$ collisions is nearly 100%. But in $p + p$ collisions the involved multiplicities are much smaller and the expected efficiency must be carefully simulated, taking into account not only the response function of the T0 detector but also all the details of geometry, location and thickness of the beam pipe, support structures, etc. In carrying out these simulations a particle was registered if the signal from the PMT was larger than 50 photoelectrons. This threshold value was based on our actual experimental data. The background from the interaction of primary particles coming from the IP with the beam pipe was taken into account, as shown previously (Figs. 4.7 and 4.8).

The simulated data produced in the Physics Data Challenge 2008 (PDC08) and the Physics Data Challenge 2009 (PDC09) and staged on CERN Analysis Facility (CAF) was used in the subsequent T0 efficiency calculations. One way to estimate the efficiency of each of the T0 PMT arrays is by using the T0 OR module. Fig. 4.12 presents a typical T0 OR–C spectrum. The efficiency for a given T0 array can be then determined by checking how many OR signals were generated in the predefined 'gate'. In Fig. 4.12 in 12 098 of 20 000 events OR–C generated a valid signal yielding 60.5% efficiency. Similarly, the T0 Mean Timer module can be used to calculate the efficiency of T0–A and T0–C arrays in coincidence. The efficiency of either of the arrays registering a valid event (T0–A OR T0–C) can be calculated as a difference between the sum of efficiencies of each array and the efficiency in coincidence: T0-A + T0-C – T0-A&T0-C.

Tables 4.1 and 4.2 summarise the T0 efficiencies for 900 GeV and 10 TeV $p + p$ collisions obtained with Pythia and Phojet. The difference between productions LHC08c11 and LHC09a4 was accounted for by the different geometry[7] used in the

[7] In addition to different geometry, full misalignment/decalibration was used in LHC08c11 while

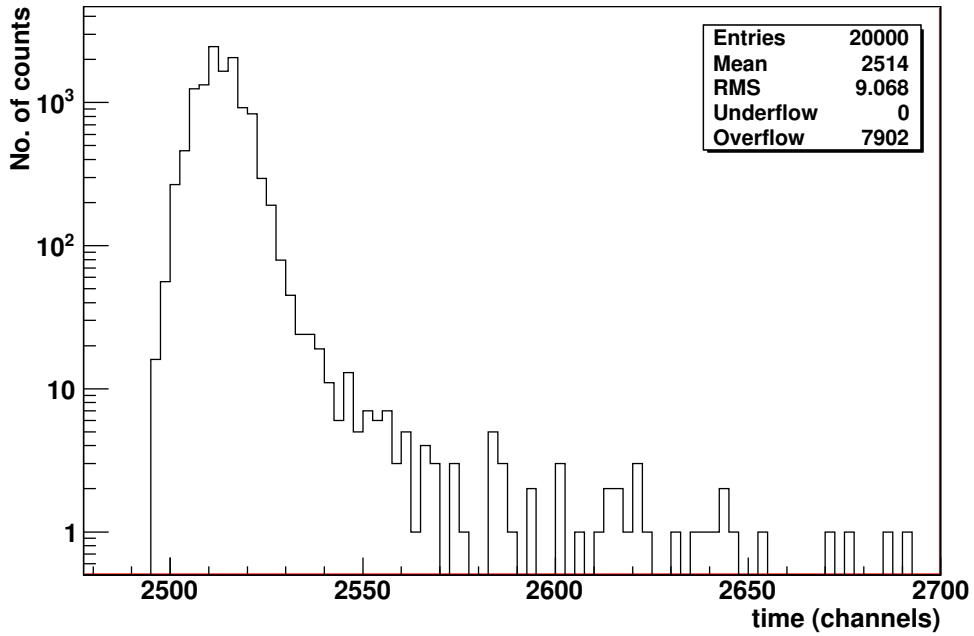

FIGURE 4.12 T0 OR–C in $\sqrt{s}$ = 10 TeV $p + p$ minimum bias collisions.

TABLE 4.1 T0 efficiencies in percent for 50 000 $p + p$ minimum bias collisions at $\sqrt{s}$ = 900 GeV obtained with Pythia and Phojet. Magnetic field strength is given in Tesla.

	Phojet		Pythia	
B	0 T	0.5 T	0 T	0.5 T
PDC Dataset	LHC08c18	LHC08c16	LHC08c14	LHC08c12
T0–A	37	39	33	35
T0–C	52	53	45	46
T0–A & T0–C	21	22	18	19
T0–A OR T0–C	68	70	60	62

TABLE 4.2 T0 efficiencies in percent for 50 000 $p + p$ minimum bias collisions at $\sqrt{s}$ = 10 TeV obtained with Pythia and Phojet. Magnetic field strength is given in Tesla.

	Phojet		Pythia		
B	0 T	0.5 T	0 T	0.5 T	
PDC Dataset	LHC08c17	LHC08c15	LHC08c13	LHC08c11	LHC09a4
T0–A	56	58	52	54	60
T0–C	62	63	57	57	60
T0–A & T0–C	38	40	38	39	44
T0–A OR T0–C	80	81	71	72	76

LHC09a4 was performed using ideal/residual misalignment conditions (see Chapter 4.6.3).

two productions [38]. T0 efficiency for non–diffractive (ND), single–diffractive (SD) and double–diffractive (DD) events has been studied with Pythia for $\sqrt{s}$ = 10 TeV $p+p$ collisions [29]. The result, obtained based on PDC09a4 data, are listed in Table 4.3. The minimum bias efficiency is a combination of efficiencies for ND, SD and DD

TABLE 4.3 T0 efficiencies in percent for 10 TeV $p+p$ non–diffractive (ND), single–diffractive (SD) 1 and 2 [29], and double–diffractive (DD) events based on PDC09a4 data. Minimum bias (MB) efficiency is also given.

	ND	SD 1	SD 2	DD	MB
% of events	67	10	9	14	100
T0–A	72	39	11	28	60
T0–C	73	23	25	25	60
T0–A & T0–C	56	15	2	6	44
T0–A OR T0–C	89	47	34	47	76

processes.

The efficiency simulations for 14 TeV $p+p$ collisions were performed at Louhi [39], Murska, Sepeli, Opaali [40] and Linuxfs clusters in Finland. The results are presented in Table 4.4.

TABLE 4.4 T0 efficiencies in percent for 14 TeV $p+p$ minimum bias collisions.

	T0–C	T0–A	T0–A & T0–C	T0–A OR T0–C
T0 only	32	31	28	35
T0 with beam pipe	57	54	39	72
T0, beam pipe, ITS, V0, FMD, PMD	59	55	41	73
T0 with everything else	59	56	42	73

The increase of the efficiency in the presence of the beam pipe is caused mainly by the conversion of gammas into electrons in the material of the pipe. The efficiencies given in Table 4.4 are averaged over all multiplicities.

The efficiency for multiplicities larger than 20 is given in Fig. 4.13.

At multiplicities $M > 150$ the efficiency of the T0 detector, measured as a coincidence of T0–A and T0–C, is already about 90%. Hence for $Pb + Pb$ collisions, the efficiency is 100%, except for the ultra–peripheral collisions. It has been confirmed by the results from PDC07e and PDC08d6[8] production: the T0-A, T0-C, T0-A & T0–C and T0–A OR T0–C registered 100% of the events generated.

[8]PDC07e and PDC08d6 are the only Hijing central PDC productions performed so far (status for 20/07/2009).

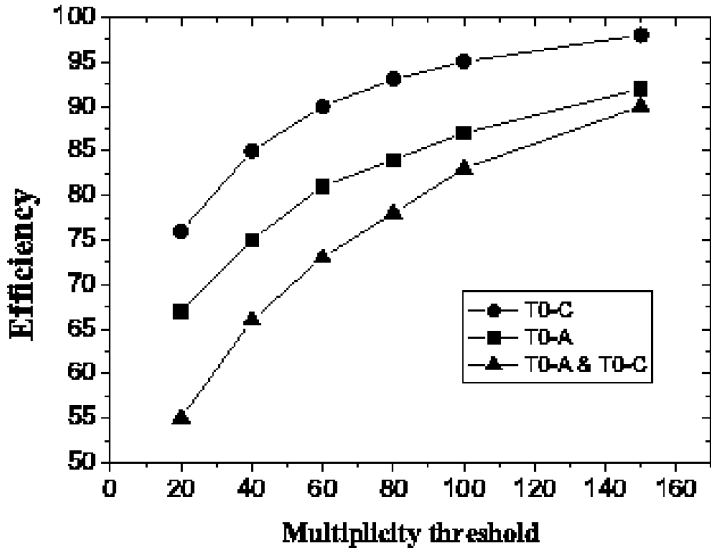

FIGURE 4.13 Efficiency for $p + p$ collisions as function of total multiplicity of events.

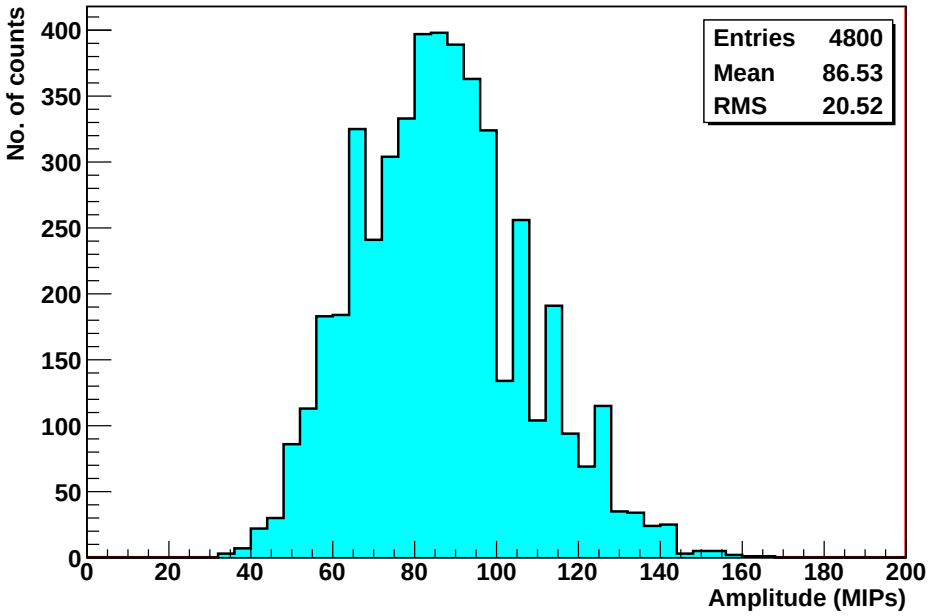

FIGURE 4.14 Amplitude distribution from 24 T0 PMTs averaged over 200 $\sqrt{s_{NN}}$ = 5.5 TeV $Pb + Pb$ Hijing events from PDC08d6 production.

4.3 T0 construction

The T0 detector consists of two arrays of Cherenkov counters, 12 counters per array[9]. The T0 arrays are located on the opposite sides of the IP, allowing measurement of the exact time of the collision and the vertex position along the z–axis. The location of the two T0 arrays inside ALICE is shown schematically in Fig. 4.15.

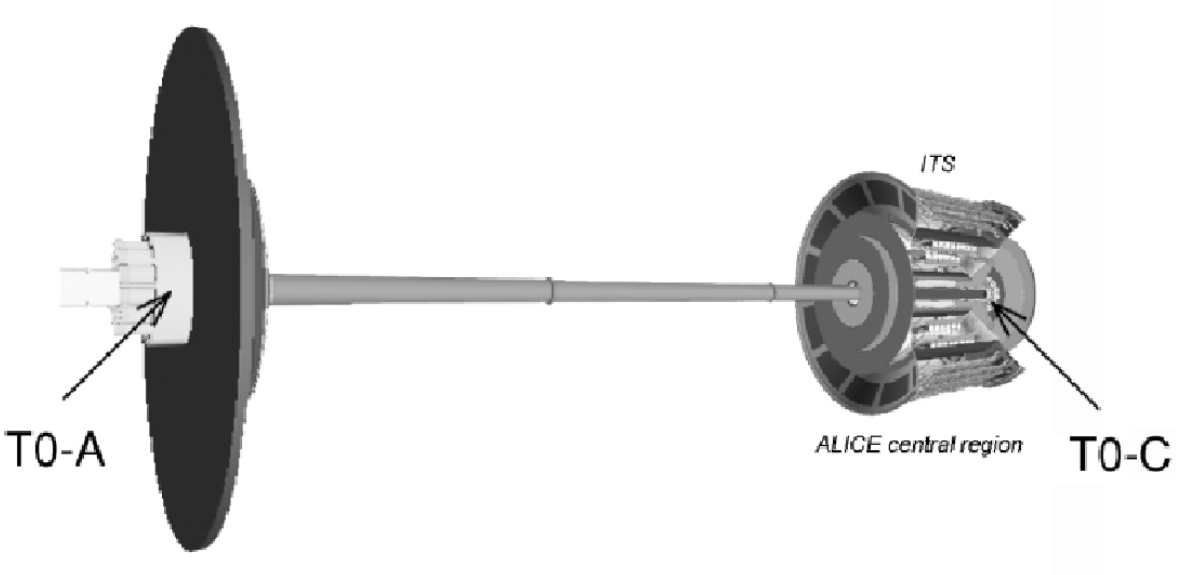

FIGURE 4.15 Position of the T0 arrays with respect to ITS in ALICE.

On the A–side, the distance from the geometrical center of the front of the T0 array to the IP is about 3.75 m. Fig. 4.16 shows the placement of T0–A with respect to the IP and two other forward detectors. On the Muon spectrometer side, the position of the array is limited by the presence of the Front absorber nose. The T0–C is placed 72.7 cm away from the IP – as close as possible to the absorber, as sketched in Fig. 4.17.

Fig. 4.18 shows the pseudorapidity range covered by the detector, for T0–C it is –2.967< $|\eta|$ <–3.276, and for T0–A: +4.605< $|\eta|$ <+4.915.

The mechanical support structure of the T0 arrays consists of a cone section on which 12 PMT's are installed and the cylindrical part, which fixes the whole structure to the support. In order to allow assembly of the entire structure around the beam pipe, both mechanical structures were divided into 2 halves[10], as depicted in Fig. 4.19. The T0–C array consists of 12 PMT's mounted around the beam axis on a supporting mechanical structure, which is fixed to the front surface of the front

[9]Initially two design options were considered for the T0 arrays: a smaller version, with just 12 detectors in each array forming a single layer of photomultiplier tubes wrapped around the beam pipe, and a version with 24 detectors arranged in 2 layers. Due to the space constraints on the Muon spectrometer side the version with 12 PMTs was chosen. All the same, simulations indicate that, unlike on A–side, the second layer on the C–side would not considerably improve the efficiency as it

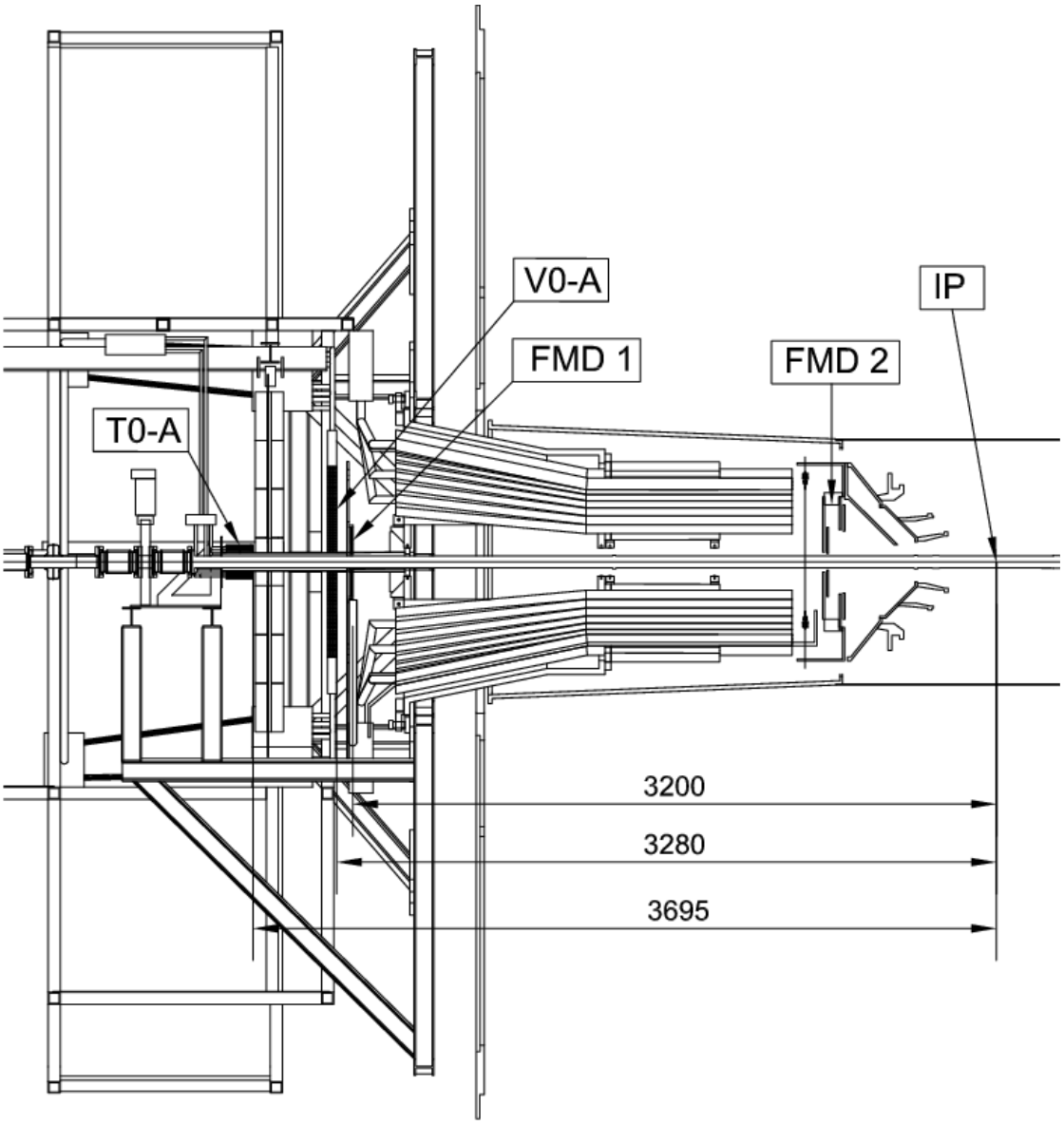

FIGURE 4.16 Position of the T0–A and other forward detectors on RB24 side of ALICE.

absorber. The central axes of the PMT's are placed on a cone surface with a vertex at the IP. The angle between those axes and the beam axis is 5.4 degrees. Several constraints determined the exact location of T0–C:

would already be too far away ($|\eta| < -2.9$).

[10]The bake–out of the central beam pipe, which requires moving the Time Projection Chamber (TPC) to its parking position and removal of the Inner Tracking System (ITS) and Forward Detectors, is foreseen during the long LHC shutdowns, in order to guarantee high vacuum quality during the whole operation period. This implies the removal of the ITS and Forward Detectors from the operating position and re–installation. Therefore all the Forward Detectors and their support structures are divided in half and assembled around the beam pipe.

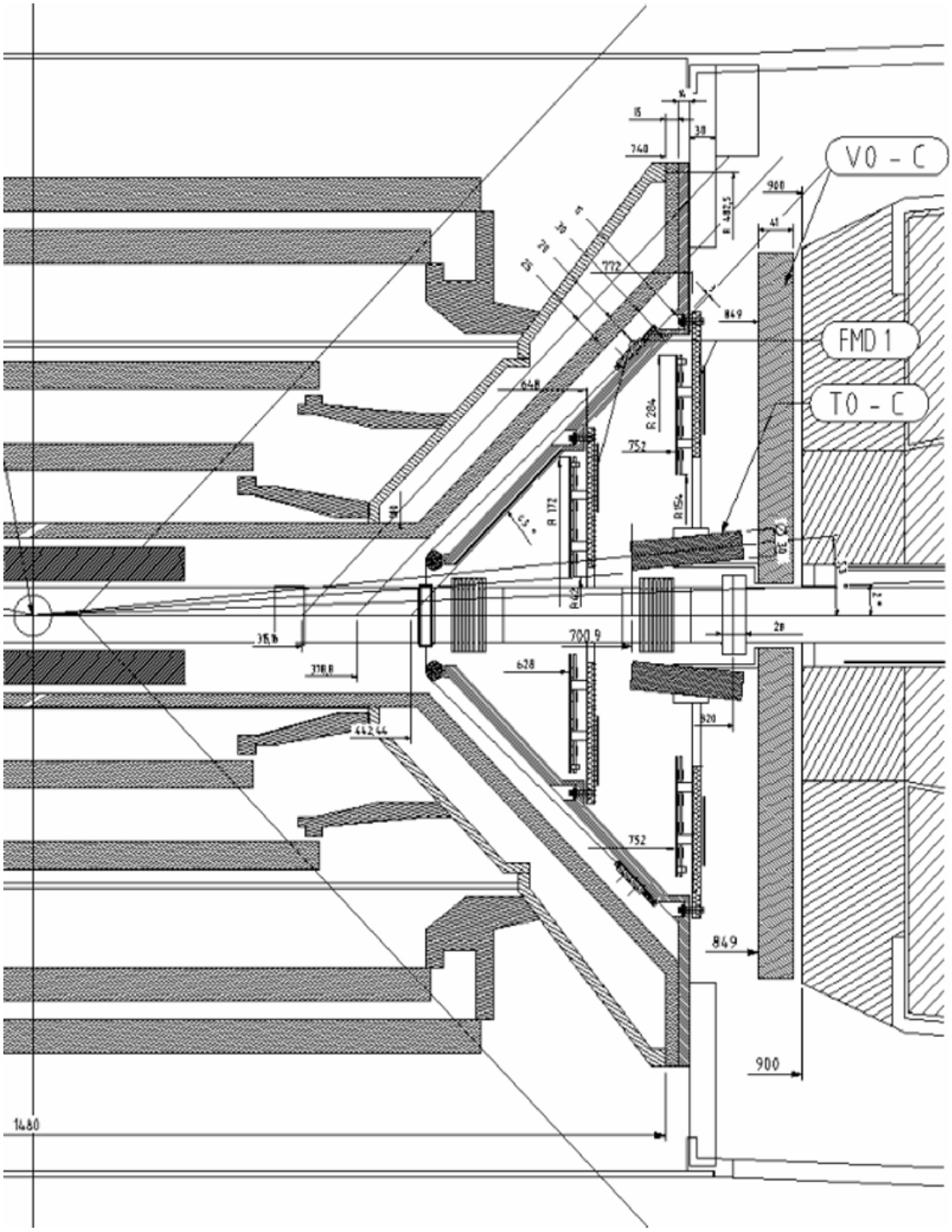

FIGURE 4.17 Position of the T0–C detector and other forward detectors on RB26 side of ALICE.

- at least 8 mm distance from the vacuum pipe to the T0–C support[11];

[11] Diameter of beam pipe is 60 mm. A radial clearance of 8 mm to the beam pipe has been respected taking into consideration all the design and fabrication tolerances of all the components for T0–C.

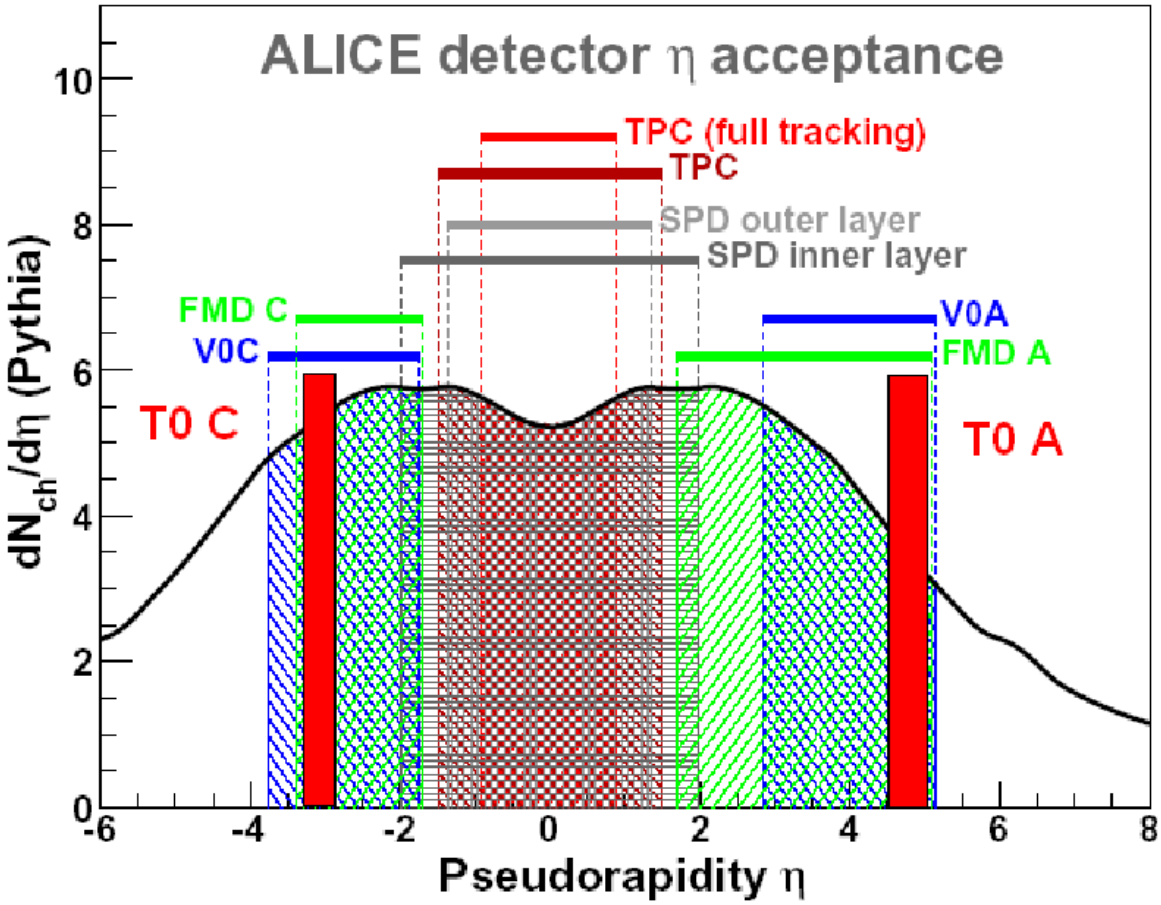

FIGURE 4.18 ALICE detector η acceptance.

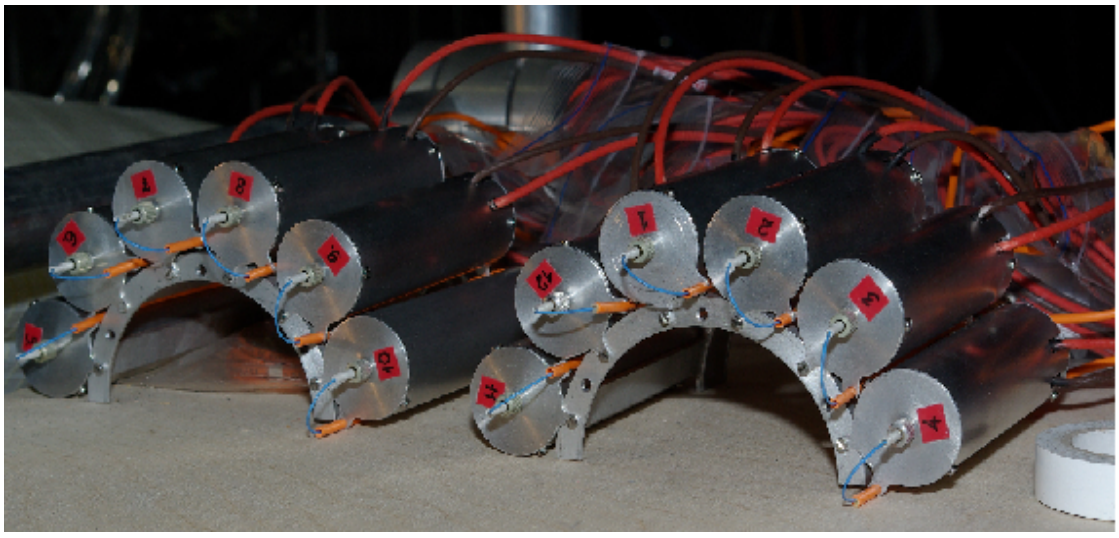

FIGURE 4.19 Two halves of the T0–A array.

- integration with V0 detector which influenced the dimensions and geometry

of the support (see Fig. 4.20).

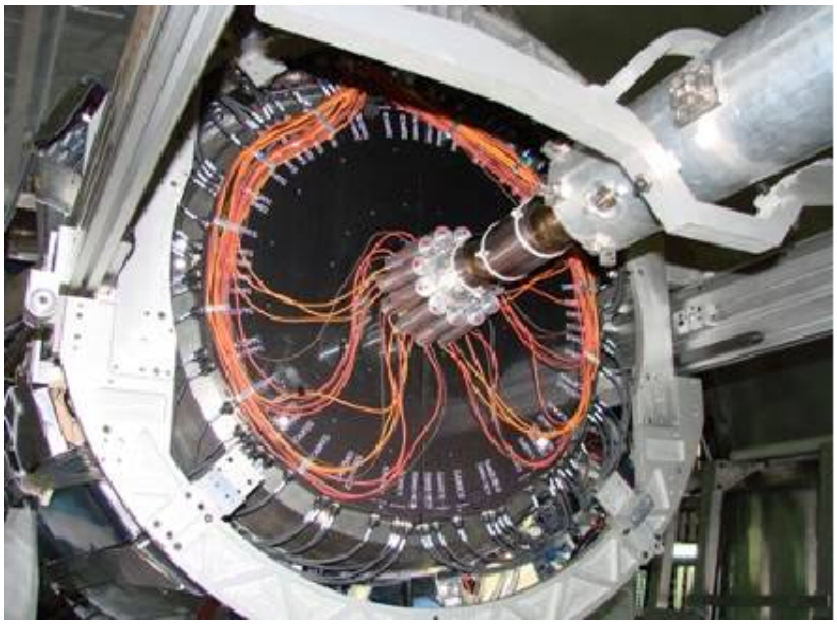

FIGURE 4.20 Placement of forward detectors in RB26 side of ALICE: V0C (covered with T0 optical fibres) and T0–C detectors.

Since the TPC has been installed in its operating position in 2007, there is no access to T0–C, which has been since then completely hidden between the ITS and the Muon arm[12].

The 12 T0–A PMTs are installed on the cylindrical support structure in the same way as T0–C. The support structure is fixed to a panel on the vacuum pump stand placed nearby the miniframe. The PMTs used in T0–A are identical to the ones in T0–C.

4.3.1 PMTs

The T0 photomultiplier tube (PMT) consists of an aluminium case, in which a quartz radiator, the $FEU - 187$ – a magnetic field–resistant photomultiplier, and a high voltage divider are assembled. Separate parts of the PMT are shown in Fig. 4.21. Fig. 4.22 shows the technical drawing of an FEU–187 assembled in the tube. The quartz radiator is installed and centred in a special plug of fluoroplastic. The front part of the case is covered by a lid, having an opening for an optical fibre in the centre, which is necessary for calibrations (see Chapter 4.4). A spring on the rear side presses against the lid to bind the quartz radiator and PMT, providing stability for the optical contact. The HV and signal cables are led out perpendicularly to the detector axis through corresponding slots in the case made near the rear lid.

[12] Accessing T0–C requires moving the TPC to its parking position and removing the ITS.

FIGURE 4.21 Photomultiplier tube with its constituents: quartz, FEU–187 and divider.

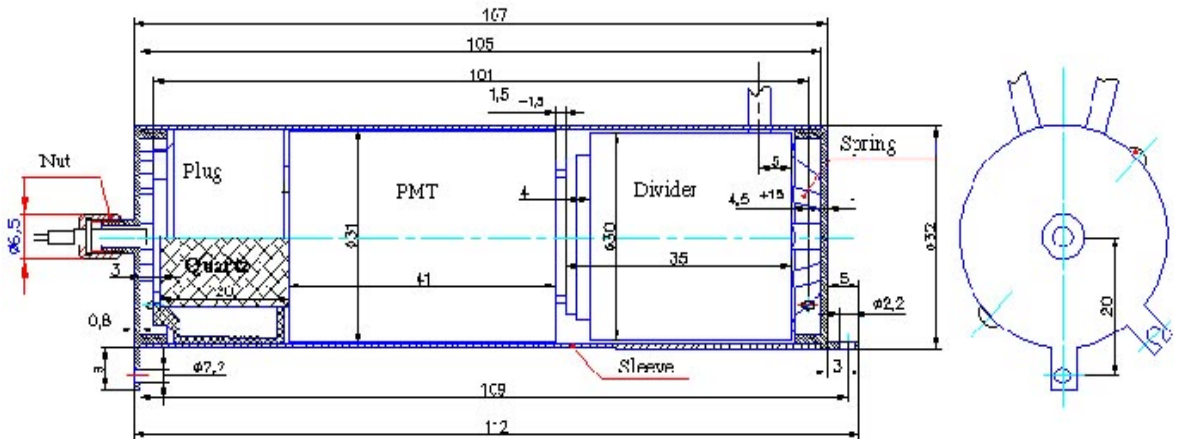

FIGURE 4.22 Side view of the parts of FEU–187 assembled in the tube (left). Rear view of the tube (right) [32].

It is uncertain whether a plastic scintillator would survive 10 years of operation under LHC conditions, since organic materials exposed to radiation become brittle and lose transparency, especially at short wavelengths. For these reasons we have opted for a Cherenkov system with fused quartz radiators. Quartz is known to be radiation hard and is transparent to UV. The other advantage of the Cherenkov option is a very fast light emission in comparison with fast scintillators. The size of quartz radiators has been optimised to obtain the best time (below 40 ps) and amplitude (below 1 MIP) resolution.

The length of the quartz radiator was estimated based on the assumption that the PMT responds to the 200–550 nm band of the Cherenkov light emission spectrum (see Fig. 4.23).

The average number of emitted photons per 1 cm of radiator is given by the

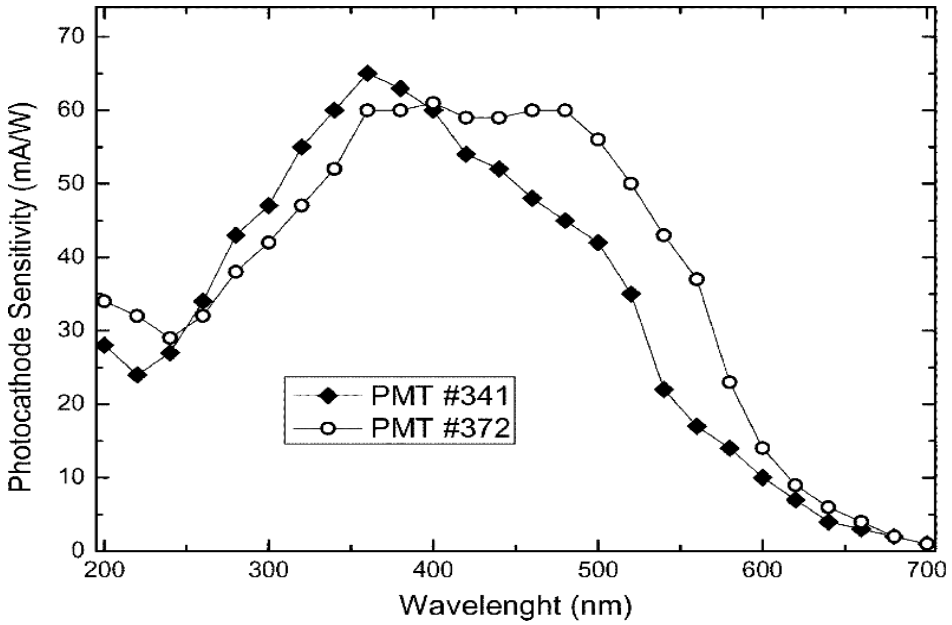

FIGURE 4.23 Photocathode sensitivity measured for two different production batches of FEU–187 PMT.

expression:

$$N_{ph} = 2\pi\alpha\,(1/\lambda_2 - 1/\lambda_1)\sin^2\Theta\,. \tag{4.1}$$

For fused quartz the refraction index n = 1.458, yielding $\cos\Theta$ = 1/n = 0.686 and $\sin^2\Theta$ = 0.53. Hence the average number of photons per 1 cm length is about 770, 440 and 250 for the wavelength bands 200–550 nm, 300–550 nm, and 350–550 nm, respectively. With these values, assuming an average quantum efficiency of the photocathode equal to 15%, we get 112, 66, and 38 emitted photons for the corresponding wavelength bands for a 1 cm long radiator. To double the number of photons one needs a 2 cm long quartz radiator. According to the actual experimental data given in [49], Hamamatsu R5505 with a conventional borosilicate glass entrance window (spectral sensitivity 300–550 nm) or R5506 with a UV glass entrance window (spectral sensitivity 200–550 nm) should give enough photoelectrons to achieve a 50 ps time resolution for the very short and well–focused Cherenkov light emission. We have verified this with our own measurements of the time resolution and dynamic range of the three types of PMTs: Hamamatsu R3432–01 (which is quite similar to R5505), Hamamatsu R5506, and FEU–187 manufactured by the Russian company Electron. The tests described in Chapters 5.1 as well as calculations indicated that a 2 cm long quartz optically coupled to FEU–187 is a good choice for the Cherenkov radiators and adopted it for the ALICE T0 detector. Another solution for a trigger detector, optimised for full coverage of the available acceptance, is used by the Beam Beam Counter (BBC), a forward detector at the PHENIX experiment at RHIC. The BBC, made of Hamamatsu PMTs, is described in Appendix A.2.

4.3.2 Cables

Regardless of how sophisticated the system is constructed, the failure of a single cable can ruin the whole effort. Therefore the T0 cables have been thoroughly examined before the installation in the ALICE cavern and their performance is continuously monitored (further information on measuring the exact length of the signal cables can be found in Chapter 5.4). Figs. 4.24 and 4.25 presents diagrams of cables used on the A– and C–side. All cables are divided into several shorter sections

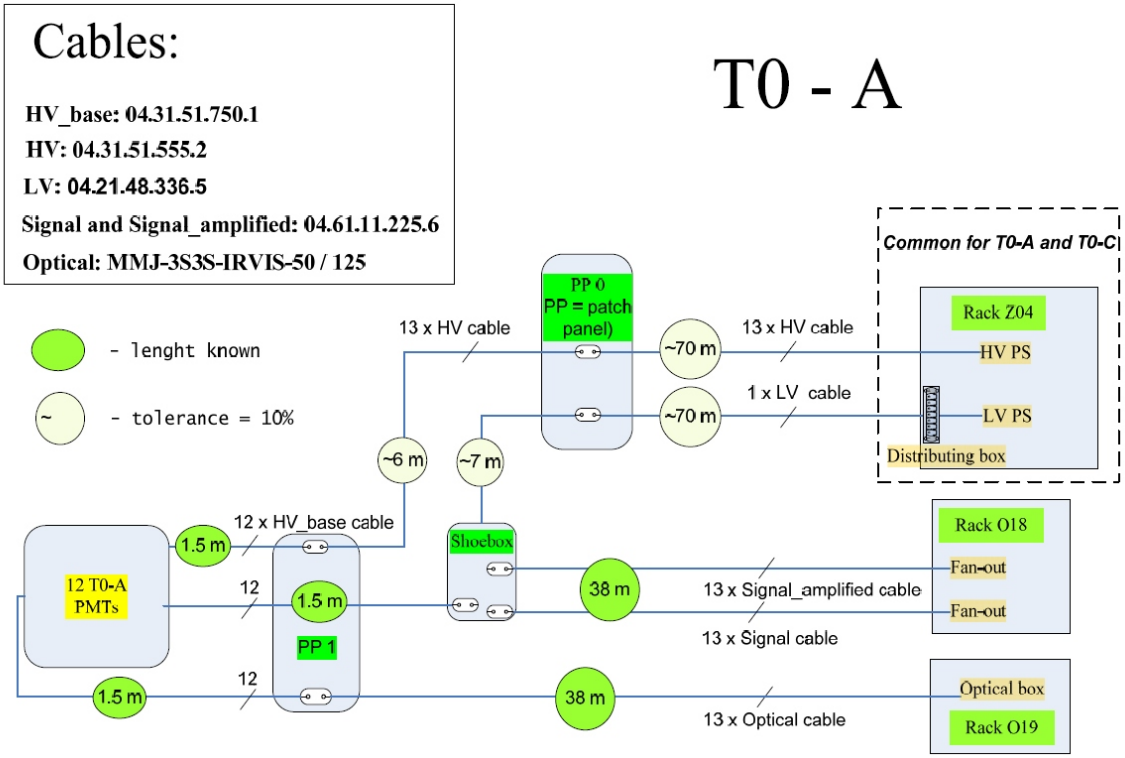

FIGURE 4.24 T0–A cable diagram.

for practical considerations, e.g. in case of urgent need of access to a given zone. The connections between sections are done in so–called patch panels. The standard patch panels, e.g. the ones mounted in the racks, were purchased globally for the whole ALICE experiment. The path of the T0 cables required that we design and produce several special patch panels. One such panel, the T0 patch panel 0, marked as *PP 0* in Fig. 4.24, is presented in Fig. 4.26.

Table 4.5 lists T0 DAQ, trigger, DCS and TOF cables. In addition, there are 5 ethernet cables connected to rack O18.

Spare cables are pulled together with nominal ones whenever possible. Therefore there are 13 instead of 12 cables on Figs. 4.24 and 4.25. This had become important a few months after installing the optical fibers on the C–side, when we noticed that our fibers were damaged during installation of other detectors. As a result, one

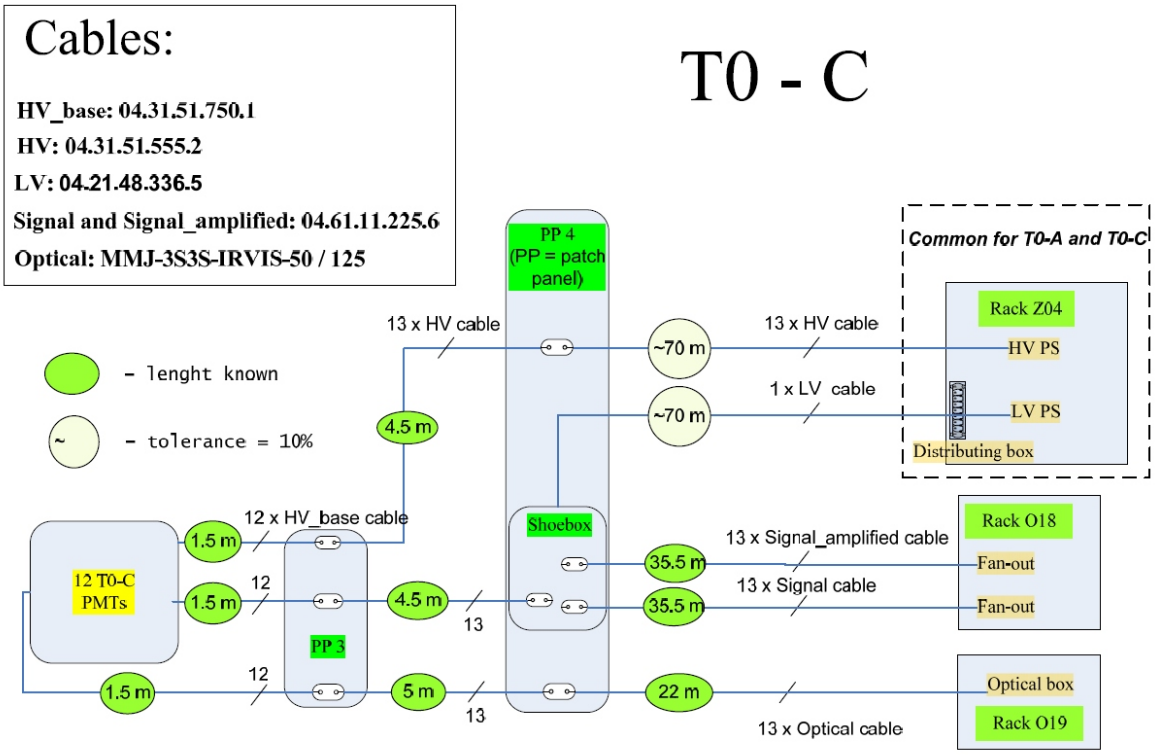

FIGURE 4.25 T0–C cable diagram.

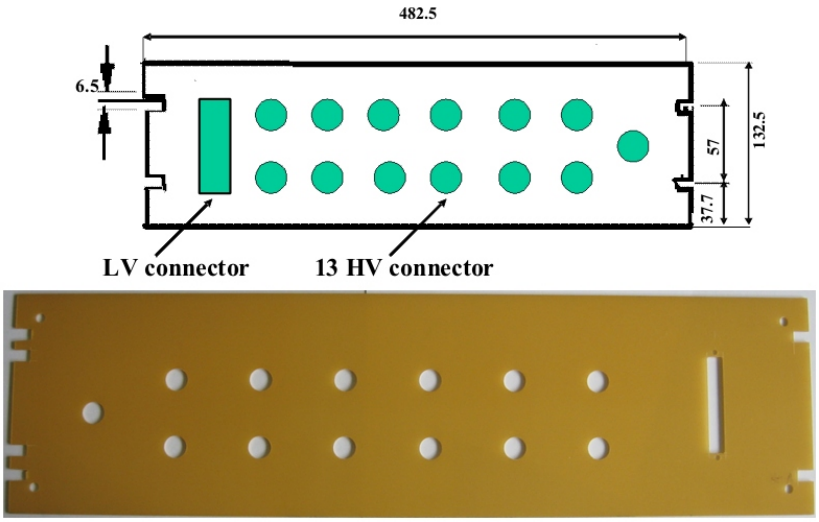

FIGURE 4.26 Design (top) and practical realisation (bottom) of T0 patch panel 0.

of the optical fibers was completely broken and the light did not propagate through it.

TABLE 4.5 T0 DAQ, trigger, DCS and TOF cables. All the cables are originating from the rack O18.

lp	Origin	Destination / Function	No. of cables
1	T0TU	CTP	5
2	DRM	LTU	1
3	DRM	TTCvi	1
4	DRM	TTCex	1
5	CPDM	TOF clock Fan-out	1
6	T0 readout	T0 BUSY	2
7	DRM	DCS Optical link	1
8	ELMB	DCS Optical link	1
9	TOF crate	48V control	1
10	TOF crate	48V power LV	1

Grounding

Grounding is realised by connecting the T0 detector's mechanical parts that might have some electrical potential to the ground. For example, the crates in racks 018, 019 and CR4–Z04 have a common ground with the front absorber on which the T0-C detector is installed. The body of the T0–C is then at this common potential. It is therefore not needed to have a specific grounding cable. T0–A is grounded in a similar manner. However, many other parts of the T0 system require grounding. Fig. 4.27 presents a complete T0 grounding scheme. A special emphasis has been put on grounding the shoebox.

Safety

The high voltage (1–2 kV) delivered to each of the 24 PMTs is the only safety hazard T0 poses. Fig. 4.28 shows schematically how HV is supplied to the PMTs from the rack CR4–Z04. T0 uses the standard HV cables and SHV connectors.

Uninterrupted Power Supply (UPS) prevents a power cut to the Digital Variable Attenuator[13], which is used for modulating the Picosecond Injection Laser of the T0 Laser Calibration System.

4.4 Laser Calibration System

The Laser Calibration System (LCS) is intended for adjustment and calibration of the 24 T0 PMTs before and during the ALICE runs. For that it is necessary to provide

[13]Digital Variable Attenuator [34] is a very small unit in terms of size and power consumption. If the power cut happened, the power on the attenuator would automatically be cut off. If UPS was not used, one would have to go down to the rack O19 to turn on the attenuator again.

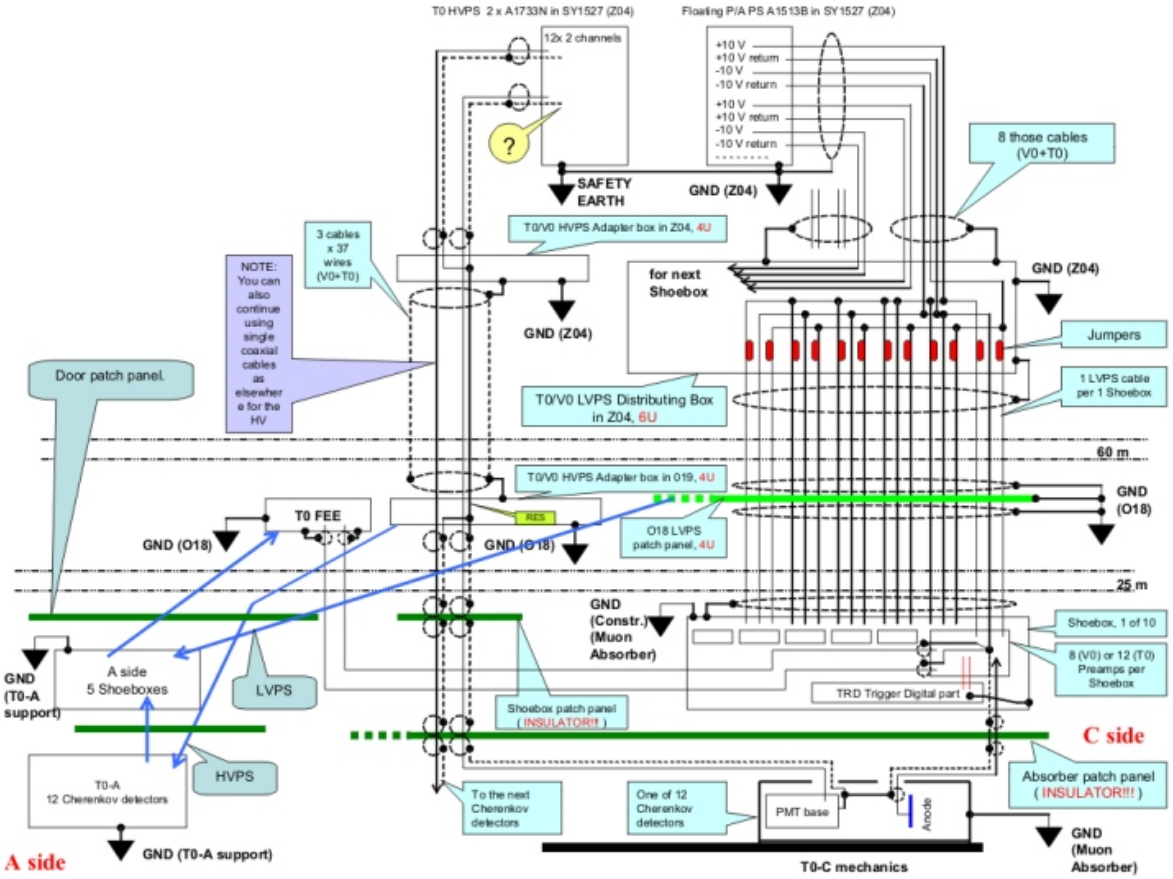

FIGURE 4.27 T0 grounding scheme.

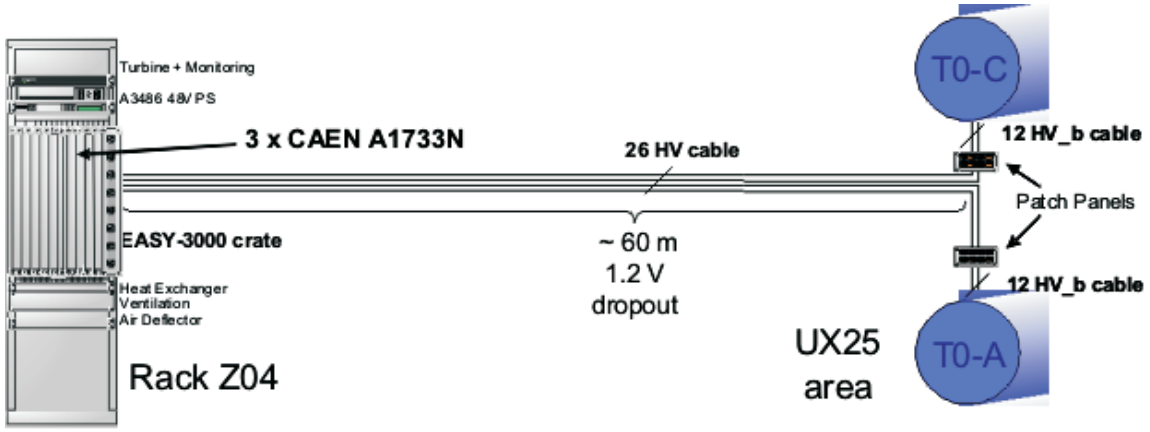

FIGURE 4.28 HV supply for T0 PMTs.

simultaneous and sufficiently short light pulses with adjustable amplitudes for all 24 PMTs of the T0 detector. The diagram of the T0 LCS is shown in Fig. 4.29.

In order to test T0, the time resolution of the laser pulses is required to be considerably better than 50 ps, the amplitudes of the pulses at the input of each PMT

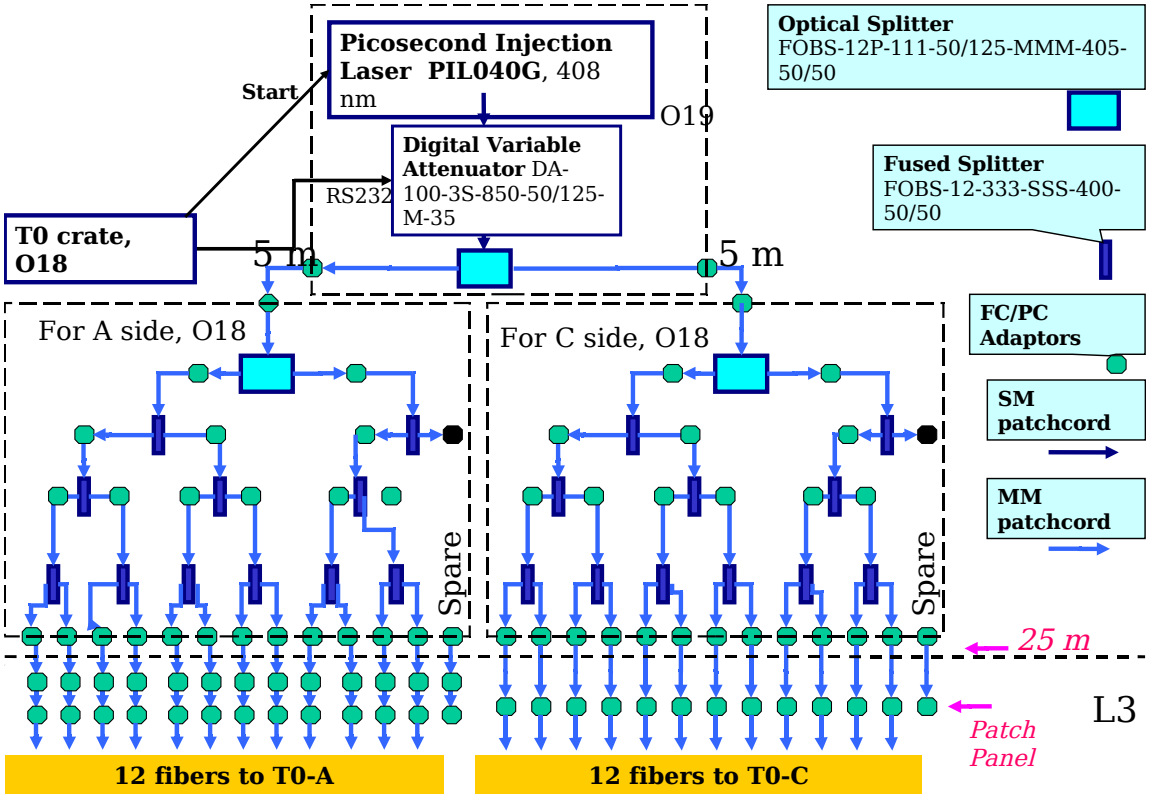

FIGURE 4.29 T0 Laser Calibration System.

should cover the full dynamic range of the detector and the wavelength must be well within the sensitivity range of the photocathode. Regrettably, the last requirement excluded red lasers, which are widely used e.g. in telecommunication, and therefore have a very broad range of relatively inexpensive accessories. Only one laser has been found to match the specifications and price range: the Picosecond Injection Laser PIL040G 408 nm [36], depicted in Fig. 4.30. The maximum power of this laser

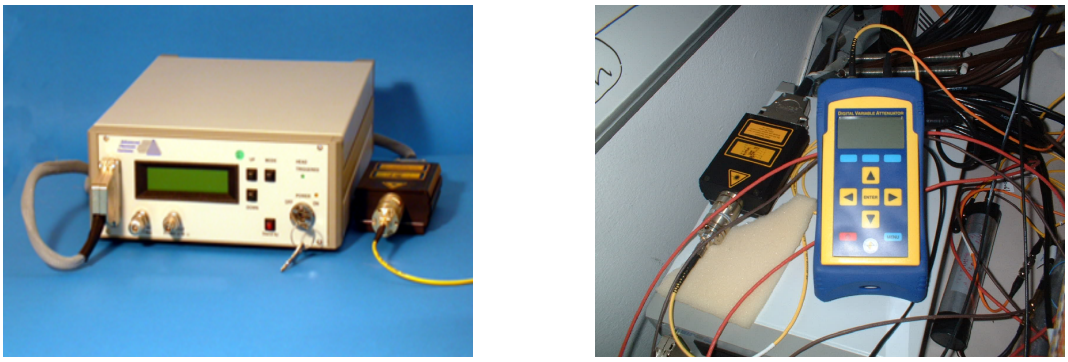

FIGURE 4.30 Integral parts of T0 LCS: Picoseconds' Injection Laser PIL040G (left) and Digital Variable Attenuator DA–100 [34] (right).

is close to the limit of that required by our application. Therefore it was essential to minimise signal loss along the optical wire and couplings. It was also important

that the timing characteristics of the laser pulse are preserved on the way to the PMT. Otherwise it would be impossible to tune the arrays to better than 50 ps accuracy. The PIL040G pulse laser has a pulse duration less than 40 ps at a wavelength of 400 nm, corresponding to the spectral band of the PMT. The laser is connected to an optical system, consisting of an optical attenuator and optical splitters, through which the light pulses are fed to all 24 detectors simultaneously. The pulse splitter was expected to generate minimal loss of amplitudes and delays at all 24 outputs. To meet this requirement all available splitters were tested by feeding laser pulses to a PMT through splitters' outputs, and the best splitting chains were chosen. Fig. 4.31 presents the splitter used for T0.

FIGURE 4.31 Optical splitter with a splitting factor 50/50 with fiber patchcords terminated with FC connectors [34]. Each splitting causes optical power dissipation of about 3 dB.

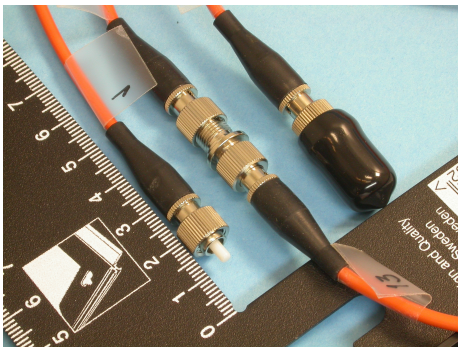

FIGURE 4.32 Optical fiber patchcords used for the transmission of laser pulse to the PMTs.

After splitting, the transmission of the laser pulse to 24 PMTs is carried out by optical fibers. They are encased in plastic sheaths and terminate with optical connectors of FC type [34] (see Fig. 4.32). The optical lengths of all T0 fibers is equal within 5 mm accuracy. Due to the protective sheath, there appears a different signal delay in optical cables of equal geometric length. This has been taken into account in designing the optical path of the LCS and selecting its elements. The high–precision delay measurements have been performed in every calibration channel (one calibration channel corresponds to one PMT). Since an absolute equality of delays in all channels is practically unachievable, the possible divergence in time of pulse signals due to the optical fiber system and differences in the delays of detector switchover may be corrected further by controlled digital picosecond delay lines installed at detector outputs.

A mating unit, depicted in Fig. 4.33 has been designed in order to attach the laser fiber patchcord to the PMT assembly in such a way as to illuminate the photocathode of the PMT.

The unit consists of a guiding sleeve on the detector lid, where the ceramic tip of the optical fiber patchcord is fixed by a nut. Such a design allows a quick replace-

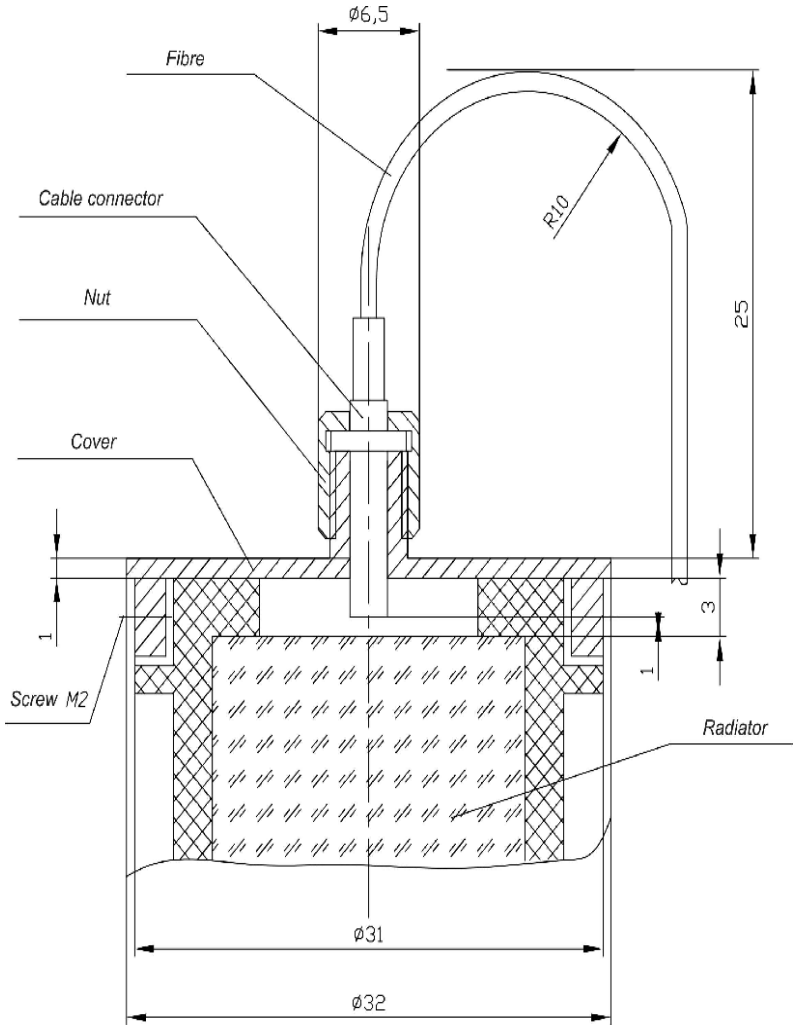

FIGURE 4.33 Attachment of fiber optic to PMT case [32].

ment of the patchcord. It also ensures the perpendicularity of light injection relative to the radiator plane of the Cherenkov detector. The use of a thin optical fiber with a protective sheathe, 0.9 mm in diameter, results in a small bending radius of the optical fiber. The given design provides a highly efficient inlet of optical radiation into the quartz radiator keeping the radiator area shaded by the patchcord input relatively small. 1.5 m long optical fibers protected by plastic sheathes of 3 mm in diameter [34], are used for the inlet system. All connections of optical cables and optic connectors are implemented with FC sockets, which provide a connection of single–mode fibers at losses within 0.2 dB.

4.5 T0 Electronics

T0 electronics' modules are located at considerable distances from the detector itself, as shown in Fig. 4.34. Our tests have proven that for the best performance, no elec-

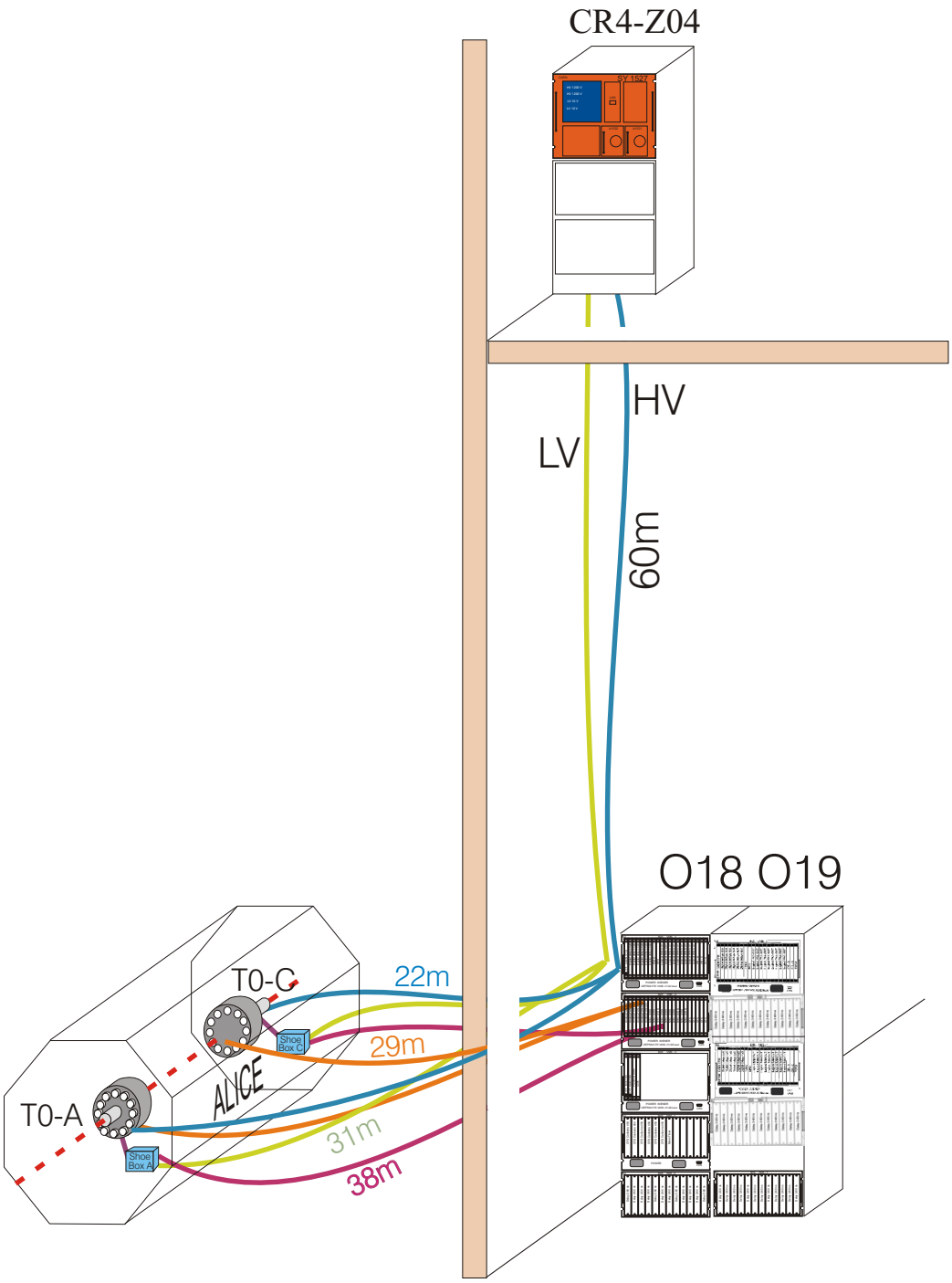

FIGURE 4.34 T0 system. PMT arrays (T0–A, T0–C) and shoeboxes are in the central region of ALICE, some 20–30 m from the O18 and O19 racks housing e.g. T0 fast electronics. Rack CR4-Z04, in which e.g. HV/LV power supply is placed, is 60 m further away.

tronics should be placed in–between. This was nonetheless not possible because, in addition to its role in timing and trigger, T0 must generate a wake–up signal for the TRD, with a total latency below 200 ns. Therefore the two so-called shoeboxes are located 1.5 m (A–side) and 6 m (C–side) from the PMT. The main role of the shoeboxes, apart from generating a wake–up call for the TRD detector, is to split and amplify the T0 signals. The splitted T0 signals are fed to the T0 electronics placed in racks outside the L3 magnet. There the T0 pulses are processed and used to produce the required trigger signals. In addition, the time and amplitude information from each PMT is read out and stored by the ALICE DAQ. The T0 readout is nearly identical to that of the TOF detector. This solution was adopted to cut costs and to guarantee the performance of the T0. TOF is currently the only ALICE sub-detector that needs non–trigger information from T0.

The electronics of the T0 detector can be divided into Fast electronics and Readout electronics, as depicted in Fig. 4.35. Some T0 modules are using a VME control

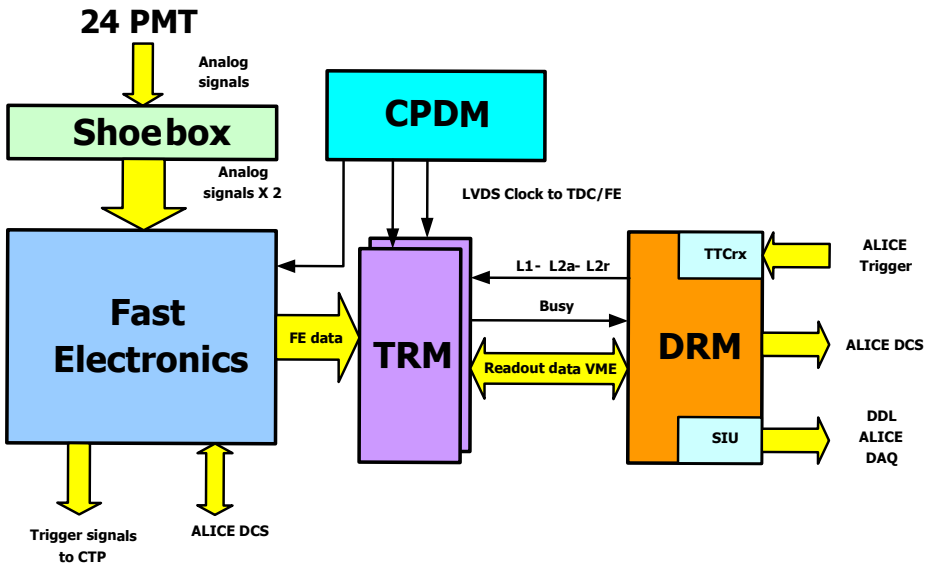

FIGURE 4.35 T0 Fast and Readout electronics scheme. CPDM, TRM and DRM are the Readout modules.

interface, the rest, which do not require individual periodic control, were manufactured in the NIM standard. Fig. 4.36 presents the two racks outside the L3 magnet in which most T0 electronics modules are located. The Fast and Readout electronics modules are descriptions in the following chapters.

4.5.1 Fast electronics

Fast electronics processes the signals from each T0 PMT. It produces the required trigger signals as well as feeds the time and amplitude information to ALICE DAQ for read out, digitisation and storing. The overall diagram of T0 electronics is shown

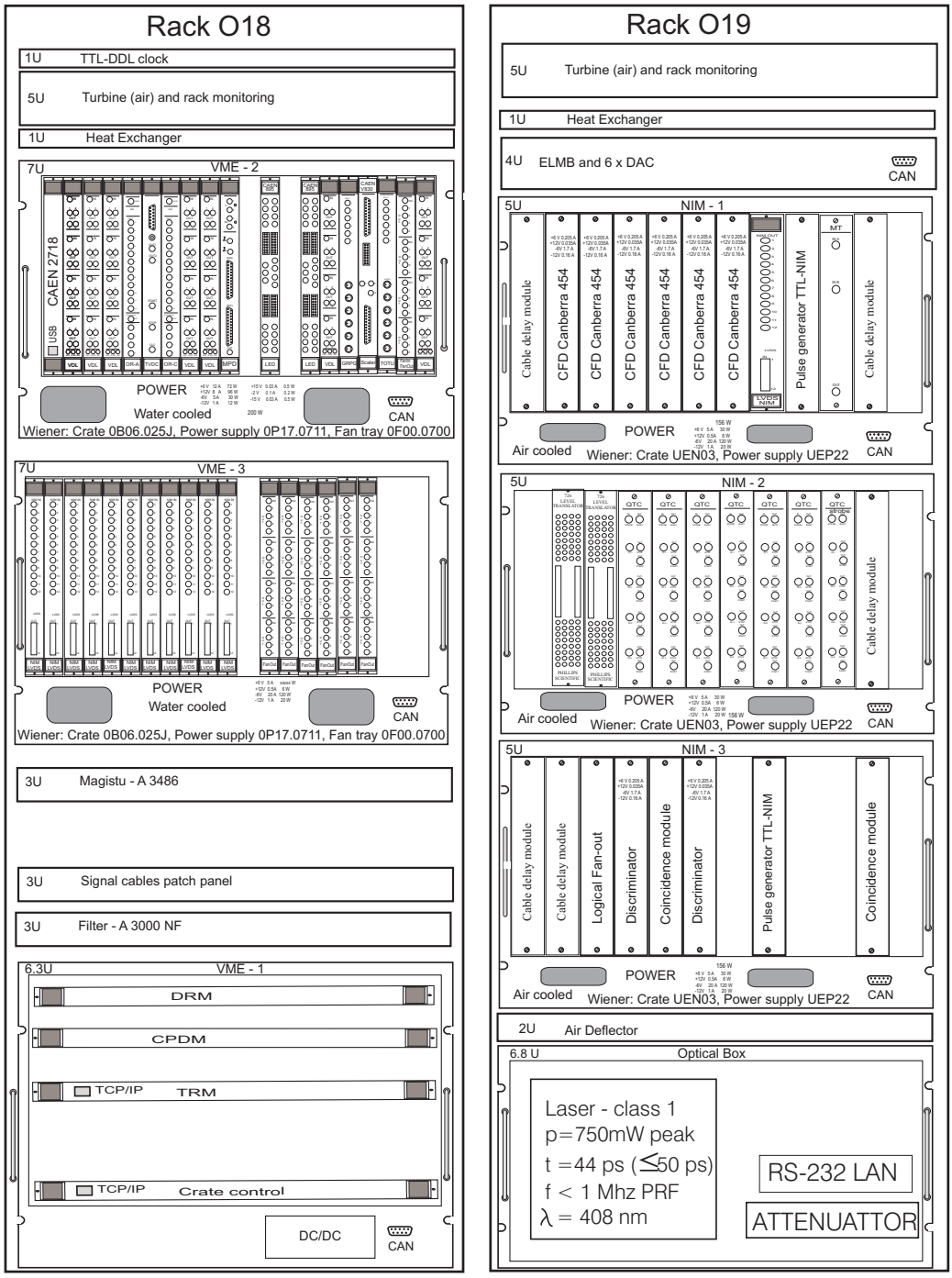

FIGURE 4.36 Configuration of T0 electronics in racks O18 and O19.

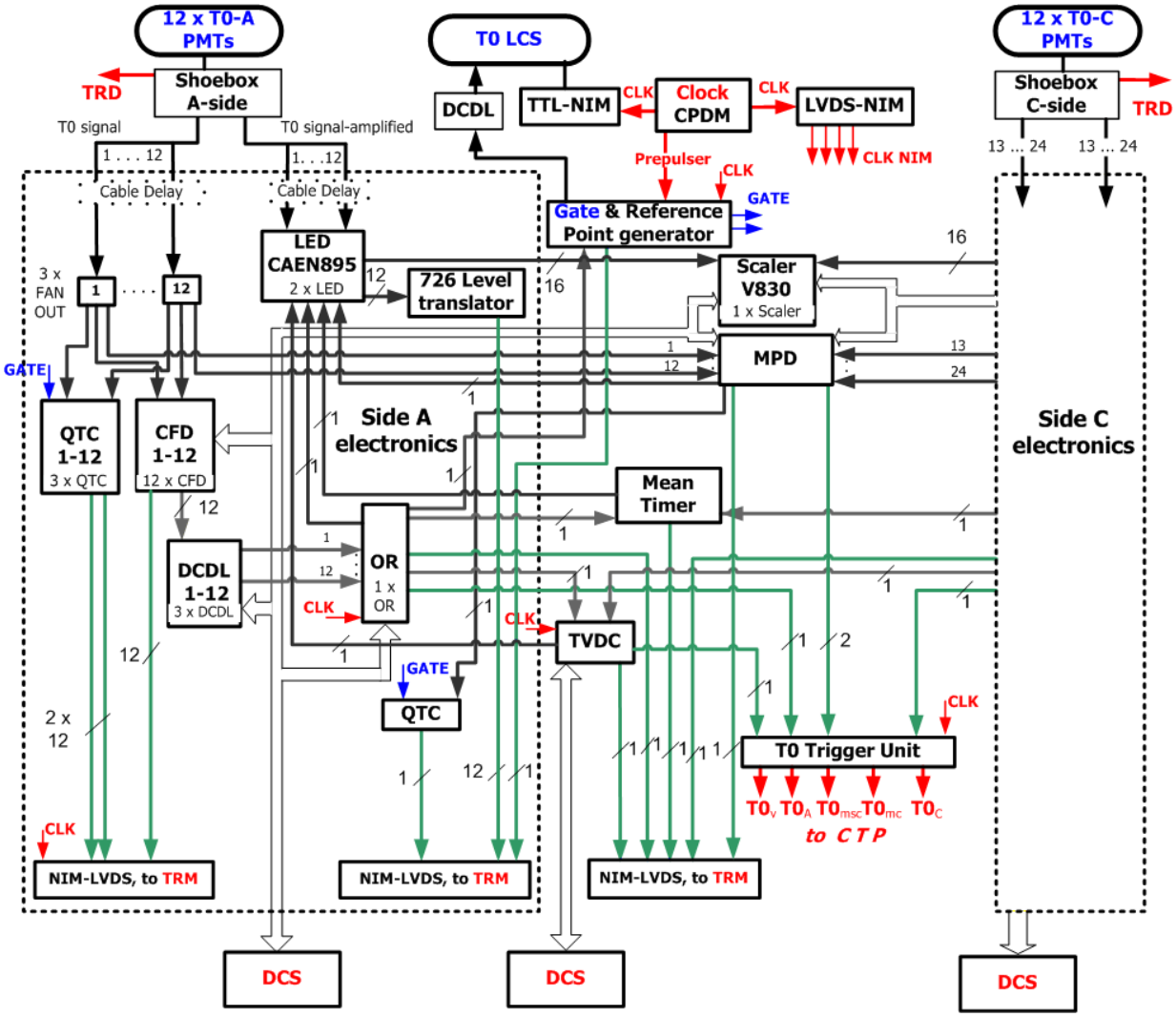

FIGURE 4.37 Fast electronics scheme.

in Fig. 4.37. T0 time and amplitude are obtained using the Constant Fraction Discriminator (CFD), Leading Edge Discriminator (LED) and Charge to Time Converter (QTC). CFD provides a very precise, independent on input's amplitude, time signal. The time signal from LED is amplitude dependent and needs to be corrected in the Offline (slewing correction). But in case of failure of CFD, the precise time signal can be obtained from the combination of QTC and LED signals. The amplitude is obtained from the QTC (by subtraction of two time signals). Other way to obtain the amplitude information is to use the difference between CFD and LED signals. Ideally the CFD is used for precise timing and QTC for amplitude information. Having all the three units: CFD, LED and QTC grants us two ways to provide good time and amplitude signals.

Shoebox

The main function of the shoeboxes is to split and amplify the timing signals from T0–A and T0–C arrays. These timing signals are fed directly to the TRD and used as pre–trigger "wake–up" signals. The coincidence requirement for the "wake–up" implies the use of the shoebox and rules out implementing it in the T0 racks O18 and O19 placed approximately 40 m away. The T0 shoebox consists of a motherboard and 12 preamplifiers mounted on it. Fig. 4.38 shows a view of a shoebox with one preamplifier. The shoebox preamplifiers split the PMT signals and amplify them for

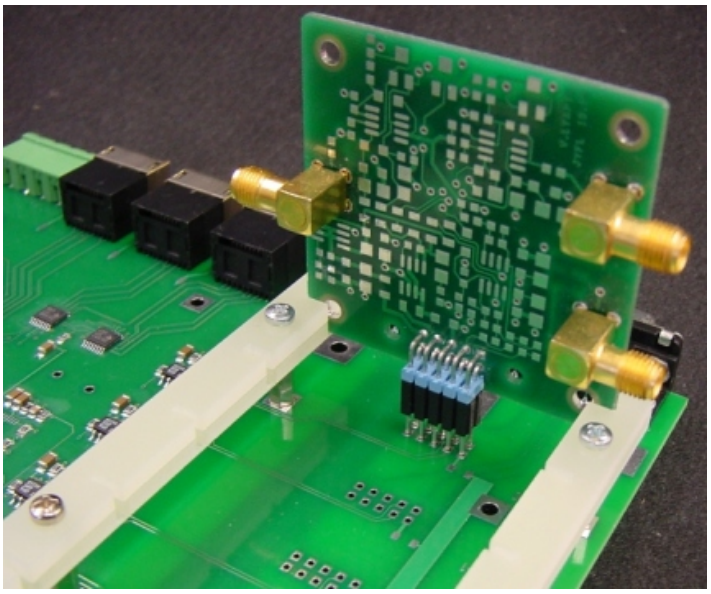

FIGURE 4.38 Preamplifier assembled to a motherboard in T0 shoebox.

transmission via a high–frequency cable over a distance of 35.5 m (C–side) or 38 m (A–side) where they are fed to the FAN analog splitter (Fan–out). Both T0 shoeboxes are in the proximity of the TRD wake–up electronics, where the pulses from all T0 and V0 detector channels merge and are processed to provide a "wake–up" signal to the TRD (see Fig. 4.39).

The expected signal amplitude on the input of the shoebox is from 15 mV up to 5 V. To assure the 50 ps time resolution throughout the entire dynamic range, it is necessary to preserve as much of the signal's original shape as possible. To prevent the zero level from floating with changing count rate, the ultra–wideband amplifier in the shoebox is of the direct current type. Fig. 4.40 shows the design of shoebox. Each channel of the shoebox has one input for PMT pulses and 2 outputs: direct (gain=1) and amplified with a gain of 10 or 3 (currently (20/07/2009) the shoeboxes with a gain of 10 are installed). The direct output goes to the wide range CFD (see section 4.5.1). If the CFD works as expected in the full dynamic range, the amplified signal shall only be used to improve the accuracy of amplitude digitisation. In case of unforeseen problems, the amplified output could also be fed to the second CFD

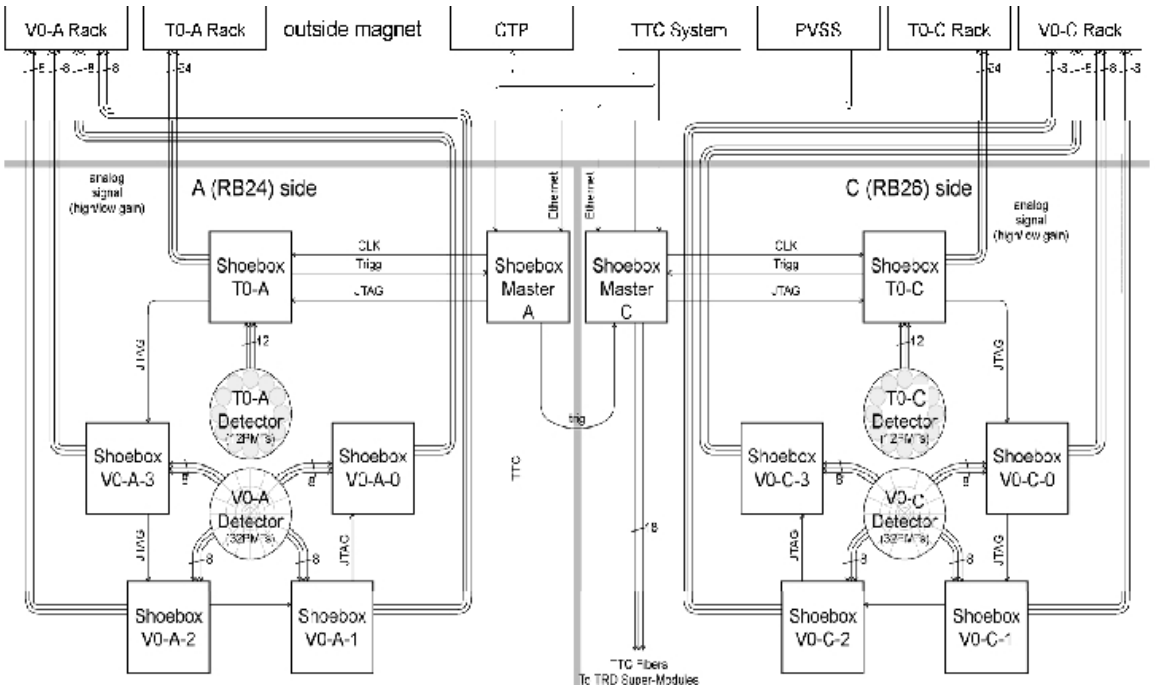

FIGURE 4.39 TRD wake–up system scheme [33].

working in parallel with the one with the direct signal, allowing for precise off–line corrections. The main elements of the shoebox are the OPA695 current–feedback operational amplifier and THS4503 – a wideband, low–distortion differential amplifier. Since even these modern operational amplifiers provide the proper bandwidth only for a gain below 8, a two–stage system, each with gain of about 5, had to be used. The Printed Circuit Board (PCB) is a size of 50 mm $\times$ 60 mm and includes two low–dropout voltage regulators providing the amplifier with a clean and stabilised power supply. In the quiescent mode the unit consumes 75 mA from +6 V to -6 V. At high counting rate the current increases to 100 mA. A non–inverting stage is used to eliminate the passive fan–out at the input.

The TRD wake–up electronics do not need the same time resolution as the TOF. Since small time shifts, such as those due to saturated pulses, are not a problem for the wake–up, and the absence of low amplitude (non amplified) pulses makes the design easier and more tolerant of electronic noise and interference, only the amplified signals will presumably be delivered to the TRD wake–up electronics.

The high–speed T0 electronics are placed in racks O18 and O19 outside the beam zone, hence the requirements on radiation tolerance are less hard than those for the Shoebox preamplifier. Tests have proven that the shoebox is radiation hard, as discussed in Chapter 5.2.3.

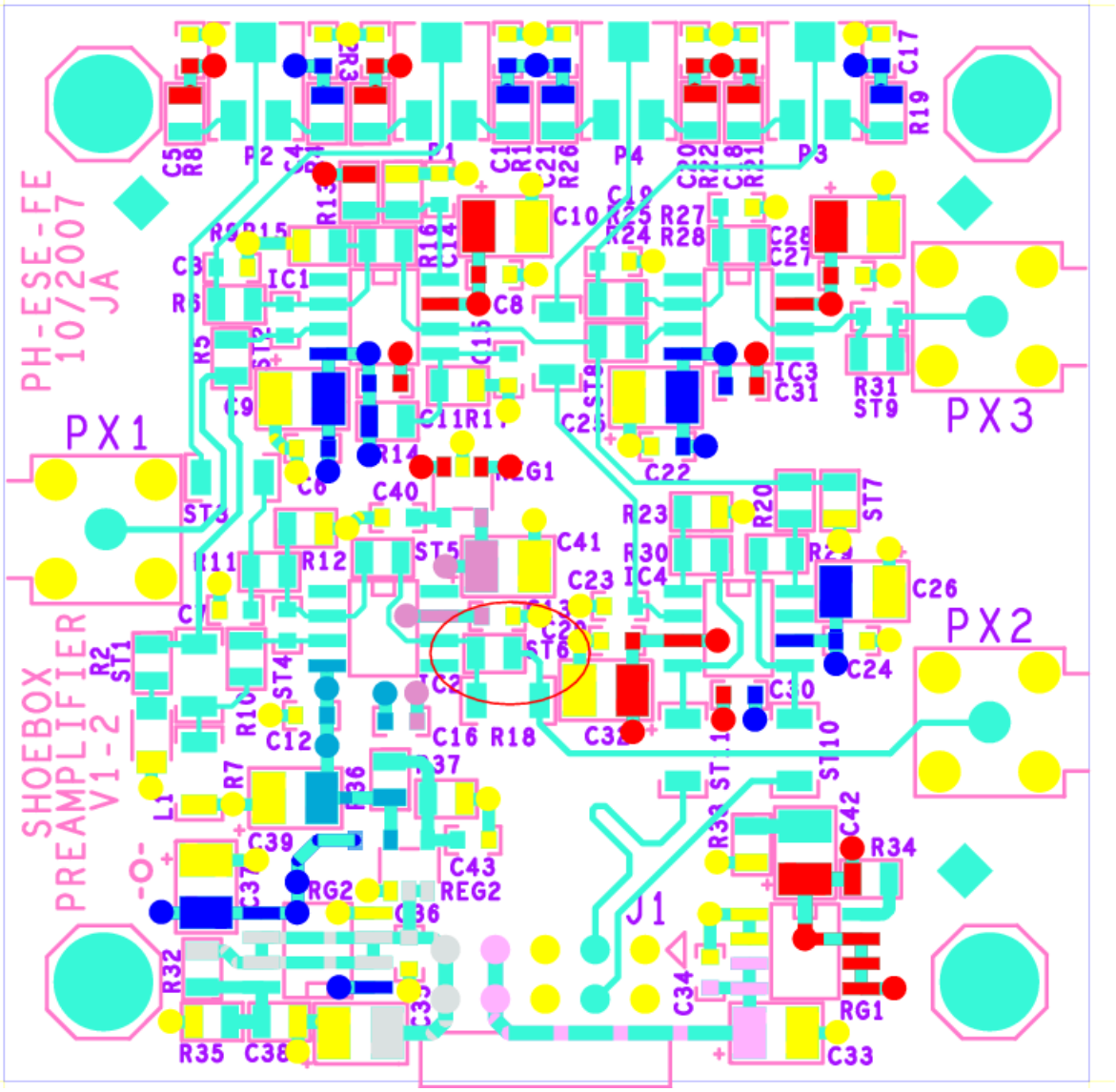

FIGURE 4.40 Scheme of the T0 shoebox (20/07/2009). PX1 is the input from the PMT (0 – 5 V). Output PX2, with a gain of 1 (0 – 5 V), has a very good linearity. PX3 is the amplified output. Depending on the resistor R27, it provides a gain of 10 (R 27 = 105 Ω), or of 3 (510 Ω). It is still being decided which version of the shoebox will be used during the ALICE data taking (currently the ones with a gain of 10 are installed).

Fan–out

The Fan–out module is intended for splitting the analog signals from each T0 PMT. The module consists of 4 channels, each having one input and 4 outputs. The PMT signal is fed through Fan–out into 4 units: Constant Fraction Discriminator (CFD), Charge–to–Time Converter (QTC), Multiplicity Discriminator (MPD) and Leading Edge Discriminator (LED)[14]. The schematic of Fan–out is presented in Fig. 4.41.

[14]Depending on the configuration, the signals to LED might also be fed directly from the shoebox (see Fig. 4.37). If this is the case, only 3 outputs of Fan–out are used, feeding the signals to CFD, QTC

Active voltage followers are used to retain signal amplitude. Through a built–in

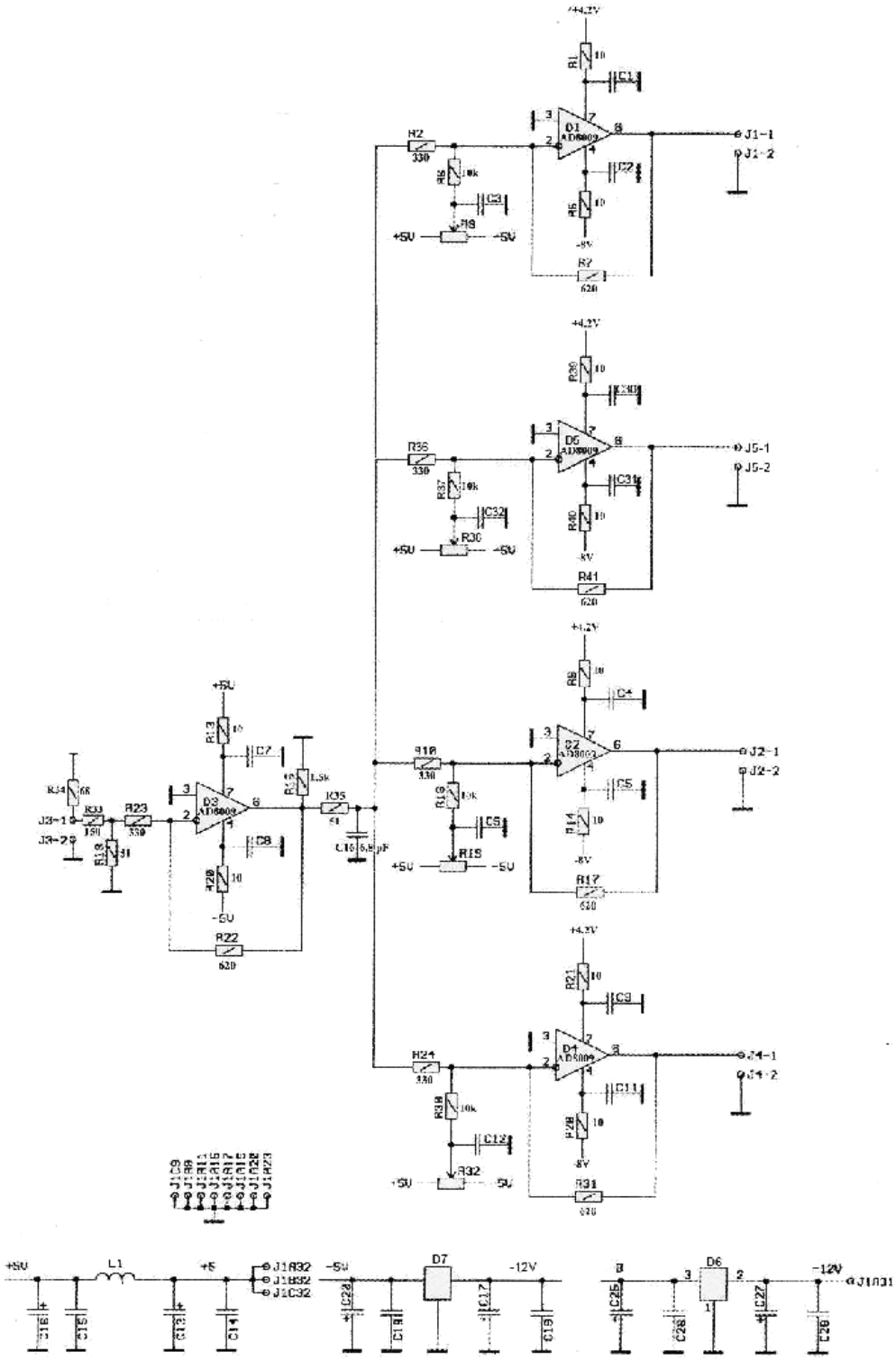

FIGURE 4.41 Schematic diagram of Fan–out [32].

and MPD.

attenuator, with a fading of 4, the input signal runs to the input of a common inverting amplifier D3 with a gain of 2, compensating the signal losses in circuits and damping the spurious high-frequency oscillations. The signal is then split and fed to the inputs of four inverting amplifiers, having a gain of 2 and permitting to provide the maximal speed. In order to get the maximal output amplitude, and not less than 5V across a 50 Ω load, the supply sources of the D(1..5) output amplifiers are made unsymmetrical (+4.2V, - 8V). To reduce the output signal influence on neighboring channels, the 4–channel analog splitter uses individual supply filters and insulated ground busses. At each output there is foreseen an individual base level adjustment by multi–revolution variable resistors. Uniformity of transfer factor in different channels is provided by using resistors with an accuracy of 1%. Bias of the analog splitter is stabilised by using secondary supply sources, built with parametric voltage regulators. The general view of the analog splitter module, implemented in compliance with the company $Euroconstructive$ [32], is presented in Fig. 4.42.

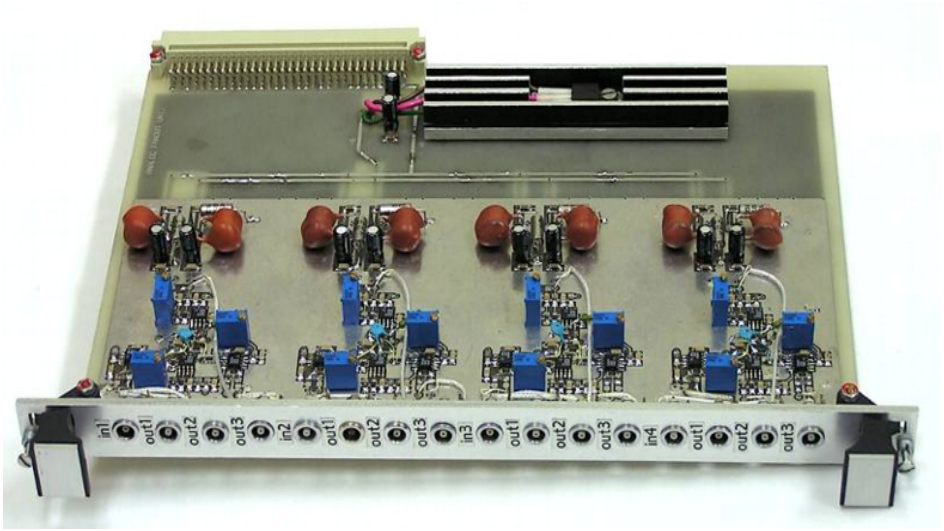

FIGURE 4.42 Photo of Fan–out unit used by T0.

The modules of the analog signal splitter were tested together with the PMTs using the LCS's PIL040G pulse laser and the CERN PS beam. The tests proved the high stability of the output base level, see Fig. 4.43 (instability within $\pm$0.5mV for 16 hours), and parameter uniformity in various splitter channels.

Fan–out circuit's optimisation permitted almost complete exclusion from the mutual influence of other channels (cross–talk or feed through), and to achieve a short intrinsic output rise–time (Tr $\sim$ 1.4 ns) at the output amplitudes up to 5 V [32].

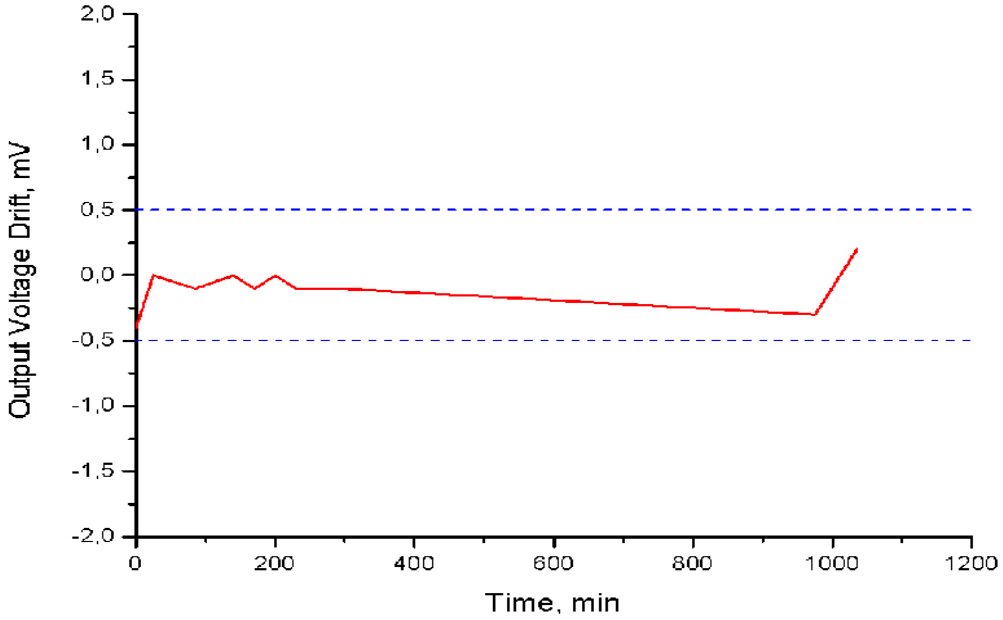

FIGURE 4.43 Stability of Fan–out's output voltage [32].

CFD

Constant Fraction Discriminators (CFDs) [15] are used to determine the arrival time of analogue pulses from fast detectors. As long as the amplitude of the pulse stays within the dynamic range of the CFD, no slewing corrections are needed. The time does not depend on the amplitude of the pulse. A very good CFD, for instance the Phillips Scientific 715 [35], exhibits typical time walk plus slewing of $\pm$ 75 ps for amplitudes between threshold and 100 $\times$ threshold. The dynamic range required in ALICE experiments is 5 times larger. In principle, off–line slewing corrections are a standard procedure that enables good time resolution even with a simpler Leading Edge Discriminator. Unlike LED, CFD attempts to produce an output signal without the amplitude dependent 'Walk Time'. It is achieved by splitting the input signal so that one half remains the same, while the other half is attenuated by a certain fraction of the original amplitude, delayed and inverted. At the end both pulses are added together and the zero crossing point is computed. The zero crossing gives the reference time produced by the CFD, which is independent on amplitude, as depicted in Fig. 4.44.

Considering the need for good on–line performance (trigger) and to stay below the 50 ps range in time resolution, we chose a commercially available CFD manufactured by Canberra (see Fig. 4.45). Small modifications in the Canberra's 454 CFD were nevertheless necessary to be able to control the threshold and walk of CFD via

[15] Discriminator is an electronic device which generates a standard logic pulse as a response to an analogue input signal. The pulse has to exceed the given threshold to trigger the output signal. This feature is needed to avoid reaction to the background noise. There are two main types of discriminators: LED and CFD.

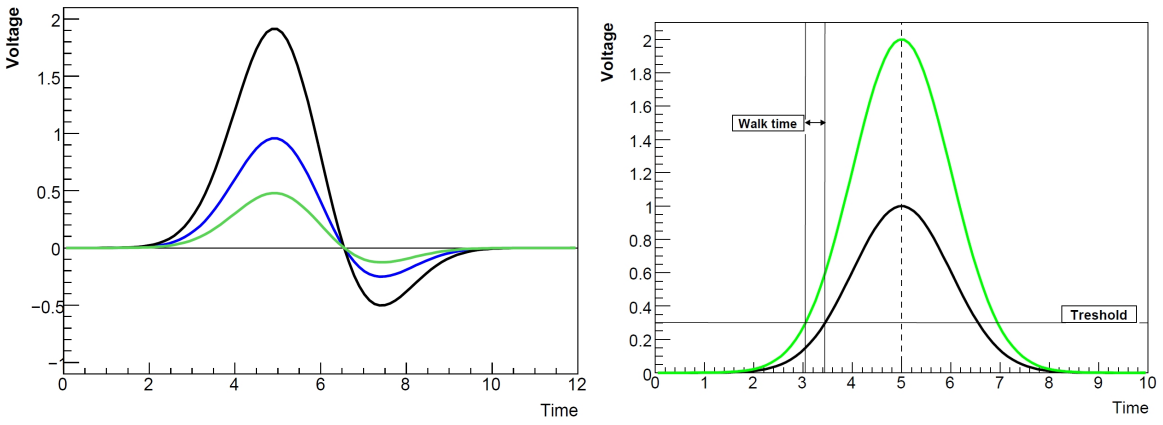

FIGURE 4.44 Working principle of the Constant Fraction Discriminator (left) and Leading Edge Discriminator (Right) [41]. The zero crossing generated by the CFD does not depend on the amplitude of the input signal. LED's Time walk dependents on the amplitude of the signal. It is worth noting that LED gives faster response to bigger pulses.

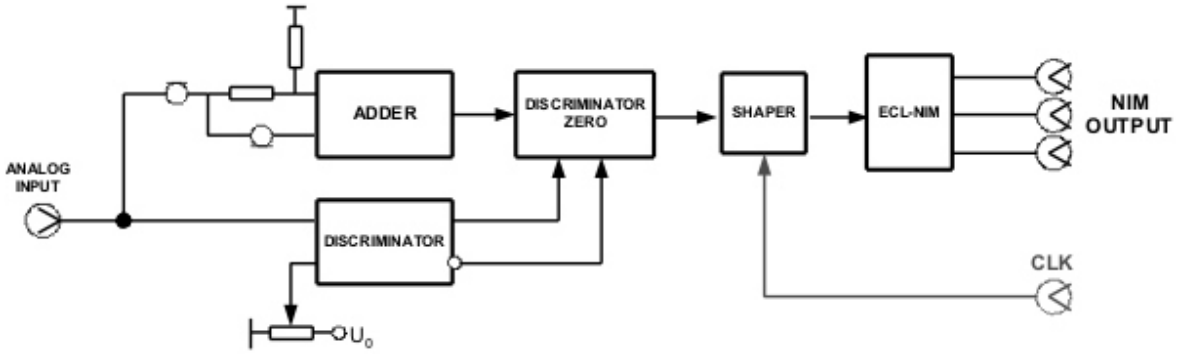

FIGURE 4.45 Schematic diagram of Canberra 454 CFD [32].

the Detector Control System (DCS). These were done at JYFL in 2006 and included installing SMC sockets as well as changing two resistors in each channel[16], as depicted in Fig. 4.46. After these alteration each CFD was tested and proven to work well.

LED

The Leading Edge Discriminator (LED) produces an output pulse when the input pulse crosses a specified threshold voltage. However, this simple operational principle produces a noticeable time dependence of the output on the amplitude of the input. Both pulses have the same rise time and centroid position but different amplitude. The smaller input pulse has a wider output response, thus it would reach

[16]The two resistors allow for changing CFD settings by external voltages instead of a built–in potentiometer.

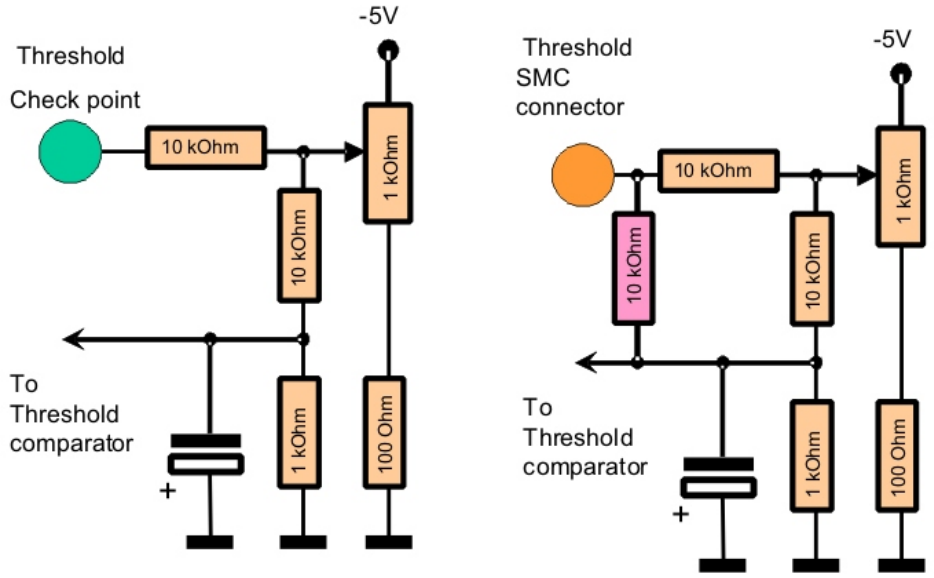

FIGURE 4.46 Canberra 454 CFD before (left) and after (right) the modifications done at JYFL in 2006.

the threshold later than the bigger pulse. The peak position however is the same in both cases.

T0 is using two LEDs manufactured by CAEN, model V895 (see Fig. 4.47). CAEN V895 is a 16 channel discriminator with a maximum input frequency of 140

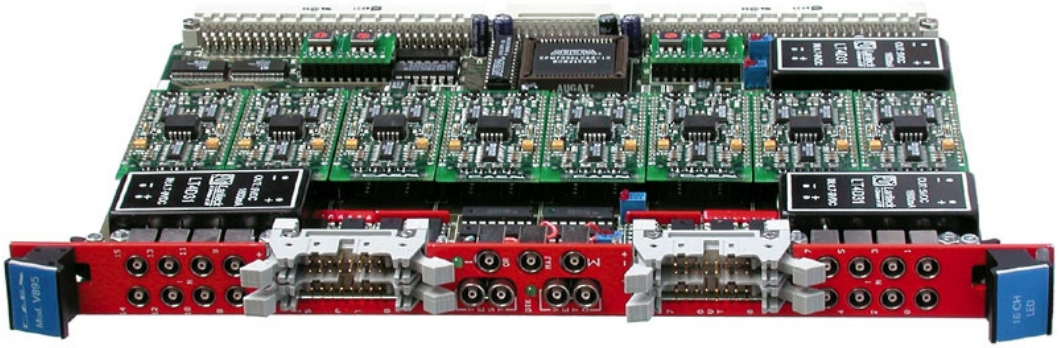

FIGURE 4.47 Photo of CAEN V895 Leading Edge Discriminator used by T0.

MHz. T0 pulses shall typically arrive with a frequency of 10 kHz in $p + p$ collisions. The maximum expected frequency reaches 40 MHz. The discriminator thresholds are set in a range from 1 mV to 255 mV via VME through an 8-bit DAC (see Chapter 4.7). Currently (20/07/2009) T0 thresholds are set to about 40 mV. The minimum detectable signal is 5 mV. The pulse forming stage of the discriminator produces an output pulse whose width is adjustable via VME and is presently set to ∼15 ns.

Scaler

T0 uses a CAEN V830 scaler shown in Fig. 4.48. It is a 1U wide VME scaler hous-

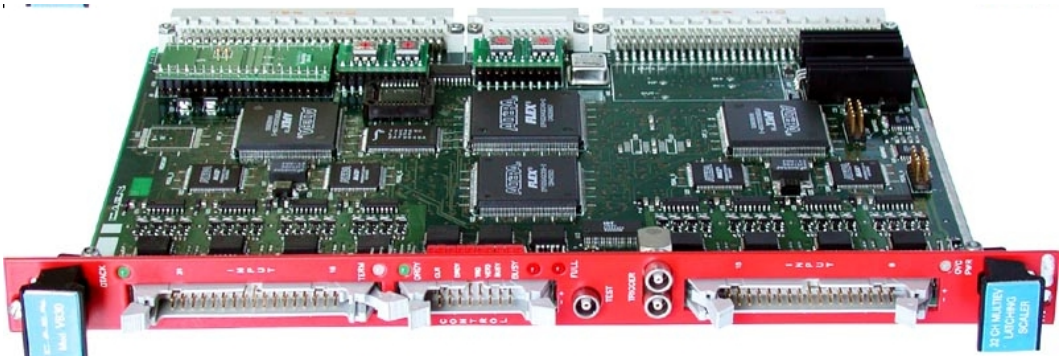

FIGURE 4.48 Photo of CAEN V830 scaler used by T0.

ing 32 independent counting channels. Each channel has 32 bit counting depth, the maximum input frequency is 250 MHz. The channels values are read on–line from the VME and shown on the T0 DCS screen as total counts and counts per second. The scaler is equipped with a 32 k x 32 bit multi–event buffer memory which stores and reads out accumulated data during subsequent counting. The Trigger signal can be provided by an external NIM/ECL signal or by a VME request. Because CAEN V830 accepts only ECL or LVDS inputs, the T0 signals are fed to it via the Leading Edge Discriminator.

T0 scaler receives signals from 12 A–side and 12 C–side PMTs, OR, TVDC, MPD, Mean timer and Reference point generator. The full list of Scaler channels is provided in Table 4.6. Each time PMTs register a valid signal, the scaler is increased

TABLE 4.6 T0 scaler channels. All channels are read in $total$ and $counts/s$ modes.

Signal	Scaler input	Registering valid signal	Valid signal from
T0 AND	t00_ac_scaler_14	T0_TVDC	at least 1 of T0–A & T0–C PMTs
T0 OR	t00_ac_scaler_15	T0_OR	at least 1 of T0–A or T0–C PMTs
T0–A OR	t00_ac_scaler_31	T0_A_OR	at least 1 T0–A PMT
T0–C OR	t00_ac_scaler_12	T0_C_OR	at least 1 T0–C PMT
T0–A[i]	t00_ac_scaler_16 – 27	T0_A[i]	i–th T0–A PMT, i=1...12
T0–C[i]	t00_ac_scaler_00 – 11	T0_C[i]	i–th T0–C PMT, i=1...12
MPD Sc	t00_ac_scaler_28	T0_MPD	MPD Semicentral
MPD C	t00_ac_scaler_29	T0_MPD	MPD Central
Ref. point	t00_ac_scaler_30	T0_RPG	Reference Point Generator
Empty	t00_ac_scaler_13	–	–

by 1 (regardless of how many MIPs hit the given PMT). Thus one can not deduce

the multiplicity of the collision from scaler itself, but can obtain the number of interactions that took place in the given period of time. Fig. 4.49 shows the T0 Scaler control panel, which was included to ALICE luminosity monitor in July 2008. The

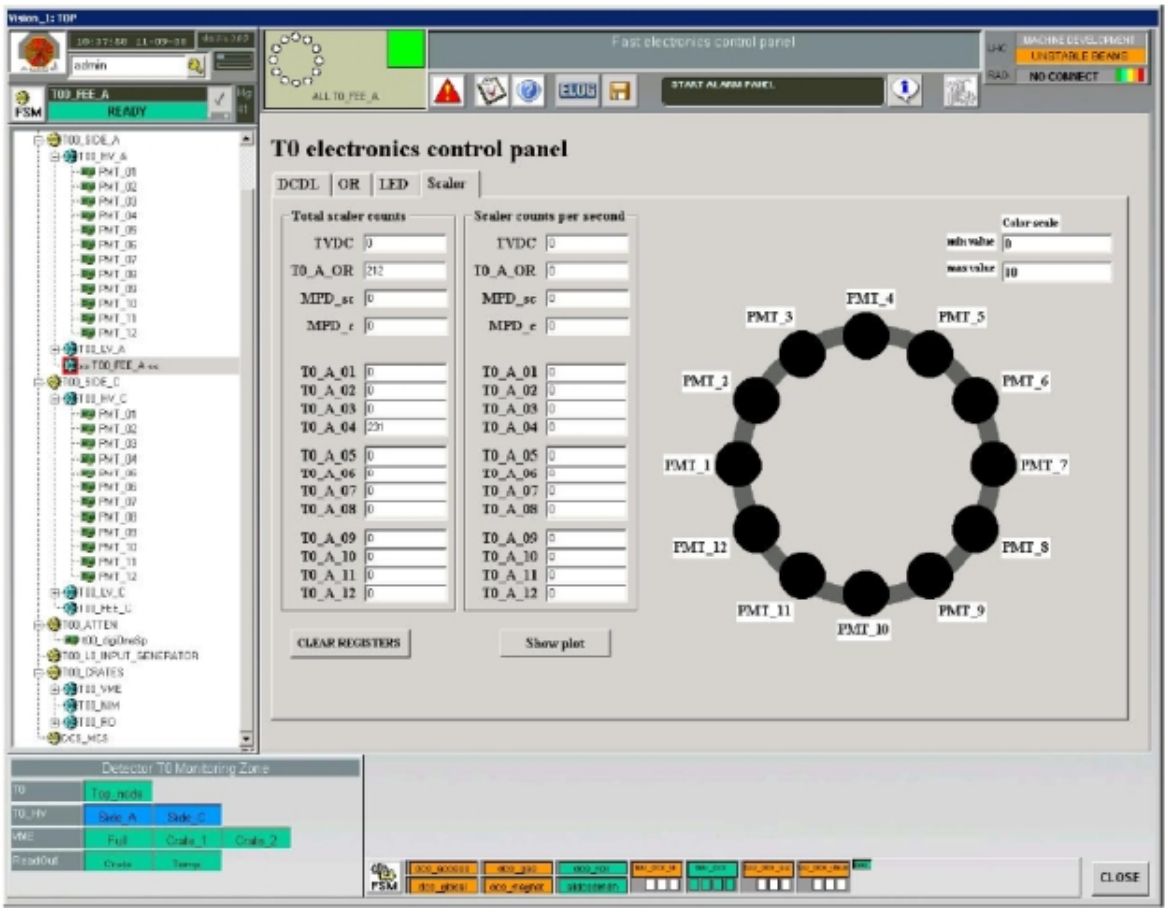

FIGURE 4.49 T0 Scaler control panel included in ALICE luminosity monitor. The number of counts and counts per second shown in the middle gives online information about T0 performance.

panel provides a visualisation of scaler performance that facilitates the control of the device. T0_TVDC channel (T0–A and T0–C in coincidence) provides the number of interactions, which is crucial for luminosity calculation (as further discussed in Chapter 6.3).

QTC

The straightforward procedure to digitise and store the amplitudes of PMT signals would be to use a Charge to Digital Converter (QDC). However, T0 is using the same readout system as the one developed for TOF (see Chapter 4.5.2), and although TOF has provision for a QDC, it does not have sufficient resolution to cope with the dynamic range expected from the T0 signals. Therefore a dedicated Charge to Time Converter (QTC) has been developed for T0 in the NIM standard. QTC produces

two time outputs with the first one being adequate to the time delivered by CFD. The amplitude from QTC is obtained by a subtraction of the two. The schematic of the T0 QTC is shown in Fig. 4.50. From the output of the comparator, the signal goes

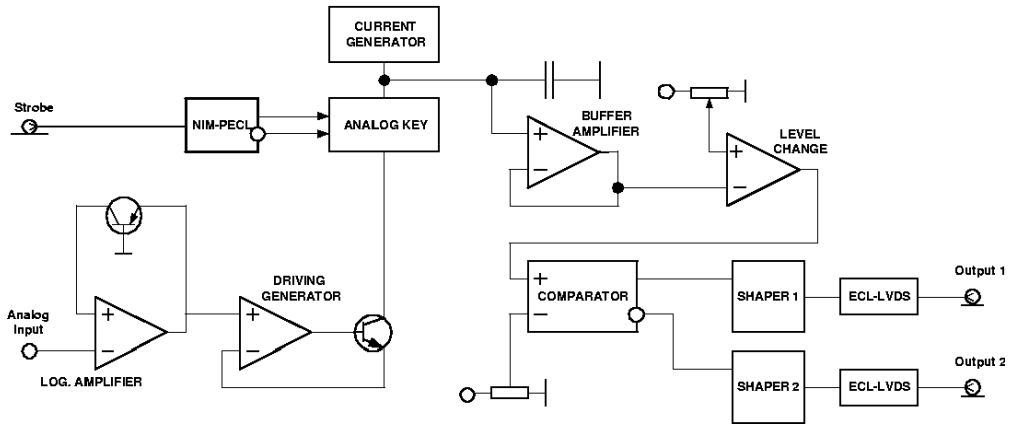

FIGURE 4.50 Schematic layout of the T0 QTC unit [32].

to the differential circuit (Shaper 1 and 2 in Fig. 4.50), generating pulses bound to the rising and falling edges of the comparator pulse. These pulses go to the ECL–LVDS level converter for shaping into the LVDS formats. The output of the QTC is connected to the TOF TDC for digitisation, readout and storage. The same approach is used to digitise the summed amplitude used for multiplicity determination. For unification of the measurements and data transmission to the DAQ, High Performance TDC (HPTDC) converters are used for final charge-to-code conversion. Thus, the QTC converts the amplitude (charge) to the time delay adequate for coding using an HPTDC converter. The logarithmic characteristic of the converter is necessary due to the wide range of the PMT signal amplitude. The T0 QTC units were for the first time successfully tested during the June 2004 experiment at CERN and mounted in the rack O19 at Point 2 in 2007.

Mean timer

Just as the time difference between T0–A and T0–C gives the vertex position along the z—axis, the average of T0–A and T0–C arrival times cancels this dependence and yields a position–independent collision time (plus some fixed delay along the cables, fast electronics, etc.). On–line calculation of the collision time is accomplished by a time–coordinate compensator (Mean Timer), whose schematic diagram is shown in Fig. 4.51. The Mean Timer has been tested in in–beam conditions at CERN in 2003 and yielded a consistency of about 10 ps of compensation error, as shown in Fig. 4.52. Since the Mean Timer signal (T0) is extracted from two independent pulses, T0 time resolution is better from that of a single detector by about $\sqrt{2}$. The resolution of σ_{T0} = 28 ps has been obtained during the test at CERN PS. More details on the test results can be found in Chapter 5.3.2.

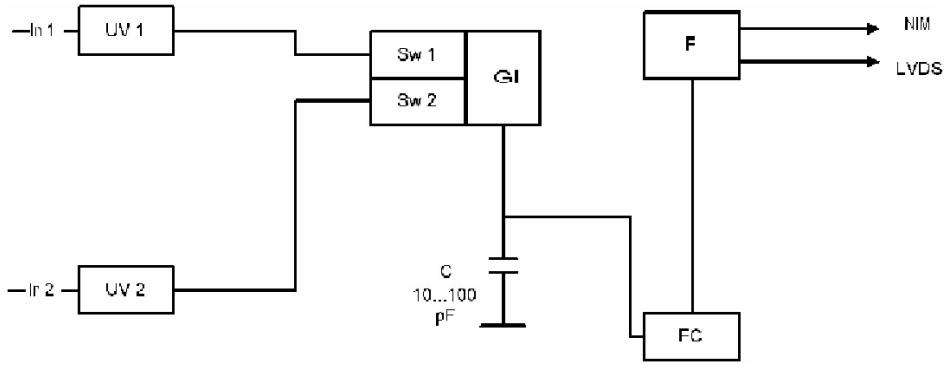

FIGURE 4.51 Mean Timer. UV1, UV2 are Univibrators (monostable multivibrators); Sw1 and Sw2 indicate switches; GI is a current generator; FC = Fast Comparator; and F is a shaper for forming the output pulses.

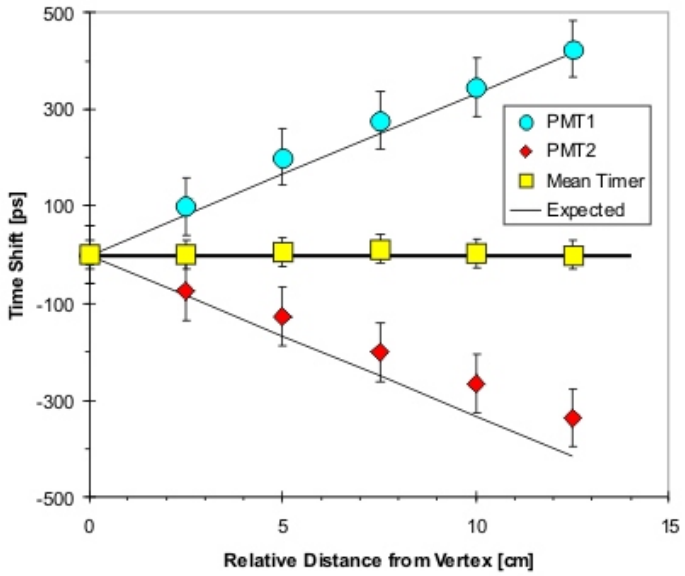

FIGURE 4.52 Performance of the Mean Timer determined during the July 2003 test run at CERN.

MPD

The Multiplicity Discriminator (MPD), shown in Fig. 4.53, generates two logical signals corresponding to the pre–set levels of desired particle multiplicity. The MPD output goes to the Trigger Signal Module (TSM) where all the other T0 trigger signals are converted to the form acceptable by the Central Trigger Processor (CTP). The T0 has a single MIP resolution thus a possibility to provide accurate multiplicity values to the CTP. But considering the relatively small acceptance of T0, it has been decided to render only a rough determination of multiplicity. The measured multiplicity by T0 is compared to 2 pre–set values to generate one of the two possi-

ble MPD trigger signals: T0 semi–central and T0 central[17].

FIGURE 4.53 Photo of T0 Multiplicity Discriminator.

In addition to the trigger function, the MPD generates an analogue sum that is digitised and stored by ALICE DAQ. The block diagram of the MPD is shown in Fig. 4.54. The 12 analogue signals originating either from T0–A or from T0–C arrive

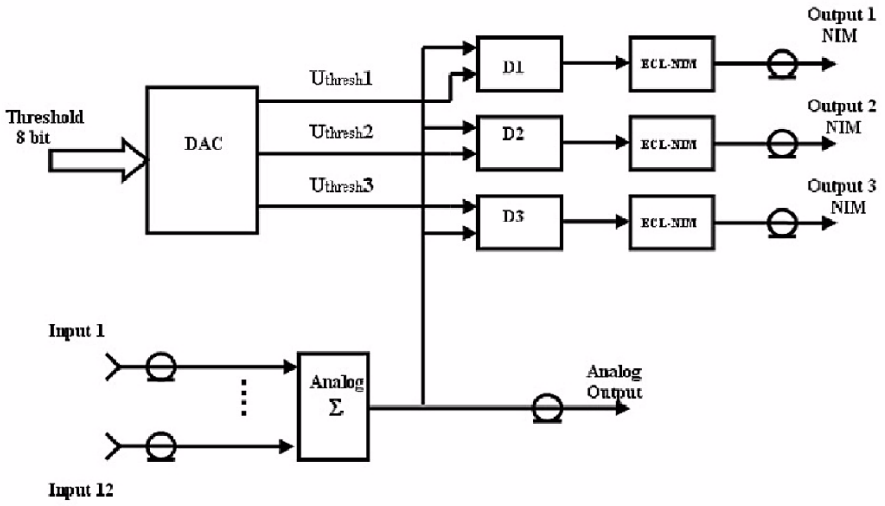

FIGURE 4.54 Multiplicity Discriminator. DAC stands for Digital to Analogue Converter; D1, D2, D3 indicate Comparators (Discriminators).

at the input of an analogue summator (Σ). The summed–up signals then go to the inputs of the three comparators (D1, D2, D3) and one analogue output. The threshold voltages, set with 8-bit resolution, correspond to the low, middle, and high level of multiplicity. These voltages are shaped by the multi-channel Digital to Analogue Converter (DAC) using the digital octal codes written to the RG1 – RG3 data registers, allowing for remote control. After additional stretching, the output signals

[17]The third trigger signal, T0 minimum bias, is generated by the T0 TVDC. It is worth noting that T0 minimum bias signal is equal to T0–vertex signal.

from the comparators come to the outputs of low (Output1), middle (Output2), and high (Output3) levels of multiplicity.

TVDC

Determination of the position of the IP of each collision and comparing it to the minimum and maximum values is the main trigger function of the T0 detector. The unit performing these operations is the T0 Vertex Unit or TVDC. The main parameters of the TVDC are determined by the expected size of the interaction area (0.7 m), nominal resolution of the measurements ($\pm$ 1.5 cm), and the working frequency of the LHC (40 MHz). Accordingly, the TVDC, shown in Fig. 4.55, meets the following

FIGURE 4.55 Photo of T0 Vertex Unit (TVDC).

requirements:

- time range of $\pm$ 2.5 ns (5 ns);
- nominal time resolution of 20 ps (for 8–bit conversion);
- total dead time below 25 ns.

The block diagram of TVDC is presented in Fig. 4.56. The main components of the TVDC are the Time to Amplitude Converter (TAC) followed by a flash ADC with digital discriminators for T0 Vertex signal generation. The TAC is designed to generate an output signal only when both input signals come within the allowed time interval (4 ns) and in the presence of the clock signal (or Bunch Crossing signal). The 8–bit flash ADC AD9002 has the encoding frequency 50 MSPS (Mega–Samples Per Second), and 20 ps granularity. The digital comparator K1500CP166 has a delay equal to 3 ns. It generates the T0 Vertex output signal when the code of the flash ADC coincides with one of the preset (allowed) codes of the vertex position. The total dead time of the TVDC unit is, as expected, below 25 ns. The performance of the T0 Vertex Unit obtained during the July 2003 test run at CERN is shown in Fig. 4.57.

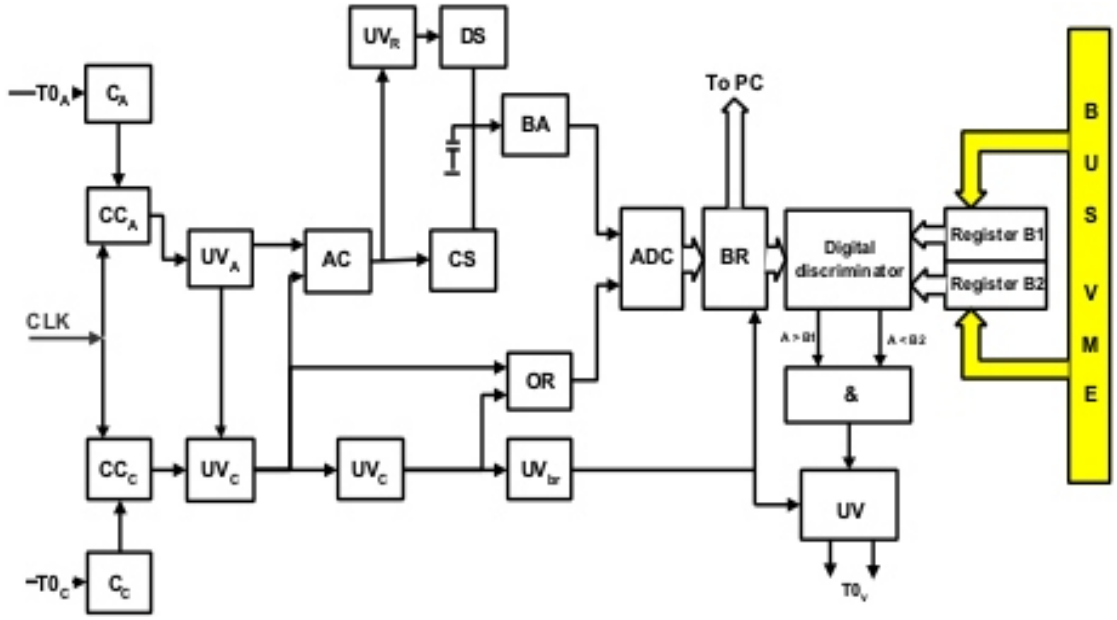

FIGURE 4.56 T0 Vertex Unit (TVDC).

C	= Comparator	BR	= Buffer Register
CC	= Coincidence Circuit	ADC	= Amplitude-Digital Converter
UV	= Univibrator	BA	= Buffer Amplifier
AC	= Anticoincidence Circuit	&	= AND circuit
CS	= Charging current Switch	OR	= OR circuit.
DS	= Discharge Switch		

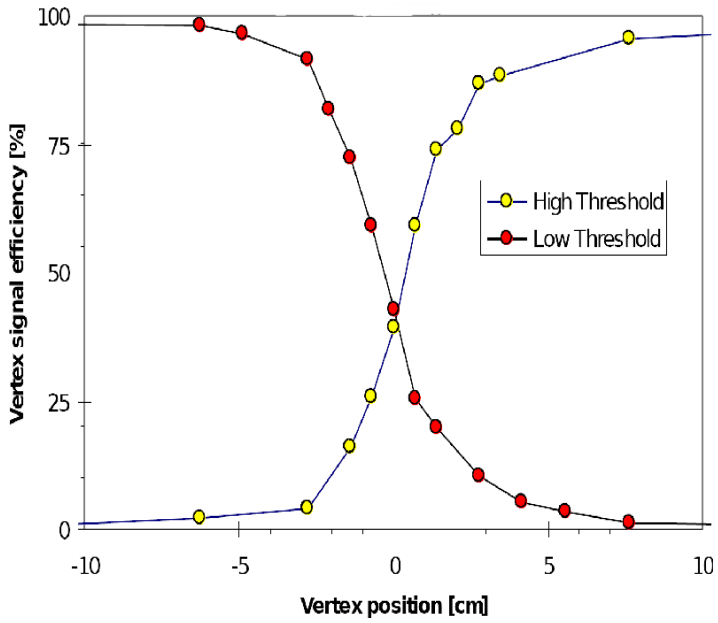

FIGURE 4.57 Performance of the T0 Vertex Unit during the July 2003 test experiment using PS beams at CERN.

VDU

Strict matching of the characteristics of all 24 PMT units forming the T0 detector is simply not possible. As a result each PMT operates at a different and individually selected voltage. This alone causes differences in the arrival times of the signals of up to few ns. To equalise these and comparable differences we have designed the Variable Delay Unit (VDU), shown in Fig. 4.58, and marked as DCDL in Fig. 4.37. Each VDU channel consists of a NIM to ECL converter, an MC100EP195 chip with

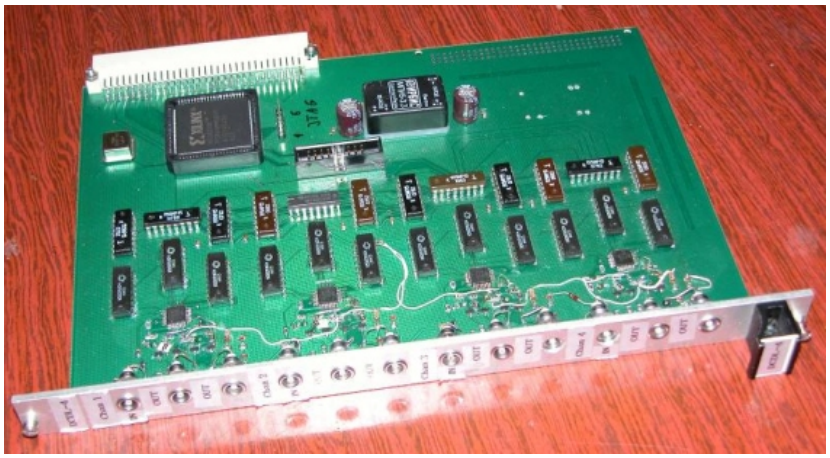

FIGURE 4.58 Photo of T0 Variable Delay Unit.

programmable delay, and an output ECL to NIM converter. A dedicated register connected through an interface with VME is used to record the value of delays. The block diagram of the VDU is shown in Fig. 4.59.

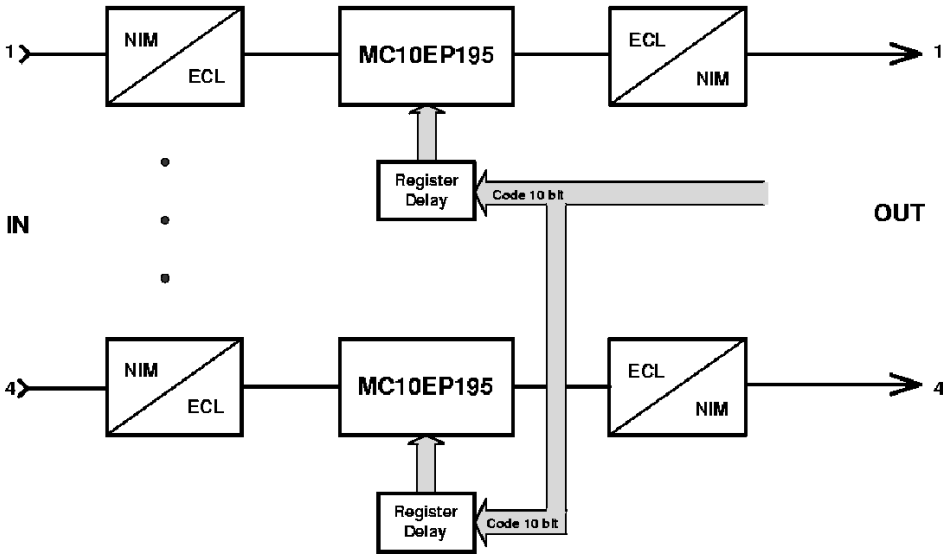

FIGURE 4.59 Block diagram of T0 Variable Delay Unit.

OR

T0 has two OR modules, one for A– and one for C–side. The PMT signals from both sides are fed via CFD and VDU to the two ORs which receive a clock from the CPDM (described in Chapter 4.5.2). Whenever there is a signal from any of the PMTs, the OR checks if there is a clock signal present. If there is, it sends signals to the TVDC, Mean Timer, Scalers, DRM, T0TU, and GRPG.

GRPG

The main tasks of the Gate and Reference Point Generator (GRPG) is to provide a gate for the QTC and a Reference point for T0 timing signals. GRPG processes the input signals from T0 OR–A and OR–C and clock from CPDM as follows:

- Reference point signal is generated whenever there is a signal from any of the ORs;
- Gate for QTC–A is generated only if there is a coincidence between signals from OR–A and the clock from CPDM;
- Gate for QTC–C is generated only if there is a coincidence between signals from OR–C and the clock from CPDM.

T0TU

The T0 detector provides the L0 trigger inputs (Level-0 trigger signal) to the ALICE Central Trigger Processor. The T0 Trigger Unit (T0TU) generates five L0 input signals (T0–A, T0–C, T0–v, T0sc, T0c). T0–C and T0–A signals inform that at least one of the T0 arrays has registered a valid pulse. T0–v (T0 vertex) serves as a minimum bias signal. T0sc (semi-central) and T0c (central) are the multiplicity trigger inputs. Fig. 4.60 presents a block diagram and Fig. 4.61 a photo of T0TU. T0TU is clocked by a local BC (bunch clock) used also by the rest of the fast electronics. The FPGA output TRIGGER_N is controlled by the D–type flip–flop (DFF), clocked by the BC signal. The input D of the flip–flop is selected by a 2–bit option code[18].

The T0 detector must ensure that its trigger signals arrive at the CTP within a 16 BC–wide interval ($\sim$400 ns) that precedes the corresponding trigger–decision time. It means, in terms of the currently approved ALICE trigger timing, that the signals should appear at the CTP in a time–window of 400 ns - 800 ns, counting from the event interaction.

[18]The selection of the properties of trigger outputs (normal, toggle, etc.) is controlled by the CTP software via a DIM server, which uses a 2-bit option code, uniformly defined for all trigger subdetectors: 00 – Normal operation (system default), 01 – Toggle option, 11 – Output inhibit (logic 0).

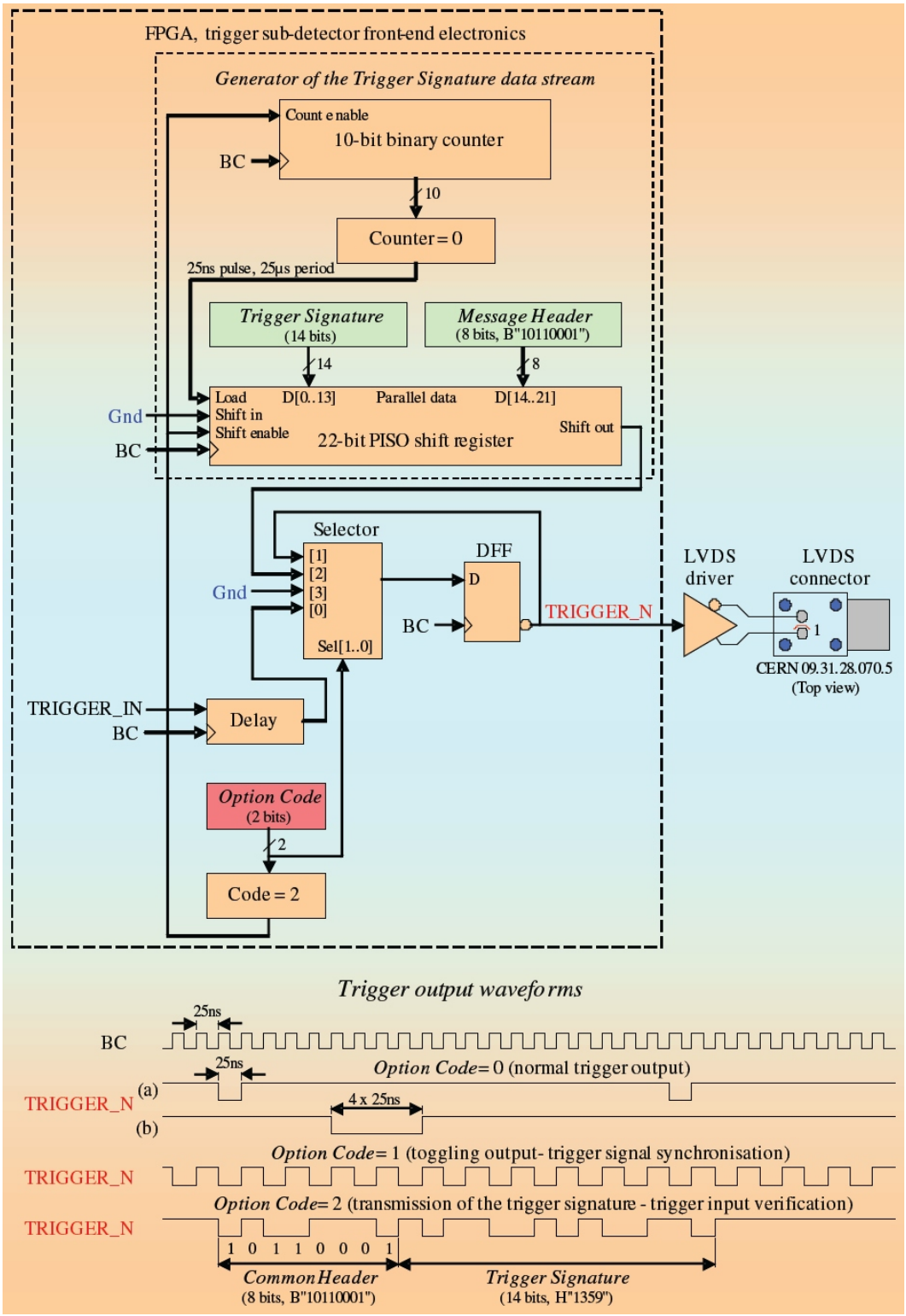

FIGURE 4.60 Block diagram of T0 trigger unit (T0TU). The input signal, TRIGGER_IN, is a fully formatted and synchronised output of T0 detector logic. The output – TRIGGER_N ("_N stands" for negative polarity) is fed to the LVDS line driver.

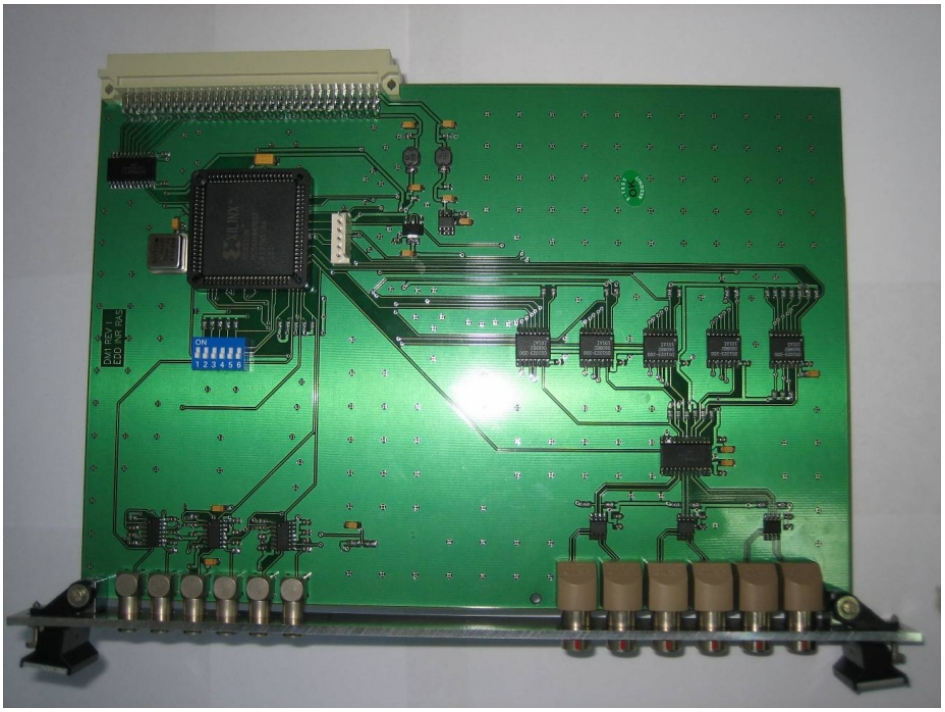

FIGURE 4.61 Photo of T0 trigger unit (T0TU).

NIM–LVDS

The NIM–LVDS module has been developed to transfer data from fast electronics to readout. It converts the NIM signals coming from the QTC, CFD, LED, GRPG, TVDC, OR, MPD and Mean Timer into LVDS signals distributing them among the inputs of the DRM (Data Readout Module). The signals are distributed such that each HPTDC chip receives only 4 signals and buffer is allotted for each. Fig. 4.62 presents the T0 NIM–LVDS module.

4.5.2 Readout

The readout electronics, shown in the centre of Fig. 4.35, consists of the CPDM (Clock and Pulse Distribution module), TRM (TDC Readout Module) and DRM cards. As mentioned in Chapter 4.5.1, the only ALICE subdetector requiring non–trigger data from T0 is TOF. TOF needs time and amplitude information from each PMT to make off–line corrections that should further improve the precision and stability in definitions of the interaction time. Otherwise, the only reason for storing raw T0 parameters would be for monitoring. Therefore, to cut costs and to guarantee the performance of T0, our readout is nearly identical to that of the TOF detector.

For conciseness, only the modifications and changes with respect to the TOF readout are discussed here. Together with arrival times and amplitudes from each PMT, a handful of other parameters (vertex, summary amplitudes, etc.) is also read out and stored by ALICE DAQ in exactly the same fashion. From the point of view of

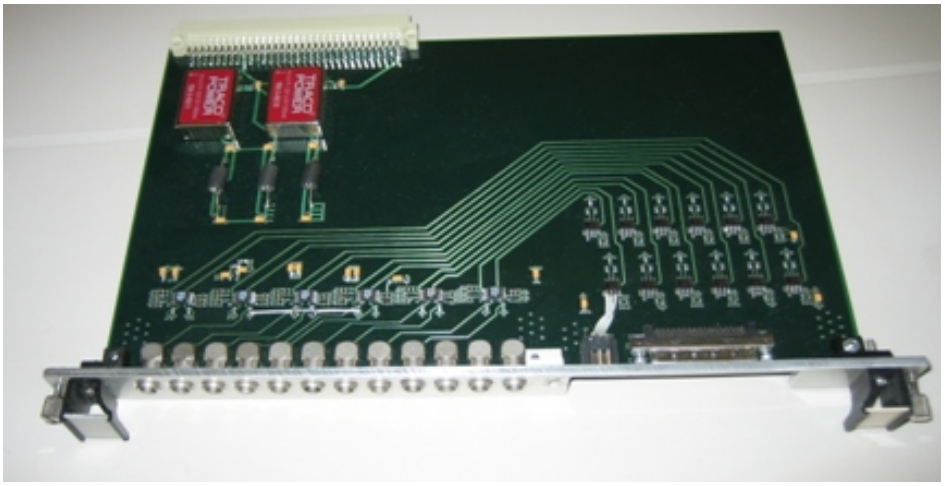

FIGURE 4.62 NIM–LVDS module. LEMO connectors are placed on the left–hand side of the front panel, 68 pin VHDCI connector is on the right-hand side.

the readout architecture, the T0 detector is just one more, fully independent, sector of the TOF detector.

The main difference between T0 and TOF pulses (relevant to the readout system) is their dynamic range. To accommodate the larger amplitude range from T0, a QTC + TDC is used instead of QDC (see Chapter 4.5.1). A more serious problem is the range of the TDC. The HPTDC developed by TOF has a dynamic range of about 200 ns, nearly one order of magnitude more than what is needed by T0. All the same the resolution is sufficient. There is a very small (below a few percent) probability that the same T0 module will produce a pulse in two consecutive bunch crossings. In $p + p$ collisions they are separated by 25 ns. The first pulse will start the HPTDC and block it for the next 200 ns which will prevent the conversion, readout and storage of the second pulse. Let's further assume that the first signal was just noise, a stray particle or a cosmic ray while the second originate from a true interaction that should be triggered and stored. In this possible but very unlikely case, the T0 will produce all the correct trigger signals but the data (time and amplitude) from that particular PMT will not be digitised. Anyhow, this unlikely case has no consequence for $Pb + Pb$ running and almost negligible effect for $p + p$. In the following the components of the T0 readout system: DRM, TRM and CPDM module are presented.

DRM

Each crate is equipped with a Data Readout Module (DRM) card that acts as the main interface between the Central ALICE DAQ, the CTP and T0 electronics. The diagram of the DRM module is presented in Fig. 4.63. The DRM receives and distributes the 40 MHz clock and the trigger signals (L1 and L2) to the T0–TRMs. The clock is received through an optical fiber patchcord, while the other signals are derived from a TTCrx [43]. The clock is distributed to the T0–TRMs via ECL connec-

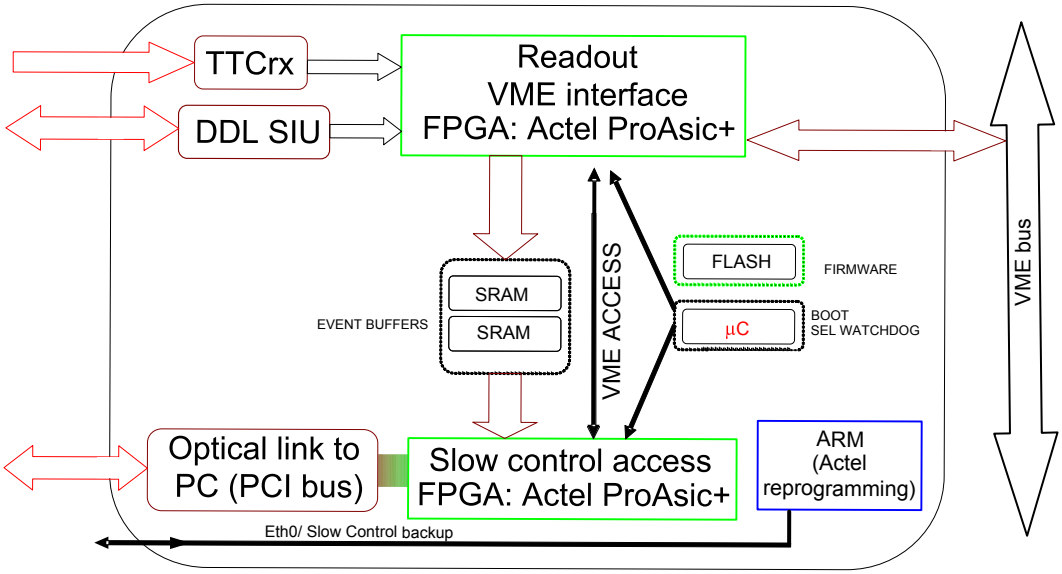

FIGURE 4.63 Block diagram of T0 DRM.

tion. The control signals (L1, L2 accept and L2 reject) are distributed with an LVDS bus to the T0–TRMs through an external flat cable.

The DRM reads the data from the T0–TRM modules. If an L2 reject is received, the corresponding event buffer is cleared on the T0–TRMs, otherwise, on L2 accept, data is transferred from all the T0–TRMs to the DRM via the VME64 backplane. This data transfer is performed by the FPGA.

The data is further processed and encoded by a Digital Signal Processor (DSP) on board and sent through a standard ALICE DDL interface to the central DAQ. A power PC allows monitoring of the data and hosts the slow controls of the T0 system (threshold setting, delay setting etc.). All these I/O devices (TTC and DDL interfaces and power PC cards) are developed as a piggy–back card in standard PMC format applied to a VME card.

TDC Readout Module - TRM unit

An FPGA performs the readout of the HPTDCs[19]. To ensure high bandwidth the FPGA acts as an external readout controller of two separate chains consisting of 15 HPTDC slaves (in token–base parallel–readout configuration). The Altera APEX family FPGA are used. A DSP controls various setup operations (including R–C delay chain calibration) and data packaging. The Analog Devices Shark family DSP are used. Memory (RAM and SRAM) is provided for event buffering and program hosting.

Program loading and general control of the TRM is managed through a VME interface, as shown in Fig. 4.64. Initialisation and setup of the HPTDC chips is nor-

[19]One HPTDC channel corresponds to 24.4 ps.

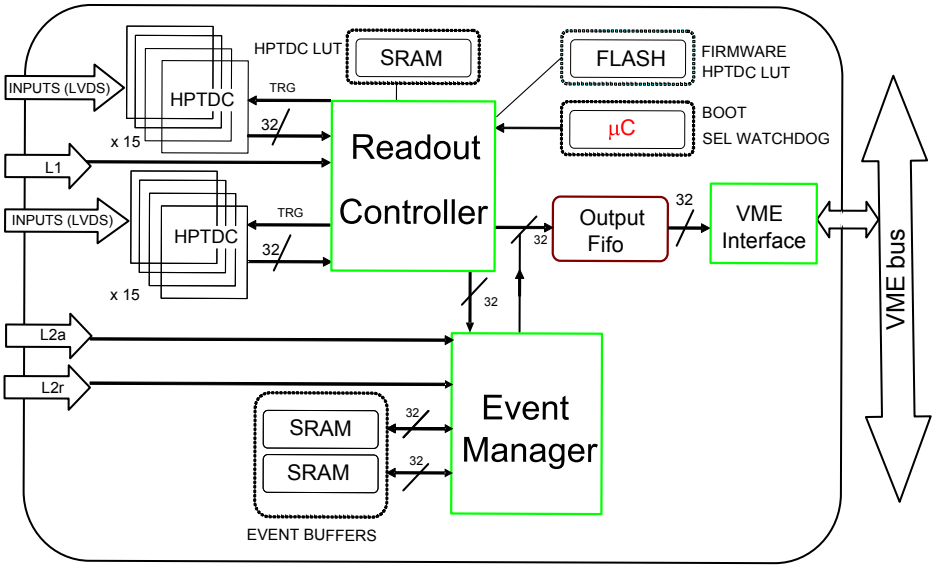

FIGURE 4.64 Diagram of T0 TRM.

mally performed through the DSP. On receival of an L1 signal from the ALICE Central Trigger Processor the HPTDCs look for hits with a time offset of 6.2 μs, moving then to the internal readout FIFO. This operation does not cause dead time to the acquisition of data by the HPTDC.

CPDM

The Clock and Pulse Distribution Module is shown in Fig. 4.65. It is used to provide

FIGURE 4.65 Photo of CPDM module.

the LHC clock signal to the T0 Fast electronics and Readout modules. This allows the synchronisation of all the T0 electronics.

4.6 Online and Offline

T0 Online as a part of ALICE Online project [43] includes data acquisition and monitoring. The relevant for T0 parts of the the Offline project [44] facilitate simulation of detector performance, alignment, data processing and analysis. Simulations have already been discussed in Chapter 4.2, hence I concentrate here on the other two. Offline uses ROOT and GEANT 3 frameworks. AliRoot is an Offline's framework for simulation, reconstruction and analysis having the ROOT system as a foundation on which the framework and all applications are built.

Data size

The data production of the LHC experiments is expected to be about 10 – 15 PB per year. It is a new scale compared to previous experiments. In ALICE, an average $p+p$ event has a size of 1.1 MB while $Pb+Pb$ event averages to about 14 MB. Some 10^9 $p+p$ events and 10^8 $Pb+Pb$ events are expected in a standard running year. It yields a total raw data volume of 2.5 PB. The average size of the reconstructed output is 40 kB for a $p+p$ and 3 MB for a $Pb+Pb$ event. This only includes high–level information needed for user analysis like the event–vertex position, reconstructed track parameters, and PID information [37].

To give an example of data size, the data taken in ALICE cosmic runs in 2008 amounts to ∼300 TB. Two thirds were taken in so-called global runs in which several ALICE subdetectors were included. Global cosmic runs resemble real data–taking. T0 detector has participated in almost all such runs performed by ALICE in 2008 and up to now in 2009 (status from 20/07/2009).

4.6.1 Data acquisition

Physics data analysis in ALICE is done by interpreting the data produced by subdetectors. Due to the acquired data size, the intermediate steps are required to extract the interesting physics information. Firstly, the data is acquired by a special data acquisition (DAQ) system. Before starting the data taking, DAQ sets up specific $runs$ of different types. In case of T0 detector there are three such types: $Physics$[20], $Laser$ and $Standalone$[21]. Every run in turn contains events divided in types, for T0 there are two such types: $PHYSICS$ and $CALIBRATION$. Data produced during the runs is saved in the so-called raw format, which means that it comes directly from the electronics.

[20]During $Physics$ run, $PHYSICS$ type of events are collected and a specific detector algorithm, i.e. $T0Physda$, is run to process them.

[21]In $Standalone$ runs the given subdetector can operate independently of the others. T0 performs $Standalone$ runs during preparations to the data taking and in the breaks between Physics runs to check the detector's performance. The LCS is operated in $Standalone$ runs in the full dynamic range of 1–100 MIPs. The $CALIBRATION$ events are processed in standalone and used for calibration of T0.

4.6.2 Data processing

The raw data taken by each ALICE subdetector has to be processed before it is available in the form of reconstructed events for further analysis. Data originating from the subdetectors is processed by the Local Data Concentrators (LDCs), global events are built by Global Data Collectors (GDCs) [43]. The so-called publish agent registers the assembled events into the AliEn system and ships them to the CERN computing center where they are stored first on disks and then permanently on tapes by the CASTOR system. Fig. 4.66 presents the T0 data flow scheme.

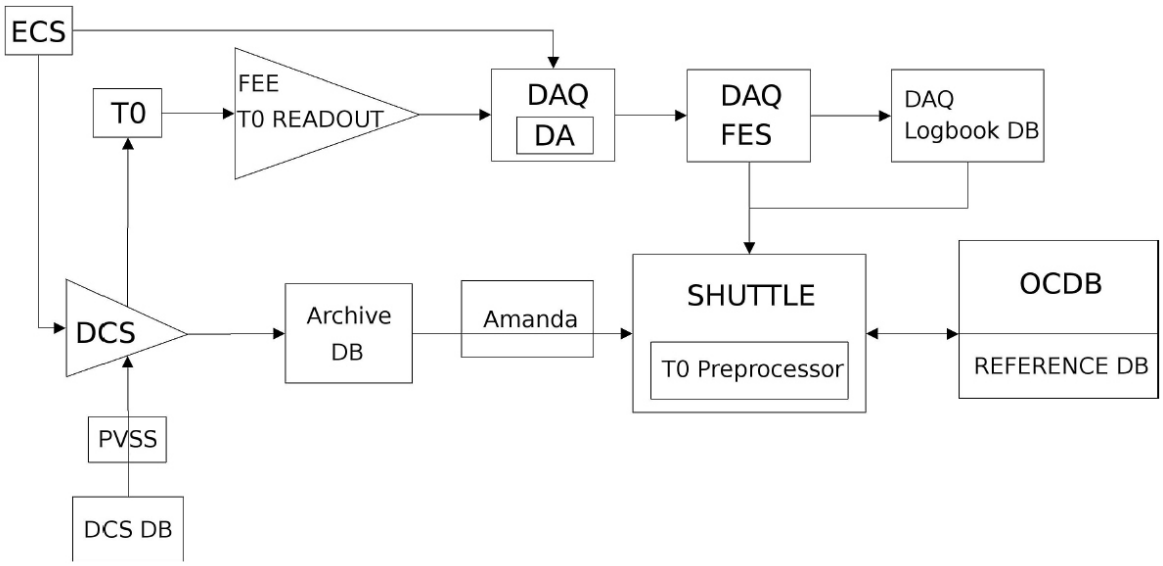

FIGURE 4.66 Data flow for T0 detector.

Raw data is processed "in–flight" during first pass reconstruction as it comes off the DAQ (in $p + p$ collisions) or the tapes (in A + A collisions). ALICE cannot afford to read it twice. The first reconstruction, provided that sufficient information on alignment and calibration is available, endues enough information for understanding the early physics. During the first reconstruction better alignment and calibration information is produced and can be used for the so-called second, third and final pass reconstruction. Alignment or calibration information which comes from the data itself is generated "in–flight" on the LDC or the GDC's. For T0, the first stage of data processing takes place in the T0 Detector Algorithm which allows calibrations and first data analysis to be performed.

T0 DA

Detector Algorithms (DA) are standalone executable programs used for calibration. They read raw data and create relevant histograms or collect parameters needed by detectors during reconstruction process. DAs are implemented and run under

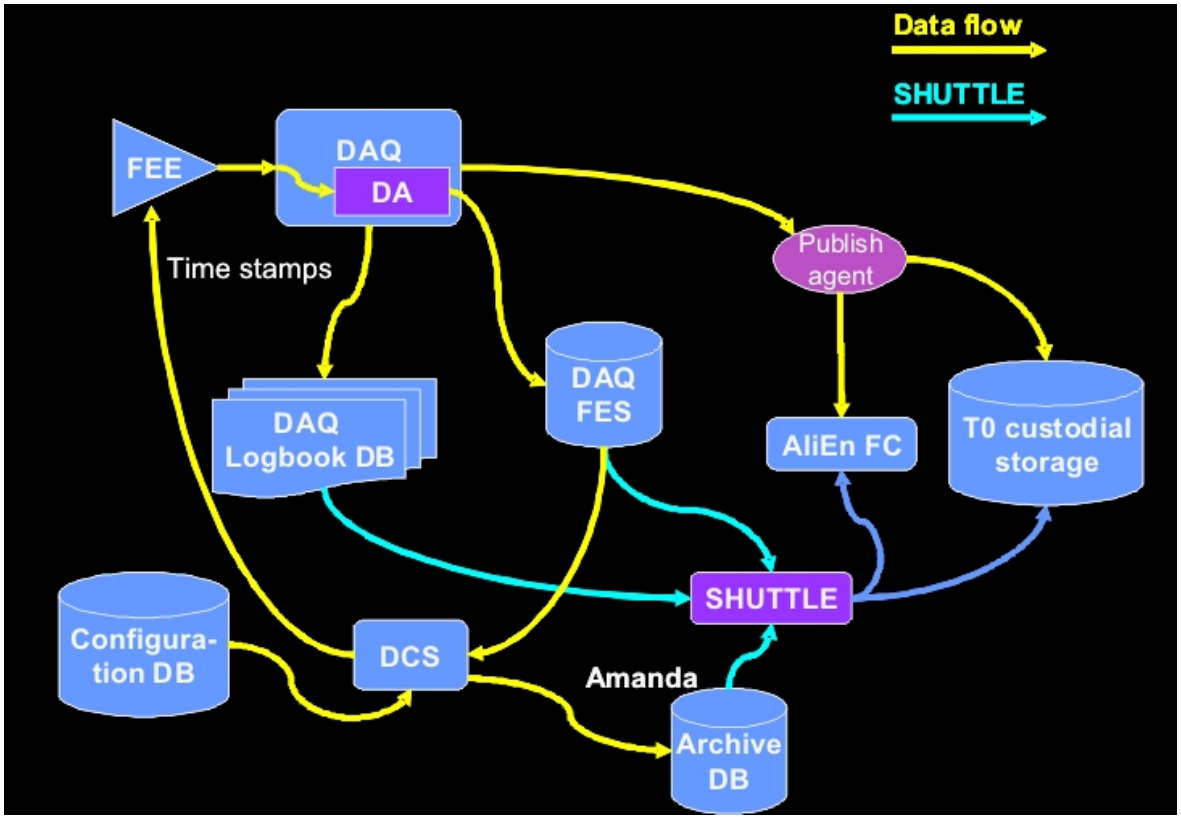

FIGURE 4.67 T0 off–line data processing use case.

DAQ (see Fig. 4.67). The T0 detector uses three different DAs which are executed on DAQ LDCs and on monitoring servers. The three detector algorithms for T0 are: $T0Physda$, $T0Laserda$ and $T0Cosmicda$ which are executed for run types $Physics$, $Standalone$ and $Laser$, respectively. $T0Physda$ computes and stores in a histogram a time difference between the reference PMT and all the others, for A– and C–side. The algorithm works on event by event basis collecting first 20 000 events – the minimum statistics to get the relevant data. It equalises the shift between each T0 PMT timing channel (CFD(i) – CFD(0)) by analysing the peak position of each histogram [41]. The mean and RMS of each channel is computed and sent to the File Exchange Server (FES) from which it is later queried by the T0 preprocessor. The LDCs are part of the data flow and their primary function is to readout the DDLs which are directly connected to the detector electronics. The monitoring servers can access data from any LDC or GDC but are not part of the data flow itself. $T0Laserda$ is used during $Standalone$ Runs. Time–amplitude and amplitude – MIPs graphs are produced both for QTCs and LED-CFDs (see Fig. 4.68). $T0Cosmicda$, that is processed in $Laser$ runs, is a variation of $T0Laserda$. It is hardly used, mostly for debugging purposes.

DAs on LDCs are launched after DAQ End of Run. DAs on monitoring servers are launched before DAQ Start of Run. In both cases, the next run can not start until DAs have completed their operations for the current run. The DAQ also provides

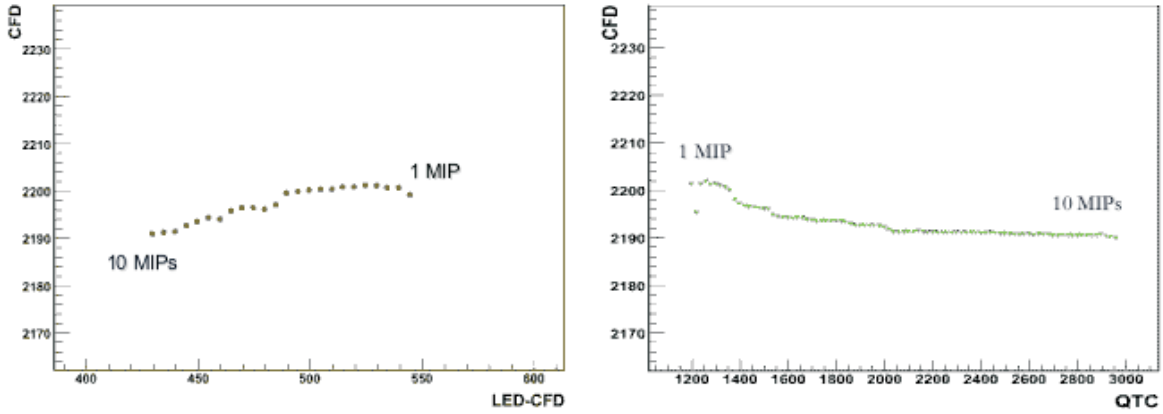

FIGURE 4.68 QTC (on the left, run number 08000025068005.10) and LED–CFD (on the right, run number 08000025068005.10) calibration spectrum. Amplitude–time corrections are done in two ways in $T0Laserda$.

a reference machine where the DAs are compiled and linked before installation on the target machines.

Monitoring of the ALICE data is done via interactive Data Quality Monitoring framework [42]. The online monitoring is needed to check that the detector is getting correct signals and also for the final tuning of the electronics. The system called MOOD used previously in ALICE for monitoring has been recently replaced with AMORE framework [42]. The AMORE provides, in addition to online monitoring of the data, also the Quality Assurance.

T0 preprocessor

The T0 preprocessor processes data obtained from DA and DCS. It retrieves a file produced by DA from the FES, computes the parameters needed by T0 and stores the result[22] to OCDB and Reference DB (Chapter 4.8.5). The differences between the times from the reference CFD and all the the others (CFD(i) – CFD(0)) are written as the value of shift between channels for equalising and also as a shift in a vertex position. If the preprocessor returns error, it means that there is some problem, e.g. technical with Shuttle or failure of the DA, which implies not storing the calibration parameters to OCDB and Reference DB[23].

[22]The results stored by T0 Preprocessor are:

- walk correction graphs (to OCDB)
- amplitude graphs (LED – CFD vs CFD, to OCDB)
- average of the scaler counts (to Reference DB)
- table with CFD time (CFD(i) – CFD(0), to OCDB).

[23]The first prototype of the preprocessor was implemented in November 2005. It has, since then, been thoroughly tested with the Shuttle Test setup (running every night) as well as the Shuttle Pro-

T0 Data points (the information recorded by the DCS relevant for T0, such as T0 scaler counts, PMT HV, Shoebox LV, etc.) are read from the DCS database server [43], processed by the preprocessor and stored to the Reference DB[24]. The list of the Data points is given in Table 4.7. Each of T0 aliases is processed using the

TABLE 4.7 T0 Data points processed in the preprocessor.

DCS alias	Data type	Unit	Value [%]	Fluct.	Update freq. [s]
t00_a_hv_imon_[00..11]	float	uA	83	0.9	3000
t00_a_hv_vmon_[00..11]	float	V	1325	0.85	3000
t00_a_lv_imon_[0..1]	float	uA	83	0.9	3000
t00_a_lv_vmon_[0..1]	float	V	6	0.15	3000
t00_c_hv_imon_[00..11]	float	uA	83	0.9	3000
t00_c_hv_vmon_[00..11]	float	V	1325	0.85	3000
t00_c_lv_imon_[0..1]	float	uA	83	0.9	3000
t00_c_lv_vmon_[0..1]	float	V	6	0.15	3000
t00_a_cfd_thre_[00..11]	float	V	0.5	10	3000
t00_a_cfd_walk_[00..11]	float	V	-0.1	10	3000
t00_c_cfd_thre_[00..11]	float	V	0.5	10	3000
t00_c_cfd_walk_[00..11]	float	V	-0.1	10	3000
t00_ac_scaler_[00..31]	uInt	1/s	3E08	50	120
t00_ac_scaler_sec[0..31]	uInt	1/s	80	50	120
t00_ac_trm_[00..09]	float	counts	35	3	SOR,EOR,if changed
t00_ac_drm[00..04]	float	counts	35	3	SOR,EOR,if changed
t00_ac_atten	int	MIP	5	50	SOR, EOR,if changed
t00_a_mpd_cent	int	MIP	40	15	SOR, EOR
t00_a_mpd_scent	int	MIP	40	15	SOR, EOR
t00_c_mpd_cent	int	MIP	40	15	SOR, EOR
t00_c_mpd_scent	int	MIP	40	15	SOR, EOR
t00_ac_mpd_mode	int	counts	2	100	SOR, EOR
t00_ac_tvdc_top	int	cm	5	20	SOR, EOR
t00_ac_tvdc_bottom	int	cm	5	20	SOR, EOR

dedicated AliRoot class. T0, and most other subdetectors, generate and process in a macro a set of 'artificial' DCS aliases that resemble the one generated by the DCS. This is done mostly for testing and debugging purposes. Due to modifications in the

duction mode (running few times a day). If problems with processing the data occur, the T0 detector experts are alerted by an automated e–mail.

[24]The query to the DCS database for the retrieval of the Data points is performed at the time when the run number is created minus a certain offset, and ends at the so-called time completed (the time when all the post-end-of-run processes have finished) plus the same offset, instead of querying the database from the DAQ Start to the DAQ End of data taking. The offset allows to avoid possible desynchronization between DAQ time and DCS time and assures the proper retrieval of the DPs.

DCS, not all T0 aliases are available (status for 20/07/2009). Therefore some of them are simulated by DCS so that the necessary tests of the preprocessor can be performed. For example, the real data from the T0 scalers was available only in 2008, therefore the AliRoot class was tested in 2007 with T0 scaler output being randomly generated distributions or values simulated with the DCS.

Reconstruction

Event reconstruction is done by the off–line code. The data stored to OCDB is processed in the reconstruction in order to obtain the accurate physics data from each of the detectors. Reconstruction includes timing and geometry corrections. T0 uses the reconstructed vertex to provide more accurate output needed for the multiplicity and luminosity measurements. The reconstructed data is used to produce Event Summary Data (ESD) [44]. There is one ESD for all detectors. Information needed for analysis and further calibration is stored in the ESD. Once reconstruction is run, there is no going back to the raw data until the next reconstruction pass[25]. All successive processing goes from the ESD. Finally, if needed, the detector or group–specific AOD (Analysis Object Data) are produced from the ESDs.

4.6.3 Alignment

Knowing the nominal position of the ALICE subdetectors is not enough. The actual position can be different from the nominal one due to e.g. a limited precision during mounting or deformations caused by various factors including movements of the earth, influence of magnetic fields[26], human mistakes, etc. Measurements of actual positions with errors are therefore needed. For T0, as well as for other ALICE subdetectors, the measurement of actual position and detector alignment is performed via a process called survey. It determines the detector positions using the fiducial marks that have been added to many detector components at well defined places. Digital images are taken from various angles of the setup and the exact positions are calculated. This method achieves a precision of 1 mm when it is performed in the ALICE pit, and somewhat better for measurements done in the lab while assembling a detector. The survey results are digitised, stored in a root file in the Reference Database and distributed through the grid. The survey sets the position of the T0 with the accuracy of better than 1 mm (more about surveys can be found in Chapter 4.8.4).

[25] Few raw events can be read in justified cases, e.g. for debugging, but no more.

[26] During the magnet test in July 2008 the relative movement of the Front absorber nose with respect to the ITS was examined. Results have shown that the Front absorber nose moves 2 mm down with respect to the ITS, with full current for L3 and the Dipole. This has been also confirmed by measurements made of the FASS arms connected to the L3 on the outside, with full current for the L3 and the Dipole magnets.

If the position of the detector is not properly set in the Offline, the so-called overlaps between detectors or their parts occur. Fig. 4.69 presents the overlaps that have been removed from the T0 geometry in June 2008. In addition, T0 alignable

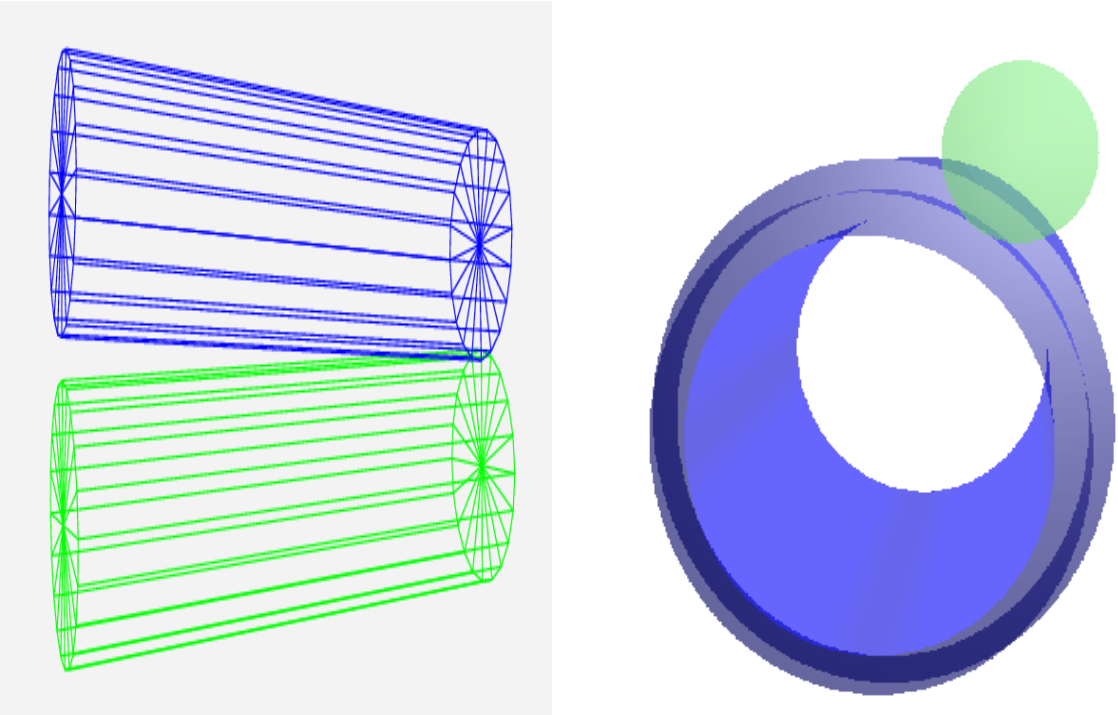

FIGURE 4.69 2 out 38 T0 overlaps removed from the ideal geometry in June 2008.

volumes (two arrays of the PMTs) must have clearance (free space, i.e. 0.01 cm, around the alignable volumes). Once survey and alignment data is used to displace those volumes, there should not be overlaps with other volumes, e.g. supporting elements. At present (20/07/2009) there are no overlaps in the T0 geometry. The clearance around T0 alignable volumes has also been implemented (there are no newly created overlaps after misaligning T0 alignable volumes by the quantities expected from the survey).

4.7 DCS

Since there is no access to the ALICE cavern during the data taking, all crucial devices must be remotely controlled. Most of the T0 detector modules is relatively straightforward, stable, and reliable which makes controlling them easier. Standard off–the–shelf products are used as high voltage and current monitoring devices. Some problems arise however from the stray magnetic fields in the vicinity of the L3 magnet and elevated radiation levels. This however is a common problem for all ALICE detectors and T0 benefits from standard solutions like the EASY system developed by CAEN. In each T0 channel there are several thresholds, delays, etc. that

have to be adjusted prior and sometimes also during the run. T0 Vertex and Multiplicity units control the main trigger signals and need to be addressed during the normal ALICE operation. Monitoring of all T0 PMTs is done with LCS during the longer breaks in the beam. This should cause no problems as even the laser power supply is remotely triggered.

The DCS scheme for the T0 detector is shown in Fig. 4.70. The main subsystems

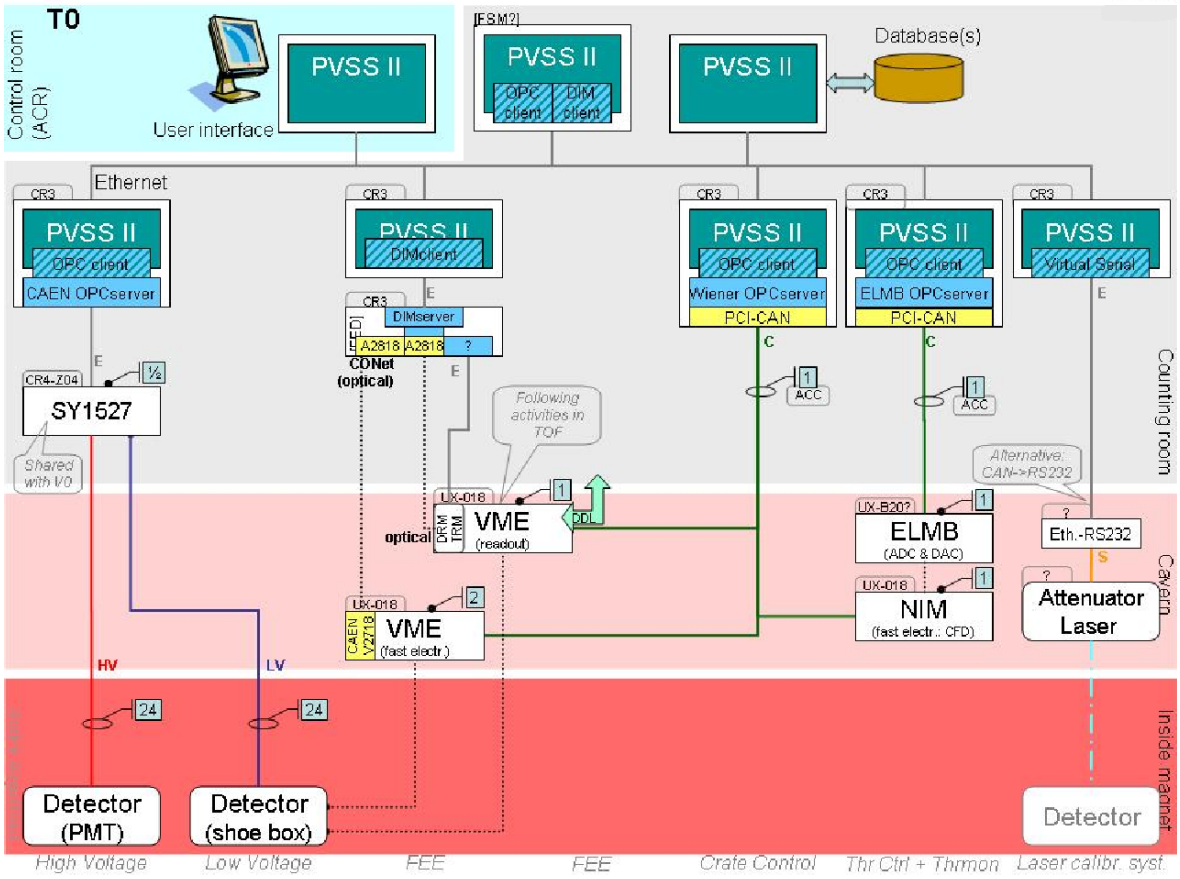

FIGURE 4.70 Scheme of T0 DCS.

are high voltage (HV), low voltage (LV), threshold and delays settings, laser control, generator control and T0–TDCs and T0–DRM readout cards. The list of signals to be monitored and controlled for the T0 detector is listed in Table 4.7. As discussed in Chapter 4.5, the T0 electronics is located in two different areas: the Shoebox is placed inside the magnet (these regions can be accessed only during a long shutdown), Fast electronics and T0 TDC/TDM cards are in the crates just outside of the L3 magnet and can be accessed even during a short shutdown. The high and low voltage to the PMTs and electronics is provided by the CAEN SY2527 system with high and low voltage boards. A CAEN OPC server interfaces the crate with PVSS through Ethernet.

The connections between the control computer and VME crates with Fast electronics is based on the CAEN V2718-A2818 VME-PCI optical link bridge. CAEN

TABLE 4.8 Main parameters of the Detector Control System for the T0.

Subsyst.	location	Controlled parameters	No.	Paramet.	Control
Fast electr.	VME	delays Thresholds for CFD Thresholds for T0 vertex Thresholds for multiplicity trigger	24 24 2 - 3	- voltage voltage - voltage	- W R/W - R/W
T0–TRM	VME crate	same as TOF			
T0–DRM	VME crate	same as TOF			
Low voltage for Shoebox	CAEN 2725	LV supply on/off LV settings and readings safety switch	24 24 1	voltage complex voltage	R/W R/W on/off
HV voltage	-	HV supply on/off HV settings and readings safety switch	24 24 1	voltage complex voltage	R/W R/W on/off
Laser system	-	switch attenuator	1 1	- complex	on/off R/W
Generator	-	switch	1	voltage	on/off

V2718 is a 1-unit wide 6U VME master module, which is interfaced to the CONET (Chainable Optical NETwork) and controlled by a standard PC equipped with the PCI card CAEN module A2818. The solutions for controlling T0–TRM and T0–DRM were developed by the ALICE TOF group and adopted by us. There was however no ready–made solution for controlling the threshold on the CFDs. A control system based on a Embedded Local Monitor Board (ELMB) presented in Fig. 4.71 was developed. A dedicated DAC unit, shown in Fig. 4.72, has been designed to provide an interface with the CFDs. The DAC output voltages are ± 2.5 and ± 5 V. The thresholds on the CFD are set via DAC as shown in Fig. 4.73.

For fast electronics, standard VME crates are used. The control and monitoring is done via a CANbus and Kvaser CAN interface card. Support for all equipments is implemented with the JCOP framework. The top–level application is a SCADA system based on PVSS software that communicates with the hardware via OPC or DIM servers. PVSS configuration panels allow to remotely change the settings of the monitored modules. Fig. 4.74 presents a configuration panel for scaler. The panel facilitates enabling or disabling each scaler's channel, which, in case of problems with a given channel, could be useful for the luminosity computation.

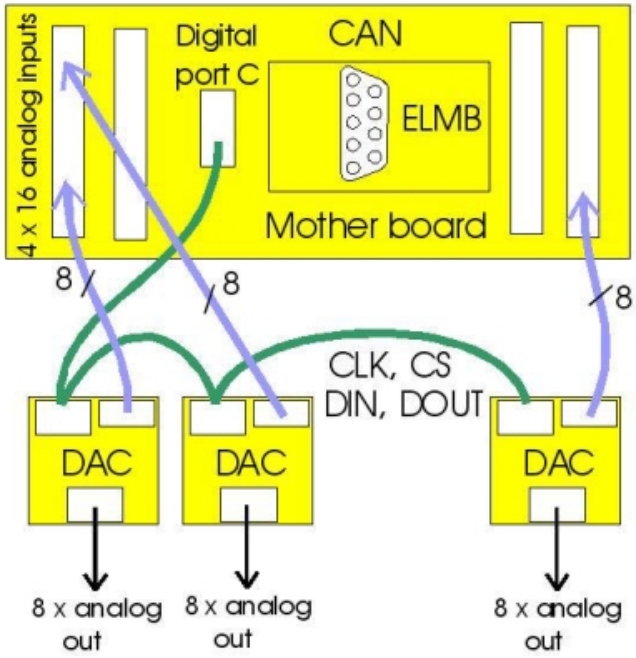

FIGURE 4.71 ELMB–based system to set thresholds on T0 CANBERRA 454 CFDs.

4.8 Databases

ALICE databases store all the relevant information about ALICE and its subdetectors. They are used during the construction of subdetectors and later to facilitate the operation of the ALICE detector. Table 4.9 lists the databases relevant for the T0. Our experience in development and use of the T0 database may be utilised in similar applications in the field of experimental and applied physics.

4.8.1 DCDB

Detector Construction Database (DCDB) [48] stores information on ALICE subdetector components, their derivation and assemblage. It consists of local (satellite) databases located in laboratories involved in subdetector production and the central repository located at CERN (see Fig. 4.75). Further information on the DCDB concept can be found in Appendix A.3.

T0 Database is the ALICE satellite database located at the Department of Physics, University of Jyväskylä. It is based on PostgreSQL. The main argument for such choice was the simplicity of PostgreSQL and that it is a freeware. The T0 database stores information on all components of the T0 detector e.g. spectral characteristics, gain vs. HV curves, time resolution as a function of the magnetic field, as well as spectra obtained with laser pulses, and from cosmic rays.

The structure of DCDB is generic. It consists of a dynamic part called Rabbit, and a static part – Dictionary Wizard. Rabbit is filled with data obtained during the

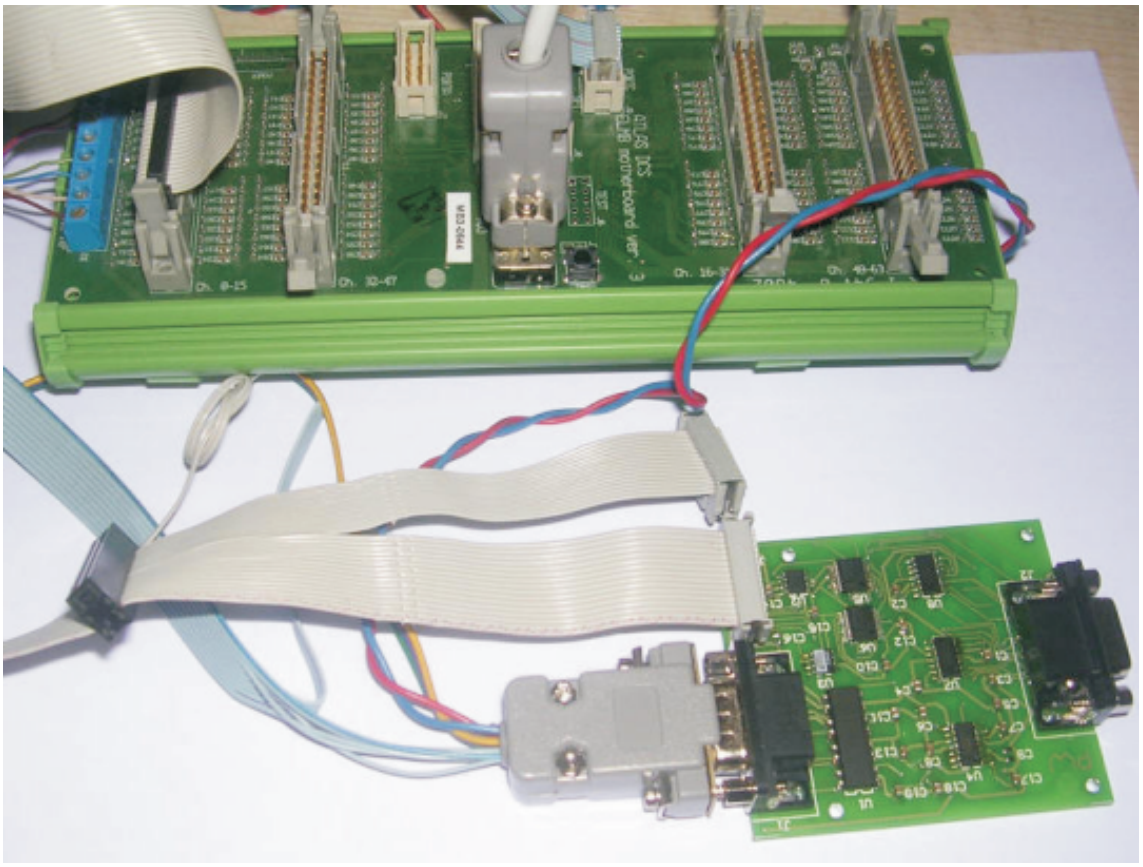

FIGURE 4.72 Photo of ELMB and DAC unit.
ELMB (top) and DAC unit (bottom) used for setting thresholds on the CFD.

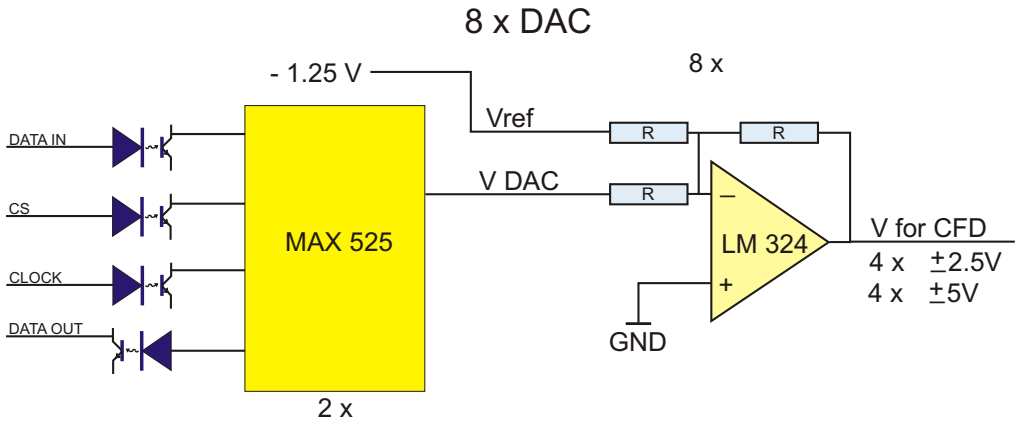

FIGURE 4.73 Control of the CFD via DAC.

manufacturing and tests of detector components. Dictionary Wizard is a dictionary containing information about the components. Rabbit and Dictionary Wizard for T0 are described in detail in Appendix A.3. The web addresses of Dictionary Wizard and Rabbit are listed in Table 4.9.

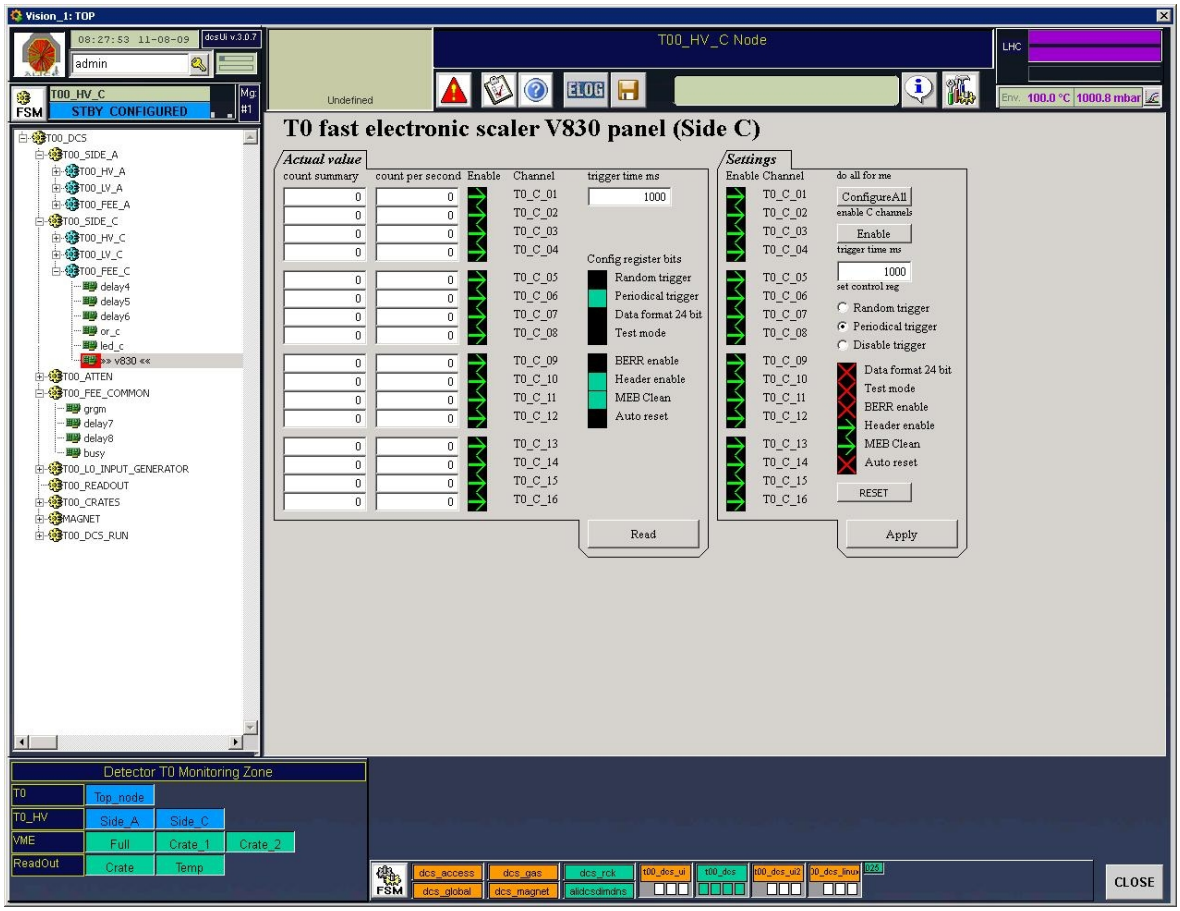

FIGURE 4.74 Config panel for T0 scalers implemented in PVSS.

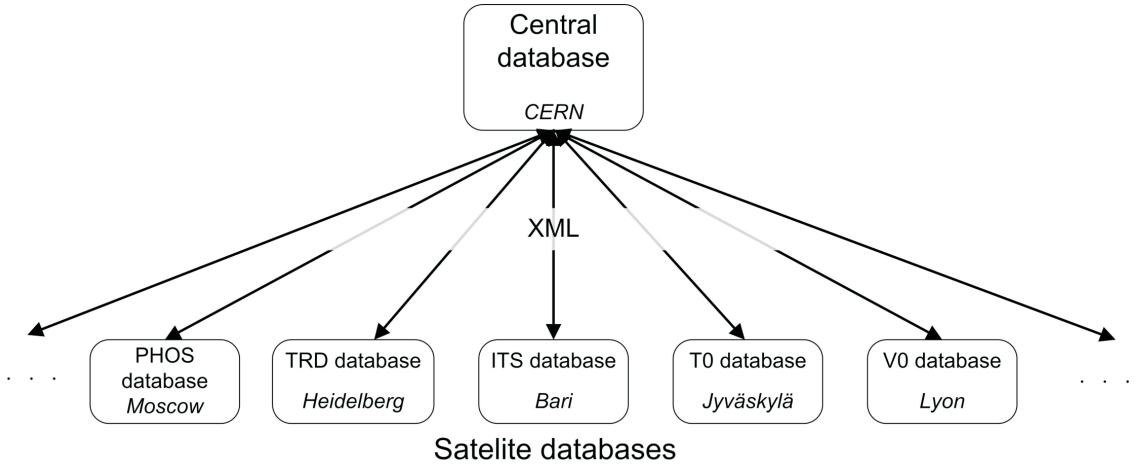

FIGURE 4.75 Detector Construction Database structure with XML-based data interchange. Satellite databases are located in the laboratories participating in ALICE, e.g. T0 database at JYFL. The central repository is at CERN.

TABLE 4.9 Databases in which data related to the T0 detector is stored.

Database	Location	Write privileges Access rights
Dictionary Wizard	http://dcdb.cern.ch/dictwizard/	T0 experts ALICE Collaboration
ServoTech	http://alice-detector-facilities.web.cern.ch/Alice-Detector-Facilities/	T0 experts ALICE Collaboration
Rabbit	http://dcdbappl1.cern.ch:8080/rabbit/	T0 experts ALICE Collaboration
Survey depot	http://dcdb.cern.ch/dcdb/	Surveyors ALICE Collaboration
Rack depot	http://dcdb.cern.ch/dcdb/	T0 experts ALICE Collaboration
Offline Databases	http://aliceinfo.cern.ch/Offline/Activities/ConditionDB.html	T0 experts ALICE Collaboration

The currently ongoing effort is to permanently move the T0 satellite database from Jyväskylä to CERN due to a lack of manpower to maintain a database in Jyväskylä in the future.

4.8.2 ServoTech cable Database

The complete information about T0 cables and fiber patchcords is stored in ServoTech database. Since the database was frozen in 2008, the changes in cable data can only introduced be introduced via "SVT Connections update request form" presented in Fig. 4.76. The T0 cables have been prepared and pulled according to the data give in ServoTech. Each cable contains unique "Mnemonic function" (fourth column from the left in Fig. 4.76), which was put on the label attached to each cable during its installation. ServoTech allows to identify and prepare a replacement in case of problems with a certain cable.

4.8.3 Rack depot

Rack depot is a database containing information on T0 electronic modules placed in racks 018, 019 and CR4–Z04 in ALICE. Fig. 4.77 presents a combined view of T0 racks in the "Rack file" that was replaced in 2007 with Rack depot. The total power dissipation has been calculated for every rack to assure the proper cooling. Fig. 4.78 presents T0 electronics modules in crate VME 2 defined in the Rack depot. Part ID is used to uniquely define each subdetectors' components. It is used to create

Detector group	Action	Part ID	Mnemonic function	Connection Type	Service Component Type	Origin Node Name	Orig. Building	Orig. Area	Orig. Side	Orig. Equipment	Origin Connector Type	Origin Connector Status	Side in Rack	Destination Node Name
HIP	modified	1TOOCER0C0005119	HV 1 T0-A	HV Cable	04.31.51.750.1	1T00HIP_PMT-401	UX25	T00	A	--	Permanent coupling	--	--	1T00U2PMNFS13B01
		1TOOCER0C0005201	HV 2 T0-A	HV Cable	04.31.51.750.1	1T00HIP_PMT-402	UX25	T00	A	--	Permanent coupling	--	--	1T00U2PMNFS13B01
		1TOOCER0C0005202	HV 3 T0-A	HV Cable	04.31.51.750.1	1T00HIP_PMT-403	UX25	T00	A	--	Permanent coupling	--	--	1T00U2PMNFS13B01
		1TOOCER0C0005203	HV 4 T0-A	HV Cable	04.31.51.750.1	1T00HIP_PMT-404	UX25	T00	A	--	Permanent coupling	--	--	1T00U2PMNFS13B01
		1TOOCER0C0005204	HV 5 T0-A	HV Cable	04.31.51.750.1	1T00HIP_PMT-405	UX25	T00	A	--	Permanent coupling	--	--	1T00U2PMNFS13B01
		1TOOCER0C0005205	HV 6 T0-A	HV Cable	04.31.51.750.1	1T00HIP_PMT-406	UX25	T00	A	--	Permanent coupling	--	--	1T00U2PMNFS13B01
		1TOOCER0C0005206	HV 7 T0-A	HV Cable	04.31.51.750.1	1T00HIP_PMT-407	UX25	T00	A	--	Permanent coupling	--	--	1T00U2PMNFS13B01
		1TOOCER0C0005207	HV 8 T0-A	HV Cable	04.31.51.750.1	1T00HIP_PMT-408	UX25	T00	A	--	Permanent coupling	--	--	1T00U2PMNFS13B01
		1TOOCER0C0005208	HV 9 T0-A	HV Cable	04.31.51.750.1	1T00HIP_PMT-409	UX25	T00	A	--	Permanent coupling	--	--	1T00U2PMNFS13B01
		1TOOCER0C0005209	HV 10 T0-A	HV Cable	04.31.51.750.1	1T00HIP_PMT-410	UX25	T00	A	--	Permanent coupling	--	--	1T00U2PMNFS13B01
		1TOOCER0C0005210	HV 11 T0-A	HV Cable	04.31.51.750.1	1T00HIP_PMT-411	UX25	T00	A	--	Permanent coupling	--	--	1T00U2PMNFS13B01
		1TOOCER0C0005211	HV 12 T0-A	HV Cable	04.31.51.750.1	1T00HIP_PMT-412	UX25	T00	A	--	Permanent coupling	--	--	1T00U2PMNFS13B01
		1TOOCER0C0005212	HV 1 T0-C	HV Cable	04.31.51.750.1	1T00HIP_PMT-601	UX25	T00	C	--	Permanent coupling	--	--	1T00U2PABSS05B00
		1TOOCER0C0005238	HV 2 T0-C	HV Cable	04.31.51.750.1	1T00HIP_PMT-602	UX25	T00	C	--	Permanent coupling	--	--	1T00U2PABSS05B00
		1TOOCER0C0005239	HV 3 T0-C	HV Cable	04.31.51.750.1	1T00HIP_PMT-603	UX25	T00	C	--	Permanent coupling	--	--	1T00U2PABSS05B00
		1TOOCER0C0005240	HV 4 T0-C	HV Cable	04.31.51.750.1	1T00HIP_PMT-604	UX25	T00	C	--	Permanent coupling	--	--	1T00U2PABSS05B00
		1TOOCER0C0005241	HV 5 T0-C	HV Cable	04.31.51.750.1	1T00HIP_PMT-605	UX25	T00	C	--	Permanent coupling	--	--	1T00U2PABSS05B00
		1TOOCER0C0005242	HV 6 T0-C	HV Cable	04.31.51.750.1	1T00HIP_PMT-606	UX25	T00	C	--	Permanent coupling	--	--	1T00U2PABSS05B00
		1TOOCER0C0005243	HV 7 T0-C	HV Cable	04.31.51.750.1	1T00HIP_PMT-607	UX25	T00	C	--	Permanent coupling	--	--	1T00U2PABSS05B00
		1TOOCER0C0005244	HV 8 T0-C	HV Cable	04.31.51.750.1	1T00HIP_PMT-608	UX25	T00	C	--	Permanent coupling	--	--	1T00U2PABSS05B00
		1TOOCER0C0005245	HV 9 T0-C	HV Cable	04.31.51.750.1	1T00HIP_PMT-609	UX25	T00	C	--	Permanent coupling	--	--	1T00U2PABSS05B00
		1TOOCER0C0005246	HV 10 T0-C	HV Cable	04.31.51.750.1	1T00HIP_PMT-610	UX25	T00	C	--	Permanent coupling	--	--	1T00U2PABSS05B00
		1TOOCER0C0005247	HV 11 T0-C	HV Cable	04.31.51.750.1	1T00HIP_PMT-611	UX25	T00	C	--	Permanent coupling	--	--	1T00U2PABSS05B00
		1TOOCER0C0005248	HV 12 T0-C	HV Cable	04.31.51.750.1	1T00HIP_PMT-612	UX25	T00	C	--	Permanent coupling	--	--	1T00U2PABSS05B00
		1TOOCER0C0005249	HV 1 T0-A	HV Cable	04.31.51.555.2	1T00U2PMNFS13B0	UX25	MINI-F	RB24	--	09.41.25.108.3	--	--	1T00U2PAL21BA001
		1TOOCER0C0005250	HV 2 T0-A	HV Cable	04.31.51.555.2	1T00U2PMNFS13B0	UX25	MINI-F	RB24	--	09.41.25.108.3	--	--	1T00U2PAL21BA001
		1TOOCER0C0005303	HV 3 T0-A	HV Cable	04.31.51.555.2	1T00U2PMNFS13B0	UX25	MINI-F	RB24	--	09.41.25.108.3	--	--	1T00U2PAL21BA001
		1TOOCER0C0005304	HV 4 T0-A	HV Cable	04.31.51.555.2	1T00U2PMNFS13B0	UX25	MINI-F	RB24	--	09.41.25.108.3	--	--	1T00U2PAL21BA001
		1TOOCER0C0005305	HV 5 T0-A	HV Cable	04.31.51.555.2	1T00U2PMNFS13B0	UX25	MINI-F	RB24	--	09.41.25.108.3	--	--	1T00U2PAL21BA001
		1TOOCER0C0005306	HV 6 T0-A	HV Cable	04.31.51.555.2	1T00U2PMNFS13B0	UX25	MINI-F	RB24	--	09.41.25.108.3	--	--	1T00U2PAL21BA001
		1TOOCER0C0005307	HV 7 T0-A	HV Cable	04.31.51.555.2	1T00U2PMNFS13B0	UX25	MINI-F	RB24	--	09.41.25.108.3	--	--	1T00U2PAL21BA001
		1TOOCER0C0005308	HV 8 T0-A	HV Cable	04.31.51.555.2	1T00U2PMNFS13B0	UX25	MINI-F	RB24	--	09.41.25.108.3	--	--	1T00U2PAL21BA001
		1TOOCER0C0005309	HV 9 T0-A	HV Cable	04.31.51.555.2	1T00U2PMNFS13B0	UX25	MINI-F	RB24	--	09.41.25.108.3	--	--	1T00U2PAL21BA001
		1TOOCER0C0005310	HV 10 T0-A	HV Cable	04.31.51.555.2	1T00U2PMNFS13B0	UX25	MINI-F	RB24	--	09.41.25.108.3	--	--	1T00U2PAL21BA001
		1TOOCER0C0005311	HV 11 T0-A	HV Cable	04.31.51.555.2	1T00U2PMNFS13B0	UX25	MINI-F	RB24	--	09.41.25.108.3	--	--	1T00U2PAL21BA001
		1TOOCER0C0005312	HV 12 T0-A	HV Cable	04.31.51.555.2	1T00U2PMNFS13B0	UX25	MINI-F	RB24	--	09.41.25.108.3	--	--	1T00U2PAL21BA001
		1TOOCER0C0005313	HV 13S T0-A	HV Cable	04.31.51.555.2	1T00U2PMNFS13B0	UX25	MINI-F	RB24	--	09.41.25.108.3	--	--	1T00U2PAL21BA001
		1TOOCER0C0005314	HV 1 T0-A	HV Cable	04.31.51.555.2	1T00U2PAL21BA00	UX25	--	RB24	--	09.41.25.108.3	--	--	1T00C4YZ04042
		1TOOCER0C0005315	HV 2 T0-A	HV Cable	04.31.51.555.2	1T00U2PAL21BA00	UX25	--	RB24	--	09.41.25.108.3	--	--	1T00C4YZ04042

Dest. Building	Dest. Area	Dest. Side	Dest. Equipment	Destination Connector Type	Destination Connector Status	Destination on Side in Rack	Routing	Length [m]	Critical Length	Maximum number of wires	Procurement	Status	Datasheet
UX25	MINI-F	RB24	--	09.41.25.108.3	--	--	ortal/en/Coll	1,5	No	1	Inst from Ext	Tested	h.cern.ch/edhcat/Browser
UX25	MINI-F	RB24	--	09.41.25.108.3	--	--	ortal/en/Coll	1,5	No	1	Inst from Ext	Tested	et/Login?REFER=https://edh.cern.ch/edhcat/Browser
UX25	MINI-F	RB24	--	09.41.25.108.3	--	--	ortal/en/Coll	1,5	No	1	Inst from Ext	Tested	et/Login?REFER=https://edh.cern.ch/edhcat/Browser
UX25	MINI-F	RB24	--	09.41.25.108.3	--	--	ortal/en/Coll	1,5	No	1	Inst from Ext	Tested	et/Login?REFER=https://edh.cern.ch/edhcat/Browser
UX25	MINI-F	RB24	--	09.41.25.108.3	--	--	ortal/en/Coll	1,5	No	1	Inst from Ext	Tested	et/Login?REFER=https://edh.cern.ch/edhcat/Browser
UX25	MINI-F	RB24	--	09.41.25.108.3	--	--	ortal/en/Coll	1,5	No	1	Inst from Ext	Tested	et/Login?REFER=https://edh.cern.ch/edhcat/Browser
UX25	MINI-F	RB24	--	09.41.25.108.3	--	--	ortal/en/Coll	1,5	No	1	Inst from Ext	Tested	et/Login?REFER=https://edh.cern.ch/edhcat/Browser
UX25	MINI-F	RB24	--	09.41.25.108.3	--	--	ortal/en/Coll	1,5	No	1	Inst from Ext	Tested	et/Login?REFER=https://edh.cern.ch/edhcat/Browser
UX25	MINI-F	RB24	--	09.41.25.108.3	--	--	ortal/en/Coll	1,5	No	1	Inst from Ext	Tested	et/Login?REFER=https://edh.cern.ch/edhcat/Browser
UX25	MINI-F	RB24	--	09.41.25.108.3	--	--	ortal/en/Coll	1,5	No	1	Inst from Ext	Tested	et/Login?REFER=https://edh.cern.ch/edhcat/Browser
UX25	F-ABS	RB26	--	09.41.25.108.3	--	--	ortal/en/Coll	1,5	No	1	Inst from Ext	Tested	et/Login?REFER=https://edh.cern.ch/edhcat/Browser
UX25	F-ABS	RB26	--	09.41.25.108.3	--	--	ortal/en/Coll	1,5	No	1	Inst from Ext	Tested	et/Login?REFER=https://edh.cern.ch/edhcat/Browser
UX25	F-ABS	RB26	--	09.41.25.108.3	--	--	ortal/en/Coll	1,5	No	1	Inst from Ext	Tested	et/Login?REFER=https://edh.cern.ch/edhcat/Browser
UX25	F-ABS	RB26	--	09.41.25.108.3	--	--	ortal/en/Coll	1,5	No	1	Inst from Ext	Tested	et/Login?REFER=https://edh.cern.ch/edhcat/Browser
UX25	F-ABS	RB26	--	09.41.25.108.3	--	--	ortal/en/Coll	1,5	No	1	Inst from Ext	Tested	et/Login?REFER=https://edh.cern.ch/edhcat/Browser
UX25	F-ABS	RB26	--	09.41.25.108.3	--	--	ortal/en/Coll	1,5	No	1	Inst from Ext	Tested	et/Login?REFER=https://edh.cern.ch/edhcat/Browser
UX25	F-ABS	RB26	--	09.41.25.108.3	--	--	ortal/en/Coll	1,5	No	1	Inst from Ext	Tested	et/Login?REFER=https://edh.cern.ch/edhcat/Browser
UX25	F-ABS	RB26	--	09.41.25.108.3	--	--	ortal/en/Coll	1,5	No	1	Inst from Ext	Tested	et/Login?REFER=https://edh.cern.ch/edhcat/Browser
UX25	F-ABS	RB26	--	09.41.25.108.3	--	--	ortal/en/Coll	1,5	No	1	Inst from Ext	Tested	et/Login?REFER=https://edh.cern.ch/edhcat/Browser
UX25	F-ABS	RB26	--	09.41.25.108.3	--	--	ortal/en/Coll	1,5	No	1	Inst from Ext	Tested	et/Login?REFER=https://edh.cern.ch/edhcat/Browser
UX25	F-ABS	RB26	--	09.41.25.108.3	--	--	ortal/en/Coll	1,5	No	1	Inst from Ext	Tested	et/Login?REFER=https://edh.cern.ch/edhcat/Browser
UX25	F-ABS	RB26	--	09.41.25.108.3	--	--	ortal/en/Coll	1,5	No	1	Inst from Ext	Tested	et/Login?REFER=https://edh.cern.ch/edhcat/Browser
UX25	F-ABS	RB26	--	09.41.25.108.3	--	--	ortal/en/Coll	1,5	No	1	Inst from Ext	Tested	et/Login?REFER=https://edh.cern.ch/edhcat/Browser
UX25	F-ABS	RB26	--	09.41.25.108.3	--	--	ortal/en/Coll	1,5	No	1	Inst from Ext	Tested	et/Login?REFER=https://edh.cern.ch/edhcat/Browser
UX25	F-ABS	RB26	--	09.41.25.108.3	--	--	ortal/en/Coll	1,5	No	1	Inst from Ext	Tested	et/Login?REFER=https://edh.cern.ch/edhcat/Browser
UX25	F-ABS	RB26	--	09.41.25.108.3	--	--	ortal/en/Coll	1,5	No	1	Inst from Ext	Tested	et/Login?REFER=https://edh.cern.ch/edhcat/Browser
UX25	F-ABS	RB26	--	09.41.25.108.3	--	--	ortal/en/Coll	1,5	No	1	Inst from Ext	Tested	et/Login?REFER=https://edh.cern.ch/edhcat/Browser
UX25	--	RB24	--	09.41.25.108.3	--	--	ortal/en/Coll	5	No	1	Cern-Store	Tested	et/Login?REFER=https://edh.cern.ch/edhcat/Browser
UX25	--	RB24	--	09.41.25.108.3	--	--	ortal/en/Coll	5	No	1	Cern-Store	Tested	et/Login?REFER=https://edh.cern.ch/edhcat/Browser
UX25	--	RB24	--	09.41.25.108.3	--	--	ortal/en/Coll	5	No	1	Cern-Store	Tested	et/Login?REFER=https://edh.cern.ch/edhcat/Browser
UX25	--	RB24	--	09.41.25.108.3	--	--	ortal/en/Coll	5	No	1	Cern-Store	Tested	et/Login?REFER=https://edh.cern.ch/edhcat/Browser
UX25	--	RB24	--	09.41.25.108.3	--	--	ortal/en/Coll	5	No	1	Cern-Store	Tested	et/Login?REFER=https://edh.cern.ch/edhcat/Browser
UX25	--	RB24	--	09.41.25.108.3	--	--	ortal/en/Coll	5	No	1	Cern-Store	Tested	et/Login?REFER=https://edh.cern.ch/edhcat/Browser
UX25	--	RB24	--	09.41.25.108.3	--	--	ortal/en/Coll	5	No	1	Cern-Store	Tested	et/Login?REFER=https://edh.cern.ch/edhcat/Browser
UX25	--	RB24	--	09.41.25.108.3	--	--	ortal/en/Coll	5	No	1	Cern-Store	Tested	et/Login?REFER=https://edh.cern.ch/edhcat/Browser
UX25	--	RB24	--	09.41.25.108.3	--	--	ortal/en/Coll	5	No	1	Cern-Store	Tested	et/Login?REFER=https://edh.cern.ch/edhcat/Browser
UX25	--	RB24	--	09.41.25.108.3	--	--	ortal/en/Coll	5	No	1	Cern-Store	Tested	et/Login?REFER=https://edh.cern.ch/edhcat/Browser
UX25	--	RB24	--	09.41.25.108.3	--	--	ortal/en/Coll	5	No	1	Cern-Store	Tested	et/Login?REFER=https://edh.cern.ch/edhcat/Browser
UX25	--	RB24	--	09.41.25.108.3	--	--	ortal/en/Coll	5	No	1	Cern-Store	Tested	et/Login?REFER=https://edh.cern.ch/edhcat/Browser
UX25	--	RB24	--	09.41.25.108.3	--	--	ortal/en/Coll	5	No	1	Cern-Store	Tested	et/Login?REFER=https://edh.cern.ch/edhcat/Browser
UX25	--	RB24	--	09.41.25.108.3	--	--	ortal/en/Coll	5	No	1	Cern-Store	Tested	et/Login?REFER=https://edh.cern.ch/edhcat/Browser
UX25	--	RB24	--	09.41.25.108.3	--	--	ortal/en/Coll	5	No	1	Cern-Store	Tested	et/Login?REFER=https://edh.cern.ch/edhcat/Browser
UX25	--	RB24	--	09.41.25.108.3	--	--	ortal/en/Coll	5	No	1	Cern-Store	Tested	et/Login?REFER=https://edh.cern.ch/edhcat/Browser
PX24	CR4	--	--	09.41.25.108.3	--	--	ortal/en/Coll	24	No	1	Cern-Store	Tested	et/Login?REFER=https://edh.cern.ch/edhcat/Browser
PX24	CR4	--	--	09.41.25.108.3	--	--	ortal/en/Coll	24	No	1	Cern-Store	Tested	et/Login?REFER=https://edh.cern.ch/edhcat/Browser

FIGURE 4.76 Excerpt of the SVT Connections update request form containing T0 cables' data from ServoTech database.

labels that are placed on each module. More on labels and labelling procedure can be found in Appendix A.3.

4.8.4 Survey depot

The Survey depot contains data from the surveys of the ALICE detectors. All survey results relevant for T0 are given with respect to the so-called Global Reference System (GRS) [46]. GRS has its center in the ALICE IP as depicted in Fig. 4.79. The basic survey units are unified with Geant 3 [50] and AliRoot and are e.g. centimeter, radian, gram, GeV. After the survey, the report is prepared by the surveyors and uploaded to the Survey depot. It is then transferred to AliEn. The exact position of T0–A and T0–C is populated to Offline databases based on the survey data read from AliEn.

T0 arrays do not need to be measured directly. They are mechanically fixed to the larger volumes that are surveyed, hence their position is computed from those

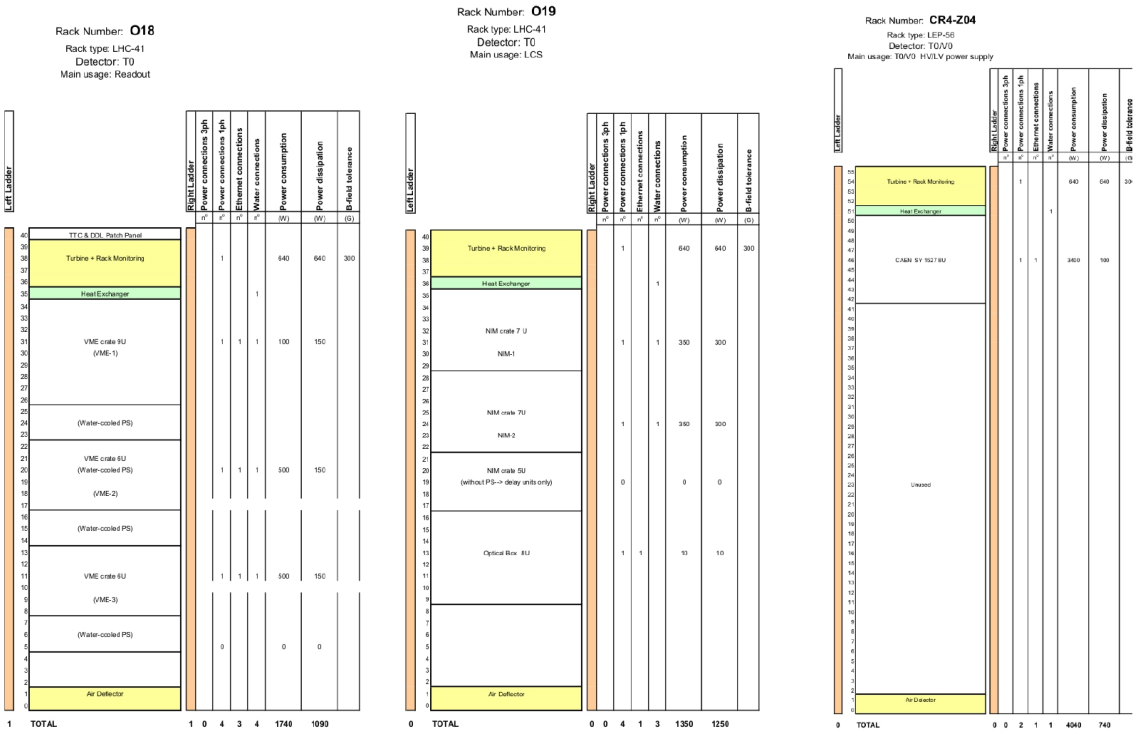

FIGURE 4.77 Consumption and dissipation of power by T0 crates in racks O18, O19 and CR4–Z04.

measurements. On the C–side the beam pipe is fixed to the Front absorber nose. The position of the beam pipe sticking out of the absorber was aligned and measured on 05.04.2007. This measurement enabled the determination of the position of T0 in X and Y from the position of the center of the beam pipe around which the T0–C is installed. A survey of the V0–C, to which T0–C is attached, allowed the determination of the position in Z with the precision of the fixing screw, i.e. $\pm$ 0.5 mm. Fig. 4.80 shows the location of fiducial marks on the alignment volumes in the proximity of T0–C, that allowed the determination of their position.

The position of T0–A is deduced based on a survey of the beam pipe flanges of the sector on the Mini frame on the A–side. The last measurement of the beam pipe flanges close to the T0–A was done on 12/08/2008, just after the final V0–A alignment. After that the position of T0–A has been changing during the shutdown of the LHC due to the removal and reinstallation of other detectors. Now (status for 20/07/2009) T0 is placed as close as possible to its nominal place, but only the survey after the final alignment of the Mini frame gives the precise value for the first beam. Such a survey is to be made together with the V0A alignment (see Fig. 4.81 presenting the position of T0–A and its support structure with respect to V0A). The Mini frame survey results are expected to be submitted to the Survey depot in the coming weeks, which would allow the update of the position of T0–A in the Offline before the first data–taking after the restart of the LHC.

T0 VME-2- VME 7U (crate + Water-cooled PS)

Front | Rear | Detached

Right side of the subrack

			Part ID	Location	Width	Detector Group*	Comments*
20	VDL (DCDL-8)	NEW	1RACHIP004028869	20	1	HIP	Delay for OR-A, Or-C and coinc [...]
19	Fan-in Fan-out LVDS BUSY	NEW	1RACHIP004032251	19	1	HIP	--
18	T0TU	NEW	1RACHIP004028871	18	1	HIP	--
17	Scaler	NEW	1RACHIP004028874	17	1	HIP	--
16	GRPG	NEW	1RACMME004032250	16	1	MME	Gate Reference Point Generator
15	VDL (DCDL-7)	NEW	1RACHIP004032632	15	1	HIP	Delay for Laser signal from GR [...]
14	LED	NEW	1RACHIP004028873	14	1	HIP	--
13							
12	LED	NEW	1RACHIP004028872	12	1	HIP	--
11							
10	MPD	NEW	1RACHIP004028870	10	1	HIP	--
9	VDL (DCDL-6)	NEW	1RACHIP004032633	9	1	HIP	--
8	VDL (DCDL-5)	NEW	1RACHIP004028868	8	1	HIP	--
7	VDL (DCDL-4)	NEW	1RACHIP004028867	7	1	HIP	--
6	OR-C	NEW	1RACHIP004028865	6	1	HIP	--
5	TVDC	NEW	1RACHIP004028866	5	1	HIP	--
4	OR-A	NEW	1RACHIP004028864	4	1	HIP	--
3	VDL (DCDL-3)	NEW	1RACHIP004028863	3	1	HIP	--
2	VDL (DCDL-2)	NEW	1RACHIP004028862	2	1	HIP	--
1	VDL (DCDL-1)	NEW	1RACHIP004028861	1	1	HIP	DCDL - Digital Control Delay L [...]
0	CAEN 2718	NEW	1RACHIP004028860	0	1	HIP	--

FIGURE 4.78 T0 electronics modules in crate VME 2. Gate and Reference Point Generator module is highlighted as the last component defined in Rack depot.

4.8.5 Offline Databases

The information relevant for ALICE Online and Offline is stored in Offline Conditions Database (OCDB) and Reference Database [52]. The OCDB is the place where the calibration and alignment data is stored. Unlike databases described in the previous sections, it is not a database in the literal sense of the word. OCDB is a set of entries in the AliEn file catalogue that point to the physical entities (Root files stored

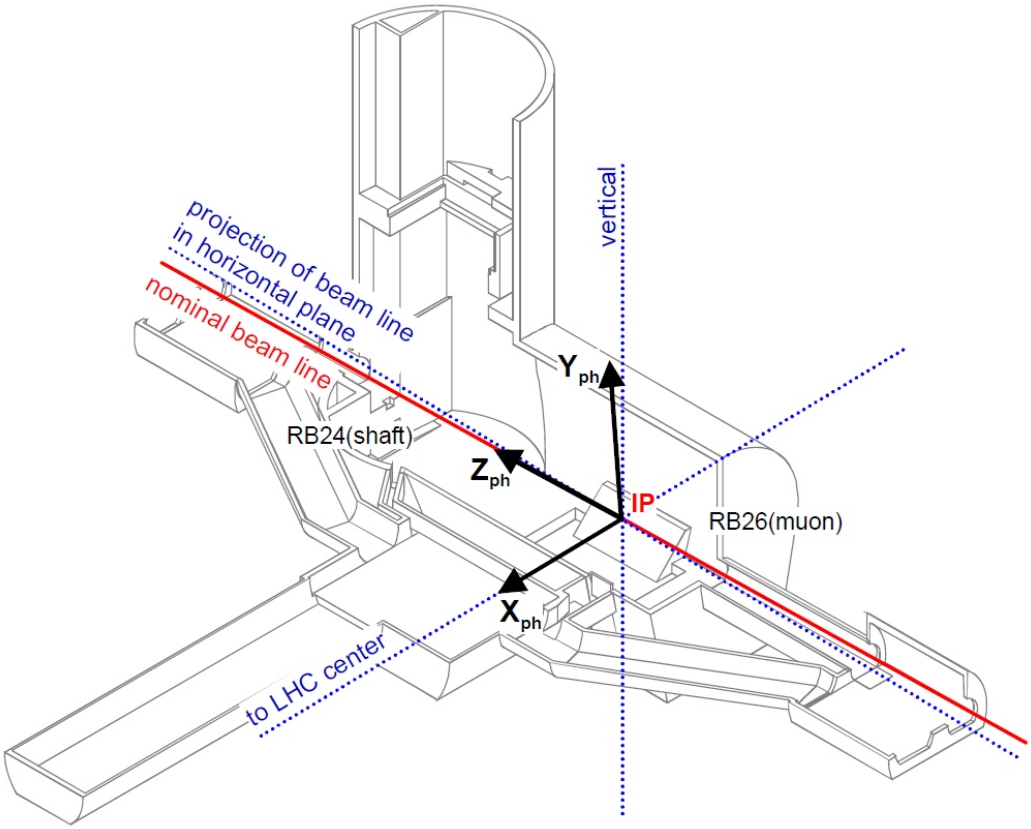

FIGURE 4.79 ALICE coordinate system [45]. The Z–axis goes along the nominal beamline and is positive in the direction of RB24/Shaft. The Z–axis has an inclination of 0.01386 rad, going up in the direction RB26/Muon. The X–axis is perpendicular to Z and horizontal. It is positive towards the LHC center.

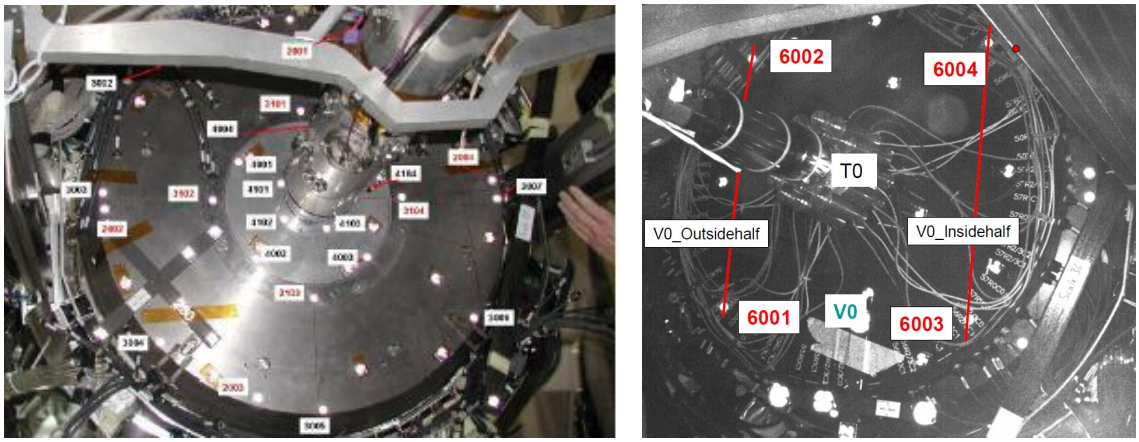

FIGURE 4.80 Survey volumes used for determining the position of T0–C [51]. Points useful for vertical alignment, i.e. X and Y coordinates, are on the left, and for horizontal, i.e. Z coordinate on the right.

in the various storage elements on the grid) containing the calibration and alignment data. The organisation of the database is handled by the CDB access framework, an

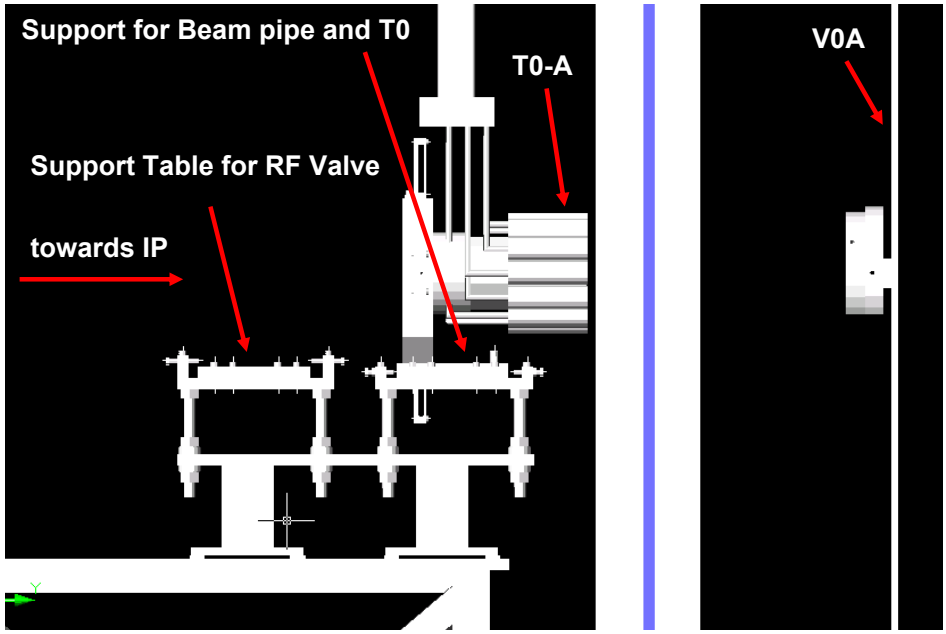

FIGURE 4.81 T0–A and its support structure. T0–A final position is determined based on beam pipe flanges in its proximity.

AliRoot–based package. The main principles of the OCDB are:

- The calibration and alignment database contains Root TObjects stored into Root files;
- The database is read-only (automatic versioning of the stored objects);
- Calibration and alignment objects are run dependent objects;
- The objects in the OCDB are identified by: a path name (path of the file in the AliEn file catalogue), a validity expressed as a run range, a grid version number[27], (a local subversion number, only for locally stored objects);

All T0 parameters used in the reconstruction of the physics data, such as time walk, are stored in the OCDB.

All detector parameters that are not used during the reconstruction are stored in the Reference Database, e.g. T0 DCS Data points. The structure of Reference DB is similar to OCDB.

[27]The local subversion is introduced to avoid version clashing during the transfer of OCDB object from Grid to local storages and vice versa.

5 T0 Tests and Installation

5.1 Tests at ITEP

Once the PMT technology was chosen, remaining issues included the selection of the photomultiplier tubes and Cherenkov radiators for the T0. Experience from the PHENIX experiment at RHIC, where a very similar detector called Beam Beam Counter (BBC) is in use, contributed to the decision–making. BBC, based on quartz radiators and Hamamatsu fine–mesh phototubes, was built and is operated by the Hiroshima group [49], further details can be found in Appendix A.2. This group, using 1.6 GeV/c negative pions, demonstrated a time resolution of 50 ps after off–line pulse shape correction. A 100 ps resolution was obtained without any off–line correction with a simple Leading Edge Discriminator. In the T0 R&D studies, various PMT – Cherenkov counter combinations have been tested. The tests included scintillation counters based on the BC–408 scintillator [28]. The first tests were performed with the mixed 1.28 GeV/c pion/proton beam from the ITEP accelerator at the Institute of Theoretical and Experimental Physics (Moscow, Russia). The experimental setup of the ALICE ITEP group [54] was used[1]. A time resolution of scintillation and Cherenkov detectors using different radiator types and shapes have been compared. The scintillation detector used the same PMT but was equipped with BC–408 plastic scintillator in place of a Cherenkov radiator. The studied radiators included:

- A cylindrical quartz radiator 26 mm in diameter and 30 mm long,
- A similar quartz radiator but with a thin Al cover to provide mirror reflection with 98% efficiency,
- A rectangular Lucite (Plexiglas) radiator of $18 \times 18 \times 30$ mm^3.

Among the studied options were Hamamatsu R3432–01 (26 mm in diameter), a Russian fine–mesh PMT FEU–187 (30 mm in diameter), a 20 mm thick BC–408 scintillator with a diameter matching that of the PMT (26 and 30 mm, respectively). A fast Leading Edge Discriminator was used in all runs, and we applied an off–line correction in order to obtain the final time resolution values of each different type of detector [5].

A summary of the obtained results is given in Table 5.1 and 5.2. The Cherenkov

TABLE 5.1 Typical time resolution values for different PMTs, radiators and scintillators obtained with a beam from the ITEP accelerator [54].

Beam geometry PMT	**Radiator/scintillator**	**Time res.**
R3432–01	Quartz diam. 26×30 mm	40 ps
FEU–187	Quartz diam. 26×30 mm	42 ps
R3432–01	BC–408, diam. 26×20 mm (with diffuse refl.)	57 ps
FEU–187	BC–408, diam. 30×20 mm (with diffuse refl.)	55 ps
R3432–01	Aluminized quartz diam. 26×30 mm	48 ps
Broad–beam geom.		
R3432–01	Quartz diam. 26×30 mm	55 ps
FEU–187	Quartz diam. 26×30 mm	57 ps
R3432–01	BC–408, diam. 26×20 mm (with a diffuse refl.)	80 ps
FEU–187	BC–408, diam. 30×20 mm (with a diffuse refl.)	89 ps
R3432–01	Aluminized quartz diam. 26×30 mm	54 ps
R3432–01	Plexiglas radiator $18 \times 18 \times 30$ mm	45 ps

TABLE 5.2 Results from ITEP accelerator obtained with 1.28 GeV/c pions, in broad–beam geometry [54]. Both Lucite and quartz radiators were 30 mm long and their diameter was matched to that of the PMT (26 mm for Hamamatsu and 30 mm for FEU–187).

Type of PMT	**Type of radiator**	**Time resolution, ps**
Hamamatsu R3432–01	Quartz	53
Hamamatsu R3432–01	Lucite	50
Hamamatsu R3432–01	Lucite	54
Hamamatsu R3432–01	Lucite	56
Hamamatsu R5506	Quartz	59
Hamamatsu R5506	Lucite	75
FEU–187	Quartz	55
FEU–187	Quartz	58
FEU–187	Quartz	52
FEU–187	Quartz	42

counters clearly give better performance than the BC–408 scintillator. As far as time resolution is concerned, both Lucite and quartz radiators are acceptable. The advantage of a Lucite radiator is a smaller radiation length: x_0 = 34.4 cm, whereas for quartz it is x_0 = 11.7 cm. However, the radiation stability of Lucite is only 100 krad, which is substantially less than the expected cumulative dose for the T0 detector. This was the main reason for choosing quartz radiators.

[1]This setup was also used in the ITEP studies of the timing properties of RPCs for the ALICE TOF detector.

5.2 Tests at JYFL

5.2.1 Characteristics of PMTs with and without magnetic field

Tests of T0 PMTs with and without a magnetic field of up 0.5 T have been carried out at JYFL during the years 2002–2007. All the tests have confirmed that FEU–187 can provide very good time resolution in a wide range of bias voltages and magnetic fields. The typical PMT time resolution with and without the magnetic field is shown in Fig. 5.1. Naturally, increasing the HV bias rapidly increases the pulse amplitude at the output (by up to 3 orders of magnitude) and changes the relative pulse delay by several nanoseconds. Therefore selection of the optimum HV has a big impact on detector performance and must be made with care. Even a slight change of HV bias necessitates retuning of all delays and thresholds, affecting the efficiency and often also the time resolution. Time performance depending on

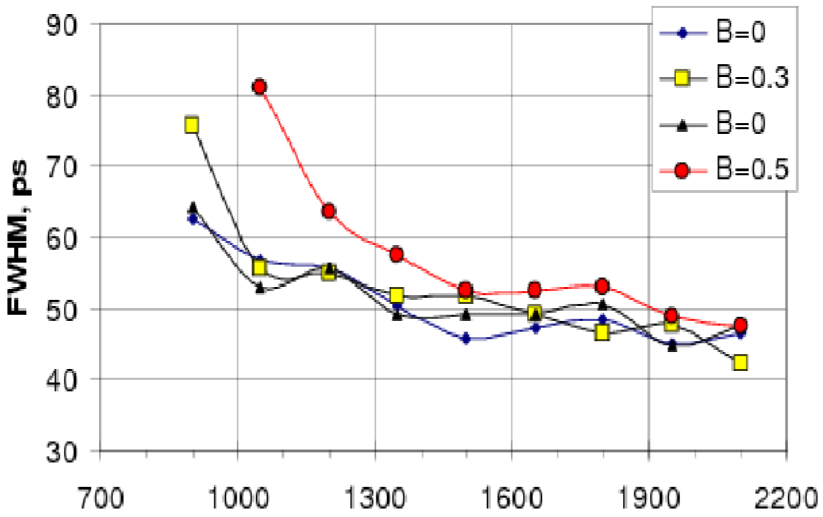

FIGURE 5.1 Dependency of time resolution on HV bias (V) as a function of external magnetic field strength (B = 0.3 and 0.5 T). To demonstrate the consistency of the results two measurements at B = 0 T are shown.

voltage supplied is shown in Fig. 5.2. Since most of the events in $p + p$ and A + A collisions at the LHC will be minimum bias events, it makes sense to operate both types of runs at the same PMT HV. Running at the same voltage is also beneficial for normalisation of the results.

The relative loss of gain of a PMT in a magnetic field is shown in Fig. 5.3. While 1 MIP performance is very important, the most interesting heavy–ion events are expected to produce up to 100 MIP signals. This is the main reason why we need signal processing with a sufficiently wide dynamic range to handle all the cases between 1 and 100 MIP. A PMT produces a maximum signal amplitude of over 5 V [53]. Assuming the linear characteristic of a PMT and taking 5 V for a 100 MIPs signal one obtains the average amplitude of 50 mV for a 1 MIP signal. Due

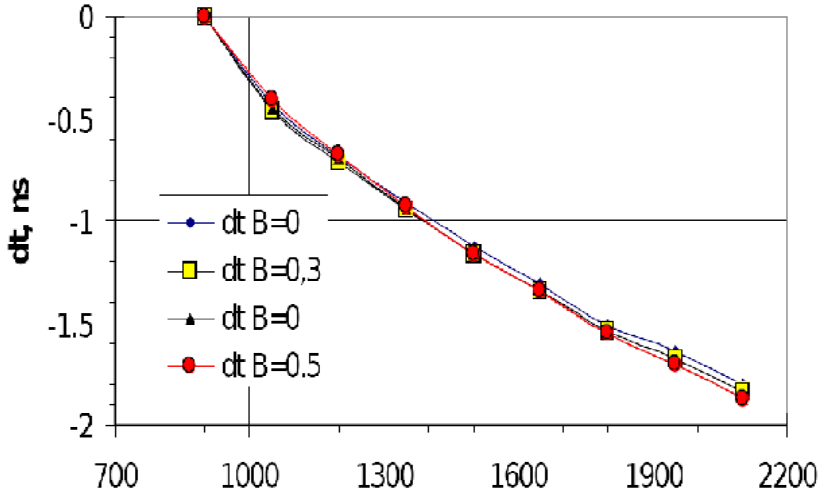

FIGURE 5.2 PMT time performance with magnetic field B = 0.3 and 0.5 T. To demonstrate the consistency of the results two measurements at B = 0 T are shown.

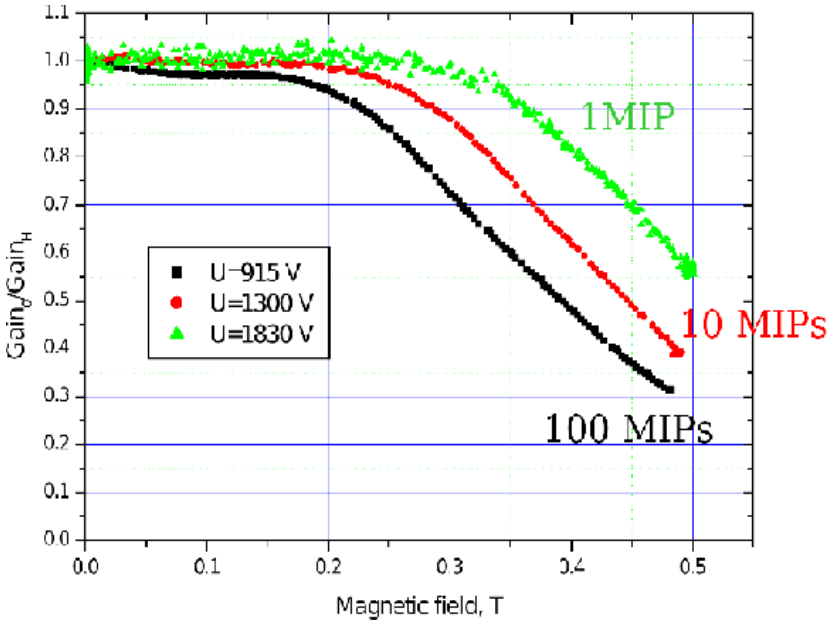

FIGURE 5.3 Relative PMT gain loss in magnetic field. The shown measurements were made at 3 different HV bias values and at 3 amplitude settings corresponding to 1, 10, and 100 MIP.

to statistics the amplitude distribution for a 1 MIP particle is very broad, so to get a reasonable efficiency the electronics threshold has to be set at about 1/3 of the average amplitude, i.e. at about 15 mV. These values (15 mV and 5 V) translate to 1:333 dynamic range. Adding a small safety margin the required dynamic range for pulse processing is therefore 1:500. We have shown that it is possible to cope with such a dynamic range with a single CFD but as a further precaution we also amplify the PMT pulses with two different amplification coefficients (1 and 10).

The next important consequence of the 1–100 MIP range is the need to use relatively low HV bias values (about 1000 V) to avoid the distortion of large pulses and minimise afterpulses. We have tested to ensure that even at such low voltages the time resolution remains quite good at 1 MIP and improves with the increase of the light emitted. Keeping the HV bias low, the pulse saturation up to the 100 MIP level has not been encountered. Furthermore, to guarantee longevity of the PMT the average anode current (not to be confused with the HV divider, whose current is larger by nearly 3 orders of magnitude) should be kept below 1 μA even if short bursts of up to 10 μA are acceptable. We have estimated that this condition is fulfilled with the proposed operation voltage giving 50 mV pulses for 1 MIP. In the calculations the nominal luminosities with occupancies and multiplicities generated by Pythia and Hijing have been used. It is known from the manufacturer that if ageing nevertheless takes place, it would lead to a slow decrease of the gain. This effect is relatively easy to compensate for by increasing the operating voltage. It is also known that after turning the HV off for a longer period the PMT partially recovers; its gain factor slowly improves [54].

We have proven that FEU–187 possesses all in all a very good time resolution, and it remains such in a wide range of supplied voltages and in the presence of magnetic fields envisaged for ALICE.

5.2.2 Tests of LCS

Tests made with the laser and 20 m long multi–mode optical fiber patchcords indicated that the LCS concept sketched in Fig. 4.29 is sound and can be used for T0 calibration. The achieved time resolution for different light outputs is plotted in Fig. 5.4. The Digital Variable Attenuator DA–100–3S–830–9/125–M–3 [34] has been

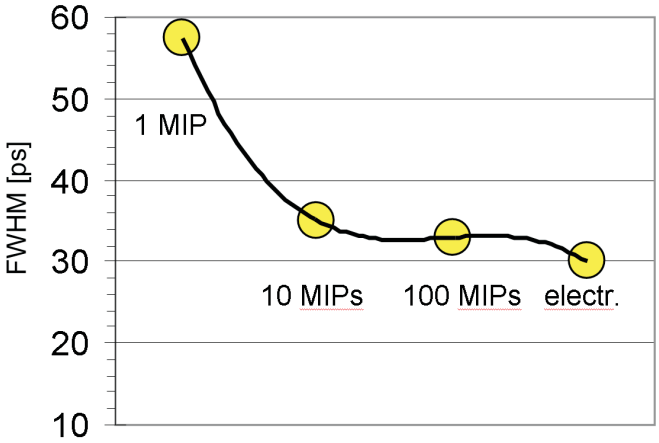

FIGURE 5.4 Time resolution measured with laser amplitudes corresponding to 1, 10 and 100 MIP. The laser pulse was delivered over 20 m of multi–mode optical fibre. The resolution coming from the electronic noise is also plotted.

used in the tests. The attenuated signal has then been split into 24 identical pulses and delivered to 24 PMTs placed about 25 m from the laser.

5.2.3 Radiation hardness tests

The Shoebox preamplifier is placed some 5 m from the IP hence it has to be radiation tolerant. Its performance has been examined during a dedicated radiation test at the RADEF facility [79] at JYFL in August 2005. Fig. 5.5 presents a setup used during the test. The tests proved that the shoebox is radiation hard and can be safely used

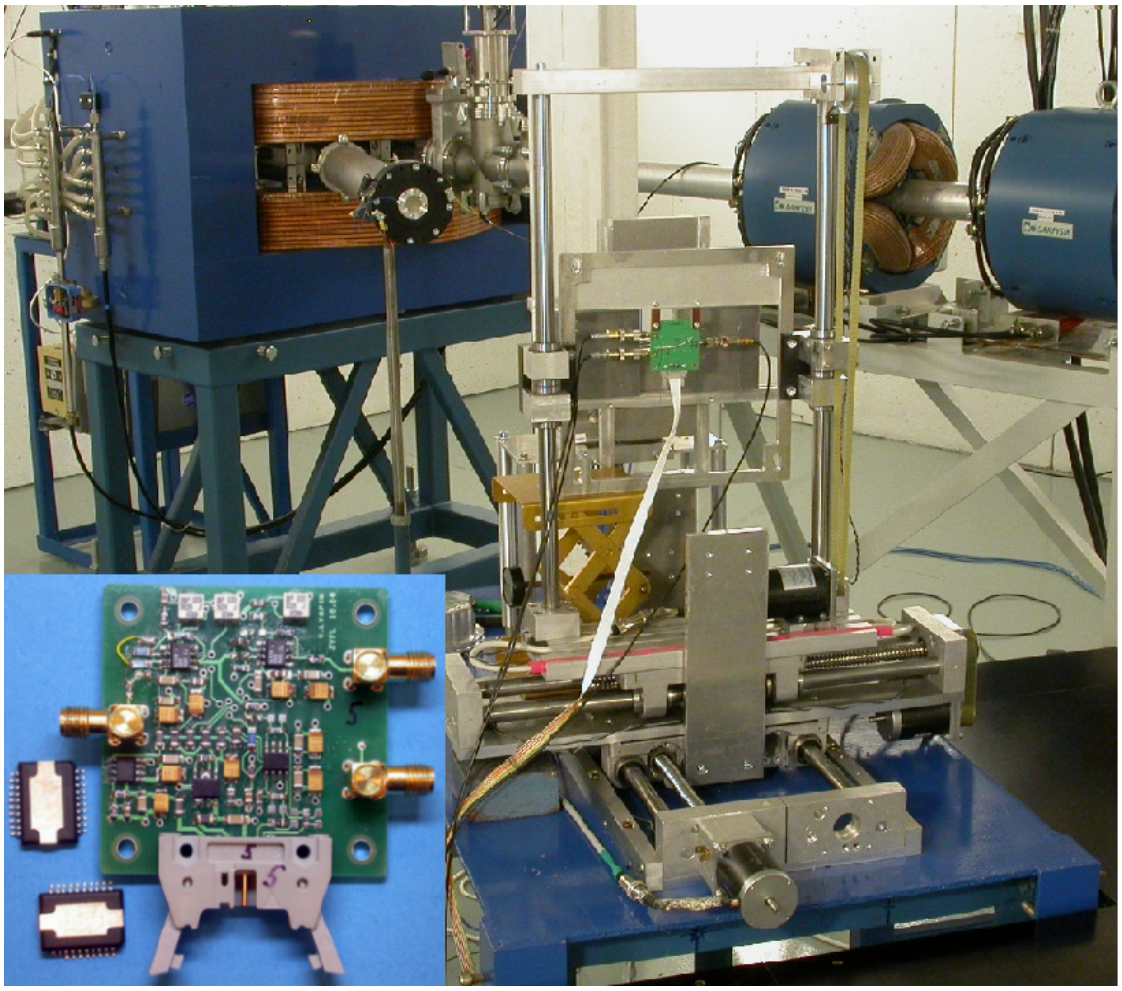

FIGURE 5.5 Shoebox radiation hardness test in Jyväskylä in August 2005. Inset on bottom left magnifies the amplifier.

at the conditions envisaged for ALICE.

The known problem with signals fed to the TRD via the shoebox are afterpulses. This effect was thoroughly studied at JYFL in 2006. Fig. 5.6 presents a comparison of signals coming directly from the PMT and after amplification in the Shoebox. The afterpulses are visible at the right hand side of the spectrum. It has been

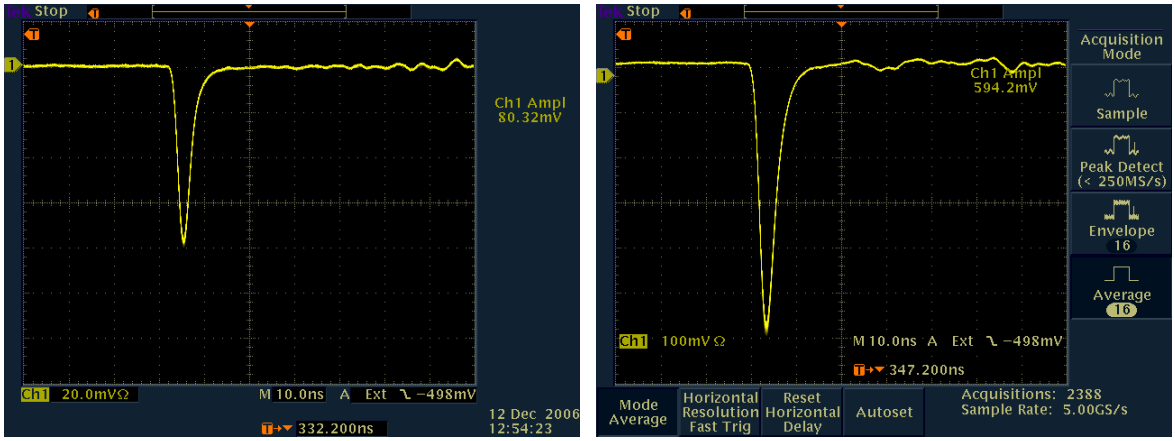

FIGURE 5.6 Signal coming directly from the PMT (left) and amplified in the Shoebox (right).

concluded that using the shoebox studied in 2006[2], afterpulses are minimised, hence their influence on the TRD wake–up is not critical and doesn't require further modifications of the shoebox.

5.3 Tests at CERN

5.3.1 Integration test

The Pre–integration test of the T0 detector was done in 2003 at CERN. Fig. 5.7 presents the prototype of the T0 used in that test. The mounting of the T0–C array

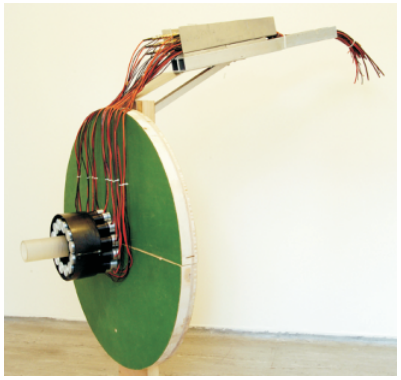

FIGURE 5.7 Prototype of the T0 used for determining the cable length required to reach the patch panel during the Pre–integration test in 2003.

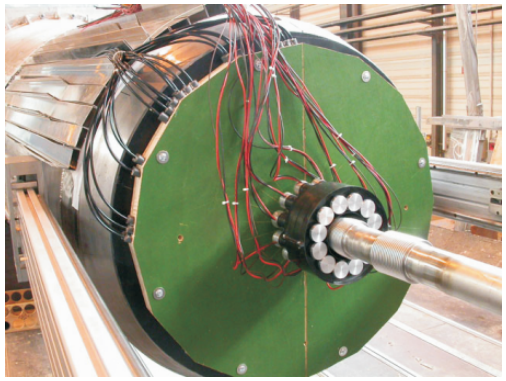

FIGURE 5.8 Prototype of the T0 mounted on a mock–up of a Front absorber (green) during the Integration test in 2003.

on the mock–up of a Front absorber has also been exercised.

[2]The studied shoebox was designed by V. Lyapin [5].

The Integration test has been performed in July 2004. Fig. 5.8 represents the prototype of the T0 mounted on a mock–up of the Front absorber for determining the actual cable length.

5.3.2 Beam tests at CERN PS

T0 detector performance has been tested at CERN PS with a mixted beam of 6 GeV/c negative pions and kaons in July 2003 and in June 2004. The 2003 run concentrated on electronics prototypes. During 2004 session, in–beam tests of the complete T0 system were performed; the second generation of prototypes was tested but the main emphasis was on light collection and the pulse shape obtained by various quartz radiators. A typical PMT configuration during the 2004 experiment is printed in Fig. 5.9.

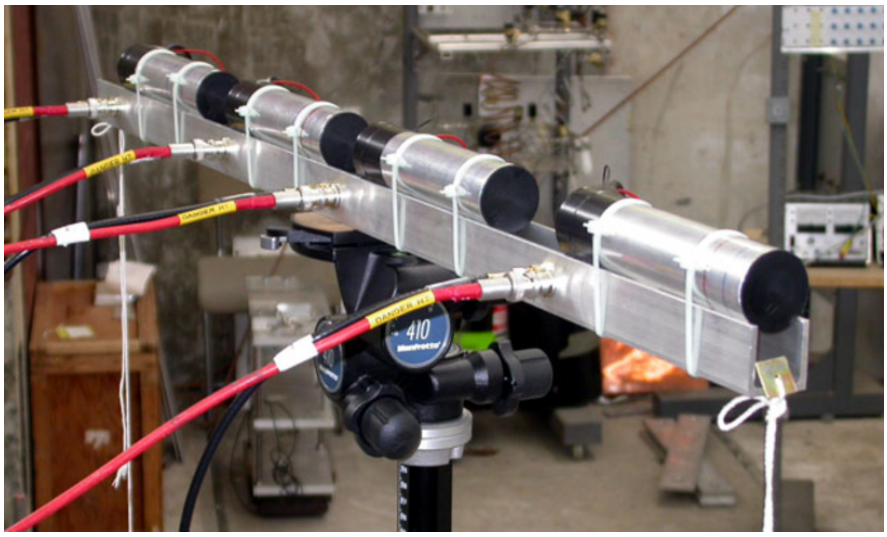

FIGURE 5.9 A typical detector configuration during the 2004 test run at CERN PS. There are four PMT + quartz detector units. Each unit has its own aluminium casting with plastic end cups.

Fig. 5.10 shows measured amplitudes of the PMT output obtained for 3 different radiator sizes. The results of the tests of various radiator diameters are shown in Table 5.3. A great improvement occurs for the smallest, 20 mm, radiator, i.e. when the diameter does not exceed that of the photocathode. In this case all the light produced inside the volume of the radiator is directed to the photocathode. The spectrum shifts up and becomes Gaussian, reflecting the statistical nature of photo conversion. There is a broad and clear area separating the peak from the noise (pedestal) level. With the 20 mm radiator we have reached a time resolution of 28 ps that is the best result achieved for these type of detectors [3]. The only drawback of the smaller radiator is the reduction in the efficiency for $p + p$ collisions, as plotted in Fig. 5.12.

[3]The resolution of ∼20 ps has been obtained in a test that did not include full chain readout as depicted in Fig. 5.11.

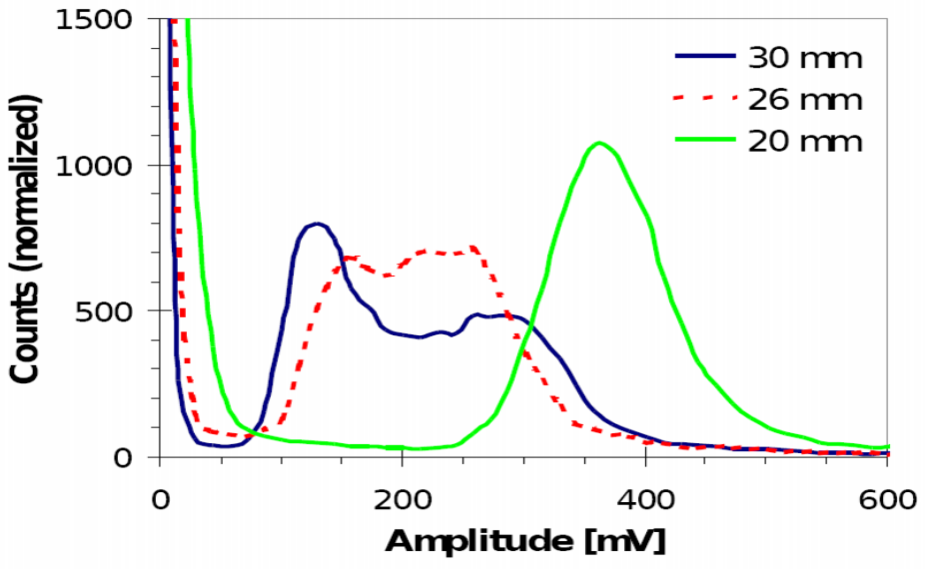

FIGURE 5.10 Dependence of the light output of a PMT on the diameter of the radiator produced with minimum ionising particles. 1 MIP results in about 180 photoelectrons ejected from the cathode of the PMT. For easier comparison the spectra were smoothed and their areas normalised.

TABLE 5.3 Time resolution obtained with various diameters of Cherenkov radiators.

Radiator diameter mm	FWHM TOF ps	σ PMT ps
30	122	37
26	112	34
20	94	28

During the tests the QTC performance was examined. At high multiplicities the final T0 resolution is considerably better than that of a single PMT(see Fig. 5.13). The test has been done with a shoebox that worked very well.

Particle Backsplash

Cherenkov radiation is strictly directional but since the polished walls of the quartz radiator work as a mirror, particles travelling in the "wrong" direction would also produce detectable light pulses. This undesirable effect can be substantially reduced by covering the front surface of the radiator with a light–absorbing layer, for instance by glueing (to get optical contact) black paper on the top [5]. It works well for particles travelling exactly in the opposite direction, but those at intermediate angles will inevitably produce some signals. This may not be a problem for T0–C, despite being just next to the Front absorber, because the absorber was designed to

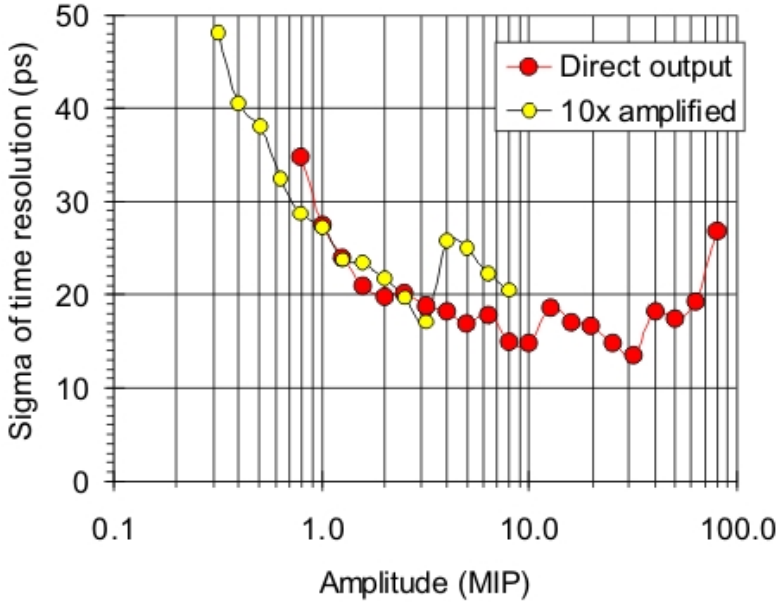

FIGURE 5.11 Single PMT time resolution during the November 2005 test at CERN which was performed without readout.

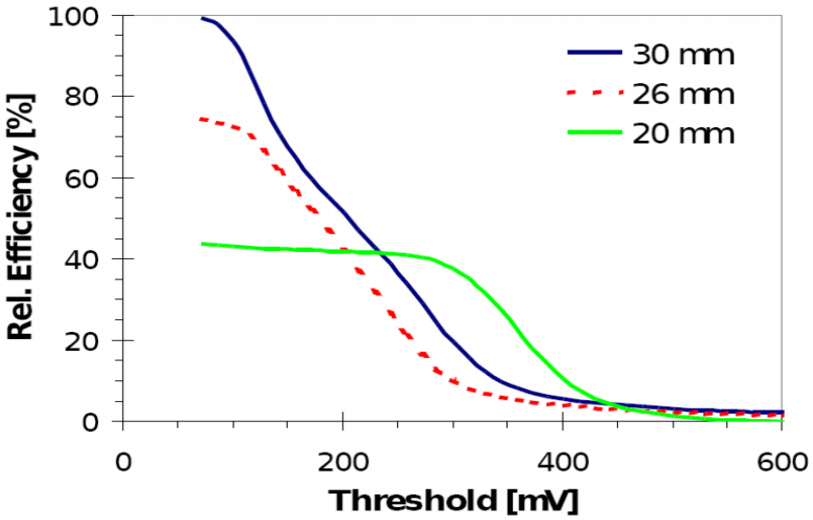

FIGURE 5.12 Efficiency as a function of the threshold calculated using measured amplitude spectra. 100% was assigned to the 30 mm radiator and the maximum values for the 26 and 20 mm diameter radiators were scaled accordingly.

minimise particle backsplash. This, however, is not the case for T0–A placed in the proximity of a vacuum pump, valve and support structure. It was therefore important to know what kind of spectra are to be expected from the "wrong" particles. The largest amplitudes from stray particles (the worst–case scenario) arise when they travel in exactly the opposite direction and the front of the radiator is free from optical contact with a light–absorbing material. The results of the tests with parti-

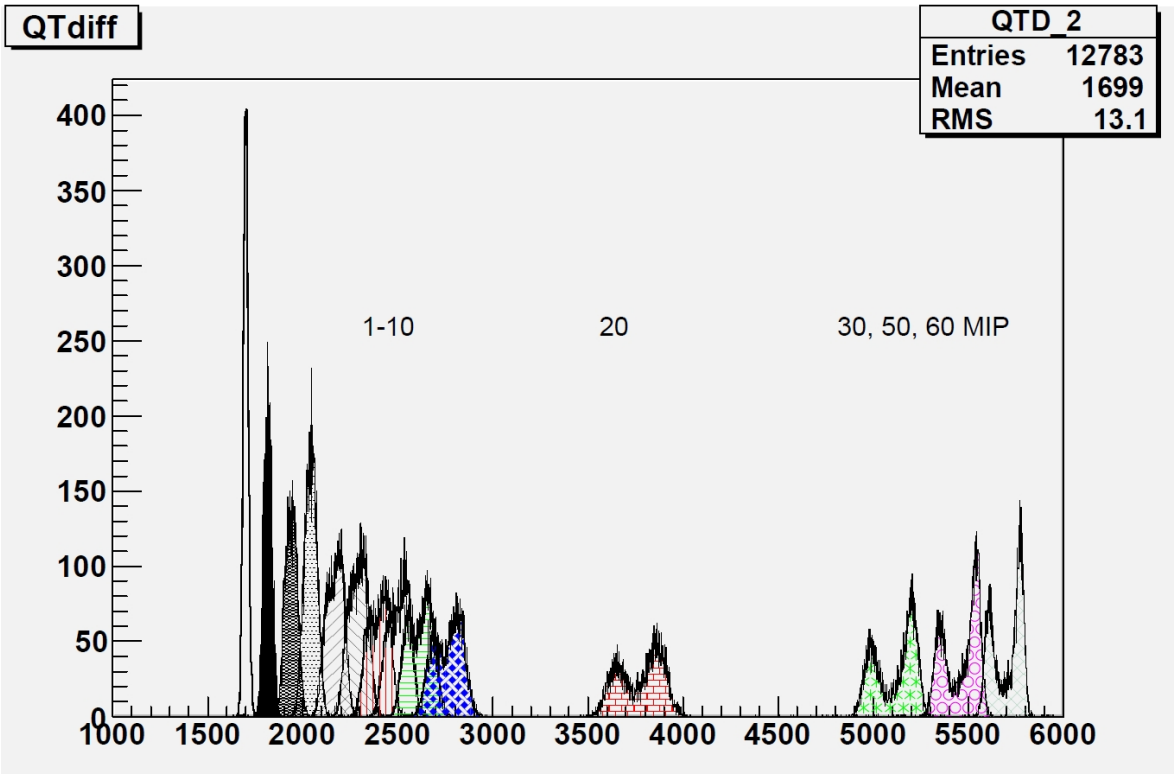

FIGURE 5.13 Amplitude from QTC (QTC 1 - QTC 0) obtained during the October 2006 full chain readout test at CERN.

cles travelling in exactly the opposite direction for a 20 mm radiator are shown in Fig. 5.14. With the 20 mm radiator, even the largest signals from stray particles can be effectively (without the loss of pulses from good events) discriminated against by raising the threshold. For 30 and 26 mm radiators this would not be the case. Following the outcome of the tests, the black paper is glued to the front surface of all 24 radiators in T0 PMTs installed at ALICE Point 2.

Light Transmission measurements

The radiators used in our tests were made at a different time and presumably also from different batches of the quartz material. To check the consistency and quality of production we have made light transmission measurements for each of the tested radiators. The covered wavelength (200–600 nm) matched that of the PMT sensitivity. The results are presented in Fig. 5.15. They show that the overall quality of all quartz radiators, including the 20 mm one, is good. Finally, the radiator of 20 mm in diameter and 20 mm in length was set as a baseline for T0, and all T0 PMTs have radiators of that size.

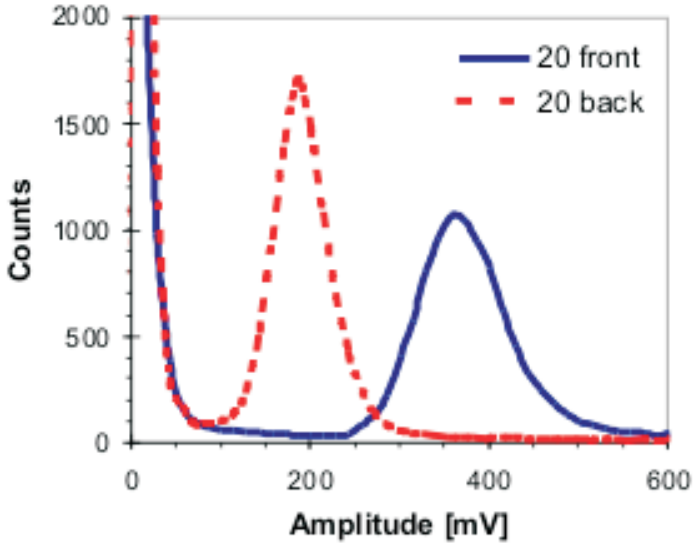

FIGURE 5.14 Response of the T0 module with 20 mm diameter radiator to MIPs entering directly from the front (solid line) and from the opposite direction (dashed line).

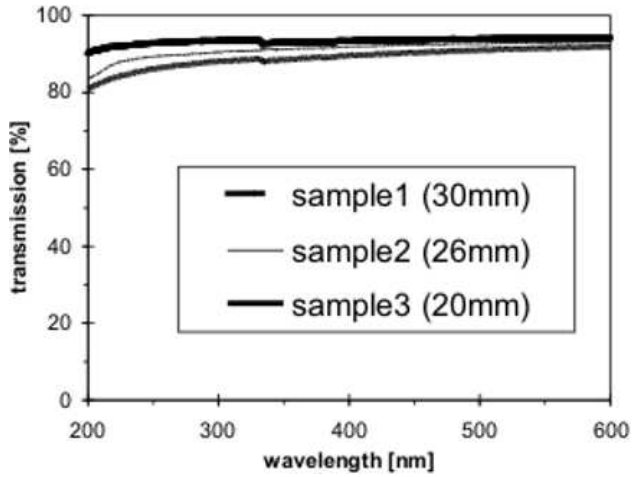

FIGURE 5.15 Light transmission through 3 cm thick samples of quartz radiators as a function of the wavelength.

5.4 Installation of T0–C and T0–A

The T0–C detector was installed in the ALICE cavern in April 2007 in the following sequence. First, the support flange has been mounted on the front surface of the Front absorber. The flange consists of two separate semi–cylinders, the position of each being fixed by a special groove on the movable plate at the Front absorber surface. After installing both flange halves on the plate, the latter was aligned as an entity relative to the beam axis and fixed to the absorber. Secondly, the V0C and T0–C detectors have been installed. After installing and aligning the flange, the V0C

detector was placed around the vacuum duct in the flange's groove and fixed to the absorber. After installing the V0C, the T0–C has been placed at its nominal position. Then, the T0–C cables were distributed and fixed on the inlet surface of the V0C detector. The next step was to distribute and fix the HV, signal cables and the optical fibers, on the inlet surface of the V0 detector in such a manner that they are placed predominantly outside the acceptance of the Muon spectrometer. Finally, the detector was tested and proven to operate well. The signal propagation time in the cables have been measured with an accuracy about 0.5 ns (see Table 5.4). The T0–A

TABLE 5.4 Results of the measurement of signal propagation time in the T0–C signal ($\times$1) and amplified signal ($\times$10) cable. Cables of PMT no.1 were used as a reference.

No.	1	2	3	4	5	6	7	8	9	10	11	12
$\times$ 1 [ns]	0	-0.15	0.2	0.7	1.0	1.5	1.2	0.9	-0.65	-0.6	-0.5	-0.9
$\times$ 10 [ns]	0	-0.15	0.05	0.8	1.15	1.7	1.5	1.1	-0.75	-0.65	-0.6	-0.95

detector was installed in February 2008 as one of the last detectors in ALICE. Its installation sequence was similar to that of T0–C. Fig. 5.16 presents T0–A shortly after installation.

FIGURE 5.16 T0–A shortly after installation at ALICE Point 2.

5.5 LHC test beams

5.5.1 Injection test

The first LHC injection test was performed on 08.08.2008. Two PMTs of T0–C were switched on during the test, but only noise was recorded. However, it has been a valuable exercise. All the T0 components were tested in order to identify vulnerabilities in the system. Just before the injection test the T0 shoebox has been installed at Point 2. The details of the installation procedure can be found in Appendix A.4.

5.5.2 Extraction test

During the T12 transfer line extraction test on 11.-13.08.2009 about 2000 single bunches of $0.4 \cdot 10^{10}$ protons/bunch intensity were dumped at the TED. Another 300 12–bunch trains of intensity up to $140 \cdot 10^{10}$ protons/bunch train were injected during the night from Sunday to Monday. Clear signals in SPD, SDD, V0, T0 and FMD detectors were seen.

T0 was one of the detectors measuring the multiplicity during the test using Scaler. Fig. 5.17 shows the response of the 4 T0 PMTs during one of the runs. During

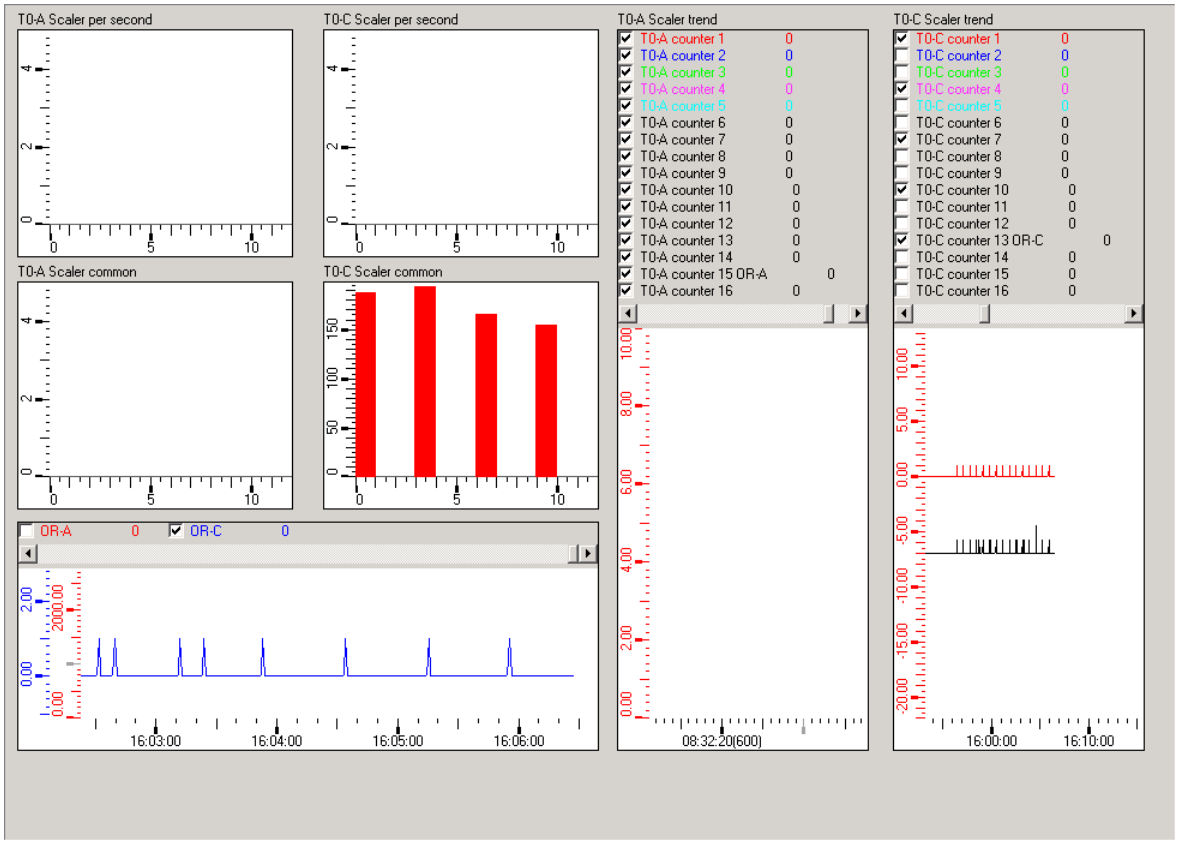

FIGURE 5.17 Four T0 PMTs response recorded by Scalers in run 75552 of the extraction test.

the entire test T0 maintained a single MIP amplitude resolution (see Fig. 5.18).

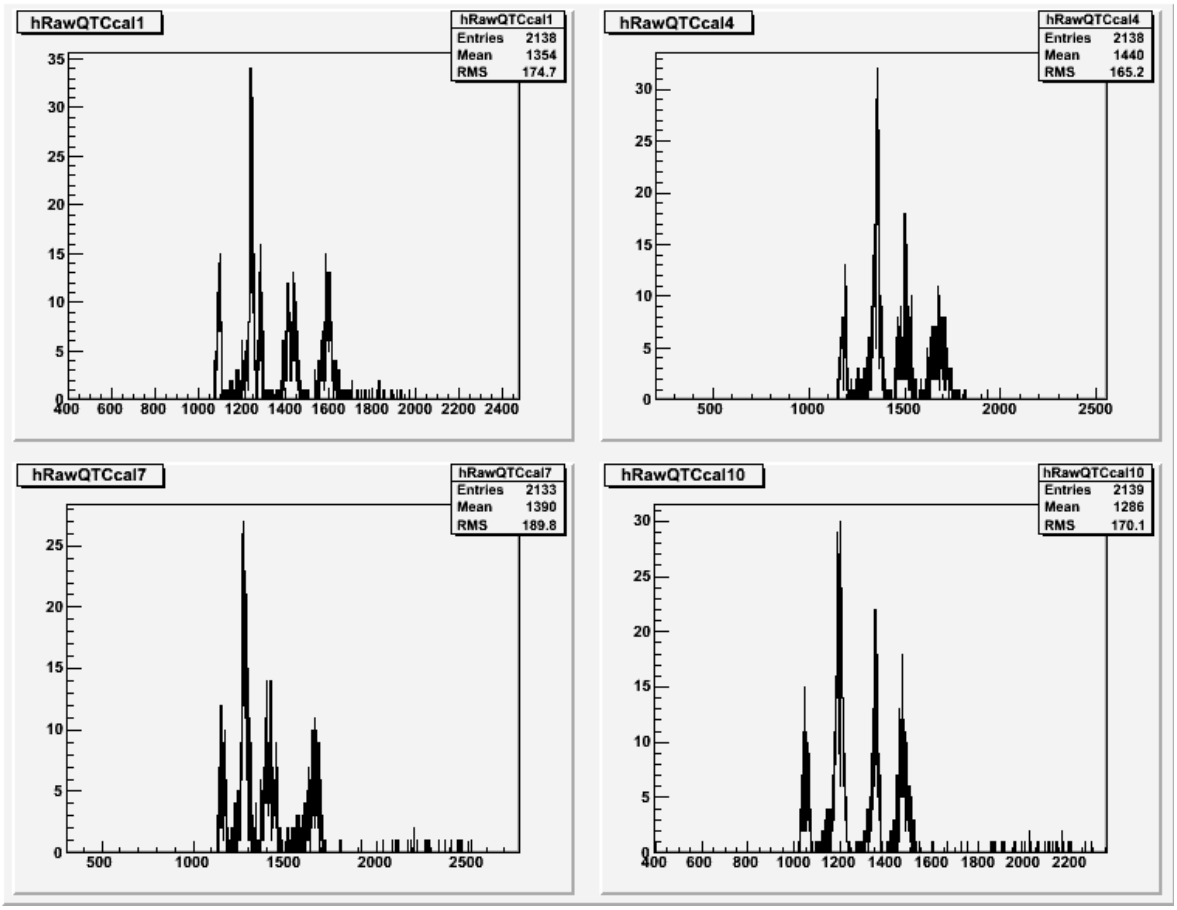

FIGURE 5.18 T0 QTC amplitude spectrum during the calibration (extraction test's run no. 75552).

6 First Physics

Although ALICE is optimised for studying strongly interacting matter in heavy–ions collisions, it also plays a role in $p + p$ collisions. During the starting period of the LHC, as long as the luminosity does not exceed 10^{32} cm^{-2}s^{-1}, ALICE will measure the charged–particle pseudorapidity density, their multiplicity distribution and other observables related to the First Physics. ALICE is able to obtain these results very shortly after starting data–taking. Moreover, $p + p$ data is important for understanding the heavy–ion data[1]. This chapter concentrates on how the T0 detector can contribute to the First Physics programme of ALICE.

6.1 First collisions

The first collisions ALICE sees will be the $p + p$ collisions. At the early commissioning phase after the restart of the LHC the centre–of–mass energy will probably be 900 GeV, that is double the energy of the SPS (no acceleration in the LHC). The beams nominal transverse r.m.s. size of approximately 270 μm and the nominal longitudinal r.m.s. size of the proton bunches of 10.5 cm is expected. One of the first tasks would be to confirm that we indeed see $p + p$ collisions and not e.g. beam–gas interactions and verify the beam quality. It can be inferred, for example, from the vertex distribution of the observed interaction vertices along the beam axis. The simulated distribution in the two pixel layer of the ITS for 900 GeV $p + p$ collisions is presented in Fig. 6.1. Vertex measurement carry also important information for beam diagnostics, e.g. the longitudinal bunch size can be inferred from it. The T0 detector can provide the vertex distribution, with a smaller precision, in real time. Figs. 6.2 and 6.3 present a simulated T0 vertex distribution for $p + p$ collisions at 900 GeV and 10 TeV. 20 000 events is already sufficient to determine the longitudinal vertex position with a precision better than 1 cm with T0 alone. The vertex from T0 is obtained online and the desired statistics, even with the luminosity far from nominal, shall be obtained in less than a second.

The most probable beam structure for the first collisions is two proton bunches per beam with an initial bunch intensity of around 5×10^{10} protons, giving a luminosity ranging from a few times 10^{26} up to 2×10^{27} cm^{-2}s^{-1}. These luminosity values

[1]It is worth noting that $p + p$ measurements at $\sqrt{s}$ of 10 or 14 TeV can not be directly used as a reference for $Pb + Pb$ collisions at $\sqrt{s_{NN}}$ = 5.5 TeV. They are used to interpolate to the heavy–ion data. In the end, $p + p$ measurement at $\sqrt{s}$ = 5.5 TeV is the preferred reference.

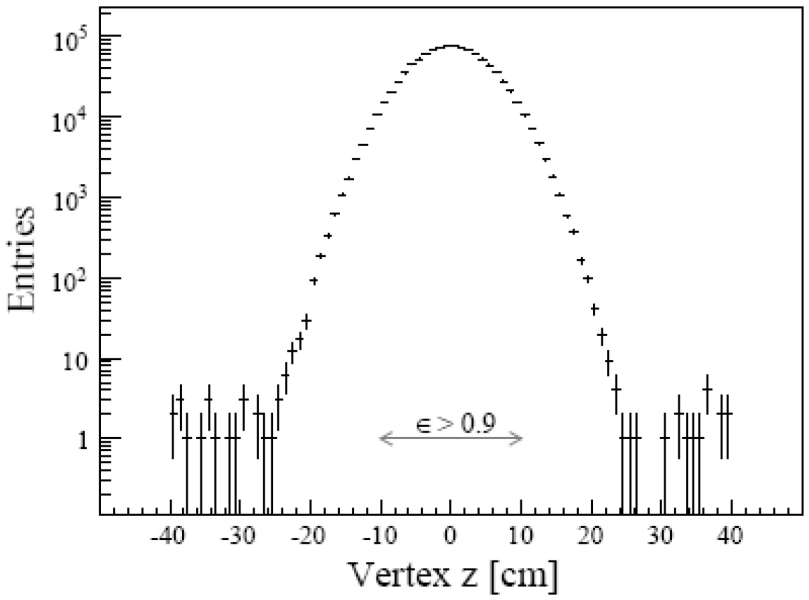

FIGURE 6.1 Longitudinal vertex distribution from hit correlations in the two pixel layers of the ITS [12]. An arrow indicates the collision region of $|z| < 10$ cm, in which the vertex reconstruction efficiency for non–single diffractive collisions is higher than 95%. The simulation has been performed for at $\sqrt{s}$=900 GeV $p+p$ with vertex r.m.s. of 7.4 cm ($\sim$10.5 cm/$\sqrt{2}$).

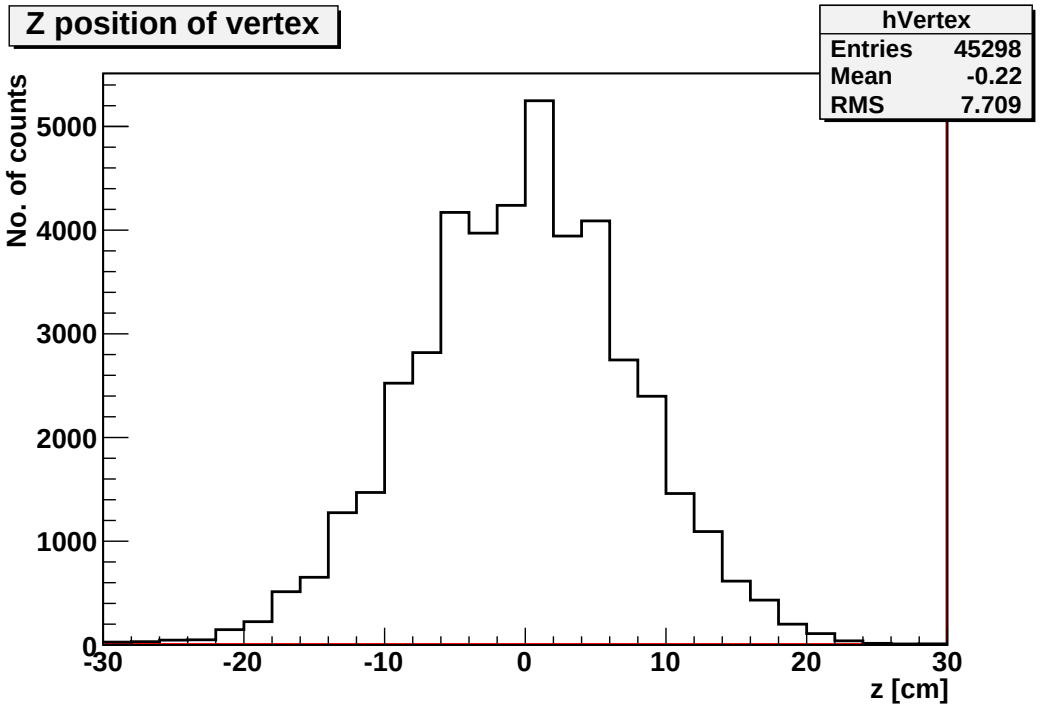

FIGURE 6.2 Simulated longitudinal vertex distributions in T0 detector for 200 000 $p+p$ collisions at $\sqrt{s}$=900 GeV with Phojet.

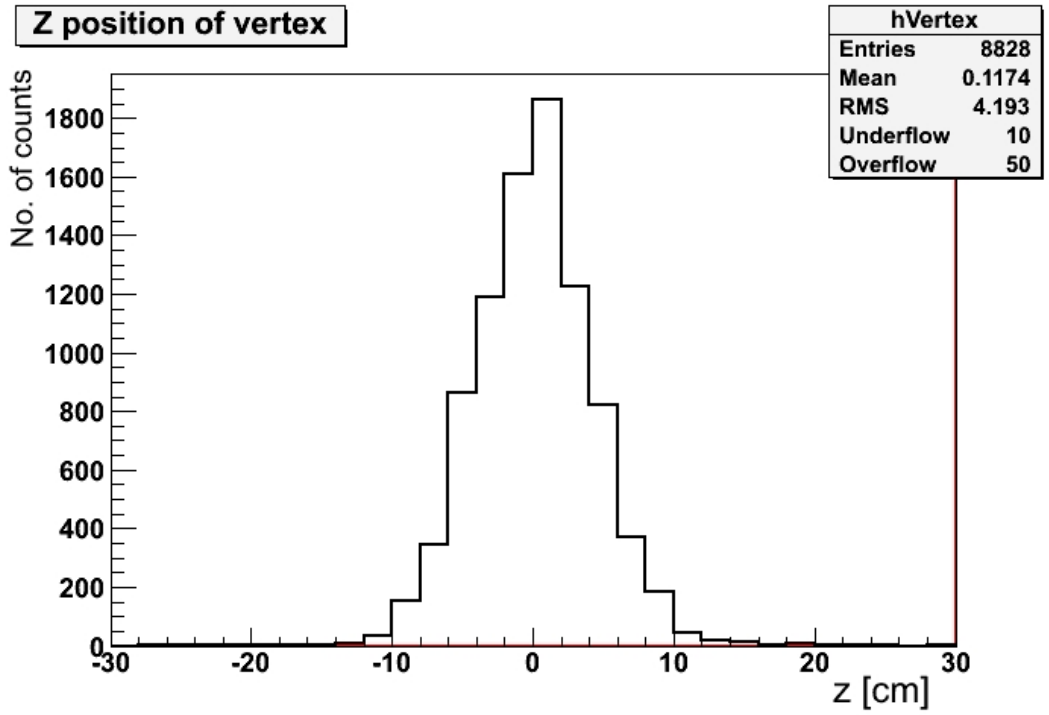

FIGURE 6.3 Simulated longitudinal vertex distributions in the T0 detector for 20 000 $p+p$ collisions at $\sqrt{s}$=10 TeV with Pythia.

correspond to a rate for inelastic $p+p$ collisions from a few tens of Hz up to 85 Hz. For most of the first data–taking period ALICE will be triggered on bunch–crossing signals with a constant rate of 11.245 kHz equal to the LHC orbit frequency [12]. This rate will be reduced to an effective trigger rate of about 100 Hz, imposed by a safe dead–time during detector commissioning. In order to understand and to subtract possible beam–induced background, the detector will also be triggered on bunches coming from either side, but not colliding at the ALICE IP. Assuming an effective running period of about 12 hours in four collider fills, the probability of an inelastic $p+p$ collision per bunch crossing varies from 2–3 $\times$ 10^{-3} up to 7.3 $\times$ 10^{-3} [12].

6.2 Charged particle density

Charged particle density will be one of the first results ALICE obtains from the first collisions at the LHC. In order to facilitate the comparison with published measurements, the results are given for three event classes: all inelastic events (INEL), inelastic non-single-diffractive events (NSD), and inelastic non-diffractive events (ND) (T0 efficiency for these type of events is discussed in Chapter 4.2.5). Multiparticle production at high energies is successfully described by phenomenological models with Pomeron exchange, which dominates at asymptotic energies. These models relate the energy dependence of the total cross–section and of the multiplicity

production using a small number of parameters and are the basis for many Monte Carlo event generators describing soft hadron collisions. The energy dependence of charged–particle density in the central rapidity region described in these models has been discussed in Chapter 2.3.1. According to Eq. 2.17, an increase of charged–particle density by a factor 1.8–1.9 is expected when raising the LHC centre–of–mass energy from 900 GeV to 10–14TeV. The uncertainty of this prediction, due to the current knowledge of the value of the intercept of the Pomeron trajectory, α_p, amounts to about 10%, which is larger than the precision expected in the forthcoming LHC measurements. Thus, the determination of charged–particle densities at LHC energies should further constrain the intercept of the α_p [12].

The T0 and V0 detectors are capable of quickly giving a rough estimate of the event multiplicity in the pseudorapidity regions covered by the two detectors. To show how it can be done, calculations for the response of the T0 and V0 detectors have been performed within the ALICE simulation framework for $p+p$ collisions at 900 GeV, 10 and 14 TeV using Pythia and Phojet event generators, and for $Pb+Pb$ collisions at 5.5 TeV using Hijing. The T0 and V0 multiplicity distributions are shown in Figs. 6.4 and 6.5, respectively, other relevant results are presented in Chapter 4.2. There is a good linearity between the simulated multiplicity and the multiplicity

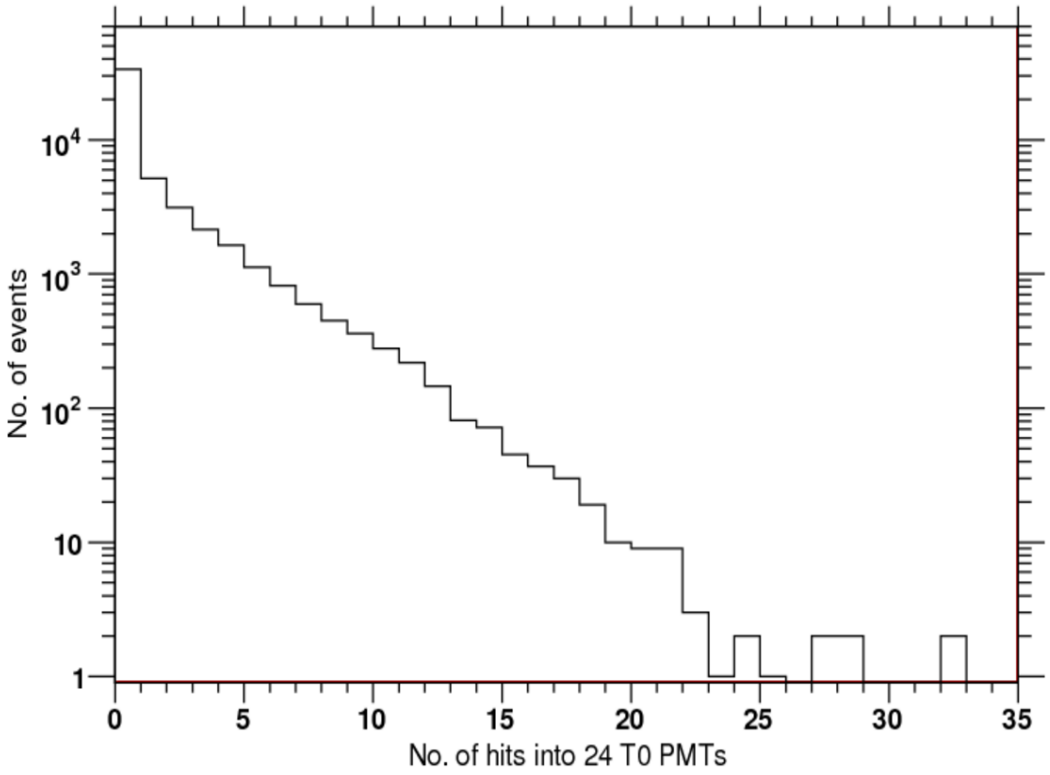

FIGURE 6.4 Average number of hit PMTs vs total number of events at $\sqrt{s}$ = 14 TeV $p+p$ collisions.

reconstructed from V0 and T0, as plotted in Fig. 6.6. At lower multiplicities V0 has

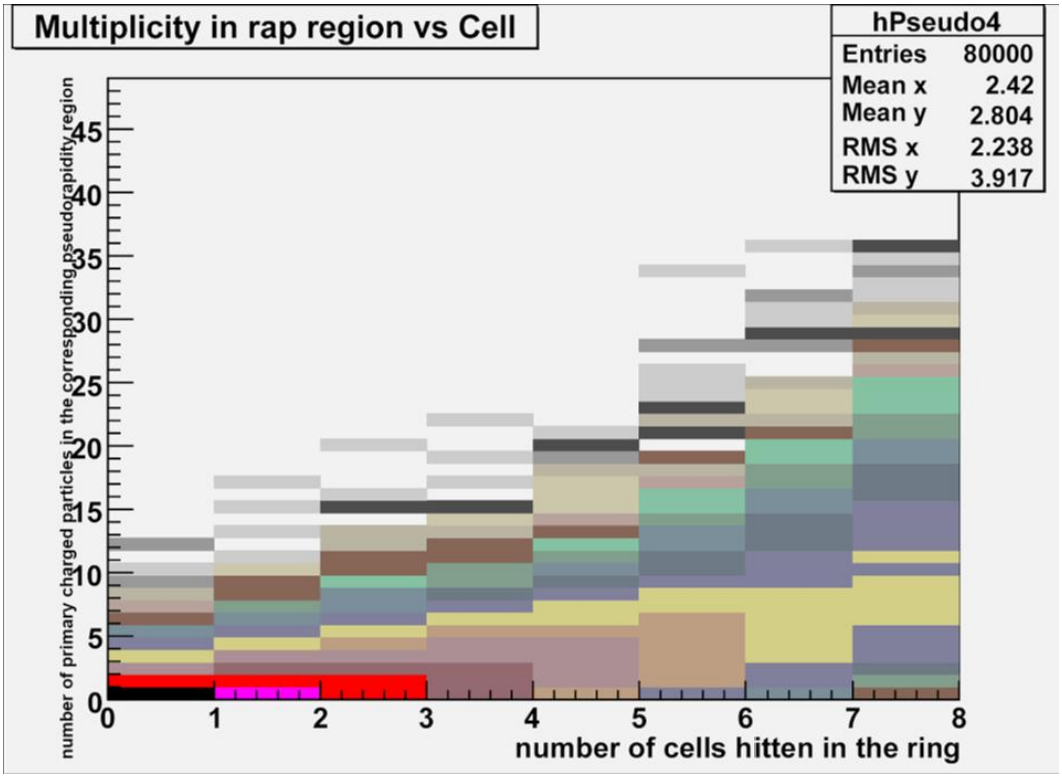

FIGURE 6.5 V0 multiplicity in $\sqrt{s}$ = 14 TeV $p+p$ collisions [58]. Distribution of 80 000 simulated events for ring 4 of V0C (logarithmic scale on z).

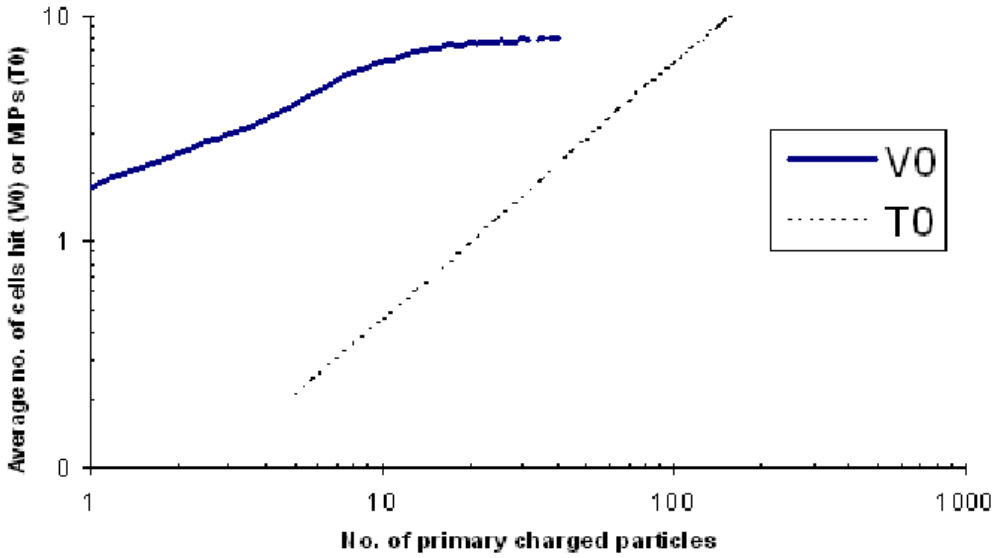

FIGURE 6.6 Average number of hit cells versus number of primary charged particles in V0 (ring 4C) number of particles reconstructed in T0 versus total number of charged particles generated.

a clear advantage because of higher acceptance. But at larger values it shows saturation that is not yet present in T0 data. Saturation occurs when the number of primary charged particles exceeds the number of V0 cells. That is not the case for T0, which has a single MIP amplitude resolution (see Fig. 6.7) in the range from 1 to 100 MIPs, thus there should be no saturation up to 3×24 primary charged particles, conservatively speaking [56].

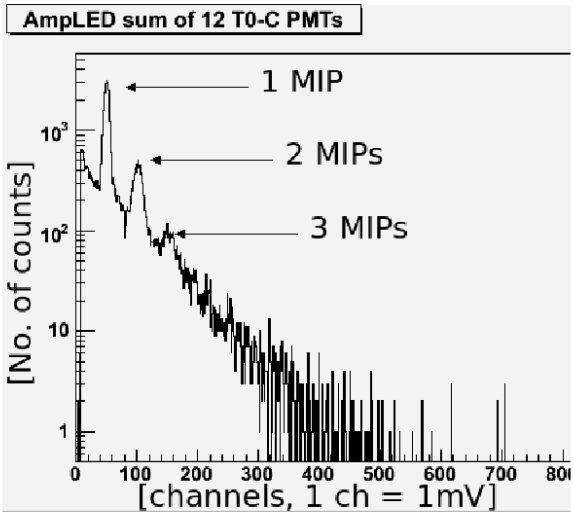

FIGURE 6.7 T0–C amplitude at $\sqrt{s}$ = 14 TeV $p + p$ collisions obtained with Pythia.

V0 and T0 can provide a rough multiplicity value practically just after registering the first collision events. The shape of the multiplicity distribution in the η range from –8 to 8 is well predicted by the theory, thus it will be possible to set the multiplicity scale based on the multiplicity recorded by the T0 and V0 (see Fig. 6.6). With T0 alone, the charged particle multiplicity in the –2.97< $|\eta|$ <–3.28, and +4.61< $|\eta|$ <+4.92 can be estimated.

6.3 Luminosity

Luminosity is the quantity that relates the rate of the process to the cross section. It's concept has been presented in Chapter 2.4. Luminosity measurements in colliding beams experiments are in principle simple but hard to perform. A particle density is low compared to solid matter and collisions are rare. The goal is to achieve a high event rate for the experiments. Luminosity in ALICE is limited by the event pile up during the drift time in the TPC and maximum acceptable illumination in the Muon spectrometer. For $Pb + Pb$ collisions, at a luminosity of 10^{27} cm^{-2}s^{-1} the TPC pile up probability is 76 % assuming a hadronic cross section of 8 barns. The TPC can be operated at luminosities above this value, however the gain in rate has to

be weighted against the loss in tracking performance. For the Muon, the maximum acceptable illumination of the trigger chambers is 30–100 Hz/cm^2 which limits the luminosity to 2 to 4 $\times$ 10^{28} cm^{-2}s^{-1} [21]. For 14 TeV p+p collisions, the corresponding highest luminosity amounts to 3 $\times$ 10^{30} cm^{-2}s^{-1} for the TPC and 5 $\times$ 10^{31} cm^{-2}s^{-1} for the Muon.

6.3.1 Luminosity in $p + p$ runs

The TOTEM experiment [20] will measure the total cross–section, R$_{tot}$. The luminosity in ALICE will be measured and monitored by measuring a fraction of the rate of inelastic interaction: R = Acceptance $\cdot$ R$_{tot}$. R is in reality the sum of the rates of the inelastic non–diffractive R$_{nd}$, the single–diffractive R$_{sd}$, and the double–diffractive R$_{dd}$ processes. The detector acceptance is different for each of these processes, as depicted in Fig. 6.8. Monte Carlo simulations to determine the trigger efficiency can be tuned to the angular track distributions measured by TOTEM.

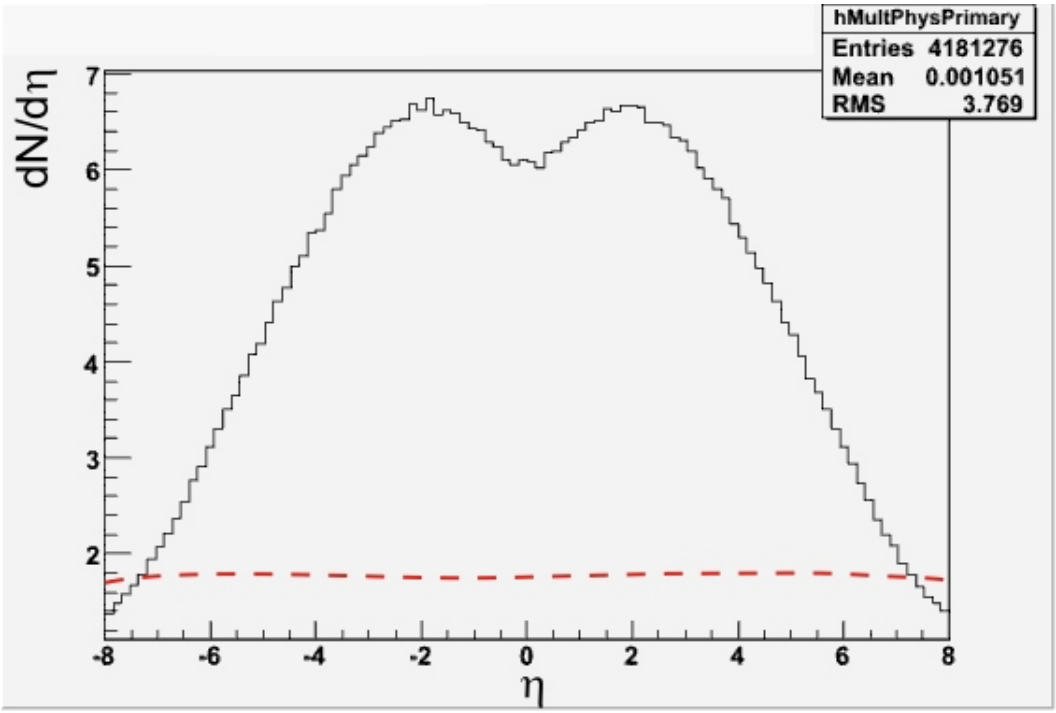

FIGURE 6.8 Charged–particle density for p+p collisions at $\sqrt{s}$ = 14 TeV obtained with Pythia. The solid line represents inelastic non–diffractive interactions. The dashed line representing diffractive interactions is to guide eye only.

In order to calculate the LHC beam luminosity using Eq. 2.21, one has to know the detector's efficiency with as high accuracy as possible. Extensive calculations for the response of the T0 have been performed within the ALICE simulation framework for $p + p$ collisions at 900 GeV, 2.2, 10 and 14 TeV using the Pythia event generator, and for $Pb + Pb$ collisions at 5.5 TeV using Hijing. The T0 efficiency has been

calculated with the exact detector acceptance. The results have been presented and discussed in Chapter 4.2.5. Table 6.1 provides the efficiency for 14 TeV with V0 results included for comparison. The efficiency for minimum bias events has been

TABLE 6.1 T0 and V0 simulated efficiency for $\sqrt{s}$ = 14 TeV $p + p$ collisions.

Mode	A–side	C–side	AND	OR
T0	0.559	0.586	0.390	0.699
V0	0.873	0.866	0.811	0.928

calculated to be about 40% for T0, with a maximum systematic uncertainty of 3%. The inelastic cross–section needed to compute the luminosity will be initially taken from theoretical calculations. Later it will be given with a good precision (∼1%) by TOTEM.

Luminosity with T0

The luminosity based on T0 can be calculated very precisely in the Offline. Since the rough estimation of the luminosity is needed already in the real time (on–line), a good way to approximate it is to use T0 signals from the CAEN V830 scaler, described in Chapter 4.5.1. The T0_TVDC channel of the scaler records the number of collisions and is a key instrument in luminosity calculations with T0. Each time the PMT arrays on both sides of the IP register a valid signal, the T0_TVDC is increased by 1. Table 6.2 presents how the luminosity is computed from T0 scaler counts. In

TABLE 6.2 Luminosity from T0 scaler. Inelastic cross–section has been computed from PDG data [57]. All calculations were made assuming L = 10×10^{27} cm^{-2}s^{-1}.

Quantity / Energy	900 GeV	2.2 TeV	10 TeV	14 TeV
σ_{in} [mb]	55	64	69	73
R [collisions/s]	5 500	6 400	6 900	7 300
T0_OR scaler counting rate[kHz]	4.02	4.67	5.04	5.33
T0_A_OR scaler counting rate[kHz]	3.08	3.58	3.86	4.08
T0_C_OR scaler counting rate[kHz]	3.22	3.75	4.04	4.28
T0_TVDC (AND) scaler counting rate[kHz]	2.28	2.66	2.86	3.03

order to perform calculations of the scaler response one has to assume some values for inelastic cross–sections. Fig. 6.9 presents the total and elastic cross–section from which σ_{in} can be computed. Knowing the cross–section and assuming a luminosity of 10×10^{28} cm^{-2}s^{-1} one can calculate the collision rate. Using efficiency values from Table 6.1 one obtains the number of T0 scaler counts.

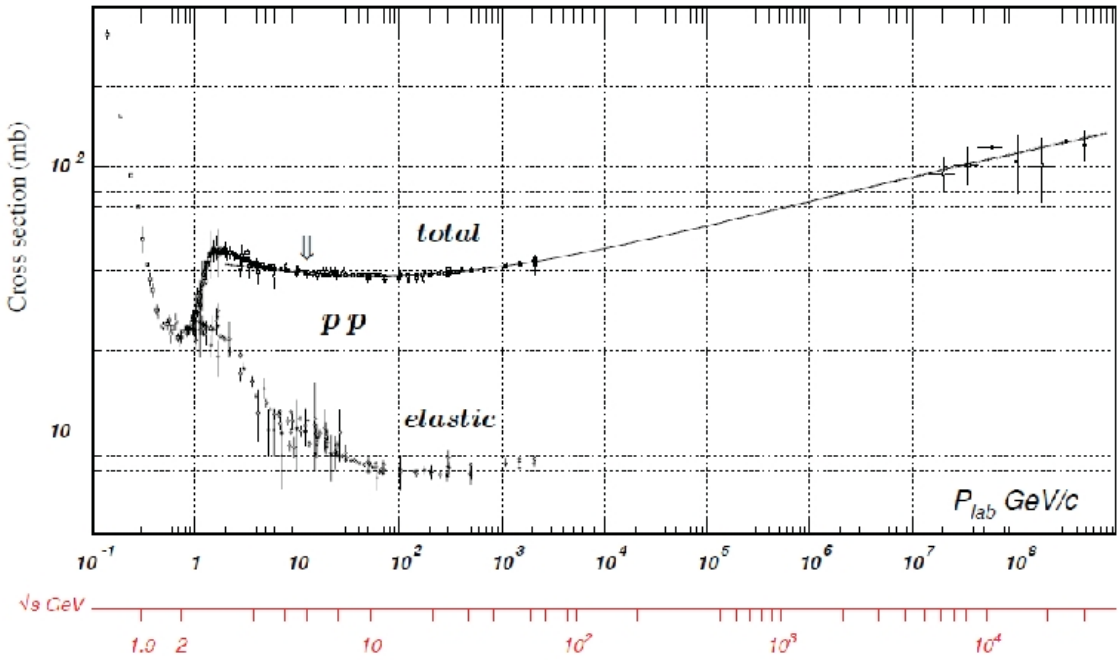

FIGURE 6.9 Total and elastic cross–sections for $p + p$ collisions from PDG data [57]. $\sqrt{s}$ energies are given at the bottom.

Luminosity with V0

The V0 minimum bias efficiency is obtained from simulation by evaluating the fraction of inelastic events detected by the coincidence between V0A and V0C (V0A & V0C) with the requirement of at least one MIP registered in each V0 array. Beam–gas interactions are rejected by an additional selection on the V0A and V0C time of flight difference. This however does not lead to a complete suppression and a low threshold on the multiplicity provided by each V0 array is necessary to improve the beam–gas event rejection capability. The multiplicity resolution of the individual V0 channels is not good enough to allow multiplicity cuts. A low threshold on the number of fired cells is applied in the V0A and V0C, respectively, to reduce a beam–gas background. Fig. 6.10 shows the V0 trigger efficiency distributions for single–diffractive (SD) and non–single–diffractive (NSD) $p + p$ events as a function of a series of cuts on multiplicity set to 1 [58]. There is no efficiency for elastic scattering due to the limited η coverage. If N_{cut} is larger than 1, the efficiency for inelastic events will decrease, consequently increasing the uncertainty on the luminosity value.

6.3.2 Luminosity in $Pb + Pb$ runs

Two interaction cross sections, known with reasonable accuracy, can be used to determine the luminosity in heavy—ion collisions. The total hadronic cross–section

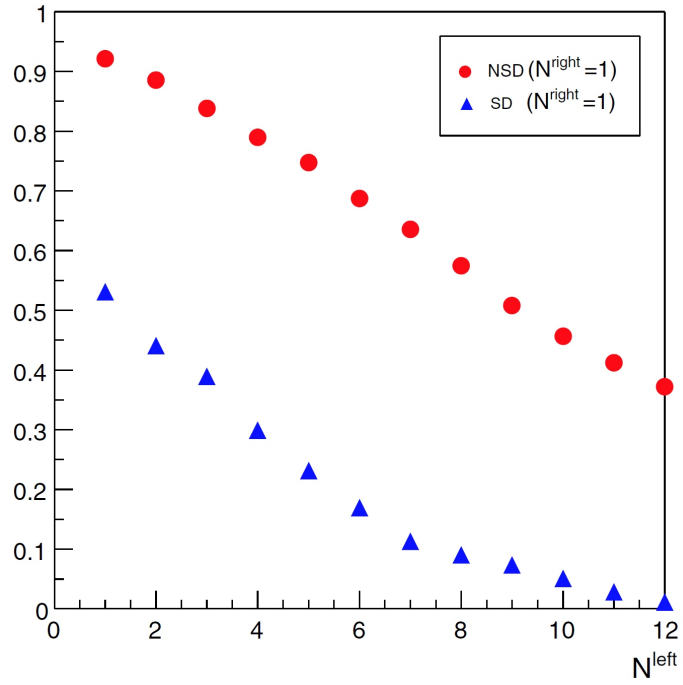

FIGURE 6.10 Contribution of the SD and NSD $p+p$ inelastic events on the V0 triggering efficiency as a function of the minimum number of cells required from the V0A array for the V0A & V0C coincidence. Here, N_{cut} = 1 [58].

σ_{had} is mainly given by the geometry of the colliding nuclei and is known with an accuracy better than 10 %. Hence, measuring the hadronic interaction rate R_{had} allows one to calculate the luminosity, $L = R_{had}/\sigma_{had}$ [4]. With this method, the luminosity in $Pb + Pb$ runs can be measured by the T0 and V0 detectors in a similar manner as for $p + p$ collisions. The measurement is only sensitive up to some maximum impact parameter. There will be thus an additional small systematic error from extrapolating to the total rate.

The second possibility is to measure the rate of electromagnetic dissociation. Assuming that the mutual electromagnetic dissociation cross–section σ_{ed} is known from theory, the rate of mutual electromagnetic dissociation events R_{ed} measured by means of Zero–Degree Calorimeters (ZDCs) allows one to compute the luminosity value: $L = R_{ed}/\sigma_{ed}$. Simultaneous forward–backward single–neutron emission from each of the collision partners provides a clear signal of the mutual dissociation process. For the most part this process proceeds through the absorption of virtual photons, also called equivalent photons, emitted by collision partners which is followed by the excitation and subsequent decay of the Giant Dipole Resonances (GDRs) in both of the colliding nuclei [4]. In heavy nuclei, like Au or Pb, the single–neutron emission channel (1n) is the main mechanism of GDR decay. The same basic idea has been adopted for luminosity measurement and monitoring in the ALICE ZDC.

6.3.3 Uncertainty in luminosity measurements

The main sources of errors in the luminosity measurements are uncertainties in the calculated cross section and in the detector simulations. The value of the former will be given later by TOTEM. The latter is less than 3%: the statistical uncertainty is 0.4% for 10000 events and is reduced with an increase of the simulated events. The systematic uncertainties come mostly from the environment (e.g. the beam pipe and the other detectors) and are of the order of 1%.

As far as the uncertainties of measured numbers of V0 and T0 are concerned, the major factors are stability in detector's acceptance, alignment, stability of the detector (e.g. PMT gain) and calibration. Other possible errors are due to beam spread (in x, y and also in z), and the background: beam gas, pileup, beam halo, etc.

The uncertainty in the luminosity is initially expected to be $\sim$10% and ultimately is expected to go down to 5% with known cross–sections and improved knowledge about the detector parameters.

6.4 Beam diagnostics

A good amplitude resolution allows one to use T0 not only for triggering and as the time reference of the collision but also for rudimentary beam diagnostics. T0 is capable of determining on–line the vertex of the collision, as discussed in Chapter 6.1. Fig. 6.11 presents a simulated T0 vertex distribution for 14 TeV $p + p$ collisions. Ten

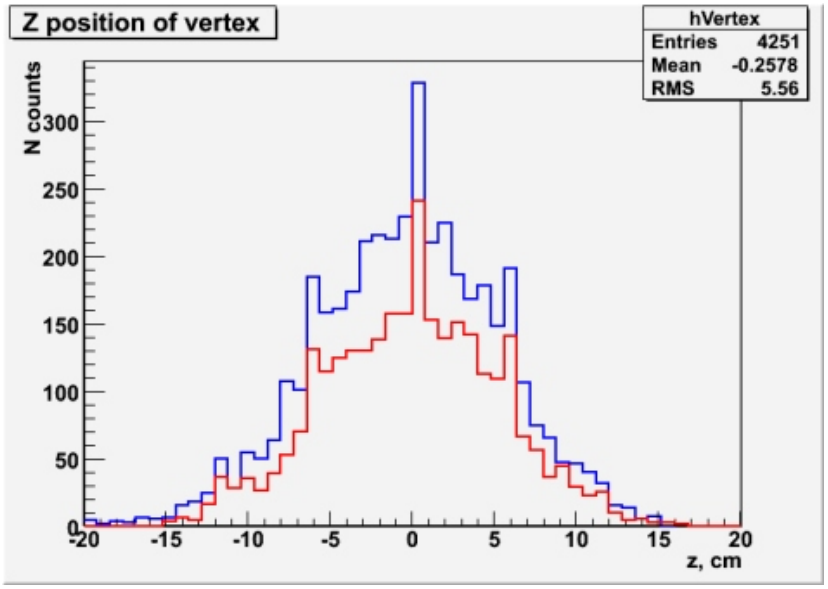

FIGURE 6.11 Simulated vertex distribution in T0 detector for $\sqrt{s}$ = 14 TeV $p + p$ collisions. Red line represents the simulation done with T0, beam pipe and forward detectors included in the geometry, blue line represents the situation where all ALICE detectors were present in the simulation.

of thousends of counts is already enough to determine the vertex with a sufficient precision for beam diagnostics. The integrated PMT count ratio from each T0 array indicates the IP displacement. The displacement can be approximated as:

$$\frac{N_i}{N_{i+6}} = 1 + A \cdot sin(\phi - \phi_0), \tag{6.1}$$

where N_i is the number of counts in the i^{th} PMT, A is the amplitude and ϕ is an azimuthal angle.

When the integrated count ratio of the opposing detector modules is plotted as the function of azimuthal angle, the asymmetry of the simulated beam location becomes clearly visible – see Fig. 6.12.

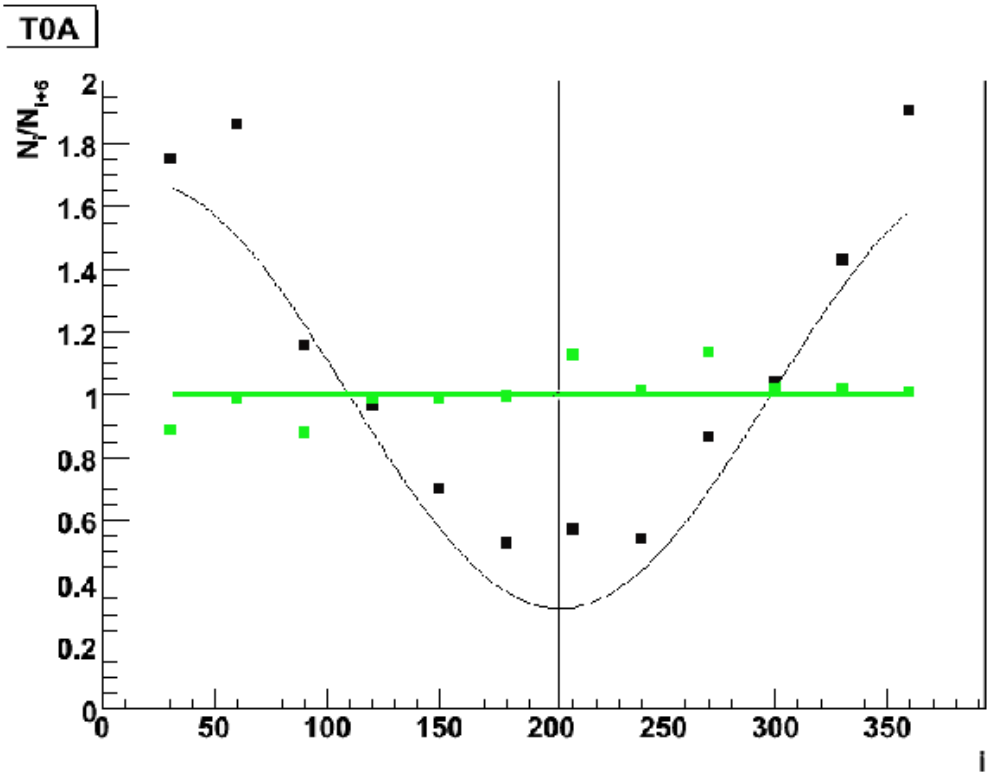

FIGURE 6.12 Integrated count ratio of the opposing T0 modules plotted as the function of azimuthal angle ϕ with 0.5 cm asymmetry of the simulated beam location (vertex). The horizontal line (green) is fitted to the distribution obtained with no shift in vertex while sine–like (black) to the one shifted by 0.5 cm from the ideal vertex.

Fig. 6.13 presents the amplitude dependence of the transverse IP displacement for 900 GeV and 14 TeV $p+p$ collisions simulated with Pythia. Already 50 000 events is sufficient to determine with T0 alone the transverse IP displacement to < 2 mm. The longitudinal vertex position is determined for each event to $\sim$ 1 cm. It is seen that T0 can be used for online determination of the longitudinal and transverse vertex positions with good accuracy [26].

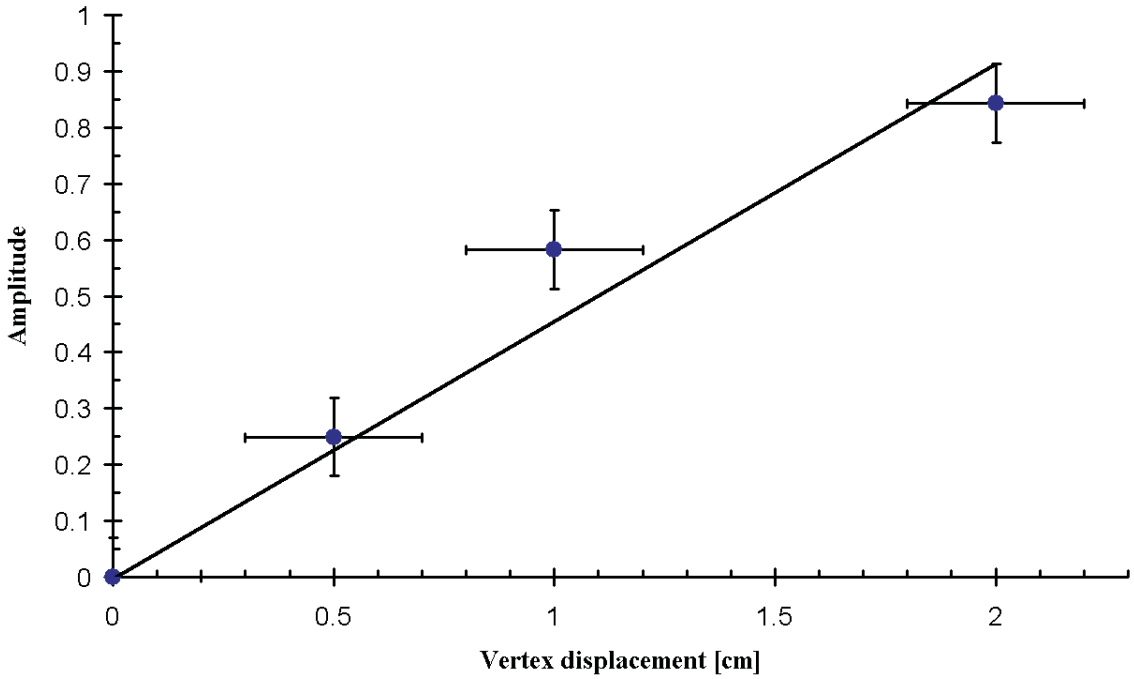

FIGURE 6.13 Transverse displacement of the IP based on the amplitude of integrated count ratio of the opposing T0 modules plotted as the function of azimuthal angle ϕ. Transverse displacements of 0.5 and 1 cm were set as an input for the $p+p$ simulations at $\sqrt{s}$ = 900 GeV, the displacement of 2 cm – at $\sqrt{s}$ = 14 TeV.

7 Conclusions

One of the main tasks of the ALICE experiment is to provide further evidence for the existence and to study the properties of quark–gluon plasma (QGP), expected to emerge in ultra–relativistic heavy–ion collisions. The new state of matter emerging from heavy–ion collisions was studied also at other accelerators, for example at SPS (Super Proton Synchrotron) in collisions of lead nuclei ($\sqrt{s_{NN}}$ = 17.6 GeV), at RHIC (Relativistic Heavy Ion Collider) in collisions of gold nuclei ($\sqrt{s_{NN}}$ = 200 GeV). However at present, experimental signatures of QGP generation cannot serve as definitive criterions of achieving the new state of matter.

ALICE is a unique experiment. Although it is optimised for studying strongly interacting matter in heavy–ions collisions, it also plays a role in proton–proton collisions. The first measurements carried out with the ALICE detector will be focused on the properties of proton–proton collisions at the LHC. The density of charged particles will be determined from the analysis of minimum bias $p+p$ events recorded at first at a centre–of–mass energy $\sqrt{s}$ = 900 GeV and later at the maximum $\sqrt{s}$ available from the machine. In the central pseudorapidity region ($|\eta| < 0.5$), separate distributions of all inelastic, inelastic non-single diffractive interaction and inelastic non–diffractive interactions will be obtained. These results will be compared with previous measurements in proton–antiproton interactions at the same centre–of–mass energy at the CERN SppS collider. The results, together with the forthcoming measurements at higher energies, will be used to determine the energy dependence of the charged–particle density.

T0 is one of the ALICE forward and trigger detectors. With a time resolution better than 50 ps and a dead time less than 25 ns, it is the fastest detector in ALICE. The main functions of T0 are to deliver a collision time reference for the TOF detector, to supply fast timing signals which will be used in the L0 trigger for ALICE and to provide a wake–up call for the TRD. In addition, the T0 detector determines on–line the point of collision with an accuracy of 1.5 cm. After full track reconstruction the location of the IP will be known with a precision of microns, however approximate on–line vertex determination is crucial for choosing the events suitable for ALICE. A substantial improvement in the amplitude resolution has led to one more, extended functionality of the T0: it can contribute to extracting the first physics results and the rudimentary beam diagnostics of the LHC.

The T0 had been extensively examined before installation in the ALICE cavern. The tests included that with a mixed beam of 6 GeV/c negative pions and kaons

from CERN PS when the time resolution of 28 ps r.m.s., a world record at that time, was achieved. The results of the recent simulations of the detector's performance for $p + p$ collisions at $\sqrt{s}$ = 900 GeV – 14 TeV using Pythia and Phojet event generators, and for $\sqrt{s_{NN}}$ = 5.5 TeV $Pb + Pb$ collisions using Hijing generator prove that, despite the small acceptance, the shape of the charged particle density can be estimated based on T0 data alone. It is apparent from the simulations that already the first runs after the restart of the LHC shall provide sufficient data for luminosity and multiplicity determination with T0 as well as for establishing the position of the interaction point along longitudinal and transverse axes. The measurement of the luminosity is important as its precision is the main source of systematic error in the cross–section determination. The expected uncertainty in the luminosity is about 10% for the initial running period of LHC and ultimately, with known cross–sections, this number is expected to reduce to 5%.

The LHC will soon provide the highest energy ever explored with particle accelerators. We did our best to make T0 ready for this exciting time.

Part II

Neutron yield measurements for SPES and SPIRAL 2

8 Introduction

Radioactive Ion Beam (RIB) facilities give the possibility for systematic studies of exotic nuclei[1], production of heavy elements and reactions of astrophysical interest[2] that are not available with other methods. Therefore the next generation RIBs are considered to be one of the most promising future developments of experimental nuclear physics. Nowadays there are several RIB facilities around the world, others are being proposed or already under construction. There are two different methods used in RIBs: in–flight and ISOL, standing for for Isotope Separator on Line.
The in–flight technique uses fragmentation of intense heavy–ion beams, mostly in thin and low Z targets, in which the forward velocity of a primary beam is transferred to the fragments and allows a selection based on the momentum to charge ratio by means of magnetic fields. This provides beams of poor optical quality and weak intensity but already accelerated, without restrictions due to physical and chemical properties of the elements. This method favours very short–lived nuclei. GSI Darmstadt has been the pioneer and leader for the in–flight method in Europe. Examples of in–flight faciliies are e.g. FRS and FAIR at GSI, COMBAS and ACCULINNA at JINR, ETNA at LNS. The in–flight method requires heavy ions of very high energies, e.g. 1 GeV/A at GSI, while 95 MeV/A at GANIL SPIRAL seems to be the lower limit for such a mechanism.
The ISOL method for radioactive beams implies on–line separation of reaction products embedded in a thick target. It provides high intensity and good optical quality beams, but limitations are the available species and significant losses if the half–life is very short. The roots of the ISOL method originate from the mass separation of neutron–rich krypton isotopes obtained via fission of uranium almost six decades ago at the Niels Bohr Institute in Copenhagen [76]. Neutrons, produced by impinging deuterons on an internal target, struck a uranium oxide target mixed with baking powder causing the release of various gaseous elements. This gas was ionised and fed using DC fields to a mass–separator, which selected desired krypton ions. Many other laboratories have made use of this method. The ISOL method exploits intense light–particle primary beams from an accelerator, e.g. 1 GeV protons at ISOLDE, or

[1] Among other possibilities are Coulomb excitation, transfer reactions and γ–ray spectroscopy produced in fusion evaporation reactions to test collective and single–particle aspects of nuclear structure.

[2] Such as synthesis of elements in the r-process, performed at low energy in inverse kinematics, i.e. RIB on a proton target.

neutrons from a reactor, which are impinged on a thick target[3] to obtain exotic nuclei. These nuclei have to diffuse (in target matter) and effuse (in the spaces between matter) into an ion source for ionisation and extraction. Subsequently, a mass separator is used to select specific ions of interest which are then fed into a post–accelerator for reacceleration up to energies comparable with those nowadays available for stable beams. ISOLDE at CERN, IGISOL at JYFL, PARRne at Orsay, ISAC at TRIUMF and HRIBF at Oak Ridge are examples of operating ISOL facilities.

I have focused in my thesis on the two European RIB programmes using the ISOL method: SPES (Study and Production of Exotic Species) [59] and SPIRAL 2 (Production System of Radioactive Ion and Acceleration On–Line) [60]. The conclusions of this work are however relevant to other RIB facilities and to other domains of applied physics. The quest in RIB development is nowadays for considerable improvement in the yields of exotic beams available. SPES and SPIRAL 2 are aiming to reach or exceed 10^{13} fissions of uranium per second, which will lead to high intensity neutron–rich beams in the mass region of 80–160.

Various methods for production of intense radioactive beams have been considered for RIBs. For producing neutron–rich nuclei beams, the so–called neutron converter method has been proposed in order to separate the heat deposited in the target from the production of radioactive elements. It is a two–step method. Firstly, a charged–particle beam is impinged on a thick target, a converter, in order to generate a neutron flux. The produced neutron flux is subsequently used to induce fissions in a target placed in its vicinity. Due to the discrepancy between existing experimental data, there has been a need for a systematic study of neutron yields from possible SPES and SPIRAL 2 converters. To fulfil this need, neutron yields produced by protons and deuterons in carbon, light– and heavy–water targets have been measured at JYFL.

The SPES project at Laboratori Nazionali di Legnaro (LNL) is intended to be the Italian contribution to RIB development [61]. In the original design of SPES, exotic species were obtained via ^{238}U fissions induced by fast neutrons generated with 100 MeV protons hitting a solid converter. The fission products were then extracted from the target owing to high temperature favouring diffusion, desorption and effusion[4]. Later on they are ionised, selected with an on-line mass separator and finally post-accelerated as high quality beams with the ALPI linear accelerator. ^{13}C was one of the possible materials to be used as a converter. Before this thesis its neutron yield has been measured using 30 MeV protons at the Department of Physics, University of Jyväskylä (JYFL) [92] and with 80 MeV protons at KVI [62]. However, after a de-

[3]Thick means that products are stopped in the target. All the same, the beam is often passing through to avoid the lower energy region of the Bragg peak with very high concentration of deposited energy.

[4]Diffusion: out of target matter, desorption: leave the surface, normally not a cause of delay and effusion: travelling between the grains of matter to the exit of the target.

cision of INFN [63] to downgrade the beam energy of SPES, new experiments at lower energies became necessary. Several experiments have been carried out from January 2004 to December 2005 at JYFL in order to determine the yield for ^{13}C(p,n) reaction. We applied two methods to measure the angular and energy distributions of neutrons, produced by 20, 25 and 40 MeV protons in ^{13}C targets: activation and TOF (Time of Flight). In this thesis positive and negative sides of both are discussed. The results of the combined TOF and activation technique provide accurate experimental data and practical guidelines that have been applied for SPES studies and for evaluating the merit of the proposed production method in comparison with other projects of the same generation.

In SPIRAL 2, the French RIB project at Grand Accelerateur National d'Ions Lourds (GANIL), the target under development as neutron converter is a rotating wheel of graphite [64] bombarded by a deuteron beam of 40 MeV. A prototype of such a target has been built and tested at Novossibirsk, Russia [65] and tested under a thermal load of 40 kW. However, the long–term (at least 3 months) reliability of a rotating wheel under the design thermal power of 200 kW and the associated high radiation flux has not been yet demonstrated. Therefore a liquid converter was recently proposed as an alternative. Heavy–water was selected as the liquid, based on the feasibility of such a converter and the assumed higher neutron yield. A facility located at Řež near Prague is actually running a 600 W beam of 37 MeV protons on D_2O as a benchmark for the International Fusion Material Irradiation Facility (IFMIF) [66]. There is also a measurement by Bem *et al.* with d+D_2O at an energy $\leq$ 20 MeV [67]. Theoretical calculations of neutron production by 40 MeV deuterons, i.e. the beam retained for SPIRAL 2, made at GANIL and CEA-Saclay using MCNPx Monte-Carlo codes [68], predict that the neutron yield of a light–water converter should not be much smaller than that of natural carbon, while the yield of a heavy–water converter is expected to be close to factor of 2 higher. In order to validate these calculations, four experiments have been conducted at JYFL from February to September 2008. The first three measured neutron energy and angular distributions, and yields for ^{12}C, H_2O and D_2O. The fourth one compared absolute and relative yields of the three converters.

9 Neutron production, activation and TOF

9.1 Production of neutrons

Since 1932, when Cockroft and Walton developed a 400 keV proton accelerator, stable beams have been used to probe and learn about the properties of atomic nuclei. Modern accelerators can deliver stable beams of charged particles of almost any desired type and with a wide range of possible energies and intensities. To understand better the nature and internal structure of the nucleus and nuclear forces, especially the way they were formed, one needs to explore the outer regions of the chart of nuclei. Next generation Radioactive Ion Beam facilities shall provide physicists with intense beams of exotic nuclei, i.e. far from the valley of beta stability.

The production method of radioactive ion beams in the original design of SPES and SPIRAL 2 is a fission of uranium nuclei induced by neutrons of intermediate energy, i.e. of several tens of MeV. This two stage scheme has been chosen to avoid excessive heating of the target through interactions of charged particles. This method differs from conventional fission of the ^{235}U isotope by thermal neutrons achieved at reactors, as for instance for studies of exotic nuclei at ILL Grenoble, by the fact that it does not need enriched uranium, nor the high flux of neutrons used in a reactor, which both are facing the problem of poor general public acceptance.

The choice of natural uranium instead of uranium enriched in ^{235}U implies an accelerator to produce fast neutrons. The threshold energy for producing neutrons is about 1 MeV, as shown in Fig. 9.1. The cross section reaches 1 barn at 8 MeV and afterwards increases relatively slowly. The projectile energies are thus chosen to generate a neutron spectrum which has a peak above this energy.

Recently the converter method for generating swift neutrons has been particularly popular. A light ion, such as proton or deuteron, is usually used as a projectile, the neutron converter is a heavier element, such as carbon, beryllium or lithium. Be and Li are superior to C in neutron production, but melt at relatively low temperatures, 1287 and 185 °C, respectively. An envisaged heat dissipation in the ^{9}Be converter for SPES is ∼100 kW, which corresponds to the limit for solid targets (non–liquid metals), requiring a specific R&D program for efficient water cooling. A lithium converter needs to be in a liquid phase. Liquid Li technology is not easy [95]. C has an advantage of better resisting the heat, avoiding the toxicity of Be and difficulties with handling of Li. For examining various neutron converters for SPES

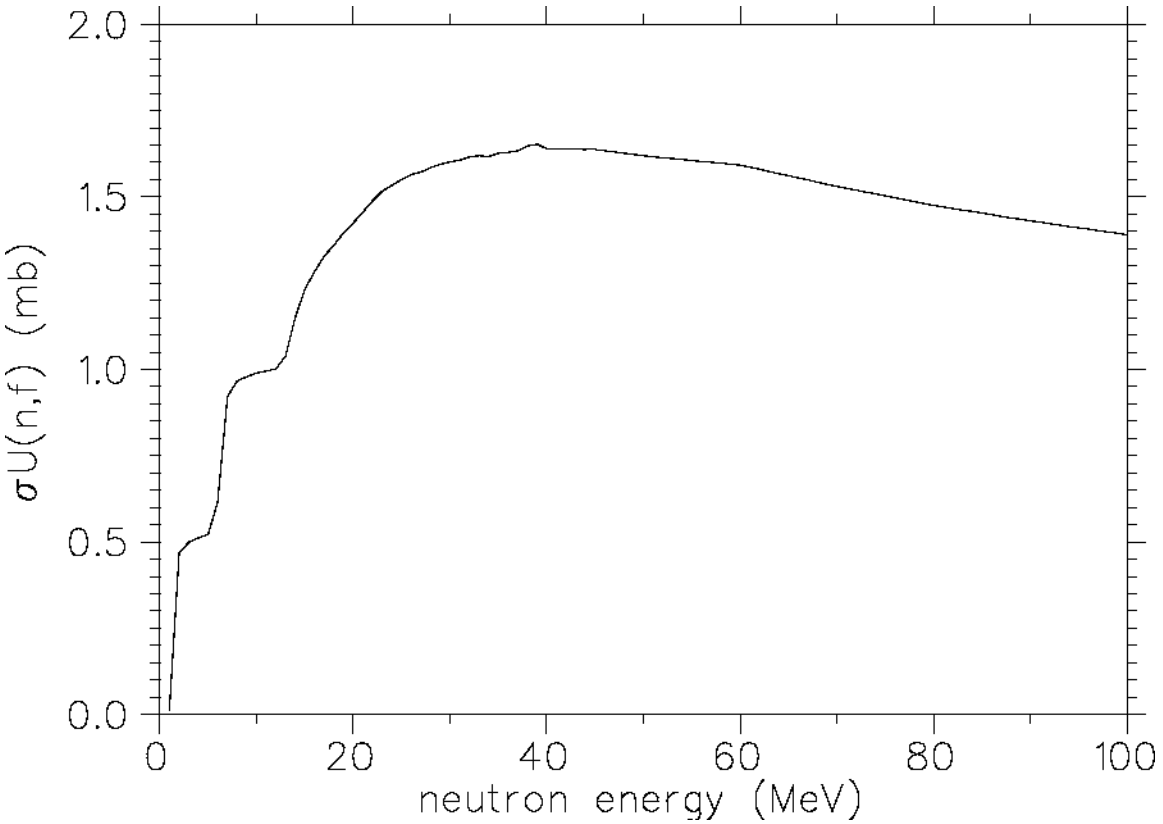

FIGURE 9.1 ^{238}U(n,f) fission cross–section. It is important to note that low energy neutrons (few MeV) are not efficient, unlike in the fission of ^{235}U which occurs with thermal neutrons and is used at nuclear reactors.

and SPIRAL 2, we were primarily interested in neutrons of the energy of 2–40 MeV (lower energy limit being motivated by the cross–sections – see Fig. 9.1). Fig. 9.2 presents a geometry of ^{13}C(p,n)^{13}N reaction used for SPES study. A desired neutron energy determined the energy of the beam impinged on the converter, e.g. 40 MeV incident beam in order to obtain neutrons of energies up to 40 MeV[1].

Neutrons have no charge and thus unlike protons or deuterons do not loose their energy in form of useless for us electromagnetic stopping power. When considering the production of radioactive nuclei that is an advantage: for the same number of nuclear reactions the target is less hot. This in turn prevents melting, which in case of a uranium target containing many long–lived residues of fission is a severe safety concern. The drawback of using neutrons is the conversion factor: neutron yields are in the range of 10^{-4}–10^{-3} per proton or slightly less than 10^{-2} per deuteron for a solid angle of 7% of 4π along the beam direction. It has to be overcome by higher proton/deuteron beam intensity impinged on the neutron converter. Hence, very high currents, e.g. 2 mA p in the original design of SPES [59] or 5 mA of deuterons

[1]The dominant process the beam particles undergo inside the target is the energy loss. Based on that, the thicknesses of the converters target have been calculated with SRIM 2006 [72] to assure that projectiles are fully stopped in it.

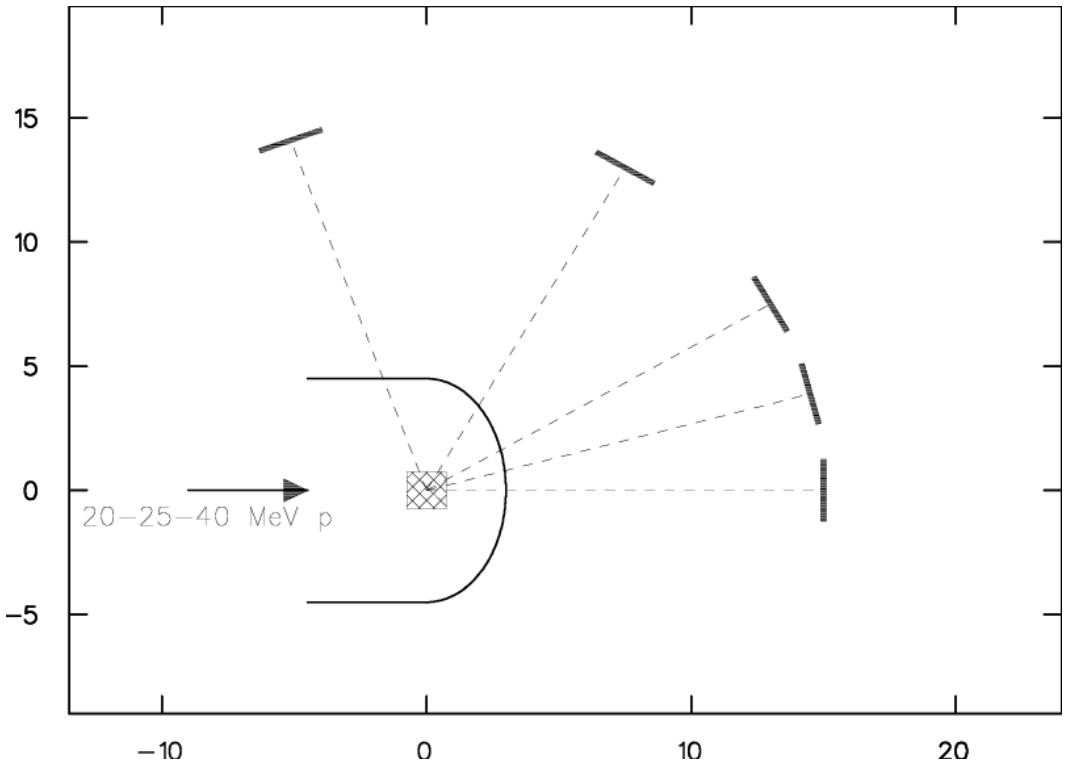

FIGURE 9.2 Geometry of the ^{13}C(p,n)^{13}N reaction setup used in our studies for SPES. Activation foils, marked with thick lines, are used to detect neutrons. Units on both x and y–axes are mm.

for SPIRAL 2 [65] are required in order to reach the goals of about 10^{14} fissions/s. The beam energy is an important parameter too, e.g. a factor of 2 higher energy in the range 40–80 MeV gives approximately 5 times more yield), yet the adopted energies remain considerably lower than those used for fragmentation.

Neutron–induced fission has multiple advantages. The fissioning nucleus is richer in neutrons, likewise the fission products, compared with charged particle induced fission, since they try to keep the N/Z ratio[2]. Moreover, the size of the target and, consequently, the number of reactions per projectile, can be increased since neutrons can penetrate several tens of centimetres[3]. It is however a challenge to efficiently release short–lived nuclei from massive targets. Both SPES and SPIRAL 2 communities collaborate with the group of V. Panteleev at Gatchina to study the properties of UC_x targets (uranium carbide). So far they have tested the release of

[2]It is experimentally shown in [73].

[3]The range of 40 MeV protons in low density uranium (about 2.3 g/cm^3) is about 1 cm (new baseline of SPES with p directly on UC_x). In case of neutron–induced fission (baseline for SPIRAL 2), half of fissions occur in 3.7 cm of high density UC_x ($\sim$11 g/cm^3 of U), which corresponds to about 18 cm of low density U. Neutrons thus allow much more nuclei to be involved in reactions, remembering that the total yield is proportional to number of nuclei $\times$ cross–section $\times$ flux. However, since the cross–section (due to neutron slowing down) and flux decrease deep inside the target, the increase in half–attenuation distance becomes less than 18. It is tentatively estimated to be around 10.

alcalines from targets up to 730 g [70,71].

The costs of building a very powerful accelerator to generate neutrons will be rewarded by potential applications, i.e., a first step towards waste burning or energy generation. Moreover, this option has an advantage in flexibility, as it alternatively can provide very intense stable beams directly for other experiments. The beam quality in a RIB facility can be in principle as high as for stable beams. It requires however an investment in a second accelerator, which is usually an existing machine originally devoted to physics experiments, being already connected to beam lines and equipment. The first built RIB facility, ARENAS at Louvain-la-Neuve, used the Cyclone cyclotron for postacceleration of light neutron–deficient beams. SPES shall use the ALPI linac while SPIRAL 2 – the CIME cyclotron.

Neutrons are of interest to other fields as well, e.g. material behaviour under intense neutron irradiation (IFMIF shall provide data for the design of materials submitted to high neutron flux in next generation reactors or in the ITER fusion reactor), a program called NFS (Neutrons for Science) is planned at SPIRAL 2 [74]). Another important area of research is medicine with irradiation or BNCT (Boron Neutron Capture Therapy) [75]. In the latter the energy is lower than that studied here, nevertheless it is a field of potential application of the method presented here.

9.2 Activation

In the standard activation method a well controlled beam (e.g. thermal neutrons from a reactor) impinges on a sample containing a minute amount of trace elements. If the cross–section is known, the amount of those is quantified without destructing the sample[4]. In our activation method, the neutron angular distributions are measured by placing stacks of metallic foils at various angles with respect to the beam direction. The neutron spectrum n(E,θ), where E is the energy of the neutrons emitted at angle θ with respect to beam direction, is obtained from the gamma spectroscopic analysis of the residual activities induced by neutron reactions in these foils.

The experimental strategy for the activation measurement is as follows: the target, i.e., ^{13}C, ^{12}C, D_2O or H_2O is irradiated typically for 2 to 20 hours with a constant proton or deuteron beam. During the irradiation, foils of Al, Co, Ni, In and Bi [5] are kept at 15 to 25 cm distance from the target at angles ranging from 0 to 110 degrees with respect to the beam direction. The activities, induced by the neutron flux, are counted off–line up to 1 month after irradiation. The production rates are obtained by standard spectroscopic techniques. After normalisation for the number of foil nuclei per unit surface, the solid angle of the foil viewed from the target

[4]This is the way how the archeologist establish via the standard activation technique that a potery found e.g. in Germany has been made in Greece and they conclude about trade in the antique.

[5]The choice of foils to be activated was suggested by neutron production measurements performed by the SPIRAL collaboration for PARRNe [69] and SPIRAL in the 1990s.

and particle beam current, one obtains at each angle a set of experimental values of overlap integrals:

$$< \sigma \cdot n >_k \;\; = \;\; \int \sigma_k(E) \frac{d^2\phi(E,\theta)}{dE\, d\Omega} dE, \tag{9.1}$$

where k is an index for the reaction in the activated foil, $\sigma_k(E)$ is the cross–section for that (n,X) reaction and $d^2\phi(E,\theta)/dE\, d\Omega$ is the double–differential neutron distribution to be determined.

Experimentally the overlap integral is obtained from the peak area of the γ–ray emitted in the decay of the residual activity via the formula:

$$\int \sigma \frac{d^2\phi}{dE_n\, d\Omega} dE_n \;\; = \;\; \int \sigma(E_n) n(E_n,\theta) dE_n \;\; = \;\; \frac{A}{\varepsilon \cdot b \cdot tf \cdot n_f \cdot \Omega \cdot \frac{I_e}{e}}, \tag{9.2}$$

where σ, ϕ, E_n, Ω, A, ε, b, tf, n_f, I_e are, respectively, cross–section, neutron flux, neutron energy, solid angle, γ–peak area, efficiency, branching ratio, explicit time factor that accounts for the history of irradiation and decay during waiting and counting, number of atoms in the activation foil per cm^2, and incident charged particle's beam current.

In the subsequent data analysis, cross–sections are regarded to be free of errors. More details can be found in Chapter 10.1. The different energy dependence of selected σ(n,xn), σ(n,p) and σ(n,α) reactions allows the extraction of n(E,θ) by unfolding, as discussed in Chapter 10.3.

9.3 TOF

Time of Flight is a well established method for neutron energy determination. Our TOF measurements benefit from many years of experience at JYFL. The start signal for Time of Flight is given by JYFL K–130 cyclotron's RF. The stop comes from reconstructing the position and the time of impact of neutrons with Position Sensitive Neutron Detectors (PSND) [88]. PSND are 10 cm by 10 cm by 1.6 m light-tight titanium boxes consisting of 1 m long, 6 cm in diameter quartz tubes filled with NE-213 liquid scintillator, and photomultipliers (PMs). PMs record the light travelling along the bar length. The signals of each PM are sent to a dedicated processor featuring two constant–fraction discriminators and two analogue pulse–shape analysis circuits. Fast time signals allow for reconstructing the position and the time of impinging neutrons. Energy signals are used to separate neutrons and γ–rays. Discrimination is based on the different pulse shapes and, consequently, on the different ratios of the charges collected during a short and a wide time gate.

The position x of an incident neutron interaction along one PSND is obtained from the difference, and time t of the interaction from the sum of the two PMT

signals as:

$$x = c_1 \cdot (t_1 - t_2) + c_2 \tag{9.3}$$

and

$$t = c_3 \cdot (t_1 + t_2) + c_4, \tag{9.4}$$

where c_i are calibration constants.

The off–line analysis of total and fast pulse components is carried out for ten 10 cm long parts of the NE–213 scintillator tube separately, allowing good quality of separation for energies greater than 0.5 MeV (see Fig. 9.3). A time resolution of 0.4

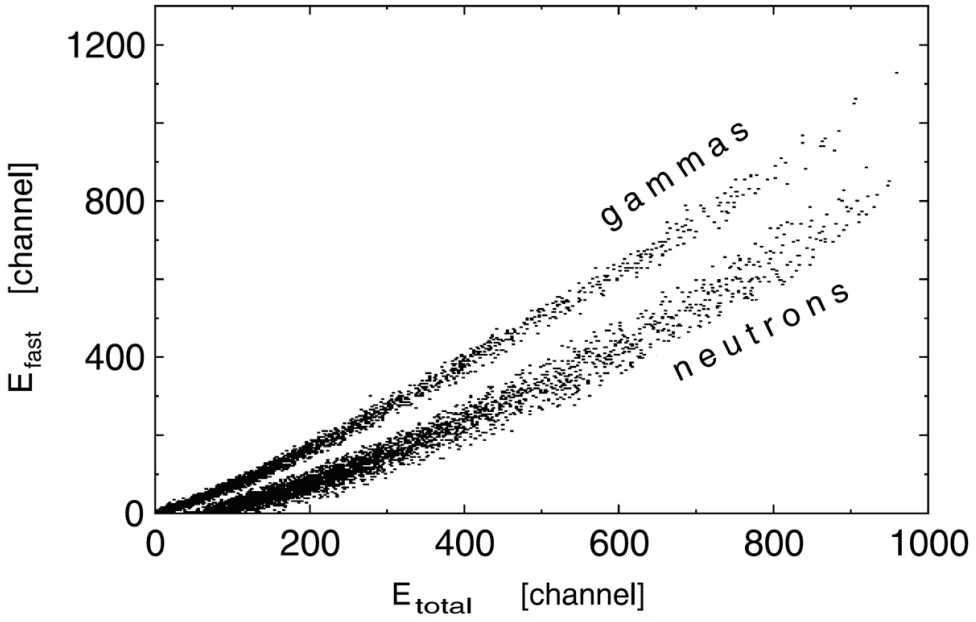

FIGURE 9.3 n-γ separation obtained by pulse shape analysis with PSND [88].

ns has been reached, which results in the position resolution of less than 4 cm.

The efficiency for neutron detection is calculated with a Monte–Carlo simulation code written for this purpose and checked with a ^{252}Cf source. The accuracy is typically about 10% above 10 MeV, but, due to the energy thresholds, the uncertainty reaches 30% at 5 MeV and further increases at lower energies. As a matter of fact, events can be uncompleted, e.g. time signals are available but the energy signals might be missing, so that the event cannot be assigned to a neutron or a γ–ray. A correction is made on the basis of empirical procedures. This correction is larger for low–energy events than for high–energy ones. As shown by the low cross–section displayed in Fig. 9.1, the uncertainty at low energy is fortunately of little consequence for applications to RIB's. However, for other applications, such as

studies of behaviour of materials under irradiation, medical applications i.e. BNCT, the spectrum of low–energy neutrons must be well known.

10 Details of activation method

The particularities of the activation method are described based on p+^{13}C experiments in the framework of SPES. SPIRAL 2 modifications, e.g. reactions of interest for 40 MeV d+^{12}C, D_2O and H_2O, are explicitely discussed in Chapter 15.

10.1 Selection of cross–sections

In order to obtain a set of experimental values of the overlap integrals (Eq. 9.1) the cross–section for a given (n,X) reaction $\sigma_k(E)$ must be known. For our activation experiments the following reactions have been evaluated: ^{27}Al(n,α)^{24}Na, ^{59}Co(n,2n)^{58}Co, ^{59}Co(n,p)^{59}Fe, ^{59}Co(n,α)^{56}Mn, ^{58}Ni(n,2n)^{57}Ni, ^{58}Ni(n,p)^{58}Co, ^{115}In(n,n') and ^{209}Bi(n,4n). Their cross-sections are depicted in Fig. 10.1.

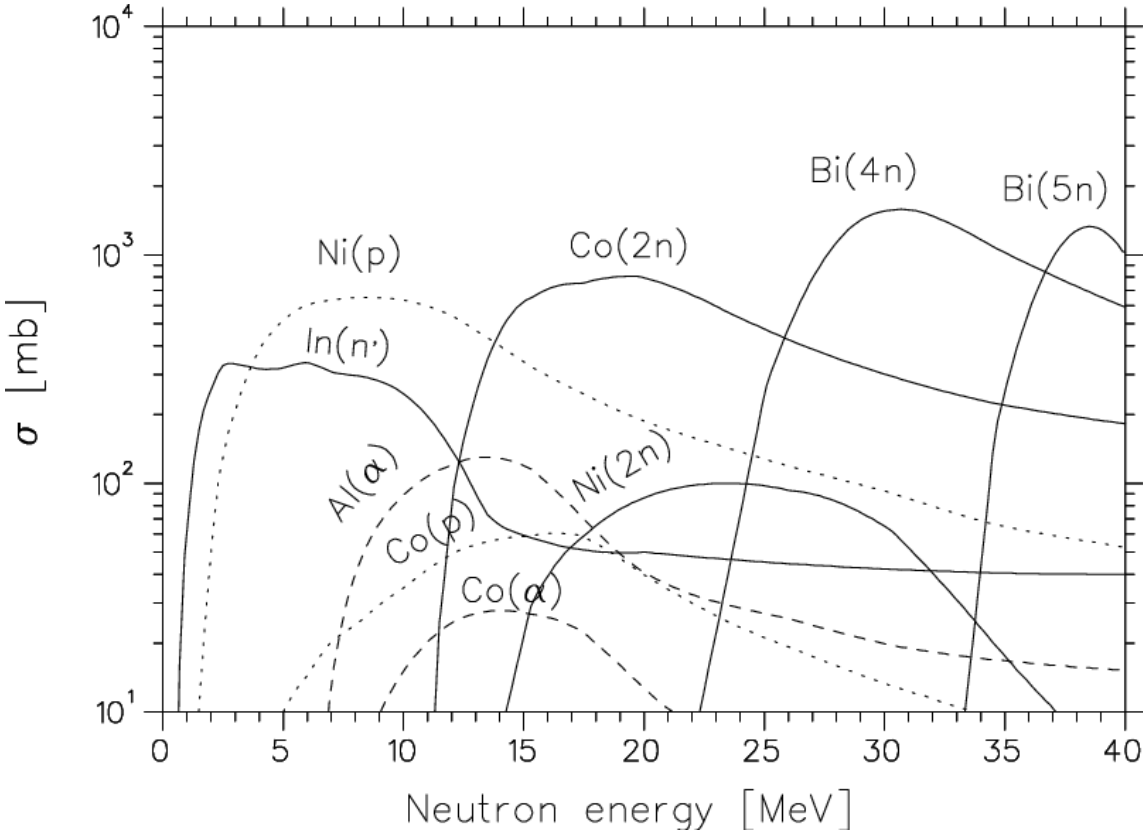

FIGURE 10.1 Cross–sections for various reactions from EXFOR [77].

The production rates inside the Al, Co, In, Ni and Bi foils are proportional to the overlap integrals $\int \sigma(E)n(E,\theta)dE$. The different energy dependences of the various cross–sections allow for the extraction of information on the neutron spectrum shape with energy, in addition to integrated production rate per projectile. For indium there is no evaluated data above 20 MeV and the tail of sigma has been guessed. The curve drawn happens to reproduce the experimental integral at a proton energy of 40 MeV while the spectrum at low energy is only defined by the yield of the ^{58}Ni(n,p) reaction. In principle, cross–sections are regarded to be free of errors with a few percent accuracy.

10.2 Activation spectra

The foil activities at each angle are measured several times after the end of irradiation. Fig. 10.2 presents an evolution of spectrum with angle.

The change in relative abundancies is reflected in the alteration of the shape of the spectrum as the angle increases. The peaks associated with reactions of high energy threshold decrease faster than ones associated with a low threshold reaction. We are witnessing the smaller fraction of high energy neutrons at large angle. The purpose of several counting periods is to check the consistency of data recorded during time intervals of different length and starting with different delays after the irradiation[1]. Typical spectra obtained just after and a few days after the irradiation are depicted in Fig. 10.3.

It makes sense to count long–lived activities for a long time and to allow the short–lived ones to disappear from the spectrum after a delay of several days. The Ge low background setup, in which we measure foil activities, is very useful to avoid a high level of background during long counting periods. The gamma rays used in the analysis are for most decay schemes only a few, since the produced nuclei are close to stability and have low decay energies. The exception is bismuth. The only Bi isotope that could be exploited was ^{206}Bi and at maximum its 8 strongest gamma peaks were integrated. If several lines can be used for a single isotope the weighted average is built.

In principle, our method would have allowed for half–life measurements. Short–lived activities decay out, while long–lived ones become visible above the background level within 28 hours. The errors of computed half–lives would have how-

[1]The strategy of counting each foil several times was motivated by statistics (as long as we obtained enough counts, usually 2–4 hours) and safety (in case of sudden breakdown of Ge detectors at some point of the experiment, we would always have some data for every foil). It is a good way to cross–check the data: after correcting for the different decay factors, counting times and dead time, values must agree within statistical fluctuations. This redundancy allows us to identify a false measurement, for instance in case of occasional malfunctioning of the pulser used for dead time correction, misreading of the start and stop times of counting, putting the stack of foils upside down, etc.

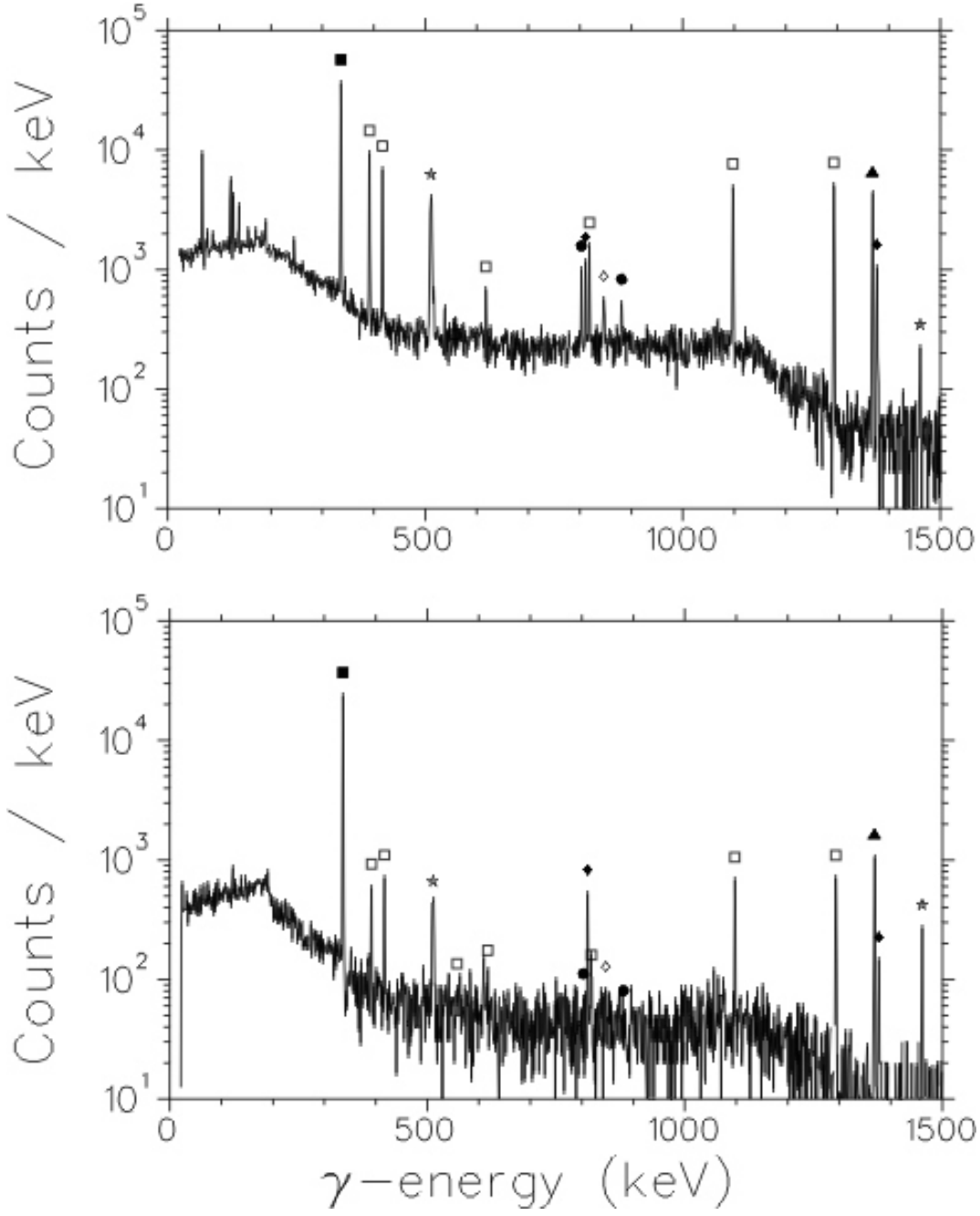

FIGURE 10.2 Al, Ni, In and Bi γ–ray spectrum for activation foils placed at 0°(top) and 60°(bottom) recorded just after the end of irradiation. Filled symbols mark the lines belonging to the decay products of the reactions used for analysis, as listed in Table 10.1. The foils are identified by triangles (Al), diamonds (Ni), squares (In) and circles (Bi). Empty symbols mark background or other lines, among which many are from the decay of ^{116}In induced by low energy neutrons on ^{115}In. 1/10 of the statistics is the lower limit for the cross–section to be usable for deducing the spectrum shape. Thus for σ of 1 mb it would not really be useful to unfold the spectra in the beam and time conditions we had, although we certainly could detect cross–sections of the order of 0.1 mb.

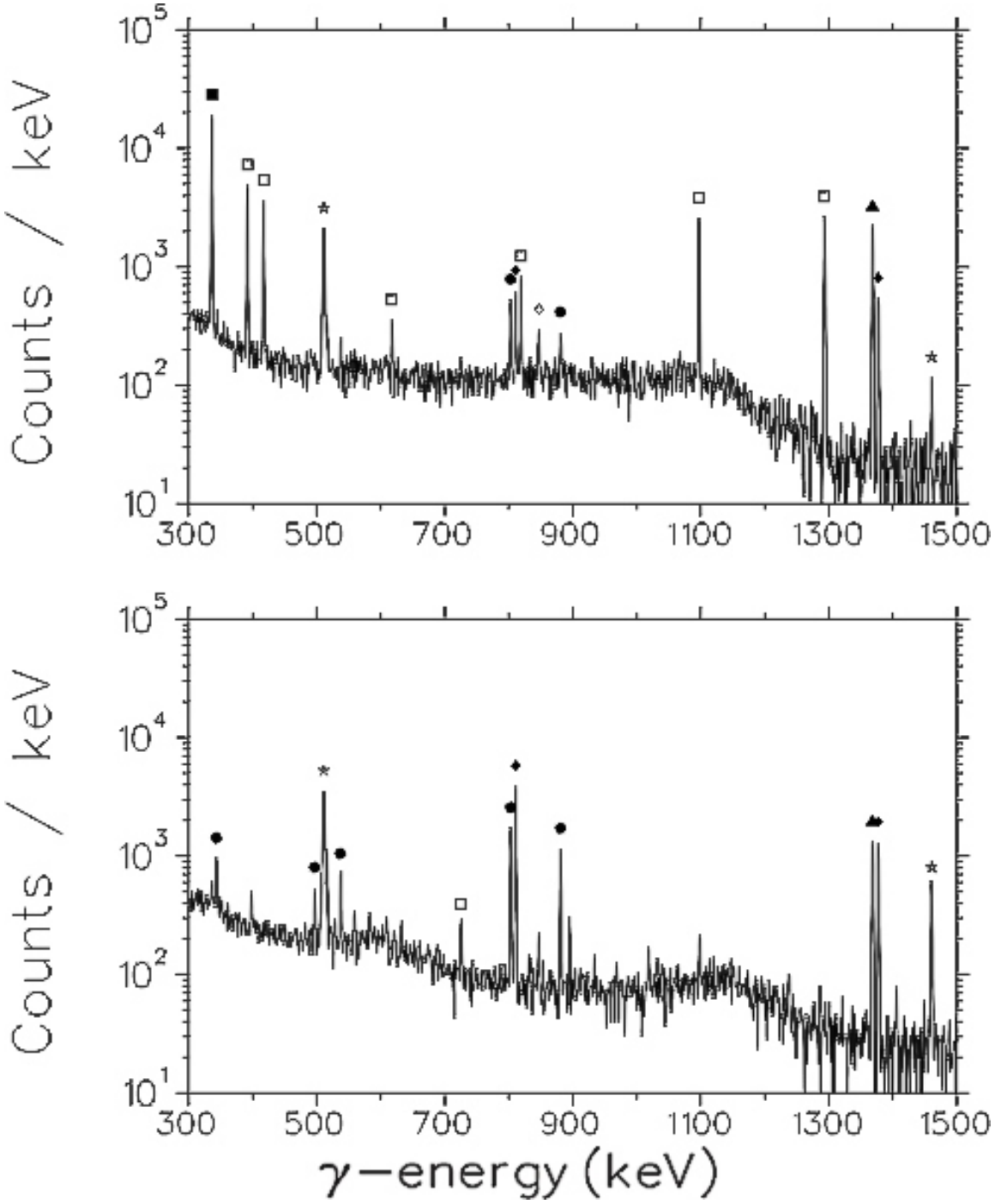

FIGURE 10.3 Examples of γ-ray spectra spectra recorded few hours (top), and two days after after the end of irradiation (bottom) for a stack activation foils. The foils, placed at 10 degrees with respect to beam direction, were submitted to neutron flux for 4 hours. Meaning of the symbols is the same as in Fig. 10.3.

ever been much larger than those reported in the literature. This is due to the non–optimised conditions and rather low counting statistics for such a purpose. Decay half–lives are thus taken from literature and kept fixed. In our procedure to convert

peak areas into overlap integrals of cross section and neutron flux, they play a role in 2 factors, the one for history of irradiation and the other of decay and counting.

10.3 Extraction of neutron spectrum

Experimentally the observable is the number of counts $A(E_\gamma)$ in a γ-ray peak, counted for a time interval $(t, t + \Delta t)$. It is expressed as follows:

$$A(E_\gamma) \;=\; (1 - e^{-\lambda t_i})\, e^{-\lambda t}\, \frac{1 - e^{-\lambda \Delta t}}{\lambda}\; F_{DT}\; b(E_\gamma)\; \varepsilon(E_\gamma)\; \bar{i}\; \chi \tag{10.1}$$

Here, λ is a decay constant, F_{DT} is a factor correcting for the dead time, i.e. fraction of active time to counting time, $b(E_\gamma)$ is the decay branching of the transition observed with efficiency $\varepsilon(E_\gamma)$, $\bar{i}$ is an effective average current and χ is the probability to produce a nucleus of interest per incident projectile (p or d). The decay branching is the ratio of the probability of decay by the mode of interest to the sum of probabilities of all possible modes. Table 10.1 presents the branching ratios considered in a 40 MeV measurement. $\bar{i}$ accounts for instability of beam by a renormalisation of the true average current.

TABLE 10.1 Reactions and their branching ratios. In addition, the last column shows the energy at which the cross-section for a given reaction is maximal.

Reaction	Product	$T_{\frac{1}{2}}$ [h]	E_γ [keV]	b_γ [%]	σ_{MAX} at [MeV]
$^{115}In(n,n')$	$^{115}In^m$	4.486	336.2	45.9	6
$^{58}Ni(n,p)$	^{58}Co	1699.7	810.8	99.5	8
$^{58}Ni(n,2n)$	^{57}Ni	35.6	1377.5	81.7	24
			1919.5	12.3	
$^{27}Al(n,\alpha)$	^{24}Na	14.96	1368.6	100	14
			2754.0	99.9	
$^{59}Co(n,\alpha)$	^{56}Mn	2.579	848.8	98.9	14
			1810.6	27.2	
$^{59}Co(n,p)$	^{59}Fe	1068.1	1099.2	56.5	16
			1291.6	43.2	
$^{59}Co(n,2n)$	^{58}Co	1699.7	810.8	99.5	18
$^{209}Bi(n,4n)$	^{206}Bi	149.8	516.2	41.2	30
			537.5	30.8	
			803.1	98.9	
			881.0	66.9	
			1718.7	32.2	
$^{209}Bi(n,5n)$	^{205}Bi	367.4	703.5	31.1	38

The factor χ depends on the geometry of the foils, the cross-section and the neutron flux impinging on the foil:

$$\chi \;=\; n_t \int \sigma(E_n)\;\; \frac{\partial^2\phi(E_n,\Omega)}{\partial E_n\;\partial\Omega}\, dE_n\, d\Omega \tag{10.2}$$

Here n_t is the number of target atoms per surface unit, Ω is the solid angle of the foil viewed from the target, σ is the cross–section and $\phi(E_n,\Omega)$ is the neutron flux per projectile. Since the foils are small, the variation of the flux can be neglected. The only integral to be carried out is on the neutron energy.

$$\chi \;=\; n_t\,\Omega \int \sigma(E_n)\;\; \frac{\partial^2\phi(E_n,\Omega)}{\partial E_n\;\partial\Omega}\, dE_n \;\;=\;\; n_t\,\Omega \int \sigma(E_n)\;\; n_\theta(E_n)\;\; dE_n \tag{10.3}$$

Here $n_\theta(E_n)$ is the neutron spectrum per unit of solid angle. The index recalls that the only angular dependence is on the angle θ with respect to the beam direction.

Eq. 10.4 is the basis of our method. E_0 is defined as the energy where σ(E) has a peak and at the limit of very narrow sigma it is the Kronecker delta(E - E_0) function. This allows one to approximate the overlap integral as:

$$\int \sigma_0\,\delta(E_n - E_0)\;\; n(E_n)\;\; dE_n \quad\;=\;\quad \sigma_0\;\; n(E_0) \tag{10.4}$$

We thus need a set of cross–sections, ideally as narrow as possible, peaking at different energies to sense different energy ranges of the neutron spectrum. The spectrum is defined by a number of pairs $(E_n, n(E_n))_k$ acting as adjustable parameters. At intermediate energies the spectrum is interpolated and all integrals corresponding to the experimental set are calculated. The best agreement with the experimental values is searched for by iterations of the parameters in order to minimise χ^2. In practice, it is faster to control the iterations by hand, starting first with the reactions of high threshold and gradually including those with lower threshold, than systematically scanning the whole range of parameters. In order to get stable solutions, the number of experimental integrals must exceed the number of parameters by at least 50%. This integral method cannot resolve structures but is well suited to get the envelope of continuous spectra. It thus suits well to our purpose. The procedure is repeated at each angle to obtain angular distributions. The method is purely numerical without a priori assumptions about the spectrum shape. The fact that at large angles the spectrum gets an exponential shape characteristic of evaporation spectra shows that the method works correctly.

It might be appropriate to practice some smoothing of the parameters by considering data including all angles at once, as the variation at fixed energy is expected to be a monotonic decrease versus θ. This can be done because the strong correlations of the parameters allow some readjustments without critical increase of the

global χ^2. In that way, the parameters are supposed to be more physical. An example of extraction of the neutron spectrum by unfolding for 25 MeV p+^{13}C is presented in Chapter 13.1.3.

In the following chapters I denote the overlap integral as $\langle \sigma \cdot n \rangle$ for short.

11 Experimental apparatus

Our experiments have been carried out in the RADEF cave at JYFL [79]. The choice of the cave has been motivated by the feasibility constraints and in such a facility we could easily accommodate all our experimental setup. Some parts of our setup, such as the target's container and chamber were the same for activation and Time of Flight, others like the Ge low background station or PSND's were used exclusively in one of the methods.

The target chamber, shown in Fig. 11.1, has been specially designed for our experiments and built in the JYFL workshop [1]. The targets we have used were held by screws in a special aluminium target holder.

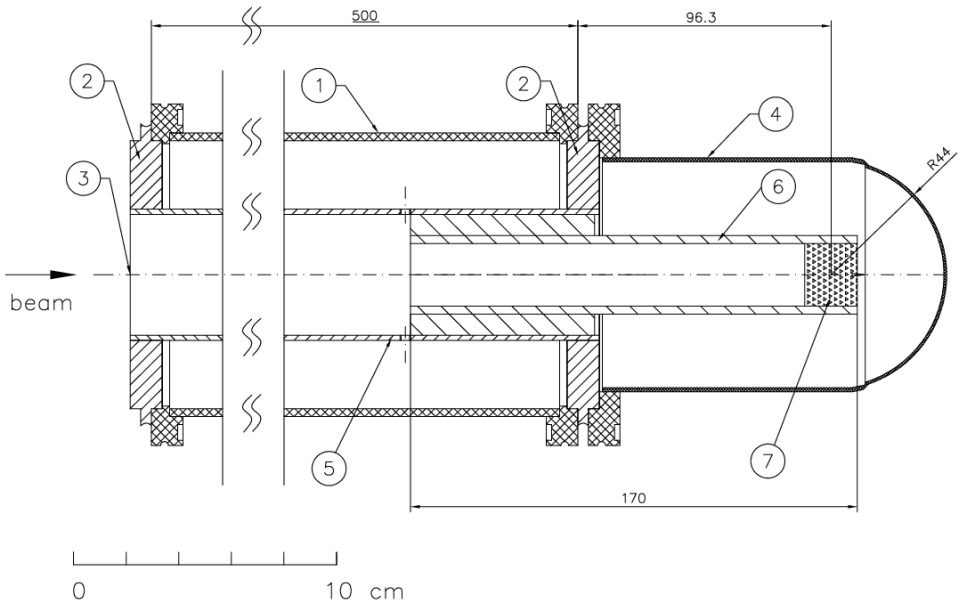

FIGURE 11.1 The target chamber used for experiments with 25 and 40 MeV protons, and 40 MeV deuterons. 1) beam line tube, 2) insulator disk supporting the inner cylinder, 3) diaphragm with 15 mm aperture for the beam, 4) end piece, 5) inner cylinder acting as Faraday cup, 6) target holder, 7) target of ^{13}C, ^{12}C, D_2O or H_2O.

[1]The chamber used for the measurements at 20 MeV turned out to shadow neutrons in the 0 degrees direction. Therefore a new chamber has been built and used in the following experiments.

Different vacuum pumps have been used to maintain the vacuum inside the target chamber. For pre–pumping we have used a mechanical one. After reaching about 10^{-1} mbar, we were switching to a turbomolecular pump. When the vacuum was $2.5 \cdot 10^{-5}$ mbar, we could finally open the valve to the K–130 cyclotron to reach the working vacuum of about 10^{-6} mbar.

11.1 Activation-specific setup

One of the advantages of activation is the relatively simple experimental setup. Its integral parts are the target's container and chamber described in the previous chapter, electronics, Ge low background setup and the support for activation foils. Fig. 11.2 shows the activation setup inside the cave just before the irradiation.

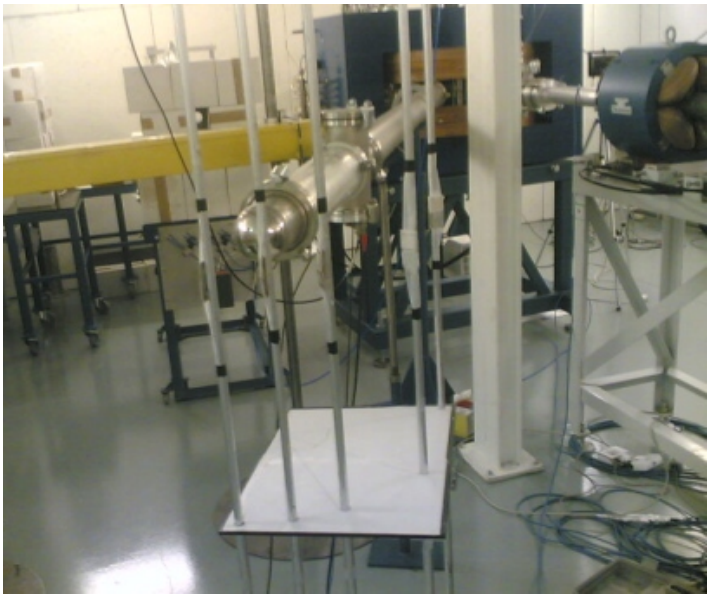

FIGURE 11.2 Placement of the activation foils around the target chamber in the 2005 SPES run. Foils have been glued at the beam height; a laser alignment system [80] has been used to justify their height.

The requirement of the activation foils being placed at a distance of a few centimetres from the target, in order to receive enough neutrons, yielded the need of a dedicated support structure constructed using aluminium and copper rods. The foils were glued to the support at various angles ranging from 0 to 110°with respect to the beam direction. During some experiments additional foils were placed in–between activation foils to monitor the background, as depicted in Fig. 11.3.

11.1.1 Electronics

The electronics used for activation consists of one setup to measure the beam current and one to count gammas with Ge detector. A scheme of the electronics used to

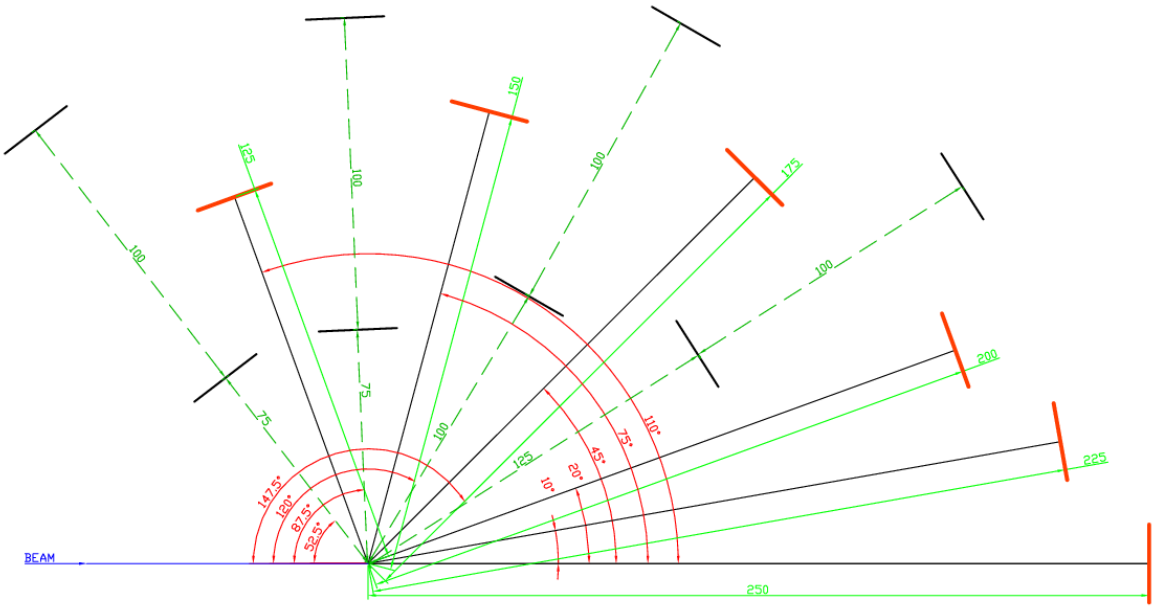

FIGURE 11.3 Placement of the activation foils around the target chamber. Foils used for activation are marked with red and the ones used for monitoring the background with black.

integrate the beam current during our experiments is presented in Fig. 11.4. The total charge was measured by a Faraday cup connected to our own custom–made CAMAC–based data acquisition system (DAQ), which monitored the stability and intensity of the beam. The beam current intensity has been measured with ORTEC 439 integrator. The extraction of the average beam current is described in detail in Chapter 13.1.1. The racks with electronic modules were placed behind the concrete walls of the experimental cave[2].

11.1.2 Ge low background setup

The activities from the irradiated foils have been measured with a CANBERRA n–type germanium detector, model GR2019, belonging previously to the NORDBALL array [78]. Its relative efficiency, measured with a ^{60}Co source, was 28%, and the peak resolution 2.6 keV FWHM. The detector was placed in the low background

[2]The 10 m cable connecting the Faraday cup inside the experimental cave with the ORTEC 439 current integrator outside the cave went through a hole in the concrete chicane made for that purpose, otherwise its length would have to be some 30 m.

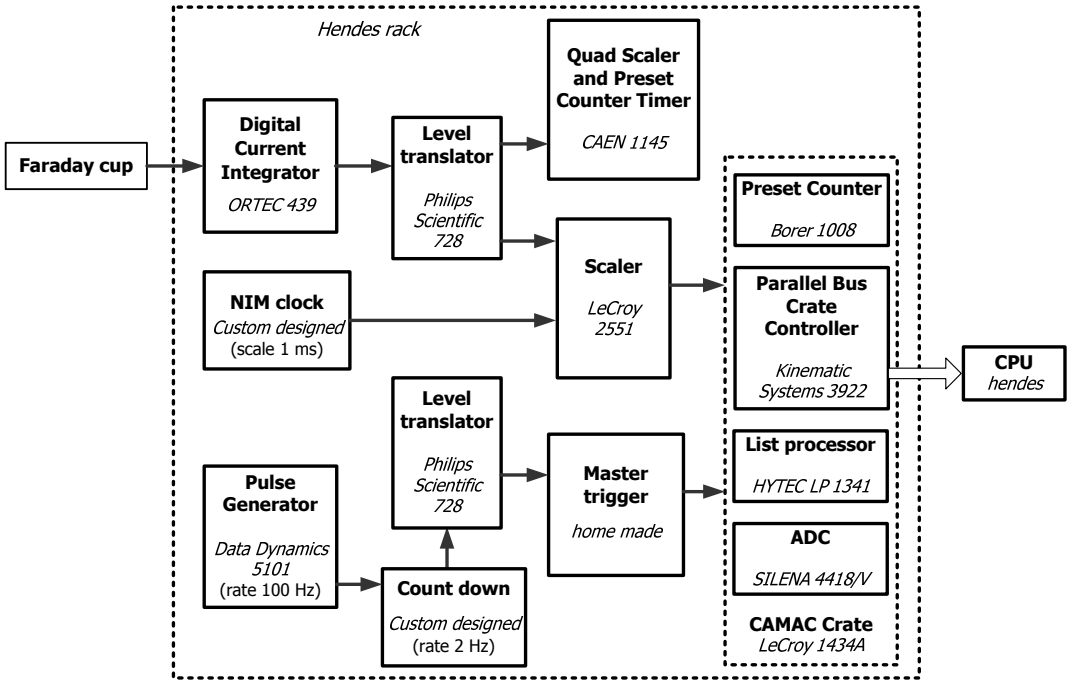

FIGURE 11.4 Scheme of the electronics used for beam current measurement.

setup depicted in Fig. 11.5. The Ge crystal was shielded by 10 cm lead, 3 mm tin and 0.5 mm copper in order to minimise the background present in the counting room[3].

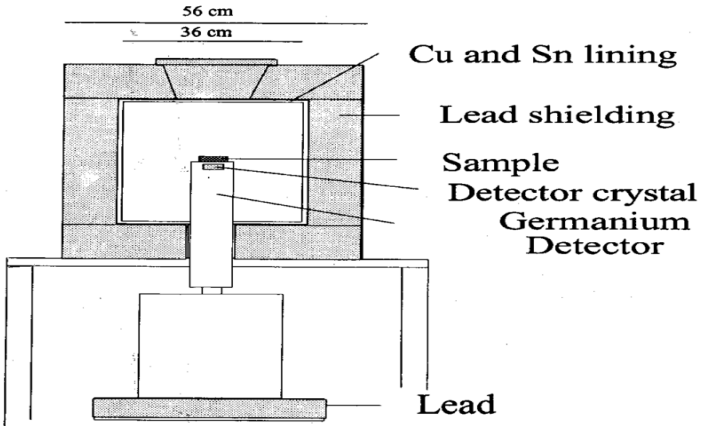

FIGURE 11.5 Low background setup used for off-line counting of activated foils.

A scheme of the electronics used with the Ge detector is presented in Fig. 11.6.

[3]The background present in the counting room essentially consists of the 1461 keV line of ^{40}K and natural radioactive alpha series due to Rn present in the air. These high energy gamma rays are absorbed by Pb which subsequently emits fluorescent X-rays of 72, 75, 84 keV. Pb X-rays are absorbed in Sn, emitting Sn X-rays which are subsequently absorbed very efficiently by Cu. The energy of Cu X-rays is so low that they are either self-absorbed or absorbed in the detector cap.

The shaping time used for collecting the charge in the Ge detector was 3 μs.

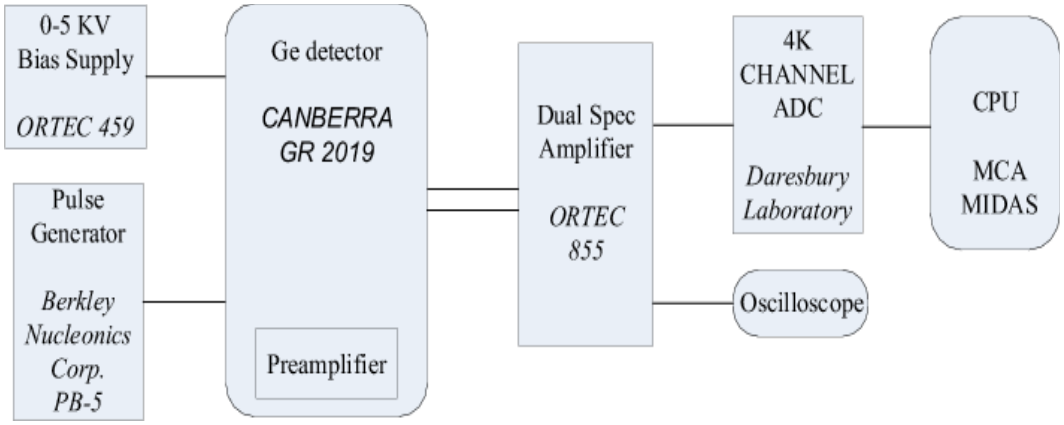

FIGURE 11.6 Electronics used with Ge detector.

11.2 Setup for Time of Flight

Position Sensitive Neutron Detectors, described in Chapter 9.3, were used for the TOF measurements. The detectors' arrangement for the measurements at 25 and 40 MeV proton energy is shown in Fig. 11.7 and 11.8.

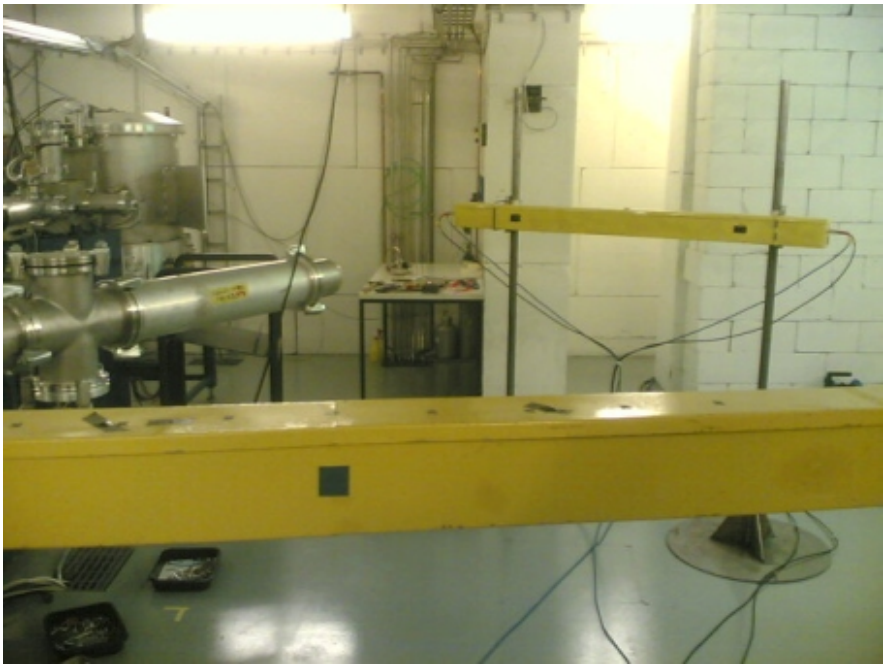

FIGURE 11.7 TOF setup in 2005 SPES run. Two PSND are placed in the horizontal plane at beam and target height. One of PSNDs remained fixed during acquisition of events. The other was rotated to cover forward angles, at this arrangement it is at 0°.

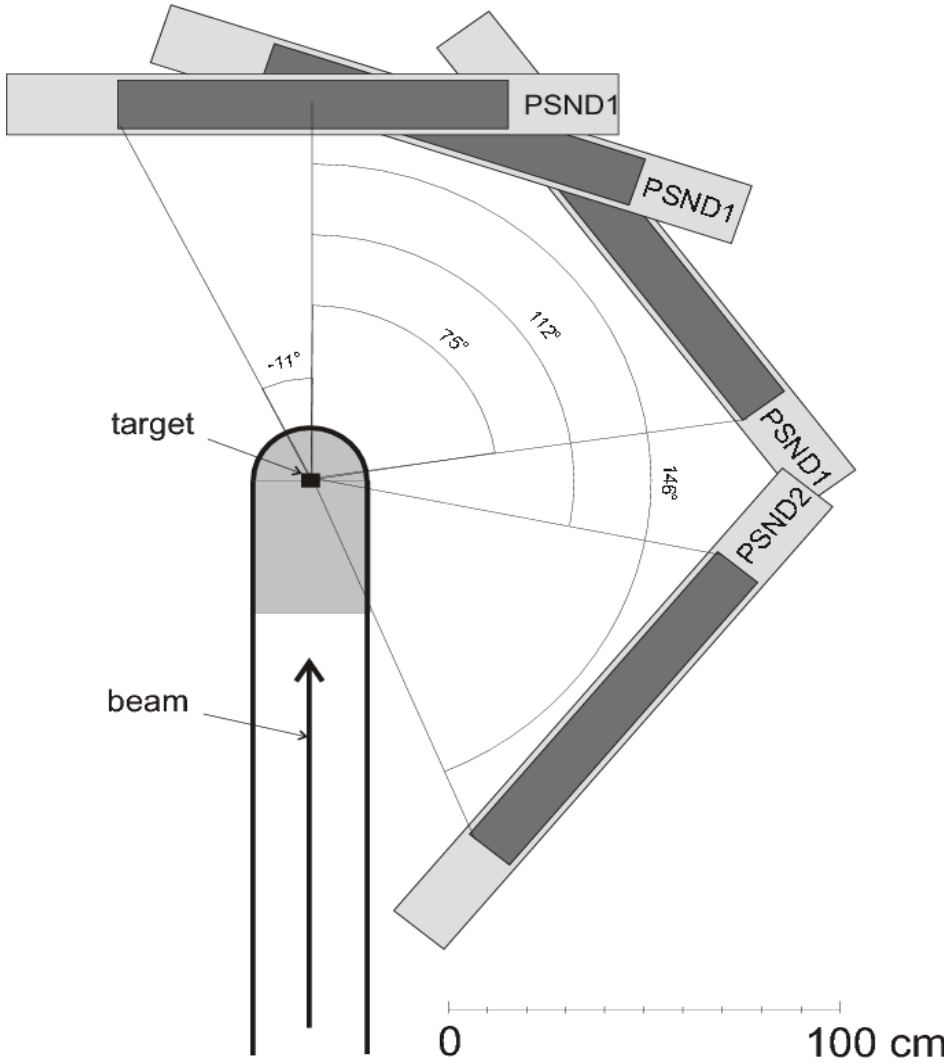

FIGURE 11.8 Detector arrangement for the TOF measurements at 25 and 40 MeV proton energies. Three positions of detector PSND1 are shown, whereas PSND2 remained fixed during acquisition of events. The active part of the detector tubes filled with liquid scintillator is shaded in black. The photomultipliers are located inside the grey areas. The shaded area around the ^{13}C target is the chamber, shown in more detail in Fig. 11.1

Two detectors were placed in the horizontal plane at beam and target height. Their centres were located 1 m from the target. One of the detectors, PSND1, was rotated to cover forward angles. The second one, PSND2, was fixed and used to detect neutrons emitted backwards (that way the angular range up to 146 degrees has been covered).

Before putting NE-213 scintillator in the light–tight container of the PSND, the liquid was "bubbled" with pure argon. The transparency of the liquid and the quality of the light was monitored by collimating a ^{60}Co gamma–source at different points along the PSND, and determining positions of the photo-peaks at both PM. The

energy calibration of the total integrated signals was performed using the ^{137}Cs and ^{60}Co gamma sources.

12 Measurements

The experiments in the framework of SPES described in this chapter have been performed at JYFL from January 2004 to December 2005. The irradiation lasted typically 1 day. The preparations as well as the offline counting of the activities after the run took several weeks.

12.1 Irradiation, beam monitoring

The impinging beam from the K–130 cyclotron must be entirely focused on the target. Otherwise we would register many neutrons coming from sources other than p+^{13}C reactions. Therefore before the run the beam was tuned to go through a 5 mm hole in a fluorescent diaphragm centred along the symmetry axis of the target.

The ^{13}C target was irradiated during typically 20 h with constant proton beam current. The currents were 100, 60 and 10 nA (which corresponds to $6.24 \cdot 10^{11}$, $3.75 \cdot 10^{11}$ and $6.24 \cdot 10^{10}$ ions per second), for the proton energies of 20, 25 and 40 MeV, respectively. These current limits are due to the level of tolerable induced activity outside the experimental vault.

12.2 Activation of foils

During irradiation of the ^{13}C target, foils of Al, Co, Ni, In and Bi were placed at 14 cm (E_p=20 and 25 MeV) and 28 cm (E_p=40 MeV) from the target centre and at angles of 0°, 15°, 30°, 60°and 110°with respect to the beam direction. The foils were 1 mm thick and 25 $\times$ 25 mm^2 area each. The activities induced by the neutron flux were counted off–line over a period of 1 month after irradiation in the Ge low background setup. During that period each foil was counted several times; a detailed description of counting procedure is given in Chapter 10.2. For the complex spectra created by Bi, decays of up to 8 lines were used to determine the yield of ^{206}Bi. For most other activities usually few lines and sometimes only 1 line was available. All lines reported in the decays of Al, Co and Ni products were used (see Table 10.1). The efficiency for detecting γ-rays is the average over the volume of the efficiency for point sources. The concept of effective efficiency for a foil source is discussed in detail in Appendix B.1.

12.3 TOF experiment

A TOF run was typically performed before activation. Several hours of beam time was usually enough to obtain the desired statistics. The K130 cyclotron's RF, which gave the start time signal, was 11.56 MHz. A valid stop was enabled by the coincidence of the time signals from both ends of a PSND detector. The 1 m neutron flight path to the detector and the RF frequency imposed the lower limit of measurable neutron energy. The proton beam current was kept below 1 nA in order to avoid count rates higher than 10^3 per second. Good n/γ separation is typically achieved for neutron energies greater then 0.5 MeV (see Chapter 9.3). The detection threshold in our experiment was near 3 MeV, the neutrons detected with energies above the threshold were therefore well separated from the gamma–ray events.

12.4 Activity of targets

The activity of the ^{13}C, ^{12}C, D_2O and H_2O targets was measured before and after the experiments. The main purpose was to make sure that residual activities in the material will have no influence on the measurements (before), and to determine the suitable storage (after).
There are several methods to measure the activity, we used two of them: gamma spectroscopy and dose measurement. The former will be described in detail in [86], the latter was performed using a radiation monitor system consisting of two γ– and X–radiation Universal Survey meters: RDS-200 and RDS-120. γ–rays emitted from ^{7}Be are the only activity in the targets detectable by gamma spectrocopy after a few days. Therefore radiation survey meters can be used with confidence to monitor it without interference of other activities. Accumulated dose and dose rate have been measured in parallel. Both gave an identical result proving correctness of the read-out. The ^{7}Be γ–ray dose has been measured at distances to the centre of the target ranging from 0.005 to 1 m. The natural backround level in the room was measured to be 0.15 ± 0.20 μSv/h. Knowing the dose rate, one can calculate the activity at the end of irradiation, A_0, as:

$$A_0 = \frac{A}{e^{-\lambda \cdot t_w}} = \frac{\dot{D} \cdot r^2}{\Gamma_D \cdot e^{-\lambda \cdot t_w}}, \tag{12.1}$$

where A, λ, $\dot{D}$, r, Γ_D, t_w are, respectively, instantaneous activity, decay constant, dose rate, distance from the centre of the target to radiation monitor system, constant for a given gamma decay and time since the end of irradiation.

Assuming r = 1 m and A = 1 MBq, Γ_D can be computed as:

$$\Gamma_D = \dot{D} \cdot \frac{r^2}{A} = 4.59 \cdot 10^{-6} \sum_i b_i E_i \left(\frac{\mu_{en}}{\rho} \right)_i \quad \left[Gy \cdot m^2 \cdot MBq^{-1} \cdot h^{-1} \right], \quad (12.2)$$

where b_i, E_i, μ_{en} and ρ are branching ratio, energy of i^{th} γ–ray transition, linear absorption coefficient and density, respectively [87].

The quantity of interest, the saturation activity A_∞, can then be calculated as:

$$A_\infty = \frac{A_0}{1 - e^{-\lambda t_{irr}}} \quad (12.3)$$

Here t_{irr} is a time of irradiation. The results of dose measurements of natural carbon target are summarised in Table 12.1.

TABLE 12.1 Activity of ^{12}C target measured after February 2008 experiment. The target has been irradiated for 14 hours with an average current of 1.05 nA. The constant current is assumed because the activity of ^{7}Be is long enough to smooth the fluctuations of the beam. The gamma constant of 7.4 $\cdot 10^{-9}$ Sv $\cdot$ m^2/MBq/h (Eq. 12.3) was used for the 477.6 keV γ–ray emitted from ^{7}Be, which has a half–life of 1279.0 hours.

Measurement no.	1	2
t_w [h]	50	236
Distance [mm]	10	20
Dose [μSv]	5.31	1.19
A [kBq]	71.8	64.3
A_0 [kBq]	73.7	73.1
A_∞ [MBq]	9.75	9.67

Apart from long–lived activities detected by activity measurements after the experiment, there are also numerous short–lived ones that might cause a safety request of intervention during the irradiation. Those ones are setting a cyclotron beam current limit under which the measurement is not interrupted by safety alarms. We've performed dedicated test irradiations in order to obtain this limit before the experiment. It is important because beam instabilities have a direct impact on error in a beam current measurement.

13 Analysis procedure

13.1 Activation

Activation data analysis starts with obtaining the number of decays in all counting bins by computing the efficiency for detecting the γ–ray with the Ge detector, the branching ratio per decay and a time factor that takes the growth (during irradiation) and decay (during measurement) of the activity into account (see Eq. 10.1). The next step is to extract the production rates per second, taking into account the build–up of activities during irradiation and their decay. Most reactions produce a single activity. However, for ^{58}Co from ^{59}Co(n,2n) and ^{58}Ni(n,p) the ground state is also populated by the decay of the 9.15 h isomer. This requires the implementation of radioactive filiation of ^{58}Co^{m} to ^{58}Co. The production rates are obtained by standard γ–spectroscopic techniques described in detail in several LNL annual reports [85], simplified calculations are presented in Appendix B.3. In the following sections we describe the effective average current $\bar{i}$ and the $\langle\sigma \cdot n\rangle$ factor that contains the required information. The $\langle\sigma \cdot n\rangle$ integrals expressed in mb per sr and per proton are deduced after normalisation for the solid angle covered by the foils (viewed from the target), the beam particle current, and the number of target atoms per surface unit.

13.1.1 Average beam current extraction

The beam from the K–130 cyclotron is very stable. However, in case of incident, one should be able to recover the data. Therefore, the beam is constantly monitored by the charge collected in the Faraday cup acting target.

The instantaneous current, measured with a Faraday cup connected to a dedicated DAQ (see Chapter 12.1), allows one to calculate the time factor numerically in case the beam had been unstable during the irradiation. The data is saved in the event–by–event mode to permanent storage as a series of binaries. These files are then read, and the instantaneous and average proton currents are calculated by a dedicated program, of which I was the author. An example of a result is shown in Fig. 13.1.

Apart from calculating the average current, we also account for beam fluctuations. During the analysis the current $i(t)$ can be decomposed into bins $(t_1, t_2)_k$

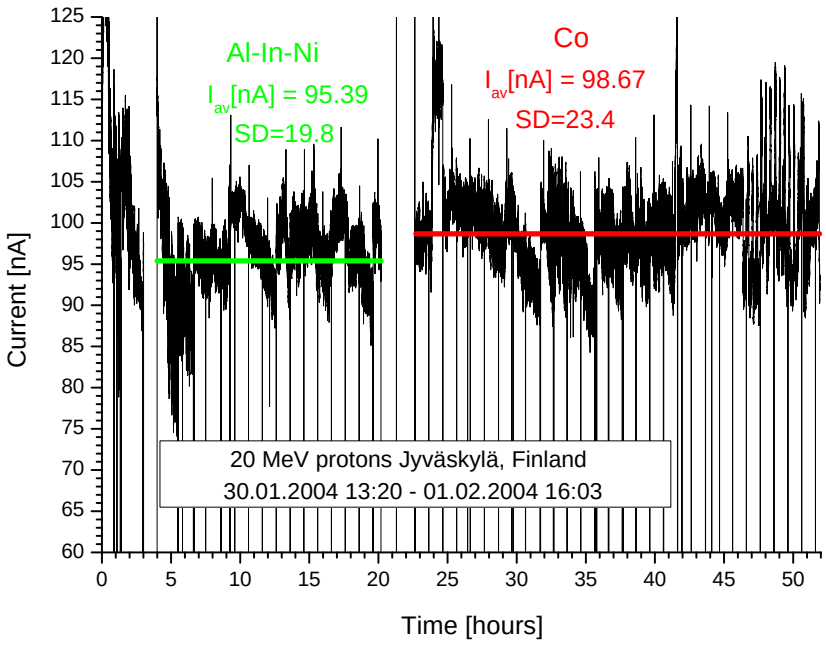

FIGURE 13.1 Beam current structure in the first measurement at JYFL in the framework of SPES in January 2004. The average current has been calculated for activation of Al, Ni and In (green) and Co foils (red line), SD stands for a standard deviation with respect to the average. The sudden drops of current were due to multiple safety requests of intervention during the irradiation.

during which $i(t)$ has a constant value i_k. The contribution of each bin to the number of nuclei present at end of irradiation is evaluated. The sum of all contributions is proportional to:

$$f_{bin} = \sum_k \left[1 - e^{-\lambda(t_{2k}-t_{1k})}\right] e^{-\lambda(t_i-t_{2k})} \; i_k, \tag{13.1}$$

which is a numerical equivalent of:

$$\int_0^{ti} \lambda e^{-\lambda(t-t')} i(t') dt' \tag{13.2}$$

Eq. 13.2 is compared with the formula using the average constant current i_{av}:

$$f_{av} = (1 - e^{-\lambda t_i}) \; i_{av} \tag{13.3}$$

Table 13.1 compares the values calculated with the average current method to the exact ones.

The results are in general similar for activities of half–life much longer than the irradiation time, as then only the total charge is relevant. In contrast, the deviations

TABLE 13.1 Comparison of exact and calculated values with average beam current values. Integration corresponds to Eq. 13.1 and calculation to Eq. 13.3. The deviations between the calculation and integration are quite severe for the short–lived activities because the January 2004 measurement was often interrupted by safety alarms leading to breaks in beam delivery. The average beam current was 95.4 nA, as shown in Fig. 13.1.

$T_{\frac{1}{2}}[h]$	Activity	Integration [nA]	Calculation [nA]
4.49	$^{115}In(n,n')$	88.62	87.33
15.0	$^{27}Al(n,\alpha)$	50.29	50.0
35.6	$^{58}Ni(n,2n)$	25.64	25.64
1699.7	$^{58}Ni(n,p)$	0.62	0.62

could become significant for the shortest–lived activities for which the current at the beginning of irradiation has little influence on the produced activity. It is customary to carry on the calculation with a constant current. This implies a renormalisation, i.e. using $\bar{i} = i_{av}\, f_{bin}/f_{av}$. Using simple formula, i.e. Eq. 13.3, would lead to errors which could be of consequence, as the beam current enters directly into the overlap integral $\langle \sigma \cdot n \rangle$ calculation. Therefore we rely on current integration, which is the safest and most reliable method of measuring the impinging beam current.

13.1.2 Correction for neutron background

In experiments with the ^{13}C target the decrease of the registered neutron flux with the increase of angle θ was slower when measured by activation than by Time of Flight. We have explained this discrepancy by taking into account neutron background: TOF is much less sensitive to it. It is indeed reasonable to assume that neutrons could originate from the interaction of the beam with elements of the beam line upstream of the target. These neutrons could thus be emitted with approximately constant intensity inside the small area in which the foils are placed. They should contribute evenly as a background B_γ specific to the reaction channel but independent of the angle. The equation for the peak area obtained for a certain reaction channel at angle θ is thus conveniently rewritten as the sum of two contributions as follows.

$$N(E_\gamma, \theta) \quad = \quad \kappa_\gamma(\theta)\, \Omega \, + \, B_\gamma \tag{13.4}$$

The (κ, B) parameters can be extracted if at angle θ at least 2 foils are placed at different distances from the target. A check of the assumption of a constant background is that the B_γ parameters must be independent of the angle. The experimental peak area to use in the subsequent analysis is thus $N(E_\gamma, \theta) = \kappa_\gamma(\theta)\, \Omega$. However,

in practice, one avoids the masking of foils by putting them at same angle. The analysis has then to proceed through iterations. With B set to zero (the assumption of no background), a first–order solution for the set of $\kappa(\theta)$ values is obtained. Values at missing angles are obtained via smooth interpolation and the equations are solved for B. The procedure is resumed starting with the new B value and repeated a few times until the solutions are stable. This method of calculating the neutron background has been used for experiments at 25 and 40 MeV. However the foils to measure background were placed at 1 m distance. That was probably too far. If the background neutrons would be emitted from a point upstream with a small divergence from the beam axis. Nevertheless with this method we could have detected a more uniform room background which we did not. After background foil data analysis we proved that any background that might have an effect on the measurement was not observed. There is a low energy background that one sees in the spectrum of ^{115}In(n,γ), but the tests show that it does not disturb the measurements which are sensitive only to neutrons above 0.5 MeV. In SPIRAL 2 experiments, the control foils were put much closer (at twice the distance of measuring foils), but nothing was seen either.

13.1.3 Finding spectral distribution

The final stage of the analysis consists in finding the spectral distribution that best reproduces the set of experimental integrals. In the absence of a well established analytic expression we have chosen a numerical approach. For this, a set of $\langle \sigma \cdot n \rangle$ integrals is fitted using an ansatz of parameters for the spectrum n(E) at each angle.

A typical procedure for χ^2 minimisation applied for 25 MeV proton data is as follows. For the initial conditions, a set of energy values is chosen according to the range of the reactions, which for 25 MeV is 0.6 – 24.6 MeV, 0.6 MeV being the minimum of the reaction energy thresholds and 24.6 MeV the maximum neutron energy expected. The spectral distribution is calculated by minimizing χ^2. Minimisation starts from the highest energy, where there are no other overlapping reactions, and is performed separately for every angle. This interactive procedure has been used for p+^{13}C with a Fortran 77 program after it turned out that the systematical search of parameters on a grid used in earlier analyses was too much time consuming and could end in non–physical χ^2 minima. Later the interactive procedure was rewritten using the physica software [81]. It allowed a display for control and ease of decision about the next iteration. Fig. 13.2 illustrates the unfolding procedure with physica.

Finally, the best (minimum χ^2) n(E_i) parameters are slightly re–adjusted to obtain a set of values varying smoothly as a function of energy and angle. This is motivated by the fact that the evolution of the spectrum with angle must be smooth at any energy. It has been considered that experimental values can exceed calculated ones (in the case that reactions other than the nominal one contribute to the production) but the reverse is not allowed to occur outside of statistical fluctuations. These

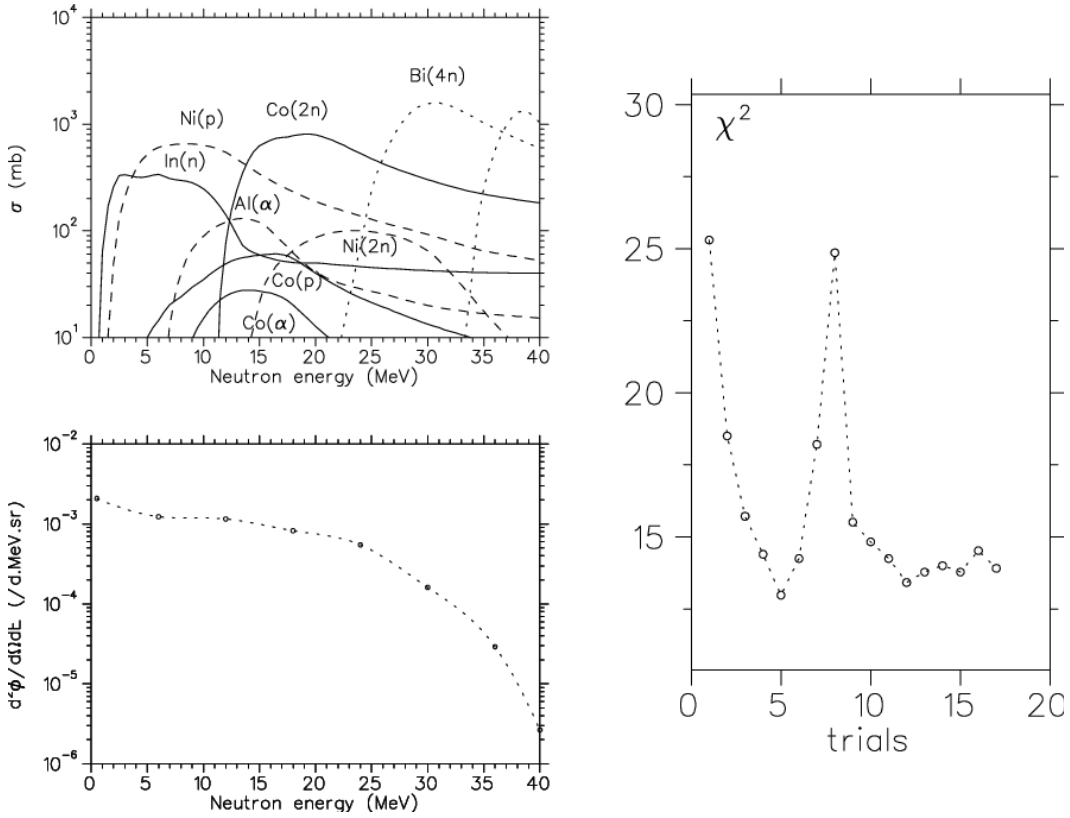

FIGURE 13.2 Example of unfolding of a heavy water spectrum at 10 degrees. Parameters are varied iteratively in order to lower the χ^2. The unfolding program contains a text window which ilustrates the cross–section (top left) in order to indicate which parameters defining the spectrum (lower left frame) have to be modified and in which direction. The right hand side window shows the history of the trials. In this case parameter values of trial no. 5 are adopted.

changes do not imply a significant decrease in fit quality owing to the strong correlations of the parameters but should result in values having more physical meaning, as the evolution of the spectrum with angle must be smooth at any energy (the χ^2 surface is rather flat).

13.1.4 Error discussion

For the reactions of interest and explicitly stated in Chapter 10.1, the integrated quantities are estimated to be accurate within 5–10%, this error being dominated by the detector efficiency. The consequences of finite foil thickness and extended foil area, which are enhanced by the close geometry (about 3.5 cm distance from foil to Ge front cap) must be included. We have determined the parameters for self–absorption by transmission measurements. The dependence of the efficiency on the foil area has been investigated by counting point sources placed at various locations. An empirical, simple but yet fairly accurate, parametrisation is presented in detail

in Appendix B.1. The actual efficiency is then calculated by integration over the volume under assumption that the activity is uniformly produced inside the foils and multiplied with the self–absorption factors.

The scale of the charge integrator is the major component of the total beam integration error which is of the order of 2%. Our error estimation was verified with the neutron/deuteron ratio obtained by comparing the 1368 keV gamma of ^{24}Na created by (d,pα) in the test foil and (n,α) in the activation foil (see more on this in Chapter 15.1). In the ratio of counts there is no influence of irradiation (current, length, instabilities), nor of Ge efficiency.

13.2 TOF

The TOF data has been analysed by D. Vakhtin according to the procedure developed for HENDES [88]. Each neutron event consisted of six parameters; three from each of the two photomultipliers at the opposite ends of the PSND. These parameters include the time, total, and fast components of the charge pulse. Standard pulse shape analysis was used to separate neutrons from gammas, as described in Chapter 9.3.

14 Results for SPES

14.1 p+^{13}C at 20 – 40 MeV

Angular and energy distributions of neutrons produced by the interaction of protons of 20 – 40 MeV in 82% enriched thick ^{13}C carbon target measured at JYFL with TOF and activation techniques are presented. These results provide accurate experimental data and practical guidelines that have been applied for SPES studies and evaluate the merit of the proposed production method in comparison with other projects of the same generation.

The convention of plotting double–differential angular and energy neutron distributions per proton, per MeV and per steradian in this and following chapters will be followed. For TOF, the distributions are obtained directly after proper binning of the continuous distributions.

14.1.1 20 MeV

Neutron distributions at this energy have been obtained by TOF in the angular range of 0 – 110°. They are shown for selected angles in Fig. 14.1. The experimental integrals obtained by activation are shown in Table 14.1.

It is worth noting that all the integrals for Co(n,2n) leading to the production of ^{58}Co had to be discarded from the data set as the experimental values exceed those calculated with the adopted parameters by a factor of about 2 to 3 depending on the angle. Spectra deduced by activation have more counts at small angles than those measured by TOF and a flatter angular dependence. The latter has been tentatively explained by invoking the presence of an 'isotropic' neutron background [90]. Here 'isotropic' means that this background is constant along a circle of 14 cm radius centred on the target. As a consequence the adopted spectra are those derived from TOF only.

14.1.2 25 MeV

Distributions have been obtained by Time of Flight in the angular range of 0 – 75°, there is a lack of data at higher angles due to a technical problem. Moreover, the high-energy range of the spectrum at 0 degree is difficult to evaluate because of the

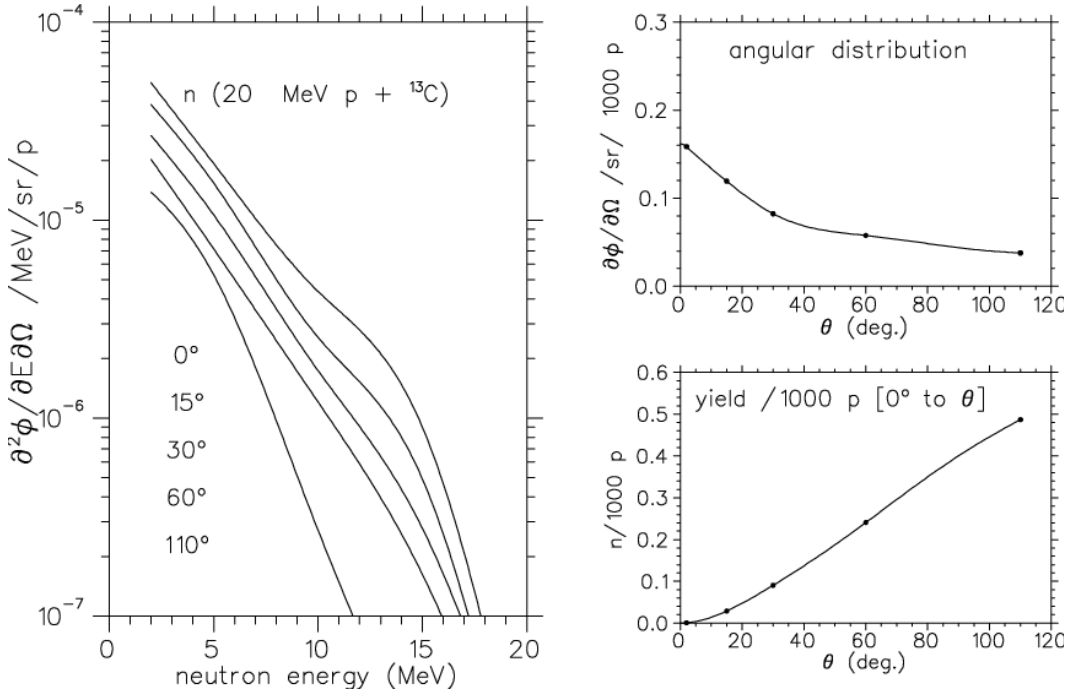

FIGURE 14.1 Neutron yield measured with Time of Flight at 20 MeV p+^{13}C. On the left: spectra deduced from unfolding overlap integrals, on top right: integrals of spectra on energy > 2 MeV versus angles, on bottom right: integrals of curves on top right times 2π sin(θ) giving the neutron flux in a revolution cone where a fission target is going to be placed.

overlap of the fastest neutron and γ-ray events. These cannot be discriminated when the energy signals are missing. The correction for losses of counts turns out to have been underestimated.

In the activation measurement extra foils were placed at 1 m from the target on each side of the beam line to check for neutron background. Deviations of γ-ray intensities from the inverse-square-distance law should have indicated the presence of neutrons emitted from elsewhere than from the target. Such deviations were observed for (n,γ) captures on Co and In but not for any of the reactions used for analysis. Near 20 MeV the spectra appear to be too high before they fall suddenly. This probably unphysical behaviour is a consequence of the parametrisation based on the assumption that there are no neutrons above the proton energy, while the limited number of free parameters does not allow the reproduction of this energy region accurately. It is remarkable that, despite the above mentioned difficulties of principle, a reasonable spectrum shape can be extracted. The experimental integrals are listed in Table 14.2.
Spectra derived from TOF and activation show fair agreement within most of the energy range however with an excess of yield in the latter, see Fig. 14.2.

The ratio of energy–integrated distributions $(dn/d\Omega)_{act}/(dn/d\Omega)_{TOF}$ is about 1.2 at θ = 0–30°, which is a deviation close to the estimated contribution of scale er-

TABLE 14.1 Experimental integrals $< \sigma \cdot n >_k$ expressed in mb/sr for 1000 protons of 20 MeV energy. All values have a 7% error contribution from the detector efficiency, and a possible increase of 10% due to the fraction of beam effectively on target.

Reaction \ θ^o	0	15	30	60	110
Al(n,α)	4.9(3)	6.5(4)	4.6(3)	3.0(2)	1.3(2)
Ni(n,2n)	0.39(3)	0.43(4)	0.17(2)	0.19(3)	0.02(1)
Ni(n,p)	122(8)	148(10)	130(10)	76(6)	53(5)
Co(n,2n)	28(5)	44(8)	14(3)	16(4)	1.3(4)
Co(n,p)	3.9(2)	4.5(2)	3.5(2)	2.6(2)	1.3(1)
Co(n,α)	1.08(6)	1.38(7)	0.99(5)	0.81(4)	0.29(2)
In(n,n')	76(4)	102(6)	93(5)	69(4)	64(4)

rors, but it raises to 2.0 at 60 degrees. This evolution with angle could once more be attributed to an 'isotropic' background. Yet, in the absence of a definite proof for the origin of the discrepancy, we adopt the geometric average (thus midway on log scale). The adopted spectra are shown in Fig. 14.3 (left–hand side). At 110 degrees the result is clearly a rough estimate since the spectrum obtained by TOF needed to be extrapolated. Considering a global agreement within a factor of two in the forward hemisphere the adopted average values could be assumed to be correct within a factor of about 1.4 either higher or lower, which is about twice outside the influence of estimated scale errors. This factor yields an error estimate of the measurements at the other proton energies.

14.1.3 40 MeV

The TOF data could not be fully exploited since the interval between consecutive beam bunches was too short, causing a fraction of neutrons to arrive after the next start signal. We therefore adopt the spectra deduced from activation, being aware that they are possibly overestimated according to the ratios observed in the comparison of both methods at E_p= 25 MeV. In any case, the spectrum shape at E_p= 40 MeV is better defined than at the lower proton energies of 20 and 25 MeV owing to the growing excitation of channels with high thresholds such as (x,2n) on Ni and Co as well as Bi(x,4n), which better decouples the y_i parameters. Moreover, the foils were put at a larger distance from the target (d = 28 cm) so that the influence of the postulated neutron background (which was also monitored by extra foils but was not established) presumably has been reduced. The adopted neutron spectra are shown in Fig. 14.4 and the activation integrals from which they have been deduced are

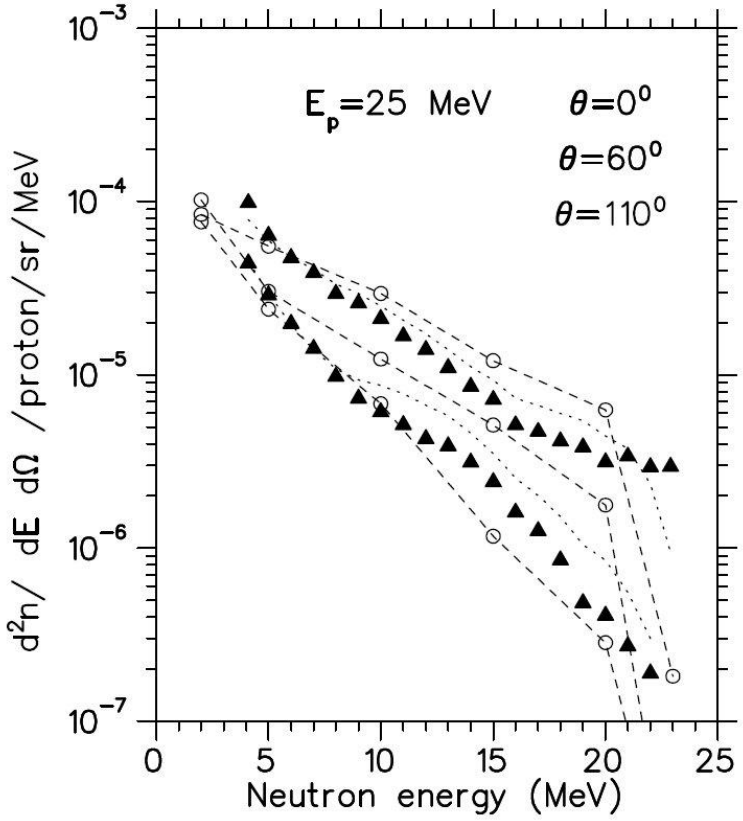

FIGURE 14.2 Summary of the 25 MeV p+^{13}C measurement at JYFL: selected neutron spectra at various angles, showing TOF (triangles) and activation data (circles are the parameter pairs). Dotted lines are the adopted values. There is no TOF spectrum at 110^o due to a technical problem. There are no error bars since most of the final errors results from the scaling factors and are thus common to all presented data. It would give a wrong idea to show the full error bars on each point.

listed in Table 14.3.

14.1.4 Validity of activation method

The adopted unfolding procedure has been very suitable to obtain neutron energy information in the experiment at E_p= 90 MeV [62]. However, within the narrow range of neutron energies produced by proton beams of 20 and 25 MeV, the available activation cross-sections are too wide and have too large overlaps to deliver sufficiently stable solutions. The main application of the activation measurement at these proton energies is therefore to cross-check the consistency of scale and angular dependence (after integration on energy) between TOF and activation results. At E_p= 40 MeV the wider range of neutron energies allows a better exploitation the energy dependence of the cross–sections in order to obtain spectral shapes.

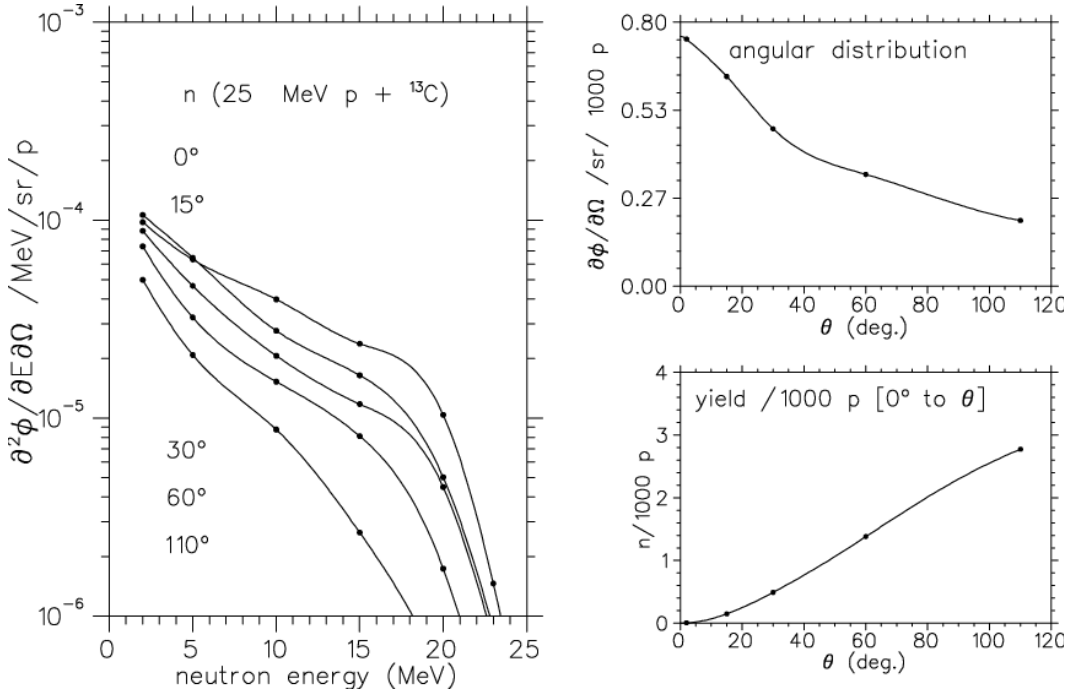

FIGURE 14.3 Neutron yield at 25 MeV p+^{13}C adopted from geometric mean of TOF and activation ($\sqrt{TOF \cdot activation}$). The meaning of spectra is the same as in Fig. 14.1, and of circles – as in Fig. 14.2.

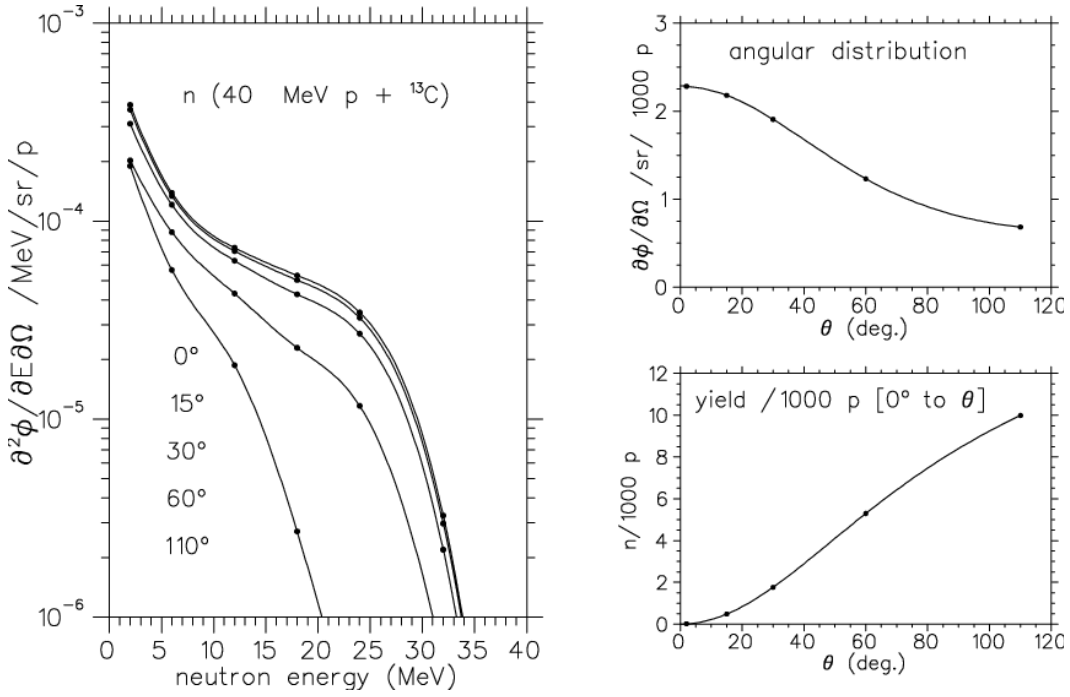

FIGURE 14.4 Neutron spectra $d^2n/dE\,d\Omega$ calculated from activation at 40 MeV. The meaning of spectra is same as in Fig. 14.1 and of the circles as in Fig. 14.2.

TABLE 14.2 Experimental integrals $< \sigma \cdot n >_k$ expressed in mb/sr for 1000 protons of 25 MeV energy. See also caption of Table 14.1. Errors quoted in the tables of $< \sigma \cdot n >_k$ presented later are only those due to counting statistics and γ-spectroscopic data. An extra 7% scaling error due to the Ge-detector efficiency should be included.

Reaction \ θ^o	0	15	30	60	110
Al(n,α)	24.5(7)	19.9(7)	13.0(6)	9.5(4)	3.9(3)
Ni(n,2n)	4.9(3)	3.5(3)	1.7(2)	1.5(2)	0.3(1)
Ni(n,p)	261(9)	232(8)	162(5)	128(4)	85(3)
Co(n,2n)	73(3)	49(2)	29(2)	27(2)	5.5(9)
Co(n,p)	10.9(5)	8.3(4)	6.1(3)	4.5(3)	2.3(2)
Co(n,α)	3.6(3)	2.5(2)	1.7(2)	1.5(2)	0.6(1)
In(n,n')	172(6)	179(7)	141(5)	109(4)	82(4)

TABLE 14.3 Experimental integrals $< \sigma \cdot n >_k$ expressed in mb/sr for 1000 protons of 40 MeV energy. See also caption of Table 14.1. Errors quoted in the tables of $< \sigma \cdot n >_k$ presented later are only those due to counting statistics and γ-spectroscopic data. An extra 7% scaling error due to the Ge-detector efficiency should be included.

Reaction \ θ^o	0	15	30	60	110
Al(n,α)	92.9(53)	87.7(51)	72.5(46)	41.5(29)	14.8(13)
Ni(n,2n)	60.7(36)	51.4(30)	30.8(21)	16.2(13)	2.5(4)
Ni(n,p)	841(48)	898(51)	624(36)	489(30)	265(21)
Co(n,2n)	533(30)	520(30)	343(21)	198(11)	48(4)
Co(n,p)	47.6(38)	29.1(30)	33.9(23)	23.3(17)	11.2(11)
Co(n,α)	19.2(17)	19.2(17)	12.9(13)	9.7(13)	5.7(17)
In(n,n')	694(40)	600(34)	516(30)	373(23)	268(17)
Bi(n,4n)	194(11)	134(8)	56.3(38)	10.3(13)	–

14.2 Comparison with theoretical calculations based on PRIZMA model

The Monte Carlo code PRIZMA has been developed at the Russian Federal Nuclear Centre – Zababakhin Institute of Technical Physics (VNIITF) Snezhinsk, by V. Plokhoi and his collaborators for various industrial or military applications [83]. It has been designed to solve three-dimensional problems of the transport of neutrons, photons and charged particles in matter.

The calculations of neutron energy distributions have been carried out for protons of up to 110 MeV on carbon targets of stopping length with the same composi-

tion (82% enrichment in ^{13}C, density 0.67 g/cm^3 and diameter 24 mm) as those used in the experiments. In addition, a calculation has been performed for a thick natural carbon target [82].

Calculated and adopted experimental neutron spectra are shown in Figs. 14.5, 14.6, 14.7 and 14.8 for the proton energies E_p= 20, 25 and 40 MeV used in this work and for E_p= 90 MeV [62].

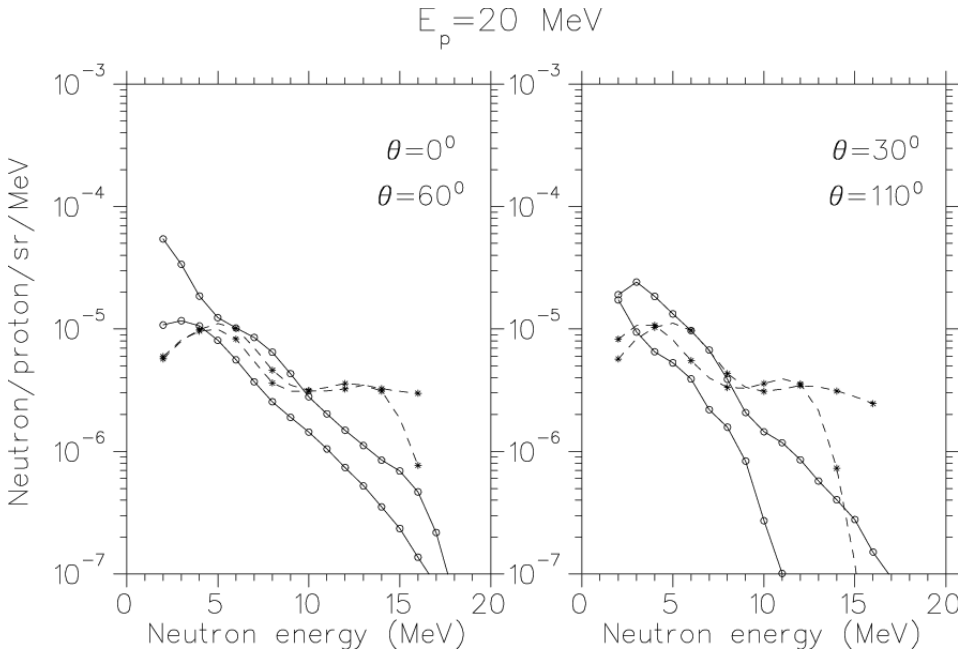

FIGURE 14.5 Comparison of spectra $d^2n/dE\,d\Omega$ calculated with the PRIZMA code (crosses) and adopted experimental spectra from this work (circles) for 20 MeV proton energy. Lines are only to guide the eye.

The agreement of experimental and calculated spectra $d^2n/dE\,d\Omega$ versus energy at fixed angle is the best at E_p= 90 MeV where the deviation seldom exceeds a factor of 2, with some larger deviations for very low and very high energies. At E_p= 40 MeV the low-energy range is better reproduced while the spectrum is overpredicted at high neutron energy. However, the energy-integrated yields $dn/d\Omega$ remain in good agreement as the counts in the high-energy range are few. This trend further develops at proton energies of 25 and 20 MeV where the calculated spectra are flatter with neutron energy than the experimental data. It is interesting to note that up to a few MeV below the proton energy E_p, the calculation better overlaps with the results of activation than with those of TOF spectra. This may, however, be accident. Angular distributions obtained by integrating the neutron spectra over an energy range from 4 MeV up to E_p are compared in Fig. 14.9.

The trend of these integrals versus proton energy is the same as discussed above. Furthermore, the calculation reproduces the neutron yields at small angles very well but overestimates the yields at large angles [89].

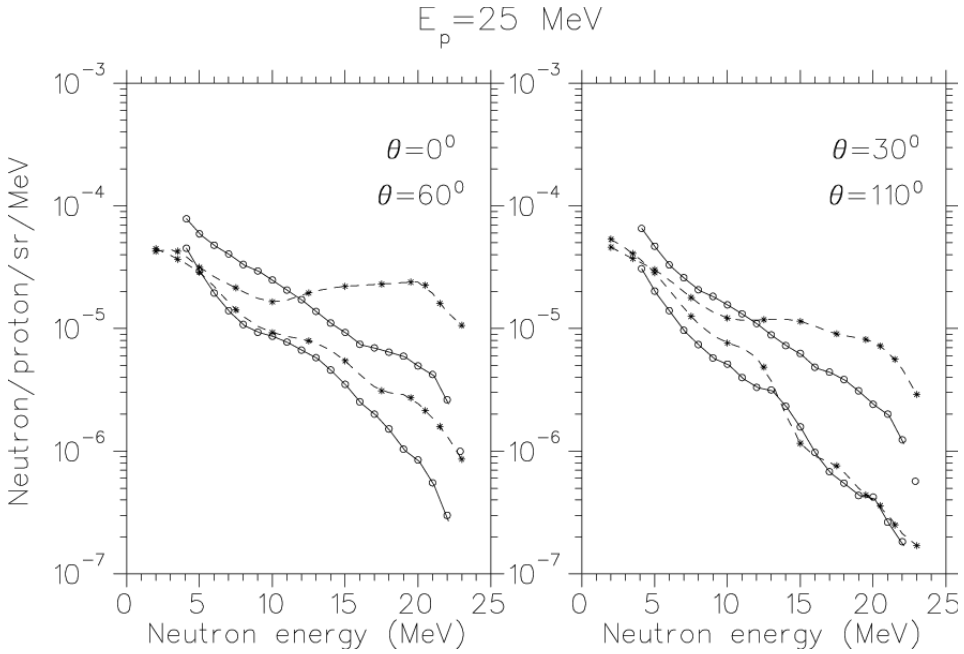

FIGURE 14.6 Comparison of spectra $d^2n/dE\,d\Omega$ calculated with the PRIZMA code (crosses) and adopted experimental spectra from this work (circles) for 25 MeV proton energy. Lines are only to guide the eye.

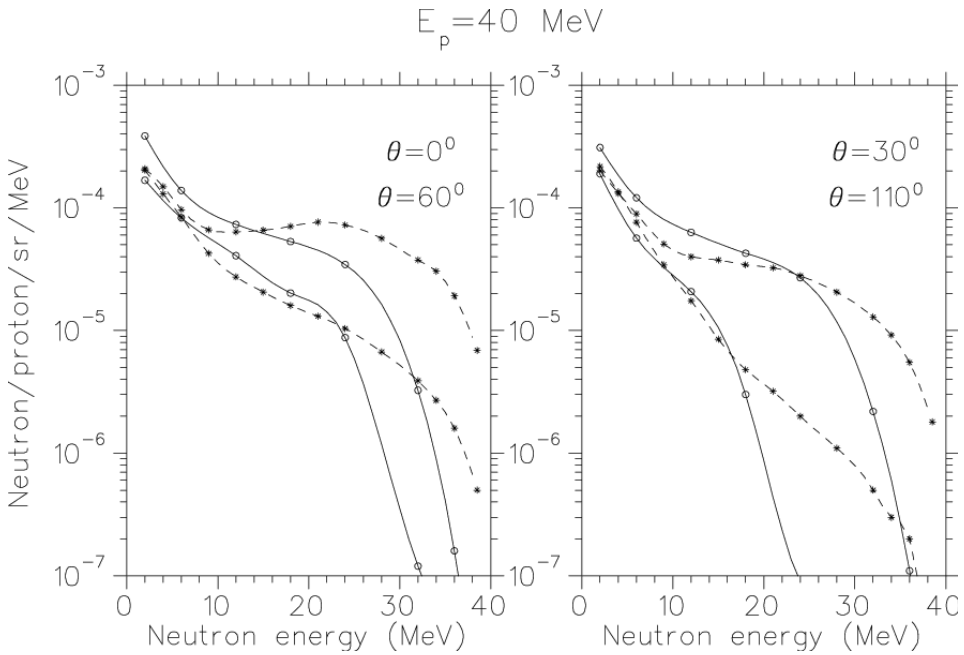

FIGURE 14.7 Comparison of spectra $d^2n/dE\,d\Omega$ calculated with the PRIZMA code (crosses) and adopted experimental spectra from this work (circles) for 40 MeV proton energy. Lines are only to guide the eye.

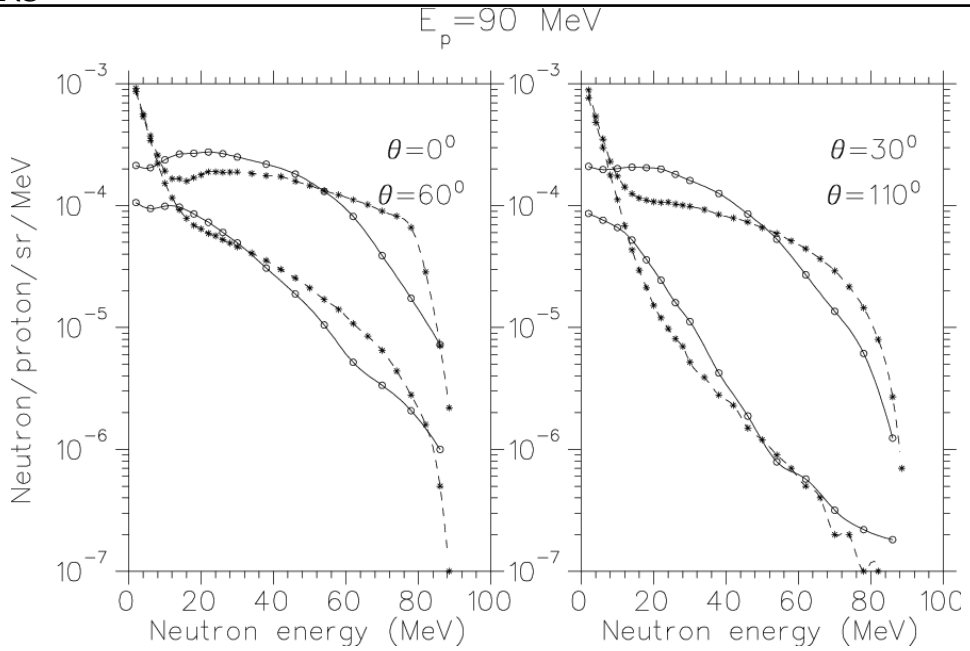

FIGURE 14.8 Comparison of spectra $d^2n/dE\,d\Omega$ calculated with the PRIZMA code (crosses) and experimental spectra from Ref. [62] (circles) for 90 MeV proton energy. Lines are only to guide the eye.

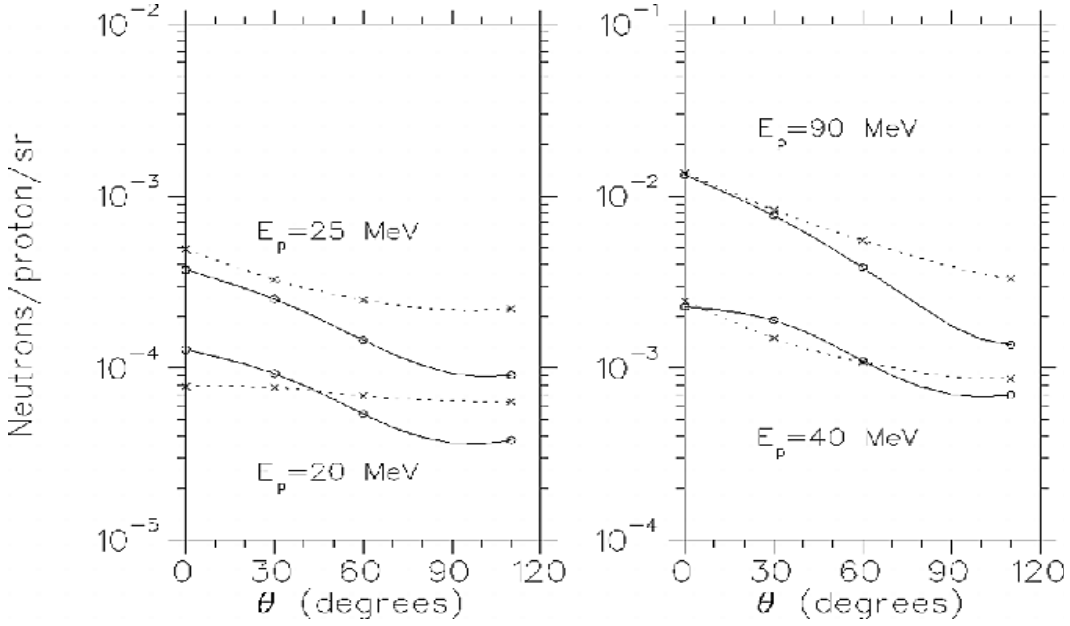

FIGURE 14.9 Integrals $dn/d\Omega$ of double–differential neutron distributions over an energy range larger than 4 MeV versus angle θ with respect to the beam direction. Circles represent the adopted experimental data and crosses the calculations. Lines are only to guide the eye.

14.3 Comparison of p+^{13}C data with other neutron yield calculations

The measurement discussed in this work for neutron yields from thick targets of ^{13}C bombarded by protons of energies 20, 25 and 40 MeV, combined with a former

measurement at 90 MeV, span the range of driver beam energies envisaged for the proton-based RIB facility SPES at Legnaro.

The baseline for SPES: production of neutrons by the p+^{13}C reaction has been supported by the result obtained in 2002 by Z. Radivojevič et al. [92], which set the neutron yield for 30 MeV protons to be $\sim 6 \cdot 10^{-3}$ in a cone with θ=30°, per proton. This value would be sufficient for SPES, which aimed at exceeding 10^{13} fissions per second for a 4 kg UC_x target. Following the SPES request to verify this value, we performed a series of activation and TOF experiments, their results have been presented in the previous sections. Figure 14.10 compares our results with those obtained by others.

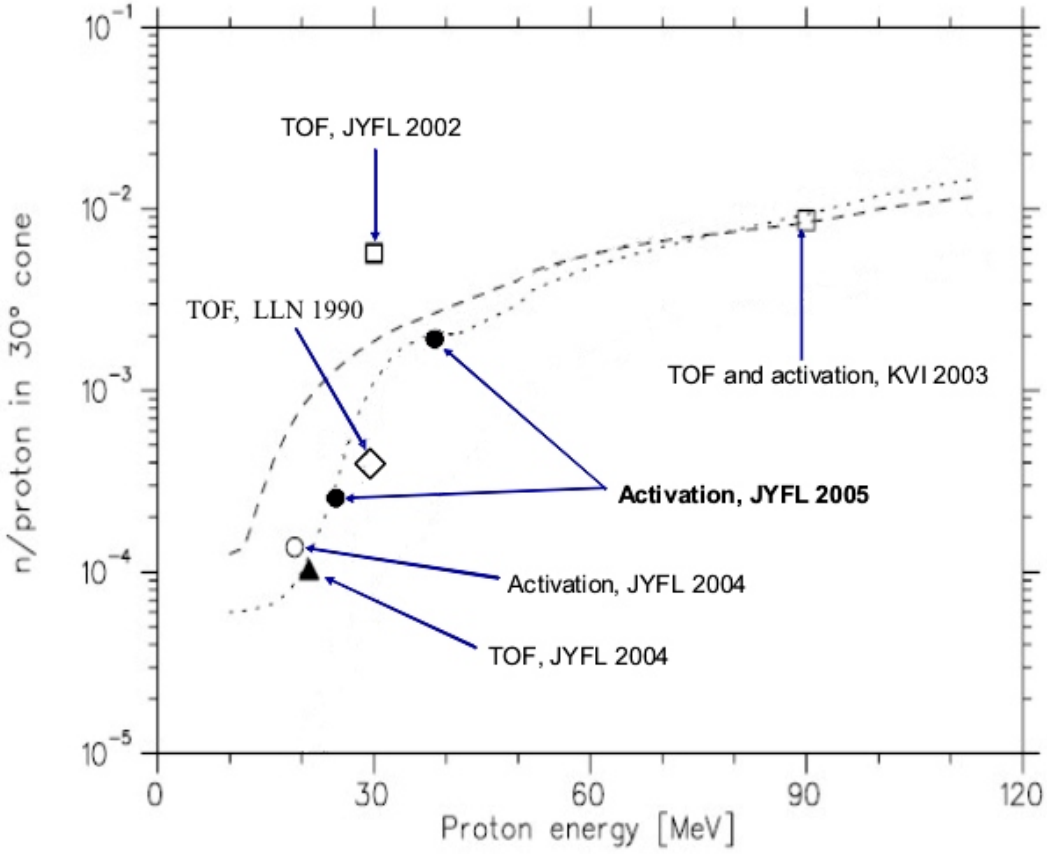

FIGURE 14.10 Neutron yields (per incident proton) emitted into a forward cone of 30^o from a thick ^{13}C target. Circles represent our activation data while the triangle and squares are TOF measurements (at 90 MeV TOF and activation [62]), and the diamond is a measurement by the Louvain-La-Neuve group [93]. Lines are simulated yields. The dashed line represents the yield calculated with MCNP [100], the dotted line with PRIZMA [83].

The value obtained by Z. Radivojevič et al. is as high as the value for E_p=90 MeV [62]. It is unrealistic since the range is much larger at 90 than at 40 MeV, thus more reactions must occur. The value in this work has also later been confirmed

in the paper by Leleux et al. [93] based on an older measurement at Louvain–La–Neuve, Belgium. Our result is in good agreement with a Monte–Carlo based calculation developed at Snezhinsk [83] and with the MCNP calculated at Legnaro [100]. Based on our values and comparison with alternatives that are discussed later, p+^{13}C is not the most efficient production scheme for a neutron source for a radioactive beam facility. The neutron yields in the proton energy region of 20 –40 MeV are in the range of 10^{-4}–10^{-3} per proton for a solid angle of 7% of 4π along the beam direction. The proton energy has been afterwards lowered to 20 MeV by INFN on the basis that priority has been given to BNCT [75], which uses a few MeV neutrons.

14.4 Inpact of our measurements on the SPES project

Our measurements showed that a very high neutron yield via the p+^{13}C reaction at 30 MeV ($\sim 6 \cdot 10^{-3}$) is not confirmed and that the yield remains lower than for d+^{12}C at same energy [94].

Following the decision of INFN to allow for 20 MeV only, the expected yield became very low (see Fig. 14.10) and there was no ground to continue the SPES project with the converter method. Consequently, the baseline of SPES has been changed. The converter method has been replaced with a direct target method. Nowadays the envisaged proton energy for SPES is 40 MeV[1]. Protons would impinge directly on uranium carbide target. With 200 μA current, this would yield $\sim 10^{13}$ fissions per second in 30 g UC_x, leading to high intensity beams in the mass region of 80–160. The SPES experiment utilizing the direct target method is scheduled to be launched in years 2013–2014.

[1] This includes a possibility for an upgrade to 70 MeV

15 Recent developments for SPIRAL 2

A linear accelerator capable of delivering deuterons of 40 MeV with an intensity of 5 mA to a neutron production target has been chosen based on systematical research as the optional design for SPIRAL 2. The first choice for the neutron converter is a carbon (graphite) target of 1 cm thickness, in which the beam is stopped. To dissipate heat efficiently, the converter target is mounted on a rotating wheel. A prototype (1 m diameter, 10 Hz rotation frequency) originally built for SPES has been further developed for SPIRAL 2. Thus far it has been successfully tested up to one fifth of the maximum power envisaged. However, another converter option, based on a heavy water loop has been proposed and is under study for its feasibility. The respective merits of these technologies show up during the study, however, in any case it appears essential to quickly compare the properties of carbon and heavy water, even natural water regarding neutron production.

Neutron yield, angular and energy distributions can be estimated by modelling with Monte Carlo codes, such as MCNPx, yielding an agreement usually better than a factor of 2 with respect to benchmark measurements. Yet for an accurate comparison of the converter properties dedicated measurements were needed. These measurements of various converters were expected to use the same method and be done in as similar as possible experimental conditions.

The activation method has been validated in the framework of SPES and proven to give reasonable results, as described in the previous chapters. This gave us confidence to use activation for defining the envelope of the continuous neutron spectrum produced by thick targets with sufficient accuracy for the purpose of optimising the converter for the SPIRAL 2 project. Neutron energy and angular distributions for deuterons on carbon have already been systematically measured only by TOF method, including at 40 MeV [96]. The other close–lying ones were 33 MeV [97, 98] and 50 MeV [99]. It was nevertheless interesting to add a new measurement at 40 MeV with a carbon target in order to have a reference and validate our activation method, hence to be able to more reliably compare the neutron gain provided by heavy water.

15.1 Improvements in experimental method

The experimental method is almost identical the one described in the previous chapters focusing on SPES.

A special aluminium target container, shown in Fig. 15.1, has been constructed at JYFL to accommodate materials considered as possible converters for SPIRAL 2: ^{12}C, D_2O and H_2O.

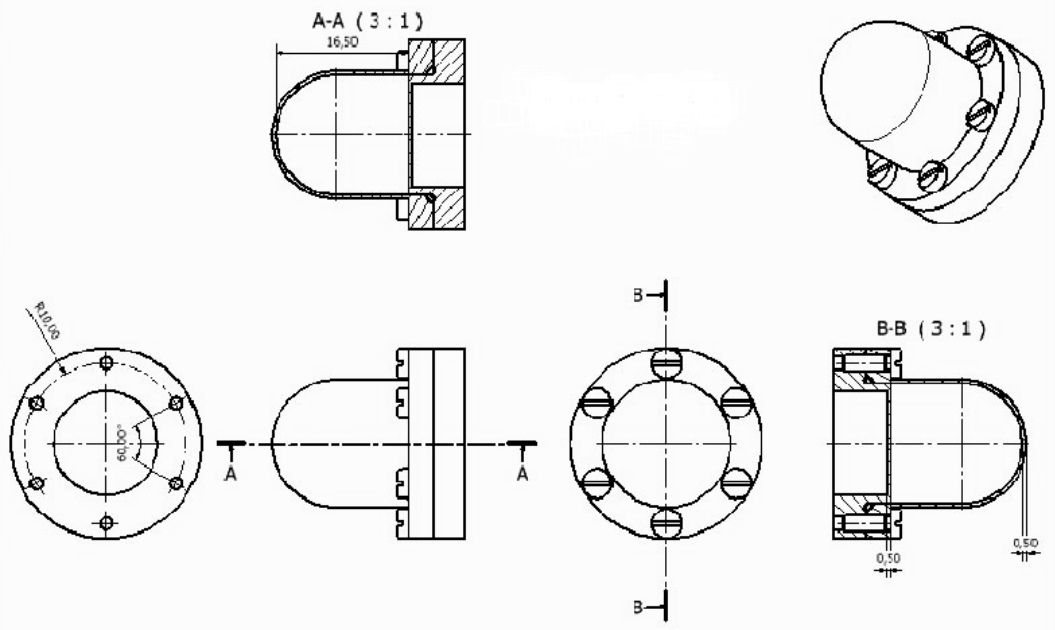

FIGURE 15.1 Special aluminium target container [84]. The bottom lid was isolated with an O–ring in order to be hermetic.

The target has a length of 16.5 mm and a diameter of 15 mm. The aluminium wall and entrance window of the container are 0.5 mm thick. The targets were either a graphite powder of density 1.76 g/cm^3, heavy water or light water. The target has proved to be hermetic, less than 20 mg of D_2O (density 1.1 g/cm^3) has evaporated out of 10.65 g during half a year.

At the angles of 0, 10, 20, 40 and 60 degrees all activation foils described in Chapter 9.2 have been used. Bismuth foils have not been placed at 90°since the previous series of experiments showed that there are too few high-energetic neutrons at this angle. Such set of angles required redesigning the foil support structure.

The deuteron beam was first focused to pass almost fully through a 5 mm hole centred along the symmetry axis. Its energy was set to 42.5 MeV in order to enter the target with 40 MeV. The carbon target was irradiated first in order to validate the method by comparison with TOF data. Irradiations of heavy and light-water targets were performed several months later to allow for a thorough analysis and validation of the measurement by comparison with TOF data. The carbon measurement was repeated shortly also during water runs in order to verify the stability of the results. Due to various issues faced in the February and May 2008 runs, including problems with the Ge detector, the calculated neutron flux generated by the carbon converter varied by up to 20% between the three measurements. Therefore, in order

to better control the scale, another experiment was conducted in September 2008. The carbon, heavy-water, light-water and again the carbon targets were irradiated one after another, each during 4 hours with a 2 nA current. Since only the normalisation of scale was of interest, fewer foils were used and fewer reactions exploited than in the first series of measurements. The consistency of the carbon data established the stability of operation during that control measurement.

A special effort was devoted to the measurement of the beam current. The intensity of the deuteron current (positive deuterium ions) was decreased to 1–2 nA and the irradiation time increased to 14 h yielding less safety interruptions and more stable beam from Jyväskylä's K–130 cyclotron. Fig. 15.2 shows the beam structure in May and September 2008 runs – the beam quality was better than during the first irradiation for SPES (Fig. 13.1).

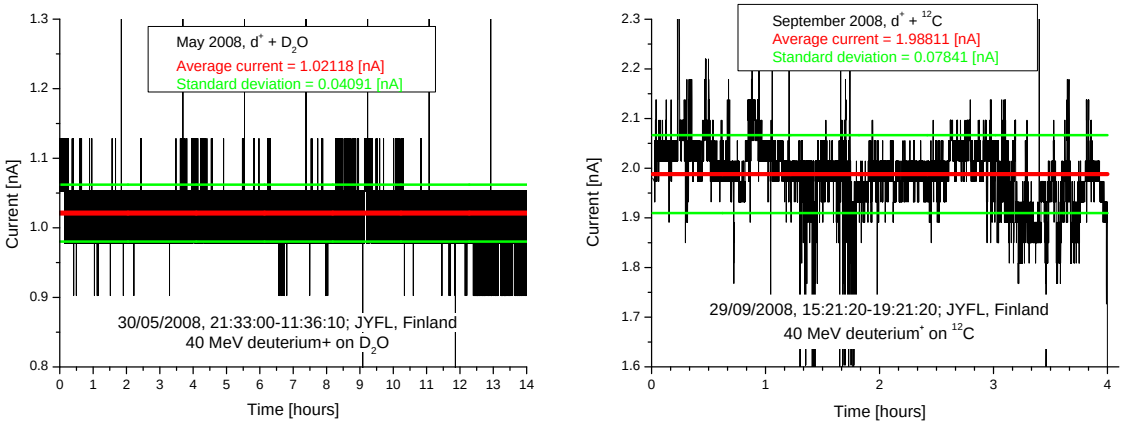

FIGURE 15.2 Average beam current during May D_2O (left) and September ^{12}C (right) irradiations.

The calibration of the current integrator was checked by replacing the Faraday cup with an external well-calibrated 2 nA current source built by G. Tyurin.

In addition, a 0.1 mm aluminium foil was placed upstream of the targets to monitor the beam via the production of ^{24}Na. The beam energy was increased from 42.5 to 43.0 MeV to account for the additional energy loss. The aluminium foil method appeared to be a good way to cross–check the correctness of the results. The details of that method are presented in Appendix B.2. The currents obtained using the Faraday cup and the production of ^{24}Na were reproduced using a cross–section $\sigma(^{27}Al(d, \alpha)^{24}Na)$ of 24.6 mb, in good agreement with an interpolation of the ENDF data (26.3(26) mb [91]). These data were used to renormalise the first series of measurements, namely they had to be multiplied with factors of 1.07(4) for the carbon, 0.87(6) for the heavy–water and 0.94(9) for the light–water targets.

15.2 Results

Fig. 15.3 summarises the activation measurement of 40 MeV d+^{12}C for SPIRAL 2. The experimental integrals are given in Table 15.1.

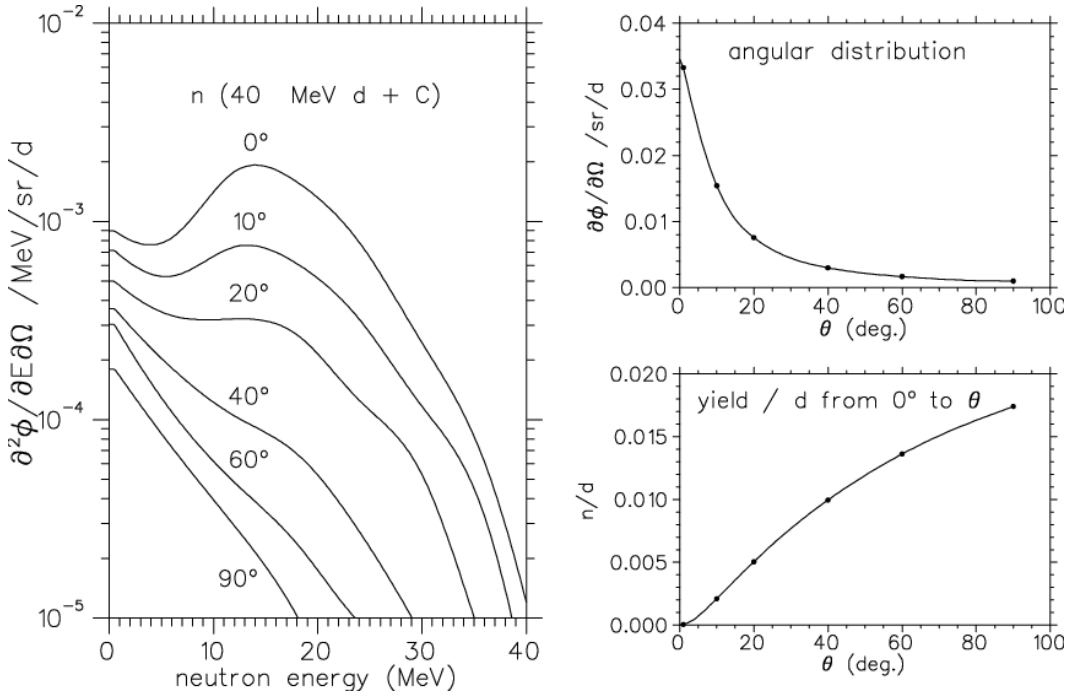

FIGURE 15.3 Neutron yield from d+^{12}C at various angles measured at JYFL in the framework of the SPIRAL 2 experiment. On the left: spectra deduced from unfolding overlap integrals, on top right: integrals of spectra of energy > 4 MeV versus angle, on bottom right: integrals of curves on top right multiplied by 2π sin(θ) giving the neutron flux in a revolution cone where a fission target is going to be placed.

TABLE 15.1 Experimental overlap integrals $\langle\sigma \cdot n\rangle$ expressed in mb/sr per deuterons of 40 MeV energy stopped in a carbon target. Errors included are statistical only.

Reaction \θ[°]	0	10	20	40	60	90
$^{27}Al(n,\alpha)$	2.017(61)	0.840(28)	0.355(14)	0.115(5)	0.052(3)	0.028(2)
$^{59}Co(n,2n)$	16.92(76)	6.09(28)	2.32(11)	0.663(32)	0.252(20)	0.087(5)
$^{59}Co(n,p)$	1.141(54)	0.494(30)	0.229(20)	0.066(5)	0.057(5)	0.022(3)
$^{59}Co(n,\alpha)$	0.546(30)	0.215(16)	0.083(8)	0.031(4)	0.013(5)	0.006(2)
$^{58}Ni(n,2n)$	1.318(44)	0.492(18)	0.194(9)	0.049(3)	0.019(2)	0.005(1)
$^{58}Ni(n,p)$	10.07(35)	5.23(20)	2.63(11)	1.04(5)	0.588(23)	0.366(14)
$^{115}In(n,n')$	5.23(31)	3.02(18)	1.59(10)	0.809(49)	0.488(31)	0.335(22)
$^{209}Bi(n,4n)$	2.676(54)	1.441(30)	0.555(13)	0.087(4)	0.032(3)	-

Errors included in Table 15.1 are contributions from counting statistics and γ-ray branching ratios only. Errors induced on the energy–integrated neutron flux are

estimated to be near 5%. When adding other sources of errors that apply in the same way to all values in the table (mostly Ge efficiency, deuteron current and solid angle covered by the foils) the final error on the integrated flux is estimated to be 12%.

It is interesting to note that the neutron yield of d+^{12}C at 40 MeV is the same as for p+^{13}C at 100 MeV, which has been the energy originally foreseen for SPES.

The comparison of neutron yield above 4 MeV emitted up to a given angle (in cone) from the d+^{12}C reaction between the TOF measurements and our activation measurements is shown in Fig. 15.4.

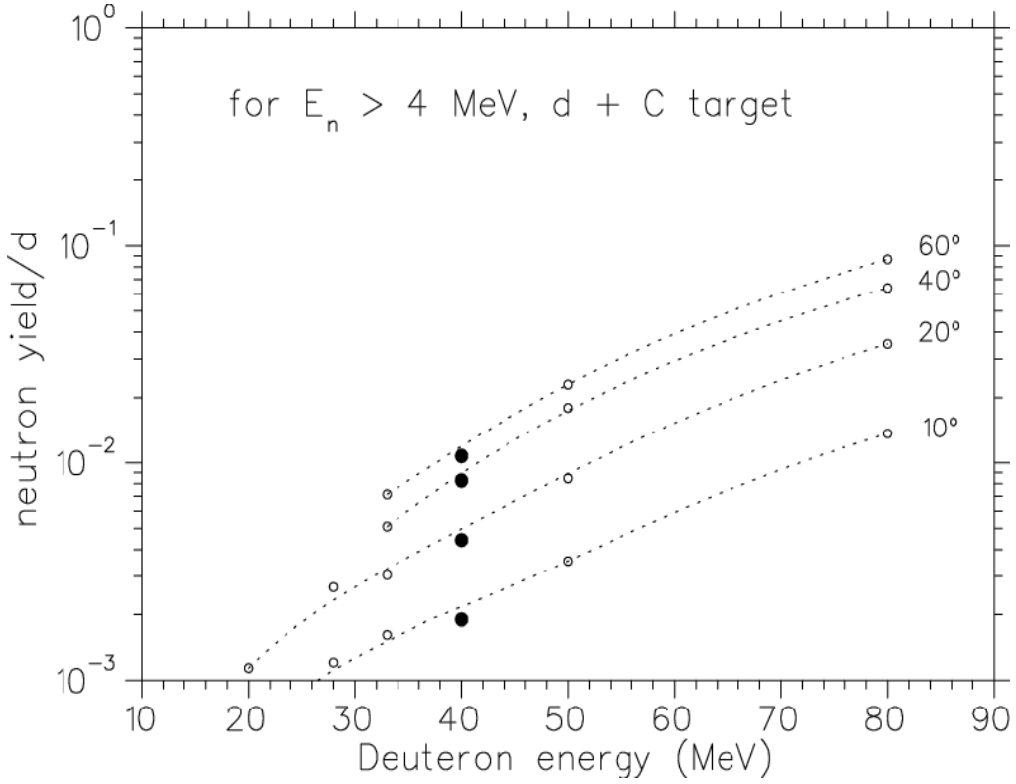

FIGURE 15.4 Comparison of number of neutrons from the d+^{12}C reaction emitted per deuteron in revolution cones of various angles and energy higher than 4 MeV with various TOF data connected by lines (lines are to guide the eye, not a theoretical description). Our results are marked with full dots. Open circles represent TOF results: Orsay-GANIL at Orsay [101,102] at 20–28 MeV; measurements at Louvain-La-Neuve and INS Tokyo [97,98] at 33 MeV; at JYFL [99] at 50 MeV; and at KVI [62] at 80 MeV.

Fig. 15.4 validates our method - the results are in fairly good agreement with well-established TOF data. The deviation with respect to interpolated TOF values is less than the 12% estimated systematical error. It proves that the scale of the measurement to be correct.

Summaries of activation measurement of 40 MeV d+D_2O and d+H_2O are presented in Fig. 15.5 and 15.6.

The spectral shapes differ a little for the three studied materials. There are more counts at low energies with D_2O and H_2O. For light–water it might be due to the

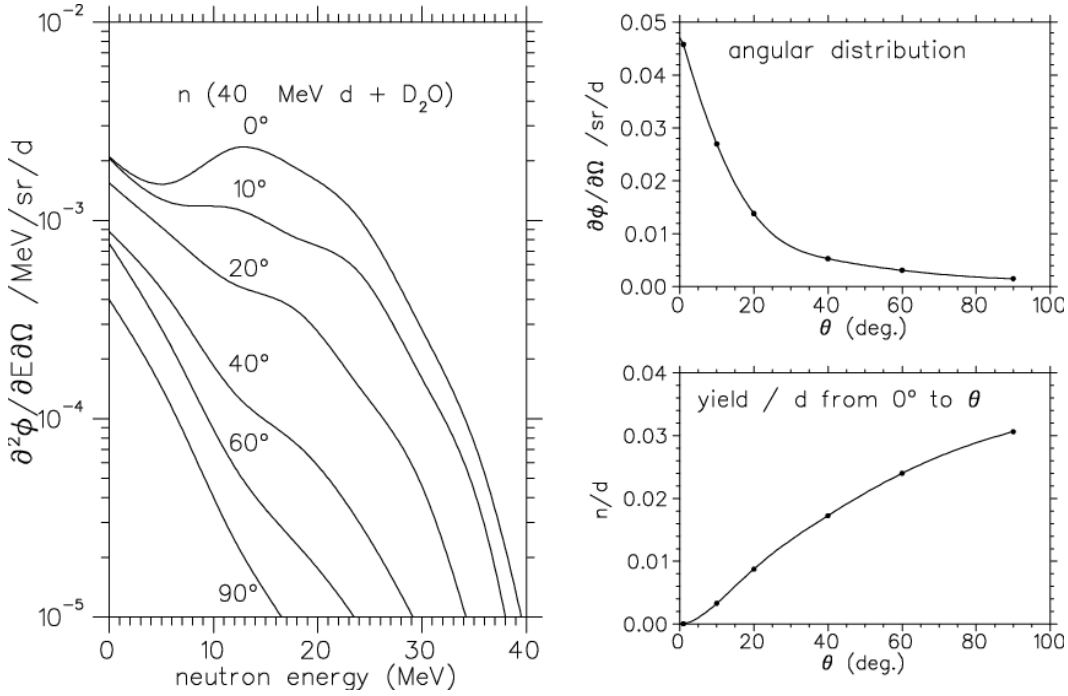

FIGURE 15.5 Neutron yield from d+D_2O at various angles measured at JYFL in the framework of the SPIRAL 2 experiment. On the left: spectra deduced from unfolding overlap integrals, on top right: integrals of spectra of energy > 4 MeV versus angles, on bottom right: integrals of curves on top right multiplied by 2π sin(θ) giving the neutron flux in a revolution cone where a fission target is going to be placed.

neutron moderation effect, for heavy–water it is possibly due to the opening on a new reaction channel: d(D,^{3}He)n. The location of the excess of neutrons at low energy does not however help proportionally to increase the number of fissions since the cross-section peaks around 40 MeV [91].

The experimental integrals for D_2O and H_2O are given in Tables 15.2 and 15.3 respectively, the meaning of errors is the same as in Table 15.1.

15.3 Comparison with simulation by MCNPx

Table 15.4 compares our data with neutron yields calculated by M. Fadil at GANIL with the Monte Carlo code, MCNPx version 2.6.0 [103].

The MCNPx simulations were performed in a manner similar to our experimental parameters: the 4.0 mm diameter, 40 MeV deuteron beam entered the targets having the dimensions and density as that measured in 2008. Further details related to the simulations can be found in [94].

The different trend of experimental and calculated yield versus angle shows the importance of measuring C, not only to get a reference for relative values, but to

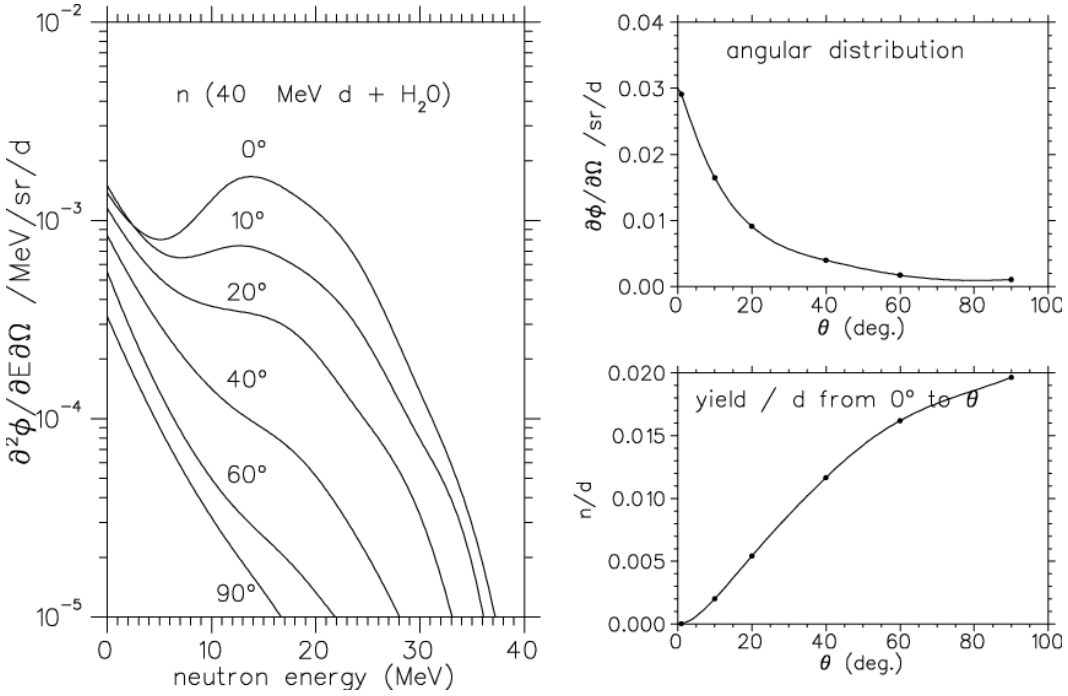

FIGURE 15.6 Neutron yield from d+H_2O at various angles measured at JYFL in the framework of the SPIRAL 2 experiment. On the left: spectra deduced from unfolding overlap integrals, on top right: integrals of spectra of energy > 4 MeV versus angles, on bottom right: integrals of curves on top right multiplied by 2π sin(θ) giving the neutron flux in a revolution cone where a fission target is going to be placed.

TABLE 15.2 Experimental overlap integrals $\langle \sigma \cdot n \rangle$ expressed in mb/sr per deuterons of 40 MeV energy stopped in a heavy–water target. Errors included are statistical only.

Reaction \ θ[°]	0	10	20	40	60	90
$^{27}Al(n,\alpha)$	2.53(12)	1.254(62)	0.444(28)	0.158(16)	0.051(8)	0.022(6)
$^{59}Co(n,2n)$	28.4(18)	12.06(86)	3.86(25)	1.12(8)	0.351(27)	0.089(9)
$^{59}Co(n,p)$	1.630(88)	0.786(47)	0.313(23)	0.109(8)	0.042(6)	0.015(2)
$^{59}Co(n,\alpha)$	0.742(57)	0.356(34)	0.110(17)	0.044(8)	0.010(5)	0.003(2)
$^{58}Ni(n,2n)$	1.70(10)	0.776(50)	0.226(21)	0.065(7)	0.023(4)	0.003(2)
$^{58}Ni(n,p)$	16.3(11)	9.60(62)	4.62(31)	2.03(15)	1.01(7)	0.485(41)
$^{115}In(n,n')$	7.52(43)	5.10(29)	2.66(16)	1.57(10)	0.880(56)	0.433(33)
$^{209}Bi(n,4n)$	3.65(24)	1.96(10)	0.482(25)	0.131(8)	0.023(3)	-

show the limits of models.

Calculations of neutron production by the 40 MeV deuteron beam adopted for SPIRAL 2, made at CEA-Saclay using MCNPx Monte-Carlo codes, predict that the neutron yield of a normal water converter should not be much smaller than that of natural carbon, while the yield of a D_2O converter is expected to be significantly

TABLE 15.3 Experimental overlap integrals $\langle \sigma \cdot n \rangle$ expressed in mb/sr per deuterons of 40 MeV energy stopped in a light–water target. Errors included are statistical only.

Reaction \ θ[°]	0	10	20	40	60	90
$^{27}Al(n,\alpha)$	1.720(64)	0.850(33)	0.407(17)	0.123(6)	0.045(3)	0.023(2)
$^{59}Co(n,2n)$	13.93(62)	6.29(29)	2.37(12)	0.571(31)	0.207(13)	0.079(6)
$^{59}Co(n,p)$	0.923(42)	0.494(28)	0.219(26)	0.067(5)	0.027(4)	0.013(3)
$^{59}Co(n,\alpha)$	0.425(24)	0.207(18)	0.094(8)	0.026(3)	0.008(2)	0.005(1)
$^{58}Ni(n,2n)$	1.086(39)	0.438(18)	0.177(11)	0.039(3)	0.015(2)	0.005(1)
$^{58}Ni(n,p)$	9.23(36)	5.27(22)	3.12(13)	1.33(7)	0.515(25)	0.331(17)
$^{115}In(n,n')$	4.59(27)	3.20(19)	2.06(12)	1.00(7)	0.478(32)	0.302(22)
$^{209}Bi(n,4n)$	1.682(38)	0.992(23)	0.386(13)	0.081(3)	0.026(2)	-

TABLE 15.4 Neutron flux integrated above 4 MeV for the 3 targets, per deuteron and per steradian.

θ[°] \ target	C		D_2O		H_2O	
	exp.	calc.	exp.	calc.	exp.	calc.
0	0.0309	0.0182	0.0408	0.0300	0.0262	0.0133
10	0.0136	0.0128	0.0223	0.0203	0.0136	0.0113
20	0.00632	0.00868	0.00954	0.0130	0.00691	0.00782
40	0.00215	0.00470	0.00360	0.00759	0.00251	0.00356
60	0.00105	0.00177	0.00165	0.00353	0.00092	0.00103
90	0.00061	0.00043	0.00076	0.00086	0.00055	0.00027

higher.

The measured gain in neutron yield for D_2O and H_2O with respect to ^{12}C, varies with energy, it is respectively around 3 and 2 considering only the energies below 2 MeV, but this excess is quite soon cancelled near 10 MeV and above, where the relative yield becomes even less than 1 for H_2O, and just 1.1 more for D_2O. We observed no gain with light water and about 1.4–1.5 with heavy water in neutron flux integrated for E > 4 MeV inside a cone of 50°, which resembles the SPIRAL 2 target. Our result thus provide a practical guideline for SPIRAL 2.

15.4 Impact of our measurements for SPIRAL 2

The modelling suggested the optimal dimensions for the fission target: diameter of 8 cm and 8 cm length. Since there is actually less neutron flux than calculated at large angles and more at small angles, it may seem better to reduce the diameter

and increase the length of the target, if its total weight is to be conserved. On the other hand, one should also consider other aspects than the sole number of fissions. Since the path of fission products to the ion–source (the exit hole is on the side of the cylindrical target) is proportional to the radius R, it could pay off to lose relatively few fissions by reducing R, but have the nuclei exit much more quickly[1]. This would also be useful in helping for construction of the oven that houses uranium and in management of waste material ($\sim R^2$).

The calculation has overestimated the neutron flux. According to simple geometric estimates, i.e. without considering the actual path of the neutron inside the target but assuming a straight line (the distance from where it enters to where it exits), the neutron production is overestimated by factor ranging from 2.0 to 2.4 (depending on the mean absorption depth). In the presently designed 2.2 kg UC_x target, the number of fissions should be rather 2.0 to 2.5 $\cdot 10^{13}$ instead of 5 $\cdot 10^{13}$ fissions/s.

It has been shown that there is no gain with respect to ^{12}C in neutron yield with light water (0.010 n/d for $\theta \leq 50°$, SPIRAL 2 target) and about 1.5 with heavy water and 1.4 in the number of fissions (the gain is mostly located in the low energy region of the spectrum, as shown in Fig. 15.7).

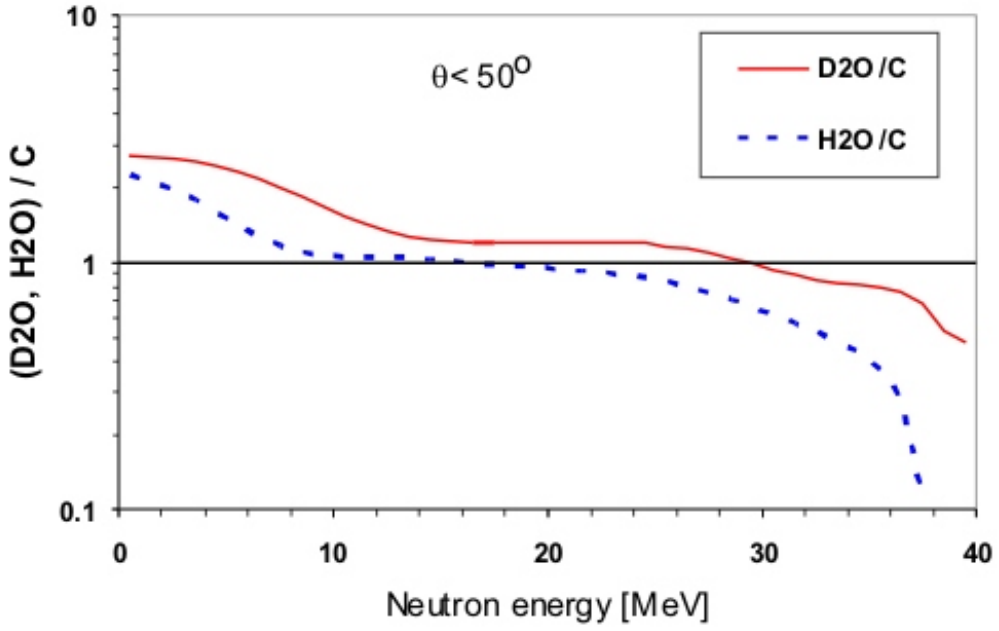

FIGURE 15.7 Ratios of neutron yields per incident deuteron emitted into a forward cone of 50^o on SPIRAL 2 targets.

The decision for choosing the SPIRAL 2 converter is thus rather to be based on the technology than the intrinsic conversion factor. We further stress the discrepancy

[1]Based on simulations, the half–attenuation distance of the number of fissions in high density UC_x is 3.7 cm. Thus adding length is not recommended, as it adds few fissions and increases the amount of uranium to be disposed of as waste.

of the TOF data at 40 MeV by Hagiwara et al. with all other measurements, their neutron yield being about 2 times lower. Importantly, this measurement has been a benchmark for various applications, among which are the SARAF neutron source (2mA, 40 MeV d) at the Weizmann Institute, Israel [95], or the International Fusion Materials Irradiation Facility to be built in Japan[2] for the purpose of preparation for the ITER fusion reactor to be located at Cadarache, France.

[2]IFMIF should be built in Japan after the years 2015–2020. The current baseline is: 2 accelerators, each of 40 MeV, 125 mA deuteron beam (yielding a summed beam current of 250 mA [66]). The converter is a flowing lithium loop. The estimated cost is $\gtrsim$10 x the cost of SPIRAL 2.

16 Overview of neutron yield measurements

Determination of neutron yields for protons and deuterons impinging on carbon, light- and heavy–water targets are of interest for various areas of applied physics. One area is the generation of intense beams of exotic nuclei in Radioactive Ion Beam facilities. The deficiency of experimental data caused noticeable discrepancies of predicted yields for neutron converters envisaged for SPES and SPIRAL 2 projects. Measurements of neutrons' angular and energy distributions performed with activation and TOF techniques have eliminated the controversies and provide accurate guidance on possible converters for RIBs.

The summary of our measurements together with p+^{12}C as the benchmark from the MCNPx simulation code is shown in Fig. 16.1. The neutron fluxes integrated over energy and solid angle for several production schemes are compared.

Measurements for p+^{13}C (20, 25 and 40 MeV presented in this thesis) are the only systematic experiments of this kind. An increase of neutron yield is visible at the same proton energy with respect to p+^{12}C. Our activation measurement of d+^{12}C at 40 MeV fits well into the systematics of the TOF measurements thus validating the activation method used here. In the absence of comprehensive data for d+^{13}C, d+^{12}C remains the best production scheme based on a carbon target. Due to the high cost of ^{13}C enriched target, it is likely that any future carbon converter will be constructed from ^{12}C. The neutron flux for d+D_2O at 40 MeV, also measured in this work, is the highest, but the gain in number of fissions is modest since the extra neutrons are located below a few MeV.

The implications of our measurements are striking. The result for p+^{13}C has led to a revised design of SPES with protons directly on uranium, now under investigation. The measurements of d+^{12}C and d+D_2O showed a gain of 1.5, which alone is not sufficient to justify a redesign of the converter for SPIRAL 2. However, the factor of 2 – 2.5 decrease in the number of fissions combined with the narrower angular distribution compared to calculations suggest a new optimisation of the geometry of the fission target has to be carried out. Considering the deficiencies of simulation codes used to design the converter+target module of SPIRAL 2, an experiment in order to validate production rates of nuclei in the target has been recommended by the project direction.

In conclusion, these measurements have had a high impact on the design of

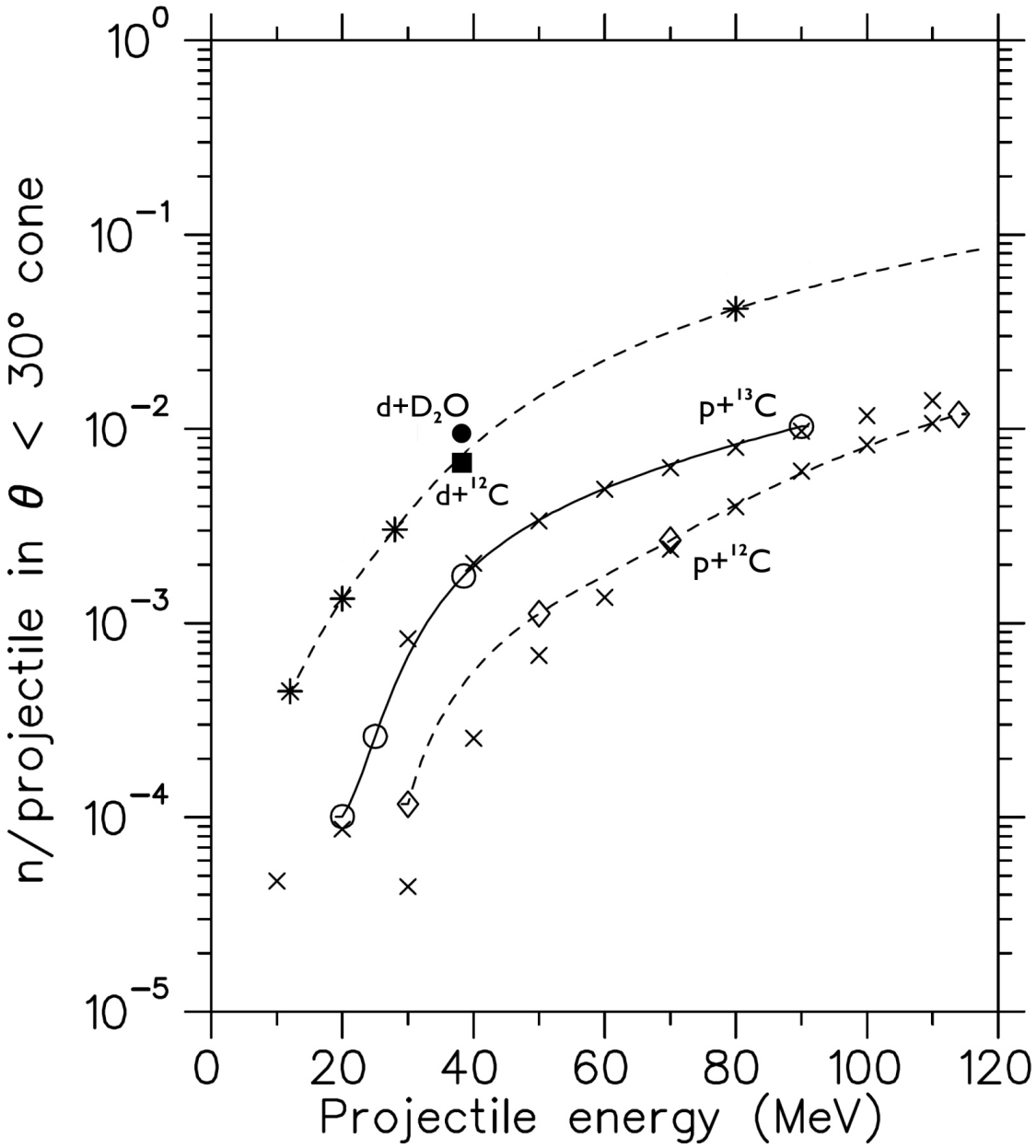

FIGURE 16.1 Energy and solid angle integrated neutron yields per projectile, E_n>4 MeV, forward cone of 30^o. Our measurements for protons on ^{13}C are marked by circles connected by the solid line. The full square and circle are our measurements for 40 MeV deuterons on natural carbon and heavy–water, respectively. p+^{12}C data used to benchmark MCNPx (diamonds) is shown for comparison. Calculations with PRIZMA for protons on both targets are marked with crosses. Stars are from works of the GANIL and IPN–Orsay groups for deuterons on natural carbon [101].

the next generation of European Radioactive Ion Beam facilities and on the benchmarking of Monte Carlo codes.

The results presented in this thesis are relevant not only for SPES and SPIRAL 2, but also for other areas of applied physics. Our data can be useful e.g. for complementing cross–section databases for the design of materials to be submitted to high neutron flux in next generation reactors, e.g. in the ITER fusion reactor project. A further important area of research is medicine with irradiation or BNCT at lower energy than that studied here but potentially a field of application of our method.

A APPENDIX: PART I

A.1 Mandelstam variables

The Mandelstam variables are numerical quantities used in theoretical physics to encode the energy, momentum, and angles of particles in a scattering process in a Lorentz–invariant way. Using natural units with c = $\hbar$ = 1, when considering a particle with energy E, a rest mass m_0, and a momentum **p**, we can write its four–momentum as: P = (E, **p**) = (E, p_x, p_y, p_z). The Mandelstam variables s, t and u are used to describe the scattering processes of 2 $\rightarrow$ 2 particles. With P_1 and P_2 being the four–momenta of the incoming and P_3 and P_4 of outgoing particles, the variables are defined as:

$$s = (P_1 + P_2)^2 = (P_3 + P_4)^2 \tag{A.1}$$

$$t = (P_1 - P_3)^2 = (P_2 - P_4)^2 \tag{A.2}$$

$$u = (P_1 - P_4)^2 = (P_2 - P_3)^2 \tag{A.3}$$

$\sqrt{s}$ is the center–of–mass energy of the colliding particles and $\sqrt{t}$ is the momentum transfer in the reaction. In ion collisions, $\sqrt{s_{NN}}$ denotes the center–of–mass energy of the collision per nucleon pair.

It is worth noting that $s + t + u = m_1^2 + m_2^2 + m_3^2 + m_4^2$, where m_i is the mass of particle i. Hence s + t + u = 0 for massless particles.

A.2 Beam Beam Counter at PHENIX experiment at RHIC

The Beam Beam Counter (BBC) is used as a forward detector in PHENIX. It is located symmetrically around the IP as depicted in Fig. A.1.

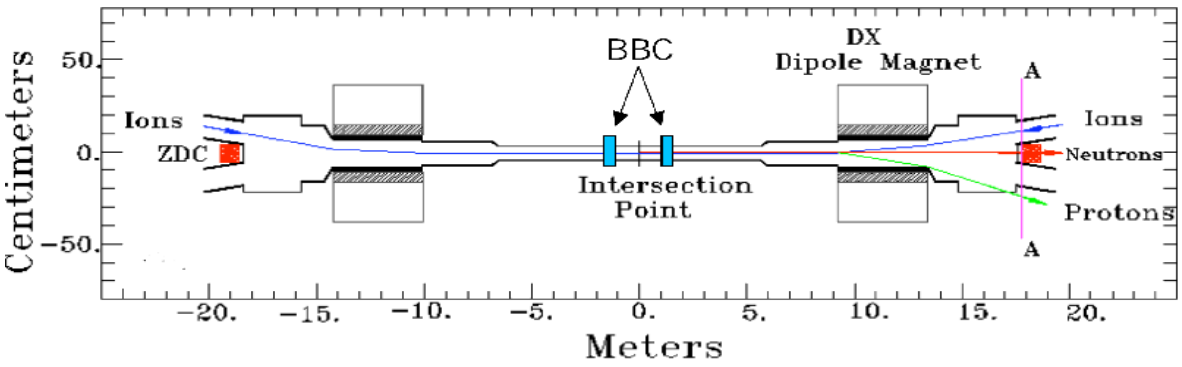

FIGURE A.1 Placement of Beam Beam Counter in PHENIX.

The technology chosen for the BBC is based on mesh–dynode photomultiplier tubes (Hamamatsu R6178) equipped with 3 cm quartz on the head of the PMT as a Cherenkov radiator. Fig. A.2 shows the assembly of the BBC.

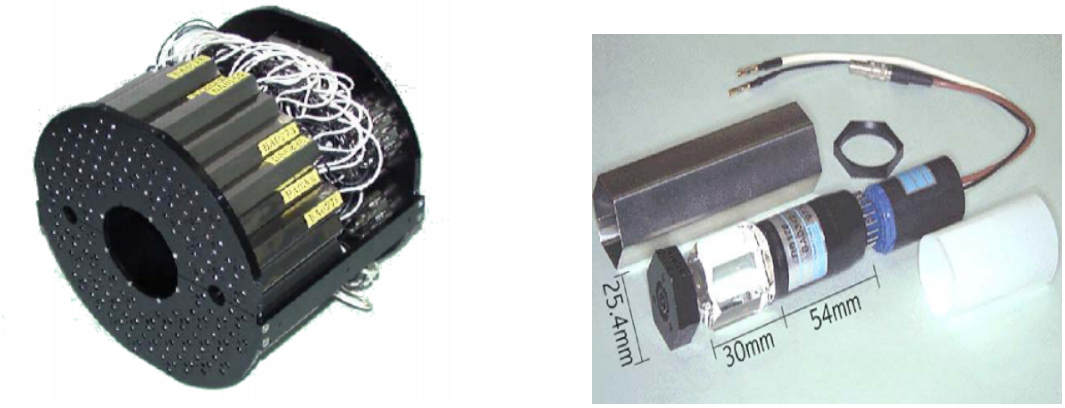

FIGURE A.2 Beam Beam Counter array at PHENIX (left). The outer diameter of the BBC is 30 cm and the inner diameter is 10 cm with clearance between the beam pipe and the BBC of 1 cm. A single BBC (right) consisting of 1 mesh–dynode photomultiplier tube mounted on a 3 cm quartz radiator.

The BBC functions are similar to those of the T0 detector. BBC determines the collision vertex, a centrality of a collision, a reaction plane, serves as minimum bias trigger and as a start for the Time Of Flight detector. The vertex, z_{vertex} is calculated as:

$$z_{vertex} = \frac{T_S - T_N}{2} \cdot c, \tag{A.4}$$

where T_S and T_N are an average hit times into BBC South and North (see Fig. A.3), c is the light velocity and L is a distance to the nominal vertex (144.35 cm).

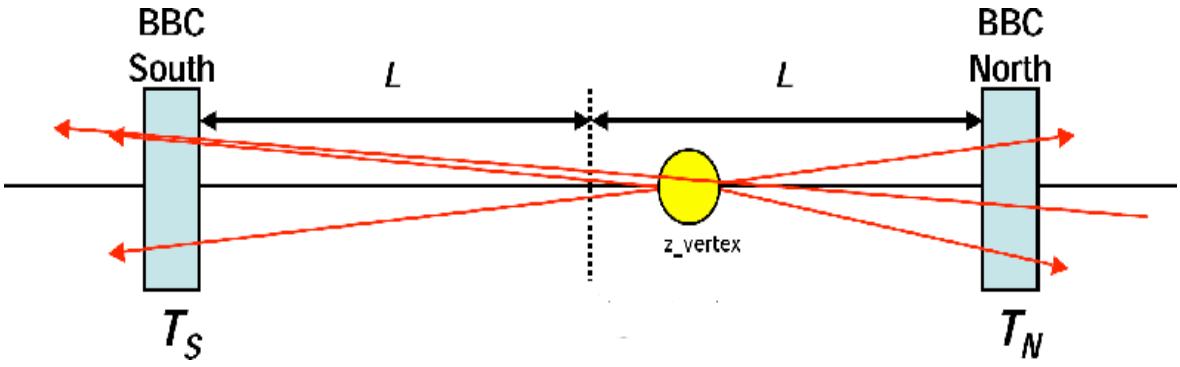

FIGURE A.3 Vertex determination with BBC.

The time of the collision (t_0) is determined as:

$$t_0 = \frac{T_S + T_N - 2L/c}{2}. \tag{A.5}$$

Similar to the T0 detector, some 50% of events registered by the BBC are external tracks coming mostly from the beam pipe that is made of beryllium (thickness 1.02 mm, length up to 75 cm on both sides of the IP) and stainless steel (thickness 1.24 mm, length up to 2 m from the IP) at RHIC. The BBC triggering efficiency for $Au + Au$ collisions is $\sim$ 93%.

A.3 Detector Construction Database for T0 detector

The Detector Construction Database (DCDB) [48] has been developed with the purpose of storing information about ALICE subdetectors. The subdetectors are designed, tested and assembled in various laboratories around the world. Many subdetector components have to migrate between manufacturers and laboratories during the various phases of the production. These movements are traced and registered, as well as the physical location of components with the proper ownership and related data. The component tests and measurements produce large amounts of data. The most relevant results are stored in the database for further analysis and use.

To avoid potential communication problems over WAN (Internet), a model with distributed local (satellite) databases located in labs involved in subdetector production and the central repository located at CERN has been selected as a baseline for DCDB. Satelite databases contain experimental data from the components tests, working copies of data from the central repository and partial copies of metadata (e.g. dictionaries). The central repository is placed at CERN. It contains a central inventory of components, copies of data from laboratories, metadata. Messages between satellite databases and central repository are passed in XML, mainly off-line (batch processing), with no satellite–satellite communication.

Oracle has been selected as a database management system (DBMS) for the central repository at CERN. MySQL, PostgreSQL and Oracle were DBMS possibilities for satellite databases.

T0 DCDB consists of a static (Dictionary Wizard) and a dynamic part (Rabbit). Fig. A.4 presents a view of Dictionary Wizard populated with T0 data. The dictionaries have a hierarchical structure. On top of this hierarchy is a database table that contains short descriptions of detectors used in the ALICE experiment. Each detector consists of components (e.g. Photomultiplier tube FEU–187 for T0 detector), which are described in the Wizard. After completing the registration the components' parameters, processes the hierarchical dependencies are defined. All components belonging to a given detector should be defined in the dictionaries - it simplifies collecting and analysing the data.

Rabbit application is an interface between the user and the data structure storing the data related to subdetectors construction. It allows the user to browse, insert and modify data concerning components, their parameters, processes performed, etc. Rabbit provides a front–end to data transfer mechanism and some simple visualisation tools. It is a web–based application and is accessible by means of a web–browser. Fig. A.5 presents a view of Rabbit filled with T0 data.

An unique ALICE identifier is generated automatically by the DCDB when a new component is entered. Based on the identifier the labels with bar–codes are generated which allow one to uniquely mark each component. Around 500 labels

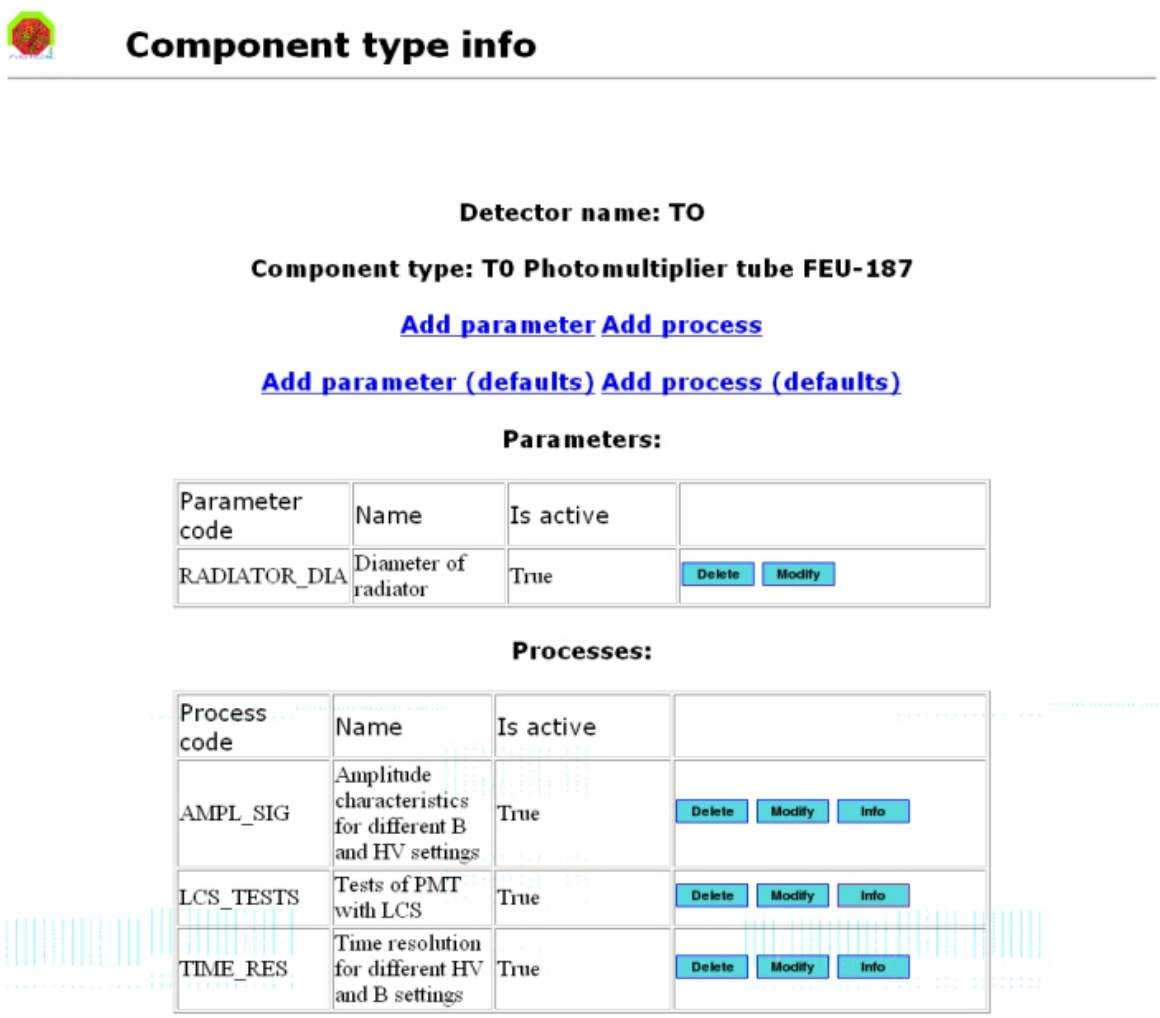

Component type info

Detector name: TO

Component type: T0 Photomultiplier tube FEU-187

Add parameter Add process

Add parameter (defaults) Add process (defaults)

Parameters:

Parameter code	Name	Is active	
RADIATOR_DIA	Diameter of radiator	True	Delete Modify

Processes:

Process code	Name	Is active	
AMPL_SIG	Amplitude characteristics for different B and HV settings	True	Delete Modify Info
LCS_TESTS	Tests of PMT with LCS	True	Delete Modify Info
TIME_RES	Time resolution for different HV and B settings	True	Delete Modify Info

FIGURE A.4 Dictionary Wizard – the static part of T0 DCDB.

were printed for T0 and put on electronics modules and cables during the installation process. For T0 arrays, numbers instead of labels have been used for simplicity (see Fig. A.6).

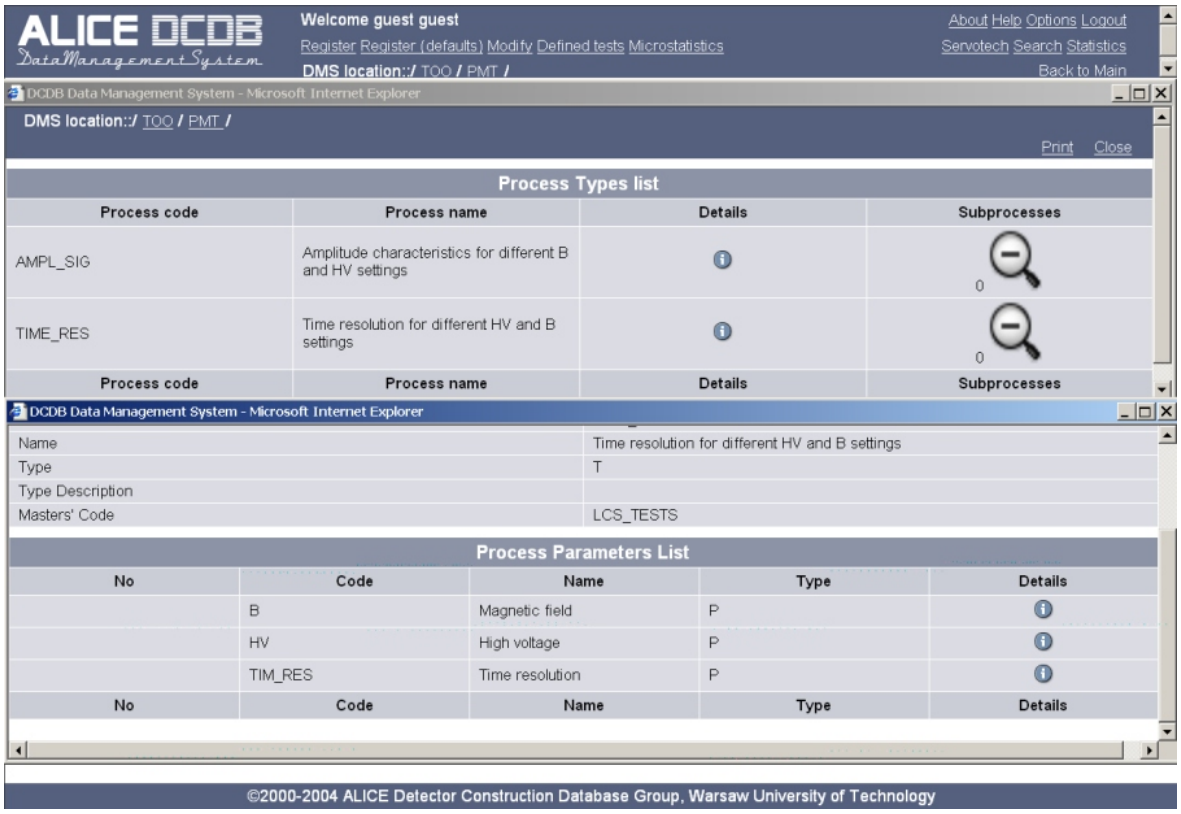

FIGURE A.5 DCDB Data Management System called Rabbit.

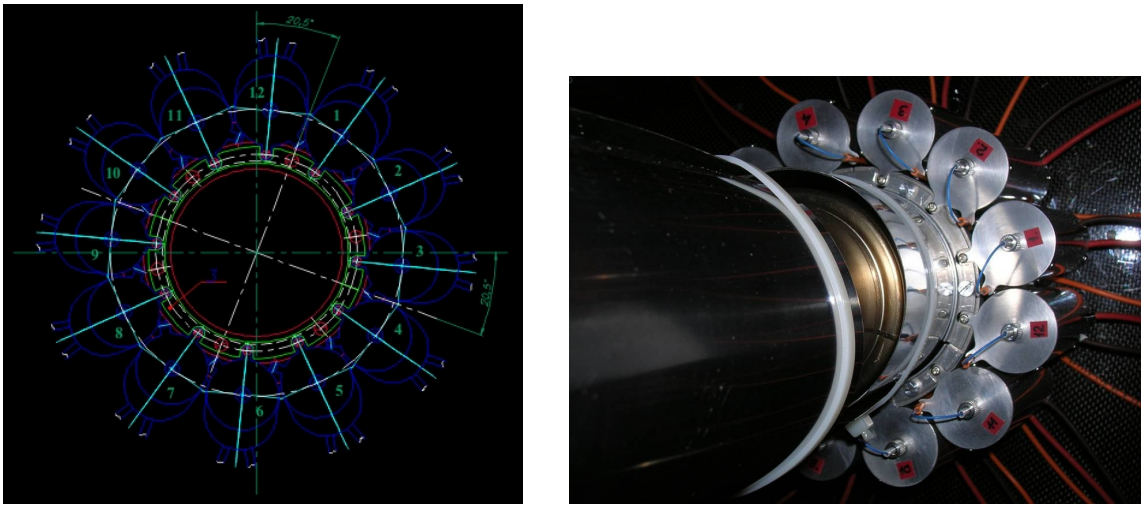

FIGURE A.6 Numbers instead of labels were used for marking T0–C PMTs. On the left – a technical drawing showing the position of each PMT, on the right - T0–C PMTs marked with numbers.

A.4 Installing shoebox on C–side at ALICE Point 2

Most of the T0 parts inside the L3 magnet were installed when the magnet was open. Accessing the C–side one month before the LHC startup when the magnet was closed required preparation of a dedicated Task Procedure. What follows is an example of such document prepared for the purpose of T0 shoebox installation on ALICE C–side.

Task Procedure for ALICE

[Task Procedure = simplified version of the Specific Plan for Health and Safety, adapted for ALICE Collaboration. - PPSPS = Plan Particulier de Sécurité et de Protection de la Santé]

Task to be realized	Installation and checks of T0 shoebox on C-side	
Location of work	Point2, L3 Magnet (closed)	
Dates of work	start 4.08.08	end 08.08.08
Sub-project T0 Heidelberg	Institutes	Jyvaskyla, INR Moscow,
Sub-project Leader	Wladyslaw Trzaska (Jyvaskyla)	phone +358 14 260 2409
Safety link-person	Tomasz Malkiewicz (Jyvaskyla)	phone 16 5810
Work-Package Engineer	Tomasz Malkiewicz	
Local Work Supervisor	Ken Oyama (Heidelberg)	phone 16 2469
Experimental-Area Manager	Sébastien Evrard	phone 16 4821

Persons involved	Tomasz Malkiewicz (Jyvaskyla)	physicist
	Ken Oyama (Heidelberg)	physicist
	Alexander Kurepin (Moscow)	physicist
	Norbert Novitzki (Jyvaskyla)	physicist

Brief description of work procedure

The T0 shoebox on the C-side has still not been installed. It has been given to W. Riegler on 08.07.2008 and found by P. Ijzermans on 01.08.2008. Now it is the last moment to install it on C-side, so that it can be used during test injection from P2 to P3, and K. Oyama can test its performance.

The work procedure consists of:

1) transporting the shoebox to the shoebox panel on C-side
2) disconnecting and reconnecting to the shoebox the T0 signal cables
3) mounting the shoebox on the panel
4) checking the connections and voltages
5) assembling LV power supply cable to the shoebox
6) further maintenance (if needed)
7) cross-checks

Detailed description (step by step) of the work procedure	Risk assessment	Preventive measures (collective)
Transporting the shoebox to the shoebox panel on C-side, disconnecting and reconnecting to the shoebox the T0 signal cables	Confined Space → check Sniffer alarms	All persons have been trained. PPEs = helmet, lamp, harness, oxybox. This activity will be carried out by a team of 3 people: 2 people inside L3, a watcher. Light installation is preferred. The work package engineer and the local work supervisors will ensure that the right access conditions will be implemented (e.g. a temporary platform) in order to minimize the risk of falls.
Mounting the shoebox on the panel	Falling objects.	
Checking the connections and voltages		
Assembling LV power supply cable to the shoebox	Falling objects.	This activity will be carried out by a team of 3 people: 2 people inside L3, a watcher. The work package engineer and the local work supervisors will ensure that the operations that imply the installation / manipulation of heavy objects/tools will only take place when no people are working underneath.
Apply LV and check that voltages are fine using voltmeter.	Electric spark. check Sniffer alarms	Applied voltage is maximum 7 V. Power supply current limit is set to reasonable low (< 1 A). Cables were already tested before and probability to have spark is negligibly small. The work package engineer and the local work supervisors will ensure that there is not flammable gas detected before applying voltage.
Cross-checks		

A.5 Sundry photos part I

FIGURE A.7 Four T0 PMTs during the November 2005 full chain readout test at CERN.

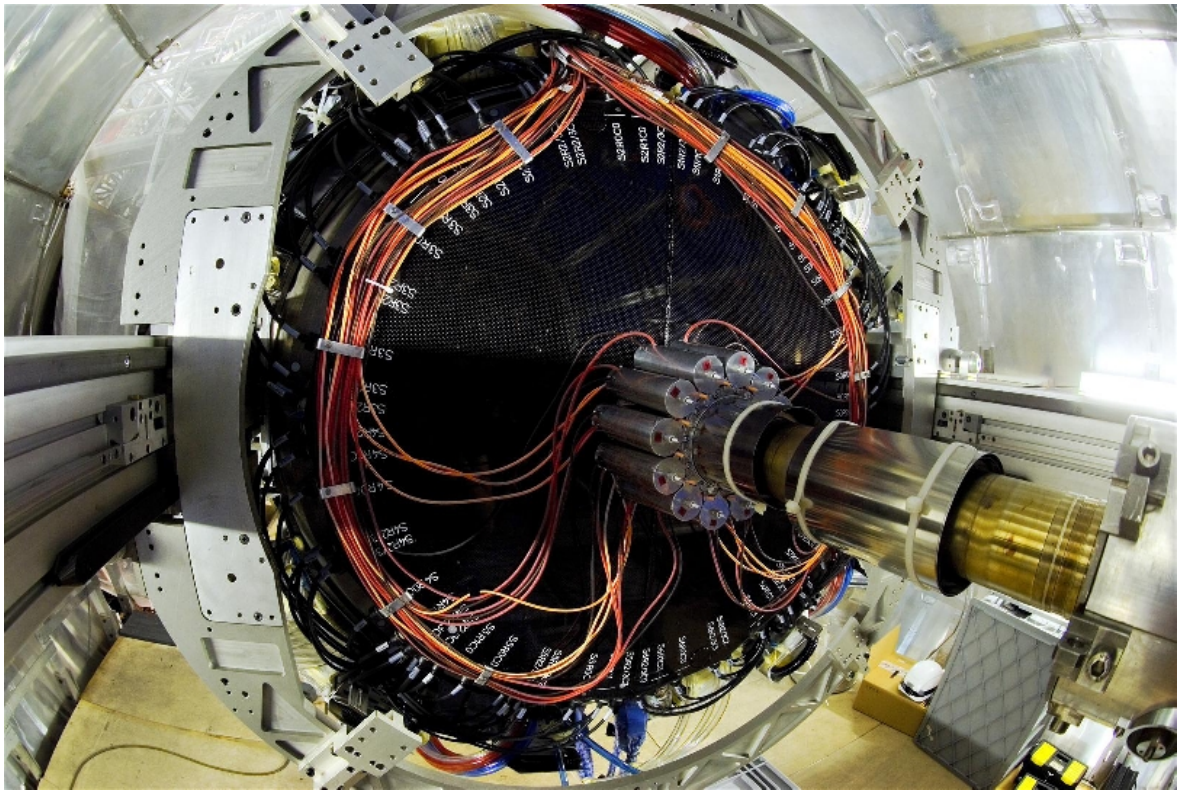

FIGURE A.8 T0–C detector after being installation in the ALICE cavern in April 2007.

FIGURE A.9 ALICE group photo taken in the cavern in summer 2008.

B APPENDIX: PART II

B.1 Effective efficiency for a foil source

Depending on the origin of the γ-rays emitted from within the source volume the efficiency varies due to the geometry and the attenuation in the source. The foils are small enough so that the activity is uniformly distributed. Thus, the efficiency for detecting γ-rays is the average over the volume of the efficiency for point sources, i.e.,

$$\varepsilon = \frac{\int \varepsilon(r,\theta,z)\, r\, dr\, d\theta\, dz}{\int r\, dr\, d\theta\, dz} \tag{B.1}$$

The origin of coordinates is along the axis of the coaxial Ge-detector at a distance D from the front face of the crystal. The foils are placed with the flat surfaces perpendicular to the detector axis (z). The narrow side has a length L. Our formalism has been introduced in a series of reports from the Legnaro laboratories [85]. In the following a simplified but still accurate formalism is presented.

In practice, the foil area is less than one fifth of the crystal front area and the thickness L is a few percent of the distance D. A first–order correction based on:

$$\varepsilon(r,\theta,z) = \varepsilon_0\, f_a(r,\theta)\, f_z(z) \tag{B.2}$$

can be used, where the essential property is to keep the functions of the coordinates of area and thickness separable. Here, ε_0 is the efficiency for a point source[1] at the origin of coordinates $(r=0,\theta,z=0)$, which can be calculated as:

$$\varepsilon_0 = e^u \tag{B.3}$$

$$u = a_0 + a_1 \cdot ln\left(\frac{E}{E_0}\right) + a_2 \cdot ln^2\left(\frac{E}{E_0}\right) \qquad if\ \ E < E_0 \tag{B.4}$$

$$u = a_0 + a_1 \cdot ln\left(\frac{E}{E_0}\right) \qquad if\ \ E > E_0. \tag{B.5}$$

[1]The standard sources at JYFL have a diameter not exceeding 2 mm, which is regarded to be punctual when compared to the size of the foils: 1 mm thick and 25 $\times$ 25 mm^2 area each.

Here E is the γ–energy, E_0 is the energy above which the dependence between energy and efficiency becomes straight (in log(efficiency) versus log(energy) coordinates – see Fig. B.1) and a_i are constants determined by fits of the experimental efficiencies obtained using conventional methods with calibrated sources.

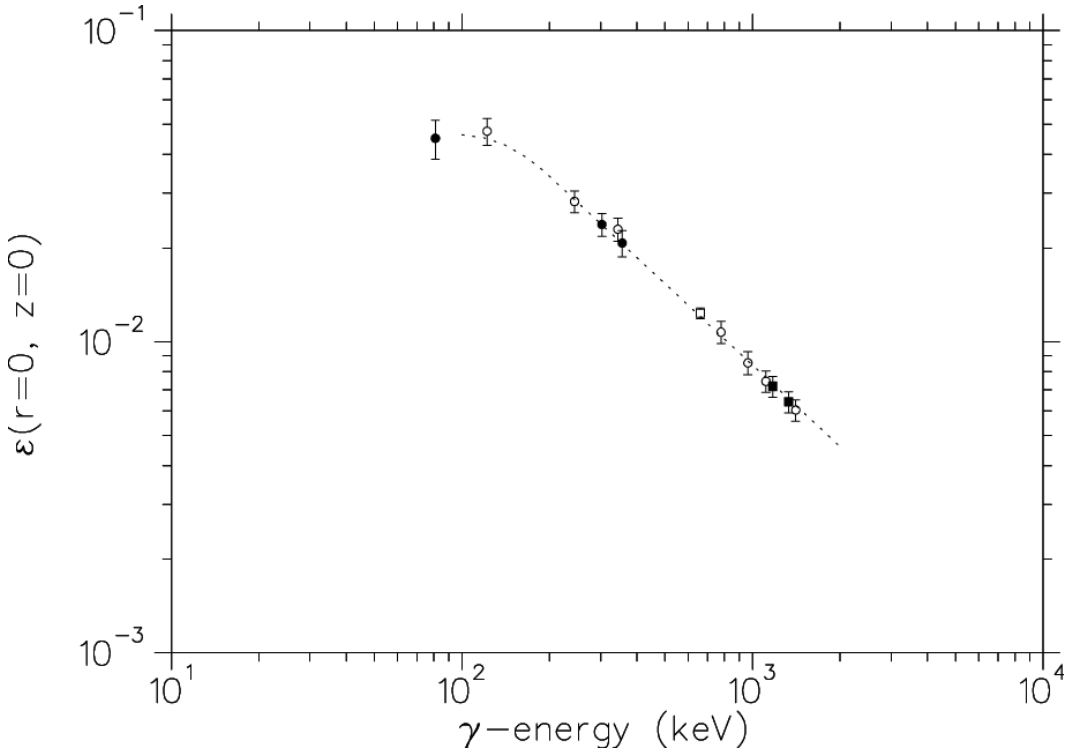

FIGURE B.1 Efficiency plot from September 2008 based on a calibration performed before the irradiation. The symbols represent four calibration sources: ^{133}Ba, ^{152}Eu, ^{60}Co and ^{137}Cs. The energy limit, E_0, where linear and quadratic functions are connected is 200 keV.

Below the E_0 the quadratic term helps to extend the fitted region, usually down to about 100 keV with reasonable accuracy. Continuity of value and derivative is satisfied by the presented formula.

The other factors in Eq. B.2 are the corrections.

$$f_a(r) \;=\; 1 + a\left(1 \,+\, b\, sin(\theta - \theta_0)\right)\ (r/R)^2 \tag{B.6}$$

describes the variation with distance and angle from the z-axis. A linear term in r is omitted since it implies a singularity at the origin. An approximate radius of the detector R (here 3.5 cm) is introduced to make the parameter a dimensionless. The angular dependence approximates in a simple way a misalignment or deviation of the crystal from axial symmetry. The phase θ_0 orientates the direction of maximum misalignment with respect to the reference coordinate system. This function defines the area correction. Integration is straightforward if the foil is a disk of radius R_f

and its centre coincides with the origin of coordinates:

$$F_a \;=\; 1 + \frac{1}{2}\, a \left(\frac{R_f}{R}\right)^2. \tag{B.7}$$

If the foil is a square the integration can be carried out easily only if the azimuthal dependence vanishes, i.e. the area correction depends only on $r^2 = x^2 + y^2$:

$$F_a \;=\; 1 + \frac{1}{2}\, a\, \frac{\pi}{3} \left(\frac{R_f}{R}\right)^2. \tag{B.8}$$

Now R_f is the radius of a circle of the same area as the square. In other foil geometries, integration is carried out numerically.

The correction for the variation of distance due to the finite thickness is chosen as the following:

$$f_z(z) \;=\; 1 + c\,\frac{z}{D} + d \left(\frac{z}{D}\right)^2. \tag{B.9}$$

This form is based on the first and second derivatives of the relative solid angle $(d\Omega/\Omega)/dz$ at z = 0, which are: -cosα(1 + cosα)/D and 3 cos$^2\alpha$ (1 + cosα)/D^2, respectively, where tgα = R/D. In our geometry the distance D of the reference plane z = 0 to the mean absorption plane of γ–rays in the crystal is found empirically to be about 5 cm.

Let (z_1, z_2) be the coordinates of the foil planes closest and farthest relative to the detector ($(z_2 = z_1 + L)$). The following correction is obtained:

$$F_z \;=\; 1 + \frac{c}{2D}(z_1 + z_2) + \frac{d}{3D^2}(z_1^2 + z_1\, z_2 + z_2^2). \tag{B.10}$$

In order to establish the parameters a ^{152}Eu/^{133}Ba point source is moved to various locations (centre of coordinates, four orientations at two radial distances) to map the count rate dependence on (r, θ) and along the z-axis. We note that low-energy γ-rays are absorbed closer to the surface of the crystal than high-energy ones. We therefore allow for an energy dependence in the linear coefficients, whereas the parameters R and D, which are in fact redundant and have been added for dimensional purposes, are kept fixed.

In order to estimate the self attenuation we start from the formula for a parallel γ-ray beam along the direction of z. Radiation emitted from a slice $(z, z + dz)$ has to cross a distance $L - z$ before exiting the foil:

$$F_{\mu_{in-foil}} \;=\; \frac{1}{L}\int_0^L e^{-\mu(L-z)}dz \;=\; \frac{1 - e^{-\mu L}}{\mu L}. \tag{B.11}$$

The foils are placed at a distance D from Ge detector in stacks of 2 or 3, allowing to save time and catch all short–lived activities. If the given foil is not at the bottom

of the considered stack, apart from self attenuation, transmission through the other foils has to be taken into account:

$$F_{\mu_{through-foil}} = e^{-\mu L}. \tag{B.12}$$

In reality, the radiations can hit the detector while having travelled various angles to the z–axis thus having a longer path than the thickness L. We account for this by using an effective μL extracted from transmission measurements with the ^{152}Eu/^{133}Ba source under a geometry similar to that used for the actual measurements.

The correction for attenuation is then: $F_\mu = F_{\mu_{in-foil}} \cdot F_{\mu_{through-foil}}$. Consider a stack of 3 foils: In (top), Ni and Al (bottom). The attenuation for In is obtained as a product of $F_{\mu_{in-In}}$ (Eq. B.11), $F_{\mu_{through-Ni}}$ and $F_{\mu_{through-Al}}$ (Eq. B.12), whereas for Al only $F_{\mu_{in-Al}}$ needs to be considered. Exact numbers are given in Table B.1.

TABLE B.1 Efficiency correction for In and Al foils. Foils were counted in the stacks, i.e. In on top and Al at the bottom of the stack of 3 foils, hence attenuation for In is obtained as a product of self attenuation (Eq. B.11) and transmission through Al and Ni foils (Eq. B.12), while for Al just self attenuation is considered. A reference point along the symmetry axis of the crystal was taken as an origin. The efficiency for a point at the center is known to 5%. The errors of the calculated corrections are not to be considered since the corrections are close enough to 1 (which is the limit meaning that there is no volume effect) so that their errors would have an impact larger that the 5% of the point source efficiency.

Foil	In	Al
Energy [keV]	336	1368
Efficiency at origin (ε_O)	0.02285	0.00656
Area (F_a)	0.9616	
Distance (F_z)	0.9832	0.9161
Attenuation (F_μ)	0.9392	0.9989
Total efficiency (ε)	0.02029	0.00621

Finally, the efficiency for the foil source is the product of all terms.

$$\varepsilon = \varepsilon_0 \, F_a \, F_z \, F_\mu. \tag{B.13}$$

The results of calculating the efficiency for In and Al foils are given in Table B.1. Efficiency (r=z=0) is measured at least before and after the counting, and once a week during the counting time.

The biggest contribution to the total uncertainty of the activation measurement comes from the Ge detector efficiency which is composed of: 3% RMS relative devi-

ation of fit from experimental points of 4 sources and 3% of accuracy on the strength of the best calibrated source (^{137}Cs).

B.2 Cross–section determination via activation

It is relevant to note that the activation method can be used not only to determine neutron yield (assuming σ to be known) but also cross–section (knowing the yield). The concept shall be presented based on ^{27}Al(n,α)^{24}Na and ^{27}Al(d,p α)^{24}Na reactions. For ^{27}Al(n,α), where Al is a thick foil placed on the rod few cm away from the target chamber, one can write (see Eq. 10.1):

$$A(E_\gamma, n) \;=\; \varepsilon \cdot b \cdot f_{irr} \cdot f_{count_n} \cdot n_{f_n}(t) \cdot \Omega_n \cdot \frac{I_e}{e} \cdot \int \sigma \frac{d^2\phi}{dE\, d\Omega} dE. \tag{B.14}$$

Here A, E_γ, ε, b, f_{irr}, f_{count}, n_f(t), Ω, I_e, σ, ϕ are, respectively, γ–peak area, γ–ray energy of interest – here 1368 keV, efficiency, branching ratio, factor that accounts for beam current measured by current irradiation, factor that accounts for counting, atomic density per cm^2(foil thickness t = 1.0 mm), solid angle, incident beam current, cross–section and neutron flux.

For ^{27}Al(d,p α)^{24}Na, where Al is a thin foil placed at the entrance window of the target container, we have:

$$A(E_\gamma, d) \;=\; \varepsilon \cdot b \cdot f_{irr} \cdot f_{count_d} \cdot n_{f_d}(t) \cdot \sigma \cdot \frac{I_e}{e}, \tag{B.15}$$

with 0.1 mm thick foil. ε in Eq. B.14 is for a foil source (volume) and ε in Eq. B.15 is for a cylinder of very small diameter along the beam. Thus the area factor in Eq. B.15 defaults to f_a = 1 (see also Eq. B.6).

After removing the common factors in Eq. B.14 and Eq. B.15, the remainder of Eq. B.14 is then:

$$A(E_\gamma, n) \;\sim\; f_{a_n} \cdot f_{count_n} \cdot n_{f_n}(t) \cdot \Omega_n \cdot \int \sigma \frac{d^2\phi}{dE\, d\Omega} dE \tag{B.16}$$

while that of Eq. B.15:

$$A(E_\gamma, d) \;\sim\; f_{count_d} \cdot n_{f_d}(t) \cdot \sigma. \tag{B.17}$$

The uncertainty of Eq. B.17 is dominated by the d+Al cross–section, while the remaining factors are well known.

Eq. B.16 and Eq. B.17 allow for a determination of the ratio between the n+Al overlap integral $\left(\sigma \frac{d^2\phi}{dE\, d\Omega} dE\right)$ and the cross–section (σ_{d+Al}). Assuming the flux in the overlap integral to be known, one gets σ_{d+Al}.

Similarly, knowing the cross–section one can get the flux. In this manner we cross–checked the correctness of the beam current measurement based on a Faraday cup in the September 2008 experiment.

B.3 Simplified treatment of ^{58}Co decay

^{58}Co has an isomer ($T_{1/2}$= 9 h) fully decaying to the ground state ($T_{1/2}$= 70 days). A thorough treatment is to record the decay curve of the 811 keV γ-ray emitted in the decay of the ground state and to disentangle the contributions from the deviation from the exponential decay. The relevant formula are presented in two steps for convenience.

The first step gives the number of nuclei at the end of an irradiation of duration t_i versus the production rates of isomer p_m and ground state p_g, assuming them to be constant:

$$n_m = \frac{1-e^{-\lambda_m t_i}}{\lambda_m}\ p_m \tag{B.18}$$

$$n_g = (\frac{1-e^{-\lambda_g t_i}}{\lambda_g} - \frac{e^{-\lambda_m t_i}-e^{-\lambda_g t_i}}{\lambda_g-\lambda_m})\ p_m + \frac{1-e^{-\lambda_g t_i}}{\lambda_g}\ p_g. \tag{B.19}$$

The second step gives the activity at a time t after the end of irradiation, when the foils are counted off line, as a function of the number of nuclei at the end of irradiation:.

$$a_m(t) = \lambda_m\, e^{-\lambda_m t}\ n_m \tag{B.20}$$

$$a_g(t) = \lambda_g\, \lambda_m\, \frac{e^{-\lambda_m t}-e^{-\lambda_g t}}{\lambda_g-\lambda_m}\ n_m + \lambda_g\, e^{-\lambda_g t}\ n_g. \tag{B.21}$$

In the particular case of ^{58}Co terms in $e^{-\lambda_m t}$ can be neglected against those in $e^{-\lambda_g t}$ after a waiting time of a few days:

$$a_g(t) = \lambda_g\, e^{-\lambda_g t}\, (C_m\, p_m\ +\ C_g\, p_g) \tag{B.22}$$

$$C_m = \frac{\lambda_m}{\lambda_m-\lambda_g}\,\frac{1-e^{-\lambda_m t_i}}{\lambda_m}\ +\ \frac{1-e^{-\lambda_g t_i}}{\lambda_g}\ -\ \frac{e^{-\lambda_m t_i}-e^{-\lambda_g t_i}}{\lambda_g-\lambda_m} \tag{B.23}$$

$$C_g = \frac{1-e^{-\lambda_g t_i}}{\lambda_g}. \tag{B.24}$$

Finally, the large difference of half–lives allows one to neglect the terms in $1/\lambda_m$. One thus directly measures the sum of the production rates:

$$a_g(t) = (1-e^{-\lambda_g t_i})\, e^{-\lambda_g t}\ (p_m + p_g). \tag{B.25}$$

B.4 Sundry photos part II

FIGURE B.2 It is non-trivial task to compress ^{13}C into a pellet. At JYFL a force of 30–50 kN has been put before it started to burn. The compressed pellet was supplied by undefined source in Russia protected by an industrial secret [65].

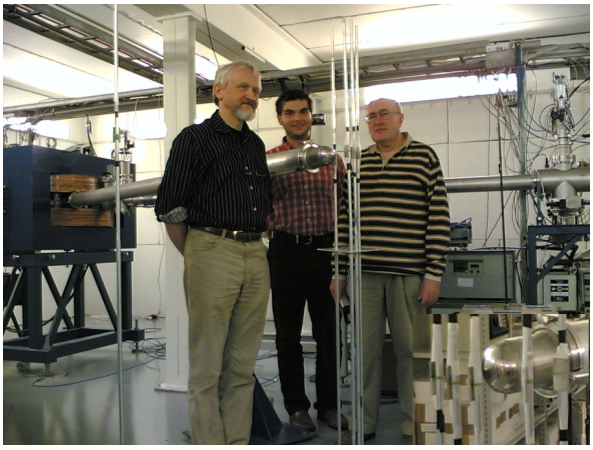

FIGURE B.3 Placement of the activation foils around the target chamber in the 2005 SPES run with insight on placement of the foils round target chamber. The alignment of the foils is checked by the author of the PhD and his supervisors.

Bibliography

[1] RHIC - Relativistic Heavy Ion Collider, see: `www.bnl.gov/rhic/`.

[2] CERN, the European Organization for Nuclear Research, see: `www.cern.ch`.

[3] ALICE geometry viewer by Ch. Holm Christensen, more at: `http://cholm.web.cern.ch/cholm/`.

[4] ALICE: PPR, Volume 1, J.Phys. G: Nuclear Part. Phys., **30** (2004) 1517, and PPR, Volume 2, J.Phys. G: Nuclear Part. Phys., **32** (2006) 1295.

[5] ALICE Collaboration, Technical Design Report 011 – Forward Detectors: FMD, T0, V0.

[6] V. Grigoriev *et al.*, Instrum. Exp. Tech.: **43** (2000) no. 6, 750.

[7] M. Bondila *et al.*, IEEE Trans. Nucl. Sc., **52** (2005) 1705.

[8] J. Bjorken and S. Drell, "Relativistic Quantum Mechanics", McGraw–Hill Book Company, N.Y., 1964.

[9] J. Rak, *Experimental Ultra–relativistic Heavy Ion Physics*, course held at fall 2006 at the University of Jyväskylä, Finland.

[10] K. Hikasa *et al.*, Phys. Rev. D **45** (1992) 1.

[11] The Particle Data Group particle codes, see more at: Review of Particle Properties, Phys. Lett. B **204** (1988) 113.

[12] ALICE Collaboration, ALICE-INT-2008-023 (2008) 1.

[13] A. Szczurek *et al.*, Zeitschrift für Physik A Hadrons and Nuclei, **337** (1990) 4.

[14] W.H. Trzaska, *Methods in high–energy physics*, course held at spring 2009 at the University of Jyväskylä, Finland.

[15] W. Thomé *et al.*, Nucl. Phys. B **129** (1977) 129.

[16] Ch. Holm Christensen, Ph.D. Thesis, Niels Bohr Institute, University of Copenhagen (2007).

[17] M. Bleicher *et al.*, Phys. Rev. C **62** (2000) 041901.

[18] K. Eskola, *Ultrarelativistic Heavy Ion Collisions*, course held at fall 2005 at the University of Jyväskylä, Finland.

[19] J. Alam *et al.*, J.Phys. G: Nuclear Part. Phys., **35** (2008) issue 10.

[20] W. Kienzle *et al.*, TOTEM Collaboration, "Total Cross Section, Elastic Scattering and Diffraction Dissociation at the LHC", CERN-LHCC-99-007, 1999.

[21] A. Morsch, "ALICE Luminosity and Beam Reqiurements", ALICE-INT-2001-10 (2001) 1.

[22] K. Safarik, CERN, Switzerland, private communication.

[23] R. Lacey, *Collective phenomena in Heavy Ion Collisions*, summer school course held in 2009 at the University of Jyväskylä, Finland.

[24] The Large Electron Positron collider, see: `http://public.web.cern.ch/public/en/Research/LEPExp-en.html`.

[25] ALICE Collaboration, Technical Design Report 014 – Electromagnetic Calorimeter.

[26] T. Malkiewicz, *et al.*, poster presentation at Quark Matter conference in India (2008).

[27] ALICE Collaboration, A. Ahmad et al., "ALICE: Technical proposal for A Large Ion Collider Experiment at the CERN LHC. No. 3 in LHC Tech. Proposal", CERN, Geneva, (1995).

[28] V.A. Kaplin, *et al.*, "Status of the ALICE T0 detector based on Cherenkov counters", ALICE/01–07/ Internal note/T0/ (2001).

[29] T. Sjostrand et al., "High-energy-physics event generation with PYTHIA 6.1", Comput. Phys. Commun. **135** (2001) 238,
see also: PYTHIA manual, LU TP 06-13, FERMILAB-PUB-06-052-CD-T, hep-ph/**0603175** (2006).

[30] R. Engel, "Hadronic Interactions of Photons at High Energies", Ph.D. Thesis, University of Siegen (1997).

[31] M. Gyulassy and X.N. Wang, "HIJING 1.0: A Monte Carlo program for parton and particle production in high-energy hadronic and nuclear collisions", Comput. Phys. Commun. **83**, 307 (1994).

[32] T. Karavicheva, Technical report on the ISTC Project no. 2880, Institute of Nuclear Research of the Russian Academy of Science (2009).

[33] K. Oyama, Physikalisches Institut Heidelberg, Germany, private commenication.

[34] OZ Optic Ltd., see more at:
`http://www.ozoptics.com/products/fiber_optic_delivery_systems.html`.

[35] Phillips Scientific, see: `http://www.phillipsscientific.com/phisci1.htm/`.

[36] Advanced Photonics systems, see:
`http://www.advancedphotonix.com/ap_products/`.

[37] J.–F. Große–Oetringhaus, CERN–Thesis–2009–033.

[38] A. Maevskaya, INR, Moscow, Russia, private communication.

[39] The most powerful of computer at CSC, based on Cray XT4/XT5 system, see:
`http://www.csc.fi/english`.

[40] Distributed computing environment in Finland, see:
`http://wiki.hip.fi/gm-fi/`.

[41] M. Oledzki, Master Thesis, University of Jyväskylä (2009).

[42] AMORE of ALICE – The ALICE Online Data Quality Monitoring framework, see:
`http://ph-dep-aid.web.cern.ch/ph-dep-aid/`.

[43] ALICE Collaboration, Technical Design Report 011 – Trigger, Data Acquisition, High Level Trigger, Control System.

[44] ALICE Collaboration, Technical Design Report 012 – Computing.

[45] ALICE Collaboration, Internal note, ALICE–INT–2003–038 (2003).

[46] ALICE Collaboration, Internal note, ALICE–INT–2003–039 (2003).

[47] Embedded Local Monitor Board developed at CERN, see:
`http://elmb.web.cern.ch/ELMB/ELMBhome.html`

[48] ALICE Detector Construction Data Base System Website:
`http://dcdbappl1.cern.ch:8080/dcdb/docs/general.html`.

[49] K. Ikematsu, *et al.*, Nucl. Instrum. Methods Phys. Res. **A411** (1998) 238.

[50] R. Brun, R. Hagelberg, M. Hansroul and J. C. Lassalle, "Geant: Simulation Program for Particle Physics Experiments. User Guide and Reference Manual", CERN-DD-78-2-REV (1978).

[51] V0 survey report, see: https://edms.cern.ch/document/835615/1.

[52] Offline Conditions DB framework developed by A. Colla, see: http://aliceinfo.cern.ch/Offline/Activities/ConditionDB.html#Intro.

[53] V.A. Kaplin, *et al.*, "Beam tests of the first prototype of a Cherenkov counter for ALICE T0 detector" ALICE–INT–2000–05.

[54] V.A. Grigorev, *et al.*, Nuclear Experimental Techniques, **43 6** (2000), 28.

[55] J.G. Rushbrooke and B.R. Webber, Phys. Rep. **44C** (1978) 1.

[56] T. Malkiewicz, *et al.*, "Luminosity Determination in ALICE with T0 and V0 detectors", to be published in Indian Journal of Physics.

[57] Particle Data Group, see: http://pdg.lbl.gov/.

[58] F. Nendaz, "Luminosity for V0", to be published.

---

[59] A. Bracco and A. Pisent, "Technical design for an Advanced Exotic Ion Beam Facility at LNL", LNL-INFN (REP) 181/02, June 2002, and see: http://www.lnl.infn.it.

[60] see: http://www.ganil.fr/research/developments/spiral2.

[61] Laboratori Nazionali di Legnaro, see: http://www.lnl.infn.it.

[62] O. Alyakrinskiy, A. Andrighetto, M. Barbui, S. Brandenburg, M. Cinausero, B. Dalena, P. Dendooven, E. Fioretto, G. Lhersonneau, V. Lyapin, G. Prete, G. Simonetti, L. Stroe, L. Tecchio, W. Trzaska Nucl. Instr. and Meth. in Phys. Research A **547** (2005) 616.

[63] National Institute of Nuclear Physics, see: http://www.infn.it/indexen.php.

[64] G. Lhersonneau, T. Malkiewicz, D. Vakhtin, V. Plokhoi, O. Alyakrinskiy, M. Cinausero, Ya. Kandiev, H. Kettunen, S. Khlebnikov, H. Penttilä, G. Prete, V. Rizzi, S. Samarin, L. Tecchio, W.H. Trzaska, G. Tyurin, Nucl. Instr. and Meth. in Phys. Research B **266** (2008) 4330.

[65] G. Lhersonneau, GANIL, Caen, France talks at SPIRAL2 week, 26-27th January 2009, Caen, http://spiral2ws.ganil.fr/2009/.

[66] The International Fusion Materials Irradiation Facility, see: http://www.frascati.enea.it/ifmif.

[67] P. Bém, V. Burjan, M. Götz, M. Honusek, V. Kroha, J. Novák, E. Šimečková, proceedings of 12^{th} Int. Seminar on Interaction of Neutrons with Nuclei: Neutron Spectroscopy, Nuclear Structure, Related Topics (2004) 38. ISBN 5-9530-0045-6.

[68] G. Lhersonneau, GANIL, Caen, France, private communication

[69] S. Essabaa et al., Nucl. Instr. and Meth. in Phys. Research B **204** (2003) 780.

[70] V.N. Panteleev et al., Nucl. Instr. and Meth. in Phys. Research B **266** (2008) 4247

[71] G. Lhersonneau et al., Nucl. Instr. and Meth. in Phys. Research B **266** (2008) 4326.

[72] Stopping and Range of Ions in Matter 2006 computer code, J.F. Ziegler, Annapolis, MD USA (2007), see: `www.srim.org`.

[73] G. Lhersonneau et al., Eur. Phys. J. A **9** (2000) 385.

[74] D. Ridikas, X. Ledoux et al., "Neutrons for Science (NfS) at SPIRAL 2", Internal report DAPNIA 05-30, CEA Saclay, France. (2005).

[75] A. Pisent et al., J. Phys. Conf. Ser. **41** (2006) 391-399

[76] O. Kofoed-Hansen, Proc. of 3rd Internat. Conf. on Nuclei Far from Stability, CERN Report **76-13** (1976).

[77] EXFOR basis; a short guide to Nuclear Reaction Data Exchange Format, rep. BNL-NCS-63380-2000/05, see:`http://www.nndc.bnl.gov/exfor3/compilations/ndc-206.pdf`.

[78] B. Herskind, Nucl. Phys. A, **447** (1986) 395.

[79] RADEF facility at JYFL, see: `https://www.jyu.fi/fysiikka/en/research/accelerator/radef`.

[80] Laser alignment system, Laser 670, CE No:3481/00/01.

[81] PHYSICA - a high level, interactive programming environment, see: `http://trshare.triumf.ca/ chuma/physica/homepage.html`.

[82] V. Plokhoi, Zababakhin Institute of Technical Physics, Snezhinsk, Russian Federation, private communication.

[83] M.A. Arnautova, Ya.Z. Kandiev, B.E. Lukhminsky, G.N. Malyshkin, Nucl. Geophys. 7 (1993) 407.

[84] K. Ranttila, JYFL, Jyväskylä, Finland, private communication.

[85] G. Lhersonneau et al., LNL annual report 2004, ISBN 88-7337-008-x, p.196, LNL annual report 2005, ISBN 88-7337-009-8, p.165, see also: http://www.lnl.infn.it.

[86] K. Kolos, Master Thesis, University of Jyväskylä (2009).

[87] T. Poikolainen, J. Kumpulainen, *Radiation Safety*, course held at the University of Jyväskylä, Finland.

[88] A.V. Kuznetsov, D.N. Vakhtin, Z. Radivojevič, I.D. Alkhazov, V.G. Lyapin, W.H. Trzaska, Nucl. Instr. and Meth. in Phys. Research A **477**, 372 (2002)

[89] G. Lhersonneau, T. Malkiewicz, D. Vakhtin, V. Plokhoi, O. Alyakrinskiy, M. Cinausero, Ya. Kandiev, H. Kettunen, S. Khlebnikov, H. Penttilä, G. Prete, V. Rizzi, S. Samarin, L. Tecchio, W.H. Trzaska, G. Tyurin, Nucl. Instr. and Meth. in Phys. Research A **576** (2007) 371.

[90] G. Lhersonneau et al., LNL annual report 2005, ISBN 88-7337-008-x, p.194.

[91] Evaluated (ENDF) and Experimental (EXFOR) Nuclear Reaction Data Files of National Nuclear Data Center, Brookhaven Laboratory, Upton, NY 11973-5000 (USA), see: http://www.nndc.bnl.gov.

[92] Z. Radivojevič, A. Andrighetto, P. Brandolini, P. Dendooven, V. Lyapin, L. Stroe, L. Tecchio, W. Trzaska, D. Vakhtin, Nucl. Instr. and Meth. in Phys. Research B **194** (2002) 251.

[93] P. Leleux, P. Lipnik, S. wa Kitwanga, J. Vanhorenbeeck, Nucl. Instr. and Meth. in Phys. Research A **556** (2006) 397.

[94] G. Lhersonneau, T. Malkiewicz, K. Kolos, M. Fadil, H. Kettunen, M.G. Saint-Laurent, A. Pichard, W.H. Trzaska, G. Tyurin, L. Cousin, Nucl. Instr. and Meth. in Phys. Research A **603** (2009) 228.

[95] M. Hass, D. Berkovits, T.Y. Hirsh, V. Kumar, M. Lewitowicz, F. de Oliveira and S. Veintraub, J. Phys. G: Nucl. Part. Phys. **35** (2008) 014042

[96] M. Hagiwara, T. Itoga, M. Baba, M.S. Uddin, N. Hirabayashi, T. Oishi, T. Yamauchi, Journal of Nuclear Materials **329-333** (2004) 218.

[97] J.P. Meulders, P. Leleux, P.C. Macq, C. Pirart, Phys. Med. Biol. **20** (1975) 235.

[98] K. Shin, K. Hibi, M. Fujii, Y. Uwamino, T. Nakamura, Phys. Rev. C **29** (1984) 1307.

[99] Z. Radivojevič, A. Honkanen, J. Äystö, V. Lyapin, V. Rubchenya, W.H. Trzaska, D. Vakhtin, G. Walter, Nucl. Instr. and Meth. in Phys. Research B **183** (2001) 212.

[100] A. Andrighetto, LNL, Legnaro, Italy, private communication.

[101] N. Pauwels et al., Nucl. Instr. and Meth. in Phys. Research B **160** (2000) 315, see also: `http://www.nea.fr/html/science/satif/satif5_pauwels.pdf`.

[102] S. Ménard, M. Mirea, F. Clapier, N. Pauwels, J. Proust, C. Donzeaud, D. Guillemaud-Mueller, I. Lhenry, A.C. Mueller, J.A. Scarpaci, O. Sorlin, Phys. Rev. Spec. Topics - Accelerators and Beams **2** (1999) 1.

[103] Monte Carlo N-Particle Transport Code System for Multiparticle and High Energy Applications, Version 2.6.0 (November 2007). Oak Ridge National Laboratory (ORNL/RSICC), USA.